UNIVERSITY OF CALIFORNIA, SAN DIEGO

Cell Membrane-Cloaked Nanoparticles for Targeted Therapeutics

A dissertation submitted in partial satisfaction of the requirements for the degree
Doctor of Philosophy

in

Bioengineering

by

Brian Tsengchi Luk

Committee in charge:

Professor Liangfang Zhang, Chair
Professor Shu Chien, Co-Chair
Professor Michael J. Heller
Professor Andrew C. Kummel
Professor Dong-Er Zhang

2016

The Dissertation of Brian Tsengchi Luk is approved, and it is acceptable in quality and form for publication on microfilm and electronically:

_____

_____

_____

_____
Co-Chair

_____
Chair

University of California, San Diego

2016

DEDICATION

This dissertation is dedicated to all those who have helped me reach this point in my life—from teachers to coaches to friends and colleagues; all have been a mentor to me in some shape or form. Without them, reaching this point would have been an impossibility, and I am eternally grateful for the support and guidance each person has provided. A special thanks goes to my loving family, who have supported me in all my endeavors and never cease to push me to be the person they know I can be.

EPIGRAPH

Nature composes some of her loveliest poems
for the microscope and the telescope.

Theodore Roszak

TABLE OF CONTENTS

LIST OF FIGURES

LIST OF TABLES

ACKNOWLEDGEMENTS

First and foremost, I would like to thank my advisor, Professor Liangfang Zhang. He has been a great influence in both my academic and personal life. I am deeply grateful for the opportunity to have worked in his laboratory for the past 5 years. I have learned so much and grown a great deal under his tutelage. Without his mentorship, I certainly would not have had all the opportunities I did over the course of my graduate career.

Not very much of my work could have been accomplished without the help and support of my fantastic labmates. Jack (Che-Ming) Hu was a big reason for the success I have had in the lab. From my first year, Jack was always there to offer mentorship and advice. Having also been a graduate student in the Bioengineering Department, Jack understood what I was going through and always advocated on my behalf. I know Jack was always on my side, and I could count on him for straightforward and candid guidance. I am grateful I had the opportunity to work with Jack, and am so happy that he has found success running his own lab at Academia Sinica in Taiwan. Ronnie Fang, similarly, has been not only a mentor and colleague, but also a great friend. We have been friends since high school, and I could not imagine having to pursue my Ph.D. without him. He has provided so much guidance to me even starting in high school. Ronnie is a confident individual who will give no less than 100% to any endeavor he chooses to pursue. Though we are the same age, I consider Ronnie a role model—someone I deeply respect and strive to emulate. I am appreciative to everyone in Dr. Zhang's lab, all of whom have contributed to my

growth not only as a researcher, but also as a person: Dr. Weiwei Gao, Dr. Soracha Thamphiwatana, Dr. Xiaoli Wei, Jonathan Copp, Pavimol Angsantikul, Ashley Kroll, Cody Carpenter, Victoria Fu, Diana Dehaini, Jie Gao, Yao Jiang, Dr. Santosh Aryal, Dr. Zhiqing Pang, Fei Wang, Dr. Dissaya Pornpattananangkul, and many others.

I would like to thank both the National Institutes of Health F31 Fellowship and the Cancer Researchers in Nanotechnology Fellowship for providing the funding for me to pursue my graduate studies. These fellowships not only provided the funding necessary for me to complete my studies, but they also offered me opportunities to present my work orally and in writing. These invaluable experiences strengthened important skills I will need as I begin my next venture.

I would like to thank the Siebel Foundation for acknowledging my work and for the extremely generous award they bestowed upon me to supplement my studies in my final year as a Ph.D. student.

I am grateful to the Bioengineering department at UC San Diego, with all its faculty and administrative staff, for their help and support over the years. In particular, Jan Lenington was such a supportive member of the department. Without her help, I doubt that my tenure as a graduate student would have gone nearly as smoothly.

Finally, I would like to acknowledge UC San Diego for being my home for the past five years. It is here that I have met some of the greatest people and lifelong friends. It’s hard to believe that five years have passed by so quickly. It seems like just yesterday I was starting my graduate studies, ready to hunker down and take on the daunting task of dedicating a significant portion of my life to earning a Ph.D. UCSD

has grown along with me over the last several years, and I am excited to see how it continues to develop and mature.

Chapter 1, in full, is a reprint of the material as it appears in *Nanoscale*, 2014, Che-Ming Hu, Ronnie Fang, Brian Luk and Liangfang Zhang. The dissertation author was a major contributor and co-author of this paper.

Chapter 2, in full, is a reprint of the material as it appears in *Nanoscale*, 2014, Brian Luk, Che-Ming Hu, Ronnie Fang, Diana Dehaini, Cody Carpenter, Weiwei Gao, and Liangfang Zhang; *Nanoscale*, 2013, Che-Ming Hu, Ronnie Fang, Brian Luk, Kevin Chen, Cody Carpenter, Weiwei Gao, Kang Zhang, and Liangfang Zhang.

Chapter 3, in full, is a reprint of the material as it appears in *Theranostics*, 2016, Brian Luk, Ronnie Fang, Che-Ming Hu, Jonathan Copp, Soracha Thamphiwatana, Diana Dehaini, Weiwei Gao, Kang Zhang, Shulin Li, and Liangfang Zhang; *Nanoscale*, 2013, Ronnie Fang, Che-Ming Hu, Kevin Chen, Brian Luk, Cody Carpenter, Weiwe Gao, Shulin Li, Dong-Er Zhang, Weiyue Lu, and Liangfang Zhang; and *Nature*, 2015, Che-Ming Hu, Ronnie Fang, Kuei-Chun Wang, Brian Luk, Soracha Thamphiwatana, Diana Dehaini, Phu Nguyen, Pavimol Angsantikul, Cindy Wen, Ashley Kroll, Cody Carpenter, Manikantan Ramesh, Vivian Qu, Sherrina Patel, Jie Zhu, William Shi, Florence Hofman, Thomas Chen, Weiwei Gao, Kang Zhang, Shu Chien, and Liangfang Zhang. The dissertation author was either the primary investigator or a major contributor and co-author of these papers.

Chapter 4, in full, is a reprint of the material as it appears in *Nature Nanotechnology*, 2013, Che-Ming Hu, Ronnie Fang, Jonathan Copp, Brian Luk, and

Liangfang Zhang; *Advanced Materials*, 2015, Fei Wang, Weiwei Gao, Soracha Thamphiwatana, Brian Luk, Pavimol Angsantikul, Qiangzhe Zhang, Che-Ming Hu, Ronnie Fang, Jon Copp, Dissaya Pornpattananangkul, Weiyue Lu, and Liangfang Zhang; *ACS Nano*, 2015, Zhiqing Pang, Che-Ming Hu, Ronnie Fang, Brian Luk, Weiwei Gao, Fei Wang, Erdembileg Chuluun, Pavimol Angstantikul, Soracha Thamphiwatana, Weiyue Lu, Xinguo Jiang, and Liangfang Zhang; and *Proceedings of the National Academy of Sciences USA*, 2014, Jonathan Copp, Ronnie Fang, Brian Luk, Che-Ming Hu, Weiwei Gao, Kang Zhang and Liangfang Zhang. The dissertation author was a major contributor and co-author of these papers.

Chapter 5, in full, is a reprint of the material as it appears in *Nature Nanotechnology*, 2013, Che-Ming Hu, Ronnie Fang, Brian Luk, and Liangfang Zhang, and *Advanced Functional Materials*, 2014, Fei Wang, Ronnie Fang, Brian Luk, Che-Ming Hu, Soracha Thamphiwatana, Diana Dehaini, Pavimol Angsantikul, Ashley Kroll, Zhiqing Pang, Weiwei Gao, Weiyue Lu, and Liangfang Zhang. The dissertation author was a major contributor and co-author of these papers.

VITA

2011 B.S. in Materials Science & Engineering, Stanford University

2014 M.S. in Bioengineering, University of California, San Diego

2016 Ph.D. in Bioengineering, University of California, San Diego

PUBLICATIONS

1. Chen, W.; Zhang, Q.; Luk, B.T.; Fang, R.H.; Liu, Y.; Gao, W.; Zhang, L. “Coating nanofiber scaffolds with beta cell membrane to promote cell proliferation and function”, *Nanoscale*, 2016, 8, 10364-10370.

2. Luk, B.T.; Fang, R.H.; Hu, C.M.; Copp, J.A.; Thamphiwatana, S.; Dehaini, D.; Gao, W.; Zhang, K.; Li, S.; Zhang, L. "Safe and immunocompatible nanocarriers cloaked in RBC membranes for drug delivery to treat solid tumors", *Theranostics*, 2016, 6, 1004-1011.

3. Wang, F.; Fang, R.H.; Luk, B.T.; Hu, C.M.; Thamphiwatana, S.; Dehaini, D.; Angsantikul, P.; Kroll, A.V.; Pang, Z.; Gao, W.; Lu, W.; Zhang, L. "Nanoparticle-based anti-virulence vaccine for the management of mechicillin-resistant Staphylococcus aureus skin infection", *Advanced Functional Materials*, 2016, 26, 1628-1635.

4. Luk, B.T.; Zhang, L. "Cell membrane-camouflaged nanoparticles for drug delivery", *Journal of Controlled Release*, 2015, 220, 600-607.

5. Hu, C.M.; Fang, R.H.; Wang, K-C.; Luk, B.T.; Thamphiwatana, S.; Dehaini, D.; Nguyen, P.; Angsantikul, P.; Wen, C.; Kroll, A.; Carpenter, C.; Ramesh, M.; Qu, V.; Patel, S.; Zhu, J.; Shi, W.; Hofman, F.; Chen, T.; Gao, W; Zhang, K.; Chien, S.; Zhang, L. "Nanoparticle biointerfacing by platelet membrane cloaking", *Nature*, 2015, 526, 118-121.

6. Fang, R.H.; Luk, B.T.; Hu, C.M.; Zhang, L. "Engineered nanoparticles mimicking cell membranes for toxin neutralization", *Advanced Drug Delivery Reviews*, 2015, 90, 69-80.

7. Pang, Z.; Hu, C.M.; Fang, R.H.; Luk, B.T.; Gao, W.; Wang, F.; Chuluun, E.; Angsantikul, P.; Thamphiwatana, S.; Lu, W.; Jiang, X.; Zhang, L. "Detoxification of organophosphate poisoning using nanoparticle bioscavengers", *ACS Nano*, 2015, 9, 6450-6458.

8. Wang, F.; Gao, W.; Thamphiwatana, S.; Luk, B.T.; Angsantikul, P.; Zhang, Q.; Hu, C.M.; Fang, R.; Copp, J.; Pornpattananangkul, D.; Lu, W.; Zhang, L. "Hydrogel retaining toxin-absorbing nanosponges for local treatment of methicillin-resistant Staphylococcus aureus infection", *Advanced Materials*, 2015, 27, 3437-3443.

9. Gao, W.; Fang, R.H.; Thamphiwatana, S.; Luk, B.T.; Li, J.; Angsantikul, P.; Zhang, Q.; Hu, C.M.; Zhang, L. "Modulating antibacterial immunity via bacterial membrane-coated nanoparticles", *Nano Letters*, 2015, 15, 1403-1409.

10. Luk, B.T.; Zhang, L. "Current advances in polymer-based nanotheranostics for cancer treatment and diagnosis", *ACS Applied Materials & Interfaces*, 2014, 6, 21859-21873.

11. Copp, J.A.; Fang, R.H.; Luk, B.T.; Hu, C-M.; Gao, W.; Zhang, K.; Zhang, L. "Clearance of pathologic antibodies using biomimetic nanoparticles", *Proceedings of the National Academy of Sciences USA*, 2014, 111, 13481-13486.

12. Fang, R.H.; Hu, C.M.; Luk, B.T.; Gao, W.; Copp, J.A.; Tai, Y.; O'Connor, D.E.; Zhang, L. "Cancer cell membrane-coated nanoparticles for anticancer vaccination and drug delivery", *Nano Letters*, 2014, 14, 2181-2188.

13. Luk, B.T.; Hu, C.M.; Fang, R.H.; Dehaini, D.; Carpenter, C.; Gao, W.; Zhang, L. " Interfacial interactions between natural RBC membranes and synthetic polymeric nanoparticles", *Nanoscale* 2014, 6, 2730-2737.

14. Hu, C.M.; Fang, R.H.; Luk, B.T.; Zhang, L. "Polymeric nanotherapeutics: clinical development and advances in stealth functionalization strategies", *Nanoscale* 2013, 6, 65-75.

15. Hu, C-M.; Fang, R.H.; Luk, B.T.; Zhang, L. "Nanoparticle-detained toxins for safe and effective vaccination", *Nature Nanotechnology* 2013, 8, 933-938.

16. Fang, R.H.; Hu, C.M.; Chen, K.; Luk, B.T.; Carpenter, C.; Gao, W.; Li, S.; Zhang, D-E.; Lu, W.; Zhang, L. "Lipid-insertion enables targeting functionalization of erythocyte membrane-cloaked nanoparticles", *Nanoscale* 2013, 5, 8884-8888.

17. Gao, W.; Hu, C.M.; Fang, R.H.; Luk, B.T.; Su, J.; Zhang, L. "Surface functionalization of gold nanoparticles with red blood cell membranes", *Advanced Materials* 2013, 25, 3549-3553.

18. Hu, C.M.; Fang, R.H.; Copp, J.A.; Luk, B.T.; Zhang, L. "A biomimetic nanosponge that absorbs pore-forming toxins", *Nature Nanotechnology* 2013, 8, 336-340.

19. Hu, C.M.; Fang, R.H.; Luk, B.T.; Chen, K.; Carpenter, C.; Gao, W.; Zhang, K.; Zhang, L. "'Marker-of-self' functionalizaton of nanoscale particles through a top-down cellular membrane coating approach", *Nanoscale* 2013, 5, 2664-2668.

20. Luk, B.T.; Fang, R.H.; Zhang, L. "Lipid- and polymer-based nanostructures for cancer theranostics", *Theranostics* 2012, 2, 1117-1126.

ABSTRACT OF THE DISSERTATION

Cell Membrane-Cloaked Nanoparticles for Targeted Therapeutics

by

Brian Tsengchi Luk

Doctor of Philosophy in Bioengineering

University of California, San Diego, 2016

Professor Liangfang Zhang, Chair
Professor Shu Chien, Co-Chair

The advent of nanoparticle-based delivery systems has made a significant impact on clinical patient outcomes. In recent decades, myriad nanoparticle-based therapeutic agents have been developed for the treatment and management of ailments such as cancer, diabetes, pain, bacterial infections, and asthma, among many others.

Nanotherapeutics offer many distinct advantages over conventional free drug formulations. For example, nanoparticles are able to accumulate at tumor sites by extravasation through leaky vasculature at tumor sites via the enhanced permeability and retention (EPR) effect; nanoparticles can also be tailored to have desirable characteristics, such as prolonged circulation in the blood stream, improved drug encapsulation, and sustained or triggered drug release. Currently, a growing number of nanoformulations with favorable pharmacological profiles and promising efficacy are being used in clinical trials for the treatment of various cancers. Building on the success of these encouraging clinical results, new engineering strategies have emerged that combine synthetic nanoparticles with natural biomaterials to create nature-inspired biomimetic delivery systems.

The work presented in this dissertation focuses on the biointerfacing between synthetic and natural materials, namely in the manifestation of cell membrane-coated nanoparticles. By exploiting the natural functionalities of source cell membranes, cell membrane-cloaked nanoparticles have huge potential in the delivery of therapeutic agents for a variety of applications. The first portion of this thesis will focus on understanding the fundamentals underlying cell membrane coating on synthetic nanoparticles. First introduced in 2011, cell membrane-cloaked nanoparticles showed immediate promise in drug delivery applications, but further understanding was necessary to be able to harness the full potential of the membrane coating platform. The first section provides further insight into the interfacial interactions between membranes and synthetic nanoparticles, and how the membrane coating technique

faithfully translates the complexities of natural cellular membranes to the nanoscale. The following three sections explore potential therapeutic applications of membrane-coated nanoparticles for targeted drug delivery, biodetoxification, and immunomodulation. Ultimately, cell membrane-cloaked nanoparticles have the potential to significantly change the landscape of nanomedicine. The novel applications presented in this thesis are just a few of many examples currently being researched, with countless more avenues waiting to be explored.

Chapter 1

Introduction

Introduction

The advent of nanoparticle-based drug delivery systems has made a significant impact in the clinic [1]. In the last two decades, a plethora of nanoparticle-based therapeutic and diagnostic agents have been developed for the treatment of cancer, diabetes, pain, bacterial infections, asthma, etc. [2, 3]. Among the different nanotherapeutics, polymeric nanoparticles represent a unique class of nanocarriers that promises increased efficacy through controlled drug delivery to diseased sites. Well recognized advantages and features of polymeric nanoparticles include sustained drug release, delivery of poorly soluble drugs, multi-drug co-delivery, and the ability to be functionalized with targeting ligands for targeted delivery [4-9]. In addition, many biocompatible and biodegradable polymers, such as poly($_{D,L}$-lactide-*co*-glicolide) (PLGA), poly(lactic acid) (PLA), poly(glutamic acid) (PGA), poly(caprolactone) (PCL), *N*-(2-hydroxypropyl)-methacrylate copolymers (HPMA), and poly(amino acids) [10, 11], provide safe and non-toxic nanoparticle building blocks primed for *in vivo* administration. Extensive research efforts in nanoparticle design have enabled advanced functionalities including disease targeting [2, 12-15], stimuli-responsive triggers [16-18], combinatorial drug encapsulation [19-21], and temporally controlled drug release [22, 23]. Aided by recent developments in polymer engineering and preparation methods, polymeric nanoparticles can now be reliably manufactured and fine-tuned toward optimal performance [24-27]. These improved manufacturing techniques significantly benefit the bench-to-bedside translation of polymeric

nanotherapeutics, giving rise to a growing number of nanoformulations in clinical use or test. The increasing number of nanoparticles in clinical and preclinical studies also helps fuel continuing research interest in the various interactions between biological components and synthetic nanomaterials; much effort is devoted to developing novel immune-evasive platforms that promise enhanced pharmacokinetic profiles and therapeutic efficacy. In this article, we highlight recent clinical development regarding polymeric nanotherapeutics and review emerging stealth technologies aimed at passivating nanoparticles against the multi-faceted nature of immune clearance.

1.1 Clinical Development of Polymeric Nanotherapeutics

The advent of "stealth" nanoparticles has made great impact on nanoparticle drug delivery, particularly toward cancer treatment. First introduced in 1994 in a landmark paper by Langer and his colleagues [28], polymeric nanoparticles grafted with polyethylene glycol (PEG) can circulate in blood for an extended period of time owing to the PEG's passivation effect. By providing a hydration layer and steric barrier surrounding the polymeric core, PEG grafting can reduce non-specific binding of serum proteins to the particles, thereby reducing their clearance by cells of the mononuclear phagocytic system (MPS) [29, 30]. These long-circulating nanoparticles have been shown to benefit drug delivery to the tumor microenvironment owing to the enhanced permeation and retention (EPR) phenomenon [31-33]. A number of formulations based on PEGylated polymeric nanoparticles are currently undergoing clinical trials (Table 1.1). In general, these drug-loaded nanoparticles exhibit

prolonged systemic circulation lifetime, sustained drug release kinetics, and better tumor accumulation as compared to small-molecule drugs [34-37]. Several notable polymeric nanoformulations in clinical trial are reviewed herein.

Table 1.1 PEGylated polymeric NPs in clinical trials.

Agent	Formulation	Company	Indication	Status	Ref
SP1049C	PEGylated glycoprotein micelle of doxorubicin	Supratek Pharma Inc.	Various cancers	Phase II	[51]
CRLX101	PEG-cyclodextrin + camptothecin	Cerulean Pharma	Various cancers	Phase II	[47, 52]
NC-6004	PEG-poly(amino acid) + cisplatin	NanoCarrier Co.	Various cancers	Phase II	[53]
NK105	PEG-poly(aspartate) + paclitaxel	Nippon Kayaku Co., Ltd.	Various cancers	Phase III	[54, 55]
NK911	PEG-poly(aspartate) + doxorubicin	Nippon Kayaku Co., Ltd.	Various cancers	Phase I	[56]
NK012	Polymeric micelle SN-38	Nippon Kayaku Co., Ltd.	Various cancers	Phase II	[57]
BIND-014	PEG-PLGA + docetaxel	BIND Bioscience	Various cancers	Phase II	[27]
CALAA-01	Transferrin-targeted PEG-cyclodextrin + siRNA	Calando Pharmaceuticals	Solid tumors	Phase I	[50]
Genexol-PM	PEG-PLA + paclitaxel	Sorrento Therapeutics	Various cancers	Phase II	[41, 42, 58]

Genexol-PM was the first commercialized polymeric nanotherapeutic and it is currently approved in South Korea for the treatment of metastatic cancer, non-small cell lung cancer, and ovarian cancer. Comprising of paclitaxel and monomethoxy poly(ethylene glycol)-block-poly($_{D,L}$-lactide) (mPEG-PLA) [38], the ~25 nm micellar formulation highlights the advantage of polymeric nanocarriers in delivering poorly soluble chemotherapy drugs. Compared to Taxol®, a paclitaxel formulation solubilized in castor oil Cremophor EL, Genexol-PM has also demonstrated stronger effectiveness as a radiosensitizer for the treatment of non-small cell lung cancer while decreasing the exposure of paclitaxel in normal tissues [39]. These benefits can be attributed to the physicochemical properties of the nanocarriers, which allow them to

exploit the EPR phenomenon in tumors. In addition, Genexol-PM allows for a higher maximal tolerated dose (MTD) of paclitaxel as compared to Taxol [40], which contains a solvent that may cause allergic reactions. The formulation has undergone Phase II clinical trials in the United States and is undergoing several other trials involving combinations with other chemotherapeutics [41, 42].

CRLX101 is another example of an anti-cancer drug-loaded polymeric nanoparticle currently undergoing human clinical trials. The formulation is comprised of cyclodextrin-poly(ethylene glycol) copolymer chemically conjugated to camptothecin (CPT), a potent anticancer drug that inhibits topoisomerase 1. The cyclodextrin on CRLX101 is capable of forming inclusion complexes with hydrophobic small molecules, which helps address the poor water solubility issue of CPT. CRLX101 containing ~10wt% CPT are prepared from the self assembly of CPT-conjugated copolymers, which forms nanoparticles 20 to 60 nm in size [43]. The morphological and stealth features of the nanoparticles significantly prolong their residence time in the bloodstream, with a circulation half-life of approximately 1 day in rodents [44]. Tail vein injection of CRLX101 to mice bearing tumor xenografts has revealed that the nanoparticle can localize at the tumoral sites. The formulation has also shown increased anti-tumor activity in murine models compared to FDA-approved CPT analogues [45, 46]. CRLX101 is currently in a Phase II clinical trial and recent publications on the platform show strong evidence that results from animal studies are translatable to humans [47].

Also comprising of cyclodextrin-containing polymer is CALAA-01, which is a

nanoformulation carrying siRNA for targeted RNA interference (RNAi) therapy. These nanoparticles are prepared via the self-assembly of cyclodextrin-containing polymers in the presence of nucleic acids, which yields colloidal particles approximately 70 nm in diameter [48]. The particles are also stabilized with PEG and functionalized with a targeting ligand, transferrin, through the host-guest inclusion of adamantane tethers and cyclodextrins. The platform highlights the application of nanoengineering design to overcome the many physiological delivery barriers and facilitate effective delivery of fragile therapeutic cargoes. By providing a protective barrier that precludes siRNA from plasma degradation and renal clearance, CALAA-01 enables the nucleic acid-based therapeutic to be systemically administered. In addition, the targeting ligands are incorporated to promote the intracellular uptake of CALAA-01 [49], and the nanocarriers readily undergo particle disassembly in acidic environments to promote endosomal escape. These design rationales serve to address the many challenges of siRNA therapeutics, including poor stability and inadequate transfection efficiency. CALAA-01 is currently undergoing a Phase Ib clinical trial against melanoma; it has demonstrated evidence of successful RNAi in humans [50].

BIND-014 is another polymeric nanoformulation consisting of PEGylated PLA co-polymer loaded with docetaxel, an anti-mitotic chemotherapeutic. Particularly notable in BIND-014 is the incorporation of targeting ligands specific for prostate-specific membrane antigen (PSMA), a surface marker highly expressed in prostate cancer cells and the neovasculature of other solid malignant tumors. The development of BIND-014 involved the screening of a combinatorial library of hundreds of

nanoparticle formulations, and an optimal formulation was identified among particles with varying sizes, surface hydrophilicity, drug loading, and drug release kinetics. This rigorous screening process resulted in a robust formulation that balances the stealth properties of the PEG coating and the targeting capabilities of surface ligands. As a result, BIND-014 was shown to increase the concentration of docetaxel in mouse xenografts by up to an order of magnitude compared to conventional docetaxel formulations, resulting in a significant improvement in the drug's anti-tumor activity without increasing its toxicity. Thorough testing of the BIND-014 formulation was carried out in other animals as well, such as rats and nonhuman primates, prior to clinical translation. BIND-014 demonstrated differentiated efficacy in preclinical models of both prostate and non-prostate solid tumors. In Phase I clinical studies, the formulation was well-tolerated and demonstrated predictable and manageable toxicities [27]. There are currently two Phase II clinical trials to evaluate the therapeutic activity of BIND-014 in non-small cell lung carcinoma and metastatic, castration-resistant prostate cancer. Other examples of polymeric nanotherapeutics can be found in Table 1.1.

1.2 Development of Stealth Functionalization Strategies

A common feature behind the many polymeric nanotherapeutics in clinical development is their stealth functionality, which enables prolonged pharmacokinetics and improved biodistribution of the particles. Currently, PEG remains the gold standard for stealth functionalization in clinics, and optimization of PEG coating on

polymeric nanoparticles has been extensively studied [59]. Stealth functionality imparted by PEG to nanoparticles is found to be strongly influenced by its length and surface density on nanoparticle surfaces [60-64]. PEG can adopt either a mushroom or a brush-like conformation depending on its length and density; scarcely distributed long PEG favors mushroom conformation and densely packed, short PEG favors brush-like conformation [60, 65]. Generally speaking, higher surface coverage of PEG increases the circulation time of nanoparticles, and PEG with a molecular weight of 5000 Da provides the ideal surface coating for stealth functionalization [23, 60].

While PEGylation remains the most widely accepted standard for stealth functionalization, recent observations of anti-PEG immunological response have prompted much scrutiny over the immunological implications of PEG [66]. There has been conflicting evidence in literature in regards to the induction of PEG-specific antibodies [67-69], and it has been proposed that repeated administration of PEGylated nanoparticles leads to the production of anti-PEG antibodies, which subsequently increases phagocytosis by the reticuloendothelial system (RES) and results in an accelerated blood clearance phenomenon [70-72]. In addition, complement activation through both the classical and alternative pathways by PEG has been reported [73-75]. While fine-tuning of PEG length and density has shown much promise in attenuating PEG-associated immune responses [76, 77], researchers have also begun to explore alternative long-circulation strategies in aim of developing nanoparticles with better compatibility and improved performance. Alternative polymer-based stealth functionalization strategies for emerging polymeric

nanotherapeutics are summarized in Figure 1.1 and described in the following sections.

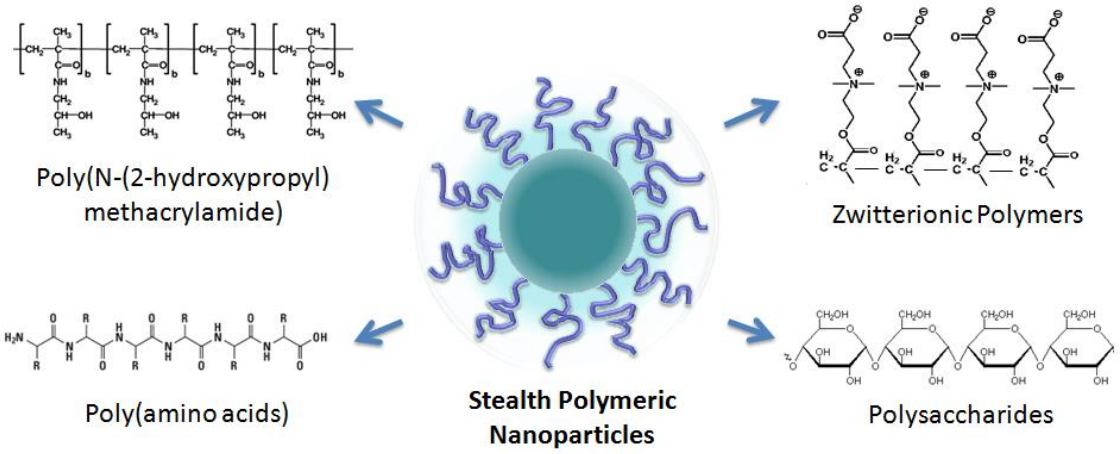

Figure 1.1 Hydrophilic polymers for nanoparticle stealth functionalization.

1.2.1 Synthetic Polymers for Stealth Functionalization

Poly [N-(2-hydroxypropyl) methacrylamide] (HPMA) is a hydrophilic polymer with multiple functionalization sites. Upon conjugation with hydrophobic drug molecules, unimolecular micelles can form via a self-assembly process. Such HPMA-drug conjugates have been extensively studied for drug delivery applications [76-80]. In contrast to PEG, the multiple functionalization sites on HPMA allow for multiple therapeutic compounds to be covalently attached. Drug-loaded unimolecular HPMA has shown significantly improved pharmacokinetic profiles as compared to free drugs [77, 81] and have entered various stages of clinical trials [82-84]. Owing to HPMA's hydrophilicity, biocompatibility, and lack of immunogenicity [80, 85], the polymer has also drawn much research interest as a stealth functionalization candidate in the

development of polymeric nanocarriers. HPMA has been applied in place of PEG to stabilize polycation/DNA micellar complexes [86, 87]. Neutral hydrophilic HPMA shells have been grafted onto gene delivery vesicles with the aim to minimize plasma protein interactions and prolong circulation time [88]. Core-shell structured nanoparticles with a biodegradable polymeric core and a hydrophilic HPMA corona have also been prepared through the self-assembly of block copolymers. Nanoparticles consisting of HPMA/poly(caprolactone)(PCL) and of HPMA/poly($_{D,L}$-lactide) (PLA) have been prepared using both A-B-A triblock copolymers and star-shaped block copolymers [89-91]. For both HPMA/PCL and HPMA/PLA copolymers, particles approximately 100-150 nm in size have been prepared. Encapsulation of hydrophobic therapeutic cargoes has also been demonstrated in these HPMA grafted nanocarriers using indomethacin and paclitaxel as model drugs.

Another type of synthetic polymer that has emerged as a compelling alternative to PEG is betaine-based polymers, which are zwitterionic materials with ultralow-fouling properties. Similar to many hydrophilic polymers, the zwitterionic material achieves its low fouling property through its hydration effect. However, in contrast to most hydrophilic polymers that bind water through hydrogen bonding, the zwitterionic material possesses a stronger hydration effect attributable to electrostatic interactions [92, 93]. Polybetaine functionalized surfaces have shown significantly reduced non-specific protein adsorption [94-97] and biofilm formation [98-100]. Therapeutic materials coated in polybetaines also display unique advantages over those decorated in other hydrophilic polymers. Notably, therapeutic proteins stabilized with

poly(carboxybetaine) (PCB) display higher substrate binding affinity as compared to those conjugated with PEG. Such enhanced bioactivity is attributed to the superhydrophilic nature of PCB in contrast to the inherent amphiphilicity in PEG [101]. Implant materials containing PCB also elicit minimal foreign-body reaction owing to the polymer's ultralow-fouling properties [102]. Numerous nanoparticle platforms, including gold [103], iron oxide [104], silica [103], liposomes [105], and hydrogels [105-107], have been successfully functionalized with PCB, which helps improve the particles' colloidal stability in protein solutions. Regarding polymeric nanoparticles, PCB-grafted PLGA nanoparticles have been prepared using PCB-PLGA block copolymers [108]. The sharp polarity contrast between the PCB and PLGA blocks allows for efficient nanoparticle self-assembly. Uniquely, the nanoparticles retain their stability even under lyophilization conditions in the absence of cryoprotectant, which can likely be attributed to PCB's strong hydration. A biodistribution study of PCB-grafted and PEG-grafted poly-(acrylic acid)-b-poly(lactide) nanoparticles also reveals comparable *in vivo* survival in the bloodstream [109], affirming PCB's potential as a stealth coating.

Many other synthetic polymers have been explored as alternative stealth coatings for nanocarriers. Examples of these polymers include poly(vinyl alcohol) (PVA) [110, 111], poly(oxazoline) [112], poly(4-acryloylmorpholine) (PAcM) [113, 114], poly(N,N-dimethylacrylamide) (PDAAm) [114, 115], and poly(N-vinyl-2-pyrrolidone) (PVP) [113-115]. In a pharmacokinetic study using a rat model, Ishihara et al. examined the circulation half-lives of polymeric nanoparticles grafted with PVP,

PAcM, and PDAAm and compared the results to that of PEGylated nanoparticles [114]. All four polymers successfully extended the nanoparticle residence time in the circulation, and PEG yielded the longest half-life among the group. Interestingly, however, upon repeated injections, PEG-grafted nanoparticles exhibited accelerated blood clearance phenomenon whereas PVP-, PAcM-, and PDAAm-grafted particles did not. The accelerated clearance was found to correlate with the production of IgM antibodies, which was elicited by PEG but not by PVP. The study highlights potential alternative materials for developing stealth nanocarriers with improved performance.

1.2.2 Biopolymers for Stealth Functionalization

Poly(amino acid)s (PAAs) are a major class of biopolymers that have been explored as stealth coating for nanocarriers. As compared to synthetic polymers, PAAs are susceptible to degradation by proteases, which helps reduce the risks of *in vivo* accumulation [116]. Deierkauf et al., first examined the anti-phagocytic property of poly(amino acid) by grafting polystyrene latex beads with polyglutamic acid. The amino acid coating proved to be an effective inhibitor of particle uptake, which was ascribed to the electrostatic repulsion between the amino acids and the external surface charge on the polymorphonuclear leukocytes [117]. The potential of PAAs in improving nanoparticles' pharmacokinetic profiles was further demonstrated on liposomes by Romberg et al., who showed that liposomes coated with poly(hydroxyethyl-L-asparagine) (PHEA) can outlast PEG-coated liposomes in the circulation [118]. Upon intravenous administration in rat at less than 0.25 μmol/kg,

PHEA-coated liposomes showed superior survival in the blood as compared to PEG-coated liposomes. In addition, upon repeated injections, PHEA-coated liposomes exhibited a less pronounced accelerated blood clearance phenomenon. The stealth functionality and the excellent biodegradability of PAAs motivated the development of PAA-grafted polymeric nanoparticles. Block copolymers consisting of biodegradable polymers and PAAs have been prepared with different types of amino acids, including poly(aspartic acid) [119, 120], poly(glutamic acid) [121-123], poly(cysteine) [124], and poly(lysine) [125]. Generally, a hydrophilic peptide sequence is conjugated with a hydrophobic polymer such as PLA for the self-assembly of PAA-grafted nanoparticles.

Polysaccharides are another class of hydrophilic biopolymers that are frequently used to coat nanoparticles. These polymers are a desirable coating material for nanoparticle development owing to their excellent biodegradability and low immunogenicity [126-128]. These biopolymers provide a hydrated surface that can be likened to the dense, carbohydrate-rich glycocalyx on cellular surfaces. In examining the effect of polysaccharides on the blood circulation half-life of polymeric nanoparticles, Passirani et al. demonstrated that the brush-like structure of heparin and dextran served to protect the nanoparticles from *in vivo* clearance. Covalent conjugation of heparin and dextran to a poly(methyl methacrylate)-based nanoparticle significantly prolonged the circulation half-life of the particles from 3 min to several hours. Sheng et al. also showed that functionalization with water-soluble chitosan reduced the phagocytic uptake efficiency and retarded the blood clearance of PLA

nanoparticles. An impressive finding was the fact that nanoparticle functionalization with both PEG and chitosan yielded a circulation half-life of 63 hr, which was much longer than that of the PEGylated particles reported in the study. The extended circulation time was attributed in part to the charge neutralization between PEG and chitosan and demonstrated the stealth potential of polysaccharides. Among other carbohydrate-based biopolymers, poly(sialic acid) (PSA) has also drawn significant interest as a stealth moiety because the human body has no specific receptors for the compound [129]. Adoption of PSA by foreign pathogens and metastatic cancer cells for antigen masking and *in vivo* survival [130-132] also suggests PSA's stealth potential. Conjugation with PSA has successfully prolonged the pharmacokinetic profiles of several protein therapeutics [133, 134] as well as quantum dot nanoparticles [135]. Sialic acid has been applied to PLGA nanoparticles for drug delivery applications and has been shown to prolong particle residence within the brain [136, 137].

1.2.3 Biologically Inspired Stealth Strategies

In the engineering of stealth nanocarriers that are capable of evading immune clearance, researchers have also taken design cues from biology by exploiting the surface mechanisms behind blood cells' long circulation. Early work on liposomal carriers demonstrated that incorporation of sialylated glycolipids and glycoproteins, which are major components on erythrocyte surfaces, significantly prolonged the liposomes' *in vivo* survival. While Surolia et al. first introduced asialogangliosides to

liposome as a biomimetic approach to improve hepatic drug delivery [138], later studies by Allen et al. showed that the incorporation of the ganglioside G_{M1} greatly prolonged the liposome's residence time in the blood. The stealth effect of G_{M1} was observed across several different liposomal formulations. For instance, addition of a 0.07 molar ratio of G_{M1} to a sphingomyelin liposome increased the blood-to-RES ratio from 0.02 to 5.7 2 hr post-injection [139]. This enhanced blood residence was attributed to G_{M1}'s dense surface carbohydrates that mimic cellular membranes. In addition, the role of terminal sialyl groups on these glycolipids was also highlighted as incorporation of asialogangliosides showed a less pronounced stealth effect. Optimization of the biologically inspired stealth liposome by Allen et al. resulted in a liposomal composition that mimicked the outer leaflet of red blood cell (RBC) membranes, consisting of egg phosphatidylcholine/sphingomyelin/cholesterol/ ganglioside G_{M1} at a 1:1:1:0.14 molar ratio [140]. Liposomal formulations containing other sialic acid-containing gangliosides [141-143], ganglioside derivatives [144-146], and glycoproteins [147] also showed extended circulation time in the blood. The stealth effect of these glycosylated complexes has been ascribed to their ability to fend off complement activation and macrophage uptake [141, 148].

Despite the early success of biologically inspired stealthy liposomes, the utilization of biomolecules for stealth functionalization remained relatively unexplored in the development of polymeric nanocarriers. This was in part due to the engineering challenge in functionalizing nanoscale substrates. To bestow nanocarriers with biomimetic functionalities, biomolecules such as proteins and glycans need to be

attached to the particles in a non-disruptive and regio-selective manner. With the advances in molecular biology and nanoengineering techniques, biologically inspired stealth polymeric nanoparticles have recently emerged. Possessing active biological components on their surfaces, these nanoparticles are unlike conventional stealth particles that rely on hydration coronas for *in vivo* survival. Currently, techniques to prepare biologically inspired polymeric nanoparticles can be classified into a bottom-up approach based on protein conjugations and a top-down approach based on cell membrane coating.

1.2.3.1 Polymeric NPs Tagged with Self Markers

Among the many surface proteins and molecules present on mammalian membranes, an integrin-associated protein CD47 has gained much research interest as a "marker-of-self" that can protect cells against macrophage uptake through an inhibitory action via SIRPα binding [149]. The protein and its analogues have been identified on cancer cells and viruses as immune-evasive masking [150, 151]. Such anti-phagocytic properties have motivated researchers to apply the protein to mask foreign materials from immune recognition [152, 153]. Recently, CD47 and its derivative peptide have been attached to polystyrene nanoparticles to enhance their delivery and inhibit phagocytic clearance (Figure 1.2). To enable controlled CD47 functionalization on nanoparticles, Rodriguez et al. mixed 160 nm streptavidin-coated polystyrene beads with a recombinant CD47 protein expressing regioselective biotinylation. The streptavidin/biotin coupling approach allowed CD47 to be coated in

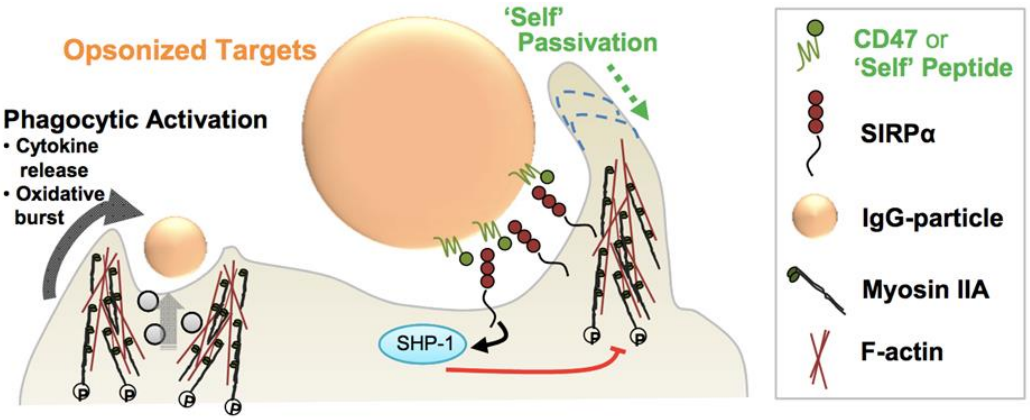

Figure 1.2 Schematic of a "self" nanoparticle prepared by immobilizing CD47 or its peptide variant on the nanoparticle surface. Signaling between CD47 or a minimal "self" peptide and their receptor, SIRPα, inhibits phagocytic activation. Reproduced from Ref. 154 with permission from the American Association for the Advancement of Science.

the proper orientation at a controllable density. In addition to CD47-functionalized beads, the authors also identified a "minimal" self peptide sequence (GNYTCEVTELTREGETIIELK), which was also applied for nanoparticle camouflage. Studies on the CD47- and self peptide-functionalized nanobeads showed that they could inhibit myosin-II recruitment at the phagocytic synapse, thereby suppressing the ensuing phagocytosis. The anti-phagocytic effect of CD47 functionalization was shown to be highly potent, requiring approximately 1 molecule per 45,000 nm^2 (equivalent to the lowest CD47 densities reported for human RBCs), suggesting that a nanoparticle 60 nm in radius needs only one CD47 molecule to achieve the active stealth effect [154].

The difference between the active stealth approach behind the "self" nanoparticles and the passive stealth approach behind conventional PEGylated nanoparticles was tellingly demonstrated in *in vivo* studies conducted with pre-opsonized nanoparticles. Recognizing the challenge in maintaining stealth functionalization following nanoparticle opsonization, Rodriguez et al. showed that

the “self” nanoparticles retained their anti-phagocytic properties *in vivo* despite controlled opsonization with IgG. In contrast, PEGylated nanoparticles were completely stripped of their stealth properties upon opsonization, exhibiting equivalent blood residence time to non-functionalized polystyrene nanobeads. The authors also demonstrated enhanced tumoral uptake and increased treatment efficacy using A549 lung adenocarcinoma cells and paclitaxel-loaded polystyrene nanobeads, validating the biologically inspired stealth approach to improve nanoparticle drug delivery [154].

1.2.3.2 Polymeric NPs Camouflaged in Cellular Membranes

In contrast to the bottom-up approach in attaching “marker-of-self” molecules to nanoparticles, a top-down approach, which exploits cellular membranes in their entirety to coat and camouflage polymeric nanoparticles from immune clearance, was first reported by Hu *et al*. Using a co-extrusion process, the investigators demonstrated successful coating of sub-100 nm PLGA nanoparticles with natural membranes derived from RBCs [155]. The resulting RBC-membrane-coated nnaoparticles (RBC-NPs) exhibited a core-shell structure, in which the RBC membrane formed a single bilayer around the polymeric core (Figure 1.3). Interestingly, the cell membrane-coating approach adopts the same immune-evasive strategy adopted by many viruses in nature. It was recently discovered that hepatitis A and hepatitis C viruses are capable of “hijacking” cellular membranes, enclosing themselves in these non-immunogenic coatings to escape from neutralizing antibodies. The cell-membrane coating technique presents a unique biomimetic approach in

nanoparticle stealth functionalization [156, 157].

From a nanoengineering perspective, the membrane coating approach provides unprecedented control in enabling biomimetic surface functionalization on nanoscale polymeric substrates. By translocating cellular membranes in their entirety to nanoparticles, the complex biochemistry on cellular surfaces can be faithfully translocated as well [155]. Careful studies of CD47 on the surface of RBC-NPs demonstrated that the particles possess the same density of the biomarker as its RBC source [158]. More importantly, the proteins were shown to be oriented almost exclusively in the right-side-out fashion with the extracellular portion displayed on the particle surfaces (Figure 1.3). This right-side-out orientation was ascribed in part to the electrostatic repulsion between the negatively charged PLGA nanoparticles and the negatively charged sialyl moieties residing on the exoplasmic side of the membranes. In addition, the stabilization effect by the exoplasmic glycans likely contributed to the observed membrane orientation. As a result of this oriented membrane coating, macrophage uptake of the RBC-NPs was significantly impeded *in vitro*. RBC-NPs also remained stable in phosphate buffered solution and serum unlike bare PLGA nanoparticles, suggesting that the glycan-rich membranes conferred stability to the polymeric cores. An important finding is that the RBC-NPs possessed longer blood survival as compared to an analogous PEGylated formulation. These results highlight the strength of the biomembrane-coated nanoparticles, whose self-camouflage presents a comprehensive evasion strategy against the multi-faceted nature of immune clearance [159, 160].

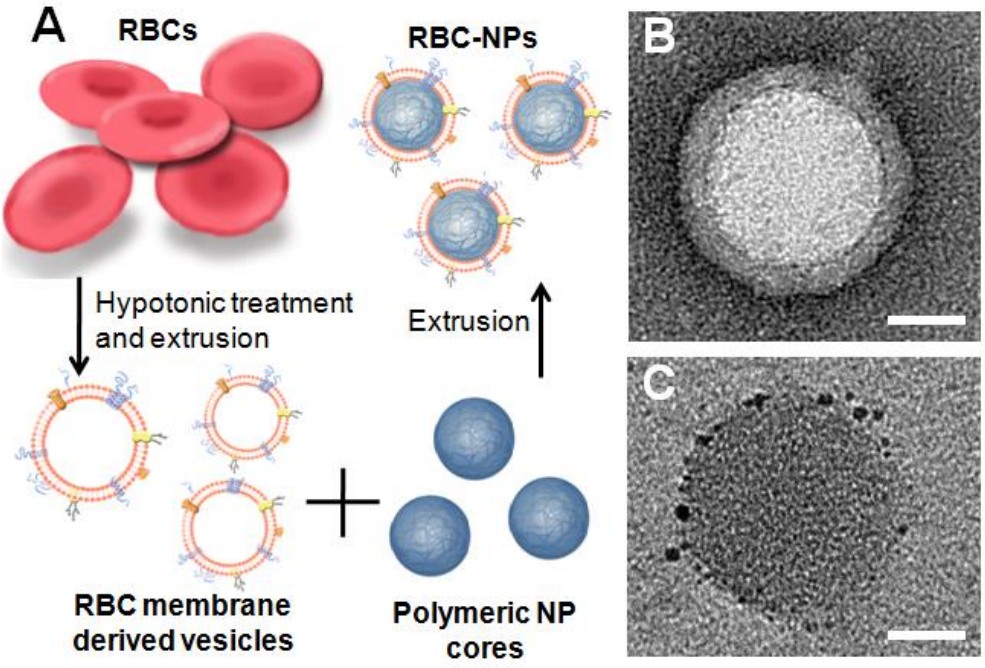

Figure 1.3 Red blood cell membrane-coated polymeric nanoparticle. (A) Schematic of RBC-NP preparation. PLGA nanoparticles are coated in natural RBC membranes. (B) TEM visualization of the RBC-NP shows unilamellar membrane coating over the polymeric core (scale bar = 20 nm). Reproduced from Ref. 155 with permission from the National Academy of Sciences. (C) Immunogold staining with anti-CD47 antibodies targeting the protein's extracellular domain shows that CD47 is present on RBC-NP in a right-side-out orientation (scale bar = 20 nm) Reproduced from Ref. 158 with permission from The Royal Society of Chemistry.

Much development on cellular-membrane coated nanoparticles has been made since RBC-NPs were first reported. Anti-phagocytic properties have been demonstrated with RBC membrane-coated gold nanoparticles [161] and white blood cell membrane-coated silica particles [162], demonstrating the broad applicability of the approach. Toward drug delivery, RBC-NPs have been successfully loaded with doxorubicin and showed treatment efficacy against a leukemia cell line [163]. The membrane bilayer coating was shown to enable a more sustained drug release profile by serving as a diffusion barrier. Incorporation of targeting ligands, such as folate and aptamers, into RBC-NPs has also been made possible through the insertion of lipid-

tethered ligands into the RBC membrane bilayer, which demonstrated the platform's potential for targeted drug delivery [164]. Perhaps most exciting is the recent demonstration of the RBC-NPs as a toxin nanosponge against pore-forming toxins. Owing to the particle's structural stability and biomimetic exterior, the RBC-NPs readily interact with the many pore-forming toxins that typically target and damage cellular membranes. Absorbed toxins remain locked-in by the nanoparticles and therefore can be safely metabolized *in vivo* [165]. The toxin nanosponge application highlights the unique strengths of the membrane-camouflage stealth strategy, which allows nanoparticle interaction with other biomolecules as opposed to inhibiting such interactions using non-fouling polymers. This biologically inspired approach provides the venue for novel therapeutic interventions against pathogenic factors that interact with cellular surfaces.

1.3 Conclusions

Polymeric nanoparticles offer a robust and versatile platform for designing novel and more efficacious therapeutics. The impact of polymeric nanotherapeutics is evidenced by the many nanoformulations currently undergoing clinical trials. Ongoing research efforts continue to explore stealth strategies with the aim of developing nanocarriers that have better immunocompatibility and improved pharmacokinetic profiles. Such efforts are highlighted by a variety of hydrophilic polymers employed for stealth functionalization.

Notably, development of biologically inspired stealth nanoparticles highlights

increased understanding of the complex immune clearance mechanisms and of the many biomolecules that contribute to immune evasion. Advancement in nanoengineering techniques has enabled nanoparticle surface functionalization with immunologically relevant components (i.e. CD47 and cellular membranes). These biologically inspired nanoparticles present a new paradigm in nanoparticle functionalization. Rather than hiding foreign particles behind a hydration layer, drug carriers can be camouflaged as "self", readily evading immune clearance despite direct interaction with biological components in circulation. While the field of "self" nanoparticles remains in its nascent stage, the growing number of cell-derived nanocarriers in literature provides a glimpse of the drug delivery potential behind biological functionalizations [166-170]. Ongoing research in biologically inspired nanoparticles promises unique carrier functionalities that combine the intricacies of natural biomolecules with the flexibility and robustness of synthetic nanomaterials.

1.4 References

1. Farokhzad, O.C. and R. Langer, *Nanomedicine: Developing smarter therapeutic and diagnostic modalities.* Advanced Drug Delivery Reviews, 2006. **58**(14): p. 1456-1459.

2. Brannon-Peppas, L. and J.O. Blanchette, *Nanoparticle and targeted systems for cancer therapy.* Advanced Drug Delivery Reviews, 2004. **56**(11): p. 1649-1659.

3. Kawasaki, E.S. and A. Player, *Nanotechnology, nanomedicine, and the development of new, effective therapies for cancer.* Nanomedicine, 2005. **1**(2): p. 101-109.

4. Fassas, A., R. Buffels, P. Kaloyannidis, and A. Anagnostopoulos, *Safety of high-dose liposomal daunorubicin (daunoxome) for refractory or relapsed*

acute myeloblastic leukaemia. British Journal of Haematology, 2003. **122**(1): p. 161-163.

5. Kreuter, J., V.E. Petrov, D.A. Kharkevich, and R.N. Alyautdin, *Influence of the type of surfactant on the analgesic effects induced by the peptide dalargin after its delivery across the blood-brain barrier using surfactant-coated nanoparticles.* Journal of Controlled Release, 1997. **49**(1): p. 81-87.

6. Leroux, J.C., E. Allemann, F.D. Jaeghere, E. Doelker, and R. Gurny, *Biodegradable nanoparticles - From sustained release formulations to improved site specific drug delivery.* Journal of Controlled Release, 1996. **39**(2-3): p. 339-350.

7. Raghuvanshi, R.S., Y.K. Katare, K. Lalwani, M.M. Ali, O. Singh, and A.K. Panda, *Improved immune response from biodegradable polymer particles entrapping tetanus toxoid by use of different immunization protocol and adjuvants.* International Journal of Pharmaceutics, 2002. **245**(1-2): p. 109-121.

8. Safra, T., F. Muggia, S. Jeffers, D.D. Tsao-Wei, S. Groshen, O. Lyass, R. Henderson, G. Berry, and A. Gabizon, *Pegylated liposomal doxorubicin (doxil): Reduced clinical cardiotoxicity in patients reaching or exceeding cumulative doses of 500 mg/m(2).* Annals of Oncology, 2000. **11**(8): p. 1029-1033.

9. Schroeder, U., P. Sommerfeld, S. Ulrich, and B.A. Sabel, *Nanoparticle technology for delivery of drugs across the blood-brain barrier.* Journal of Pharmaceutical Sciences, 1998. **87**(11): p. 1305-1307.

10. Gunatillake, P.A. and R. Adhikari, *Biodegradable synthetic polymers for tissue engineering.* European Cells & Materials, 2003. **5**: p. 1-16; discussion 16.

11. Acharya, S. and S.K. Sahoo, *PLGA nanoparticles containing various anticancer agents and tumour delivery by EPR effect.* Advanced Drug Delivery Reviews, 2011. **63**(3): p. 170-183.

12. Bibby, D.C., J.E. Talmadge, M.K. Dalal, S.G. Kurz, K.M. Chytil, S.E. Barry, D.G. Shand, and M. Steiert, *Pharmacokinetics and biodistribution of RGD-targeted doxorubicin-loaded nanoparticles in tumor-bearing mice.* International Journal of Pharmaceutics, 2005. **293**(1-2): p. 281-290.

13. Farokhzad, O.C., J.M. Karp, and R. Langer, *Nanoparticle-aptamer bioconjugates for cancer targeting.* Expert Opinion on Drug Delivery, 2006. **3**(3): p. 311-324.

14. Ruoslahti, E., *Drug targeting to specific vascular sites.* Drug Discovery Today, 2002. **7**(22): p. 1138-1143.

15. Torchilin, V.P., *Drug targeting.* European Journal of Pharmaceutical Sciences, 2000. **11**: p. S81-S91.

16. Rapoport, N., *Physical stimuli-responsive polymeric micelles for anti-cancer drug delivery.* Progress in Polymer Science, 2007. **32**(8-9): p. 962-990.

17. Schmaljohann, D., *Thermo- and pH-responsive polymers in drug delivery.* Advanced Drug Delivery Reviews, 2006. **58**(15): p. 1655-1670.

18. Romberg, B., W.E. Hennink, and G. Storm, *Sheddable coatings for long-circulating nanoparticles.* Pharmaceutical Research, 2008. **25**(1): p. 55-71.

19. Hu, C.M. and L. Zhang, *Nanoparticle-based combination therapy toward overcoming drug resistance in cancer.* Biochemical Pharmacology, 2012. **83**(8): p. 1104-11.

20. Aryal, S., C.M. Hu, and L. Zhang, *Polymeric nanoparticles with precise ratiometric control over drug loading for combination therapy.* Molecular Pharmaceutics, 2011. **8**(4): p. 1401-1407.

21. Kolishetti, N., S. Dhar, P.M. Valencia, L.Q. Lin, R. Karnik, S.J. Lippard, R. Langer, and O.C. Farokhzad, *Engineering of self-assembled nanoparticle platform for precisely controlled combination drug therapy.* Proceedings of the National Academy of Sciences USA, 2010. **107**(42): p. 17939-17944.

22. Sengupta, S., D. Eavarone, I. Capila, G. Zhao, N. Watson, T. Kiziltepe, and R. Sasisekharan, *Temporal targeting of tumour cells and neovasculature with a nanoscale delivery system.* Nature, 2005. **436**(7050): p. 568-572.

23. Wang, Z. and P.C. Ho, *Self-assembled core-shell vascular-targeted nanocapsules for temporal antivasculature and anticancer activities.* Small, 2010. **6**(22): p. 2576-2583.

24. Fang, R.H., K.N. Chen, S. Aryal, C.M. Hu, K. Zhang, and L. Zhang, *Large-Scale Synthesis of Lipid-Polymer Hybrid Nanoparticles Using a Multi-Inlet Vortex Reactor.* Langmuir, 2012. **28**(39): p. 13824-13829.

25. Rhee, M., P.M. Valencia, M.I. Rodriguez, R. Langer, O.C. Farokhzad, and R. Karnik, *Synthesis of Size-Tunable Polymeric Nanoparticles Enabled by 3D Hydrodynamic Flow Focusing in Single-Layer Microchannels.* Advanced Materials, 2011. **23**(12): p. H79-H83.

26. Kim, Y.T., B. Lee Chung, M. Ma, W.J. Mulder, Z.A. Fayad, O.C. Farokhzad, and R. Langer, *Mass Production and Size Control of Lipid-Polymer Hybrid Nanoparticles through Controlled Microvortices.* Nano Letters, 2012. **12**(7): p. 3587-3591.

27. Hrkach, J., D. Von Hoff, M. Mukkaram Ali, E. Andrianova, J. Auer, t. Campbell, D. De Witt, M. Figa, M. Figueiredo, A. Horhota, S. Low, K. McDonnel, E. Peeke, B. Retnarajan, A. Sabnis, E. Schnipper, J.J. Song, Y.H. Song, J. Summa, D. Tompsett, G. Troiano, T. Van Geen Hoven, J. Wright, P. Lorusso, P.W. Kantoff, N.H. Bander, C. Sweeney, O.C. Farokhzad, R. Langer, and S. Zale, *Preclinical development and clinical translation of a PSMA-targeted docetaxel nanoparticle with a differentiated pharmacological profile.* Science Translational Medicine, 2012. **4**(128): p. 128ra39.

28. Gref, R., Y. Minamitake, M.T. Peracchia, V. Trubetskoy, V. Torchillin, and R. Langer, *Biodegradable Long-Circulating Polymeric Nanospheres.* Science, 1994. **263**(5153): p. 1600-1603.

29. Shi, J., A.R. Votruba, O.C. Farokhzad, and R. Langer, *Nanotechnology in drug delivery and tissue engineering: from discovery to applications.* Nano Letters, 2010. **10**(9): p. 3223-3230.

30. Veronese, F.M. and G. Pasut, *PEGylation, successful approach to drug delivery.* Drug Discovery Today, 2005. **10**(21): p. 1451-1458.

31. Davis, M.E., Z.G. Chen, and D.M. Shin, *Nanoparticle therapeutics: an emerging treatment modality for cancer.* Nature Reviews Drug Discovery, 2008. **7**(9): p. 771-782.

32. Moghimi, S.M., A.C. Hunter, and J.C. Murray, *Long-circulating and target-specific nanoparticles: theory to practice.* Pharmacological Reviews, 2001. **53**(2): p. 283-318.

33. Peer, D., J.M. Karp, S. Hong, O.C. Farokhzad, R. Margalit, and R. Langer, *Nanocarriers as an emerging platform for cancer therapy.* Nature Nanotechnology, 2007. **2**(12): p. 751-760.

34. Hu, C.M.J., S. Kaushal, H.S. Tran Cao, S. Aryal, M. Sartor, S. Esener, M. Bouvet, and L. Zhang, *Half-Antibody Functionalized Lipid-Polymer Hybrid Nanoparticles for Targeted Drug Delivery to Carcinoembryonic Antigen Presenting Pancreatic Cancer Cells.* Molecular Pharmaceutics, 2010. **7**(3): p. 914-920.

35. Hu, C.M.J. and L.F. Zhang, *Therapeutic Nanoparticles to Combat Cancer Drug Resistance.* Current Drug Metabolism, 2009. **10**(8): p. 836-841.

36. Wang, A.Z., F. Gu, L. Zhang, J.M. Chan, A. Radovic-Moreno, M.R. Shaikh, and O.C. Farokhzad, *Biofunctionalized targeted nanoparticles for therapeutic applications.* Expert Opinion on Biological Therapy, 2008. **8**(8): p. 1063-1070.

37. Zhang, L., F.X. Gu, J.M. Chang, A.Z. Wang, R. Langer, and O.C. Farokhzad, *Nanoparticles in medicine: therapeutic applications and developments.* Clinical Pharmacology and Therapeutics, 2008. **83**(5): p. 761-769.

38. Kim, S.C., D.W. Kim, Y.H. Shim, S. Bang, H.S. Oh, S. Wan Kim, and M.H. Seo, *In vivo evaluation of polymeric micellar paclitaxel formulation: toxicity and efficacy.* Journal of Controlled Release, 2001. **72**(1-3): p. 191-202.

39. Werner, M.E., N.D. Cummings, M. Sethi, E.C. Wang, R. Sukumar, D.T. Moore, and A.Z. Wang, *Preclinical Evaluation of Genexol-PM, a Nanoparticle Formulation of Paclitaxel, as a Novel Radiosensitizer for the Treatment of Non-Small Cell Lung Cancer.* International Journal of Radiation Oncology Biology Physics, 2013. **86**(3): p. 463-468.

40. Kim, T.Y., D.W. Kim, J.Y. Chung, S.G. Shin, S.C. Kim, D.S. Heo, N.K. Kim, and Y.J. Bang, *Phase I and pharmacokinetic study of Genexol-PM, a cremophor-free, polymeric micelle-formulated paclitaxel, in patients with advanced malignancies.* Clinical Cancer Research, 2004. **10**(11): p. 3708-3716.

41. Lee, K.S., H.C. Chung, S.A. Im, Y.H. Park, C.S. Kim, S.B., Kim, S.Y. Rha, M.Y. Lee, and J. Ro, *Multicenter phase II trial of Genexol-PM, a Cremophor-free, polymeric micelle formulation of paclitaxel, in patients with metastatic breast cancer.* Breast Cancer Research and Treatment, 2008. **108**(2): p. 241-250.

42. Kim, D.W., S.Y. Kim, H.K. Kim, S.W. Kim, S.W. Shin, J.S. Kim, K. Park, M.Y. Lee, and D.S. Heo, *Multicenter phase II trial of Genexol-PM, a novel Cremophor-free, polymeric micelle formulation of paclitaxel, with cisplatin in patients with advanced non-small-cell lung cancer.* Annals of Oncology, 2007. **18**(12): p. 2009-2014.

43. Cheng, J.J., K.T. Khin, G.S. Jensen, A. Liu, and M.E. Davis, *Synthesis of linear, beta-cyclodextrin-based polymers and their camptothecin conjugates.* Bioconjugate Chemistry, 2003. **14**(5): p. 1007-1017.

44. Schluep, T., J. Cheng, K.T. Khin, and M.E. Davis, *Pharmacokinetics and biodistribution of the camptothecin-polymer conjugate IT-101 in rats and tumor-bearing mice.* Cancer Chemotherapy and Pharmacology, 2006. **57**(5): p. 654-662.

45. Gaur, S., L. Chen, T. Yen, Y. Wang, B. Zhou, M. Davis, and Y. Yen, *Preclinical study of the cyclodextrin-polymer conjugate of camptothecin CRLX101 for the treatment of gastric cancer.* Nanomedicine, 2012. **8**(5): p. 721-730.

46. Numbenjapon, T., J. Wang, D. Colcher, T. Schleup, M.E. Davis, J. Duringer, L. Kretzner, Y. Yen, S.J. Forman, and A. Raubitschek, *Preclinical results of camptothecin-polymer conjugate (IT-101) in multiple human lymphoma xenograft models.* Clinical Cancer Research, 2009. **15**(13): p. 4365-4373.

47. Eliasof, S.,D. Lazarus, C.G. Peters, R.I. Case, R.O. Cole, J. Hwang, T. Schleup, J. Chao, J. Lin, Y. Yen, H. Han, D.T. Wiley, J.E. Zuckerman, and M.E. Davis, *Correlating preclinical animal studies and human clinical trials of a multifunctional, polymeric nanoparticle.* Proceedings of the National Academy of Sciences USA, 2013. **110**(37): p. 15127-15132.

48. Pun, S.H. and M.E. Davis, *Development of a nonviral gene delivery vehicle for systemic application.* Bioconjugate Chemistry, 2002. **13**(3): p. 630-639.

49. Bartlett, D.W. and M.E. Davis, *Physicochemical and biological characterization of targeted, nucleic acid-containing nanoparticles.* Bioconjugate Chemistry, 2007. **18**(2): p. 456-468.

50. Davis, M.E., J.E. Zuckerman, C.H. Choi, D. Seligson, A. Tolcher, C.A. Alabi, Y. Yen, J.D. Heidel, and A. Ribas, *Evidence of RNAi in humans from systemically administered siRNA via targeted nanoparticles.* Nature, 2010. **464**(7291): p. 1067-1070.

51. Valle, J.W., A. Armstrong, C. Newman, V. Alakhov, G. Pietrzynski, J. Brewer, S. Campbell, P. Corrie, E.K. Rowinsky, and M. Ranson, *A phase 2 study of SP1049C, doxorubicin in P-glycoprotein-targeting pluronics, in patients with advanced adenocarcinoma of the esophagus and gastroesophageal junction.* Investigational New Drugs, 2011. **29**(5): p. 1029-1037.

52. Svenson, S., M. Wolfgang, J. Hwang, J. Ryan, and S. Eliasof, *Preclinical to clinical development of the novel camptothecin nanopharmaceutical CRLX101.* Journal of Controlled Release, 2011. **153**(1): p. 49-55.

53. Plummer, R., R.H. Wilson, H. Calvert, A. V. Boddy, M. Griffin, J. Sludden, M.J. Tilby, M. Eatock, D.G. Pearson, C.J. Ottley, Y. Matsumura, K. Kataoka, and T. Nishiya, *A Phase I clinical study of cisplatin-incorporated polymeric micelles (NC-6004) in patients with solid tumours.* British Journal of Cancer, 2011. **104**(4): p. 593-598.

54. Hamaguchi, T., Y. Matsumura, M. Suzuki, K. Shimizu, R. Goda, I. Nakamura, I. Nakatomi, M. Yokoyama, K. Kataoka, and T. Kakizoe, *NK105, a paclitaxel-incorporating micellar nanoparticle formulation, can extend in vivo antitumour activity and reduce the neurotoxicity of paclitaxel.* British Journal of Cancer, 2005. **92**(7): p. 1240-1246.

55. Matsumura, Y. and K. Kataoka, *Preclinical and clinical studies of anticancer agent-incorporating polymer micelles.* Cancer Science, 2009. **100**(4): p. 572-579.

56. Matsumura, Y., T. Hamaguchi, T. Ura, K. Muro, Y. Yamada, Y. Shimada, K. Shirao, T. Okusaka, H. Ueno, M. Ikeda, and N. Watanabe, *Phase I clinical trial and pharmacokinetic evaluation of NK911, a micelle-encapsulated doxorubicin.* British Journal of Cancer, 2004. **91**(10): p. 1775-1781.

57. Hamaguchi, T., T. Doi, T. Eguchi-Nakajima, K. Kato, Y. Yamada, Y. Shimada, N. Fuse, A. Ohtsu, S. Matsumoto, M. Takanashi, and Y. Matsumura, *Phase I study of NK012, a novel SN-38-incorporating micellar nanoparticle, in adult patients with solid tumors.* Clinical Cancer Research, 2010. **16**(20): p. 5058-5066.

58. Kim, T.Y., D.W. Kim, J.Y. Chung, S.G. Shin, S.C. Kim, D.S. Heo, N.K. Kim, and Y.J. Bang, *Phase I and pharmacokinetic study of Genexol-PM, a cremophor-free, polymeric micelle-formulated paclitaxel, in patients with advanced malignancies.* Clinical Cancer Research, 2004. **10**(11): p. 3708-3716.

59. Stolnik, S., L. Illum, and S.S. Davis, *Long Circulating Microparticulate Drug Carriers.* Advanced Drug Delivery Reviews, 1995. **16**(2-3): p. 195-214.

60. Perry, J.L., K.G. Reuter, M.P. Kai, K.P. Herlihy, S.W. Jones, J.C. Luft, M. Napier, J.E. Bear, and J.M. DeSimone, *PEGylated PRINT nanoparticles: the impact of PEG density on protein binding, macrophage association, biodistribution, and pharmacokinetics.* Nano Letters, 2012. **12**(10): p. 5304-5310.

61. Gref, R., M. Luck, P. Quellec, M. Marchand, E. Dellacherie, S. Harnisch, T. Blunk, and R.H. Muller, *'Stealth' corona-core nanoparticles surface modified by polyethylene glycol (PEG): influences of the corona (PEG chain length and surface density) and of the core composition on phagocytic uptake and plasma protein adsorption.* Colloids and Surfaces B: Biointerfaces, 2000. **18**(3-4): p. 301-313.

62. Avgoustakis, K., A. beletsi, Z. Panagi, P. Klepetsanis, E. Livaniou, G. Evangelatos, and D.S. Ithakissios, *Effect of copolymer composition on the physicochemical characteristics, in vitro stability, and biodistribution of*

PLGA-mPEG nanoparticles. International Journal of Pharmaceutics, 2003. **259**(1-2): p. 115-127.

63. Beletsi, A., Z. Panagi, and K. Avgoustakis, *Biodistribution properties of nanoparticles based on mixtures of PLGA with PLGA-PEG diblock copolymers.* International Journal of Pharmaceutics, 2005. **298**(1): p. 233-241.

64. Mosqueira, V.C.F., P. Legrand, J.L. Morgat, M. Vert, E. Mysiakine, R. Gref, J.P. Devissaguet, and G. Barratt, *Biodistribution of long-circulating PEG-grafted nanocapsules in mice: Effects of PEG chain length and density.* Pharmaceutical Research, 2001. **18**(10): p. 1411-1419.

65. Hamad, I., O. Al-Hanbali, A.C. Hunter, K.J. Rutt, T.L. Andresen, and S.M. Moghimi, *Distinct Polymer Architecture Mediates Switching of Complement Activation Pathways at the Nanosphere-Serum Interface: Implications for Stealth Nanoparticle Engineering.* ACS Nano, 2010. **4**(11): p. 6629-6638.

66. Knop, K., R. Hoogenboom, D. Fischer, and U.S. Schubert, *Poly(ethylene glycol) in drug delivery: pros and cons as well as potential alternatives.* Angewandte Chemie International Edition, 2010. **49**(36): p. 6288-6308.

67. Ma, H.L., K. Shiraishi, T. Minowa, K. Kawano, M. Yokoyama, Y. Hattori, and Y. Maitani, *Accelerated Blood Clearance Was Not Induced for a Gadolinium-Containing PEG-poly(L-lysine)-Based Polymeric Micelle in Mice.* Pharmaceutical Research, 2010. **27**(2): p. 296-302.

68. Tagami, T., Y. Uehara, N. Moriyoshi, Y. Ishida, and H. Kiwada, *Anti-PEG IgM production by siRNA encapsulated in a PEGylated lipid nanocarrier is dependent on the sequence of the siRNA.* Journal of Controlled Release, 2011. **151**(2): p. 149-154.

69. Xu, H., K.Q. Wang, Y.H. Deng, and W. Chen da, *Effects of cleavable PEG-cholesterol derivatives on the accelerated blood clearance of PEGylated liposomes.* Biomaterials, 2010. **31**(17): p. 4757-4763.

70. Armstrong, J.K., G. Hempel, S. Koling, L.S. Chang, T. Fisher, H.J. Meiselman, and G. Garratty, *Antibody against poly(ethylene glycol) adversely affects PEG-asparaginase therapy in acute lymphoblastic leukemia patients.* Cancer, 2007. **110**(1): p. 103-111.

71. Sroda, K., J. Rydlewski, M. Langner, A. Kozubek, M. Brzybek, and A.F. Sikorski, *Repeated injections of PEG-PE liposomes generate anti-PEG antibodies.* Cellular & Molecular Biology Letters, 2005. **10**(1): p. 37-47.

72. Wang, X.Y., T. Ishida, and H. Kiwada, *Anti-PEG IgM elicited by injection of liposomes is involved in the enhanced blood clearance of a subsequent dose of PEGylated liposomes.* Journal of Controlled Release, 2007. **119**(2): p. 236-244.

73. Mosqueira, V.C.F., P. Legrand, A. Gulik, O. Bourdon, R. Gref, D. Labarre, and G. Barratt, *Relationship between complement activation, cellular uptake and surface physicochemical aspects of novel PEG-modified nanocapsules.* Biomaterials, 2001. **22**(22): p. 2967-2979.

74. Hamada, I., A.C. Hunter, J. Szebeni, and S.M. Moghini, *Poly(ethylene glycol)s generate complement activation products in human serum through increased alternative pathway turnover and a MASP-2-dependent process.* Molecular Immunology, 2008. **46**(2): p. 225-232.

75. Szebeni, J., L. Baranyi, S. Savay, J. Milosevits, R. Bunger, P. Laverman, J.M. Metselaar, G. Storm, A. Chanan-Khan, L. Liebes, F.M. Muggia, R. Cohen, Y. Barenholz, and C.R. Alving, *Role of complement activation in hypersensitivity reactions to doxil and hynic PEG liposomes: experimental and clinical studies.* Journal of Liposome Research, 2002. **12**(1-2): p. 165-172.

76. Chytil, P., T. Etrych, C. Konak, M. Sirova, T. Mrkvan, B. Rihova, and K. Ulbrich, *Properties of HPMA copolymer-doxorubicin conjugates with pH-controlled activation: effect of polymer chain modification.* Journal of Controlled Release, 2006. **115**(1): p. 26-36.

77. Chytil, P., T. Etrych, C. Konak, M. Sirova, T. Mrkvan, J. Boucek, B. Rihova, and K. Ulbrich, *New HPMA copolymer-based drug carriers with covalently bound hydrophobic substituents for solid tumour targeting.* Journal of Controlled Release, 2008. **127**(2): p. 121-130.

78. Greco, F. and M.J. Vicent, *Combination therapy: Opportunities and challenges for polymer-drug conjugates as anticancer nanomedicines.* Advanced Drug Delivery Reviews, 2009. **61**(13): p. 1203-1213.

79. Paul, A., M.J. Vicent, and R. Duncan, *Using small-angle neutron scattering to study the solution conformation of N-(2-hydroxypropyl)methacrylamide copolymer-doxorubicin conjugates.* Biomacromolecules, 2007. **8**(5): p. 1573-1579.

80. Kopecek, J., P. Kopeckova, T. Minko, and Z. Lu, *HPMA copolymer-anticancer drug conjugates: design, activity, and mechanism of action.* European Journal of Pharmaceutics and Biopharmaceutics, 2000. **50**(1): p. 61-81.

81. Vasey, P.A., S.B. Kaye, R. Morrison, C. Twelves, P. Wilson, R. Duncan, A.H. Thomson, L.S. Murray, T.E. Hilditch, T. Murray, S. Burtles, D. Fraier, E. Frigerio, and J. Cassidy, *Phase I clinical and pharmacokinetic study of PK1 [N-(2-hydroxypropyl)methacrylamide copolymer doxorubicin]: First member of a new class of chemotherapeutic agents-drug-polymer conjugates.* Clinical Cancer Research, 1999. **5**(1): p. 83-94.

82. Duncan, R., *Development of HPMA copolymer-anticancer conjugates: clinical experience and lessons learnt.* Advanced Drug Delivery Reviews, 2009. **61**(13): p. 1131-1148.

83. Vicent, M.J., H. Ringsdorf, and R. Duncan, *Polymer therapeutics: clinical applications and challenges for development.* Advanced Drug Delivery Reviews, 2009. **61**(13): p. 1117-1120.

84. Duncan, R., *Polymer conjugates as anticancer nanomedicines.* Nature Reviews Cancer, 2006. **6**(9): p. 688-701.

85. Rihova, B., K. Ulbrich, J. Kopecek, and P. Mancal, *Immunogenicity of N-(2-hydroxypropyl)-methacrylamide copolymers--potential hapten or drug carriers.* Folia Microbiologica, 1983. **28**(3): p. 217-227.

86. Konak, C., L. Mrkvickova, O. Nazarova, K. Ulbrich, and L.W. Seymour, *Formation of DNA complexes with diblock copolymers of poly(N-(2-hydroxypropyl)methacrylamide) and polycations.* Supramolecular Science, 1998. **5**(1-2): p. 67-74.

87. Oupicky, D., C. Konak, and K. Ulbrich, *Preparation of DNA complexes with diblock copolymers of poly[N(2-hydroxypropyl)methacrylamide] and polycations.* Materials Science & Engineering C: Biomimetic and Supramolecular Systems, 1999. **7**(1): p. 59-65.

88. Konak, C., V. Subr, L. Kostka, P. Stepanek, K. Ulbrich, and H. Schlaad, *Coating of vesicles with hydrophilic reactive polymers.* Langmuir, 2008. **24**(14): p. 7092-7098.

89. Lele, B.S. and J.C. Leroux, *Synthesis and micellar characterization of novel Amphiphilic A-B-A triblock copolymers of N-(2-hydroxypropyl)methacrylamide or N-vinyl-2-pyrrolidone with poly(is an element of-caprolactone).* Macromolecules, 2002. **35**(17): p. 6714-6723.

90. Lele, B.S. and J.C. Leroux, *Synthesis of novel amphiphilic star-shaped poly(epsilon-caprolactone)-block-poly(N-(2-hydroxypropyl)methacrylamide) by combination of ring-opening and chain transfer polymerization.* Polymer, 2002. **43**(21): p. 5595-5606.

91. Kang, N. and J.C. Leroux, *Triblock and star-block copolymers of N-(2-hydroxypropyl)methacrylamide or N-vinyl-2-pyrrolidone and D,L-lactide: synthesis and self-assembling properties in water.* Polymer, 2004. **45**(26): p. 8967-8980.

92. Jiang, S.Y. and Z.Q. Cao, *Ultralow-Fouling, Functionalizable, and Hydrolyzable Zwitterionic Materials and Their Derivatives for Biological Applications.* Advanced Materials, 2010. **22**(9): p. 920-932.

93. Shao, Q., Y. He, A.D. White, and S. Jiang, *Difference in Hydration between Carboxybetaine and Sulfobetaine.* Journal of Physical Chemistry B, 2010. **114**(49): p. 16625-16631.

94. Zhang, Z., H. Vaisocherova, G. Cheng, W. Yang, H. Xue, and S. Jiang, *Nonfouling Behavior of Polycarboxybetaine-Grafted Surfaces: Structural and Environmental Effects.* Biomacromolecules, 2008. **9**(10): p. 2686-2692.

95. Yang, W., T. Bai, L.R. Carr, A.J. Keefe, J. Xu, H. Xue, C.A. Irvin, S. Chen, J. Wang, and S. Jiang, *The effect of lightly crosslinked poly(carboxybetaine) hydrogel coating on the performance of sensors in whole blood.* Biomaterials, 2012. **33**(32): p. 7945-7951.

96. Kirk, J.T., N.D. Brault, T. Baehr-Jones, M. Hochberg, S. Jiang, and D.M. Ratner, *Zwitterionic polymer-modified silicon microring resonators for label-free biosensing in undiluted human plasma.* Biosensors & Bioelectronics, 2013. **42**: p. 100-105.

97. Li, Y.T., A.J. Keefe, M. Giarmarco, N.D. Brault, and S. Jiang, *Simple and Robust Approach for Passivating and Functionalizing Surfaces for Use in Complex Media.* Langmuir, 2012. **28**(25): p. 9707-9713.

98. Mi, L. and S.Y. Jiang, *Synchronizing nonfouling and antimicrobial properties in a zwitterionic hydrogel.* Biomaterials, 2012. **33**(35): p. 8928-8933.

99. Cheng, G., G. Li, H. Xue, S. Chen J.D. Bryers, and S. Jiang, *Zwitterionic carboxybetaine polymer surfaces and their resistance to long-term biofilm formation.* Biomaterials, 2009. **30**(28): p. 5234-5240.

100. Li, G.Z., G. Cheng, H. Xue, S. Chen, F. Zhang, and S. Jiang, *Ultra low fouling zwitterionic polymers with a biomimetic adhesive group.* Biomaterials, 2008. **29**(35): p. 4592-4597.

101. Keefe, A.J. and S.Y. Jiang, *Poly(zwitterionic)protein conjugates offer increased stability without sacrificing binding affinity or bioactivity.* Nature Chemistry, 2012. **4**(1): p. 60-64.

102. Zhang, L., Z. Cao, T. Bai, L. Carr, J.R. Ella-Menye, C. Irvin, B.D. Ratner, and S. Jiang, *Zwitterionic hydrogels implanted in mice resist the foreign-body reaction.* Nature Biotechnology, 2013. **31**(6): p. 553-556.

103. Yang, W., L. Zhang, S. Wang, A.D. White, and S. Jiang, *Functionalizable and ultra stable nanoparticles coated with zwitterionic poly(carboxybetaine) in undiluted blood serum.* Biomaterials, 2009. **30**(29): p. 5617-5621.

104. Zhang, L., H. Xue, C. Gao, L. Carr, J. Wang, B. Chu, and S. Jiang, *Imaging and cell targeting characteristics of magnetic nanoparticles modified by a functionalizable zwitterionic polymer with adhesive 3,4-dihydroxyphenyl-L-alanine linkages.* Biomaterials, 2010. **31**(25): p. 6582-6588.

105. Cao, Z.Q., L. Zhang, and S.Y. Jiang, *Superhydrophilic Zwitterionic Polymers Stabilize Liposomes.* Langmuir, 2012. **28**(31): p. 11625-11632.

106. Cheng, G., L. Mi, Z. Cao, H. Xue, Q. Yu, L. Carr, and S. Jiang, *Functionalizable and Ultrastable Zwitterionic Nanogels.* Langmuir, 2010. **26**(10): p. 6883-6886.

107. Zhang, L., H. Xue, Z. Cao, A. Keefe, J. Wang, and S. Jiang, *Multifunctional and degradable zwitterionic nanogels for targeted delivery, enhanced MR imaging, reduction-sensitive drug release, and renal clearance.* Biomaterials, 2011. **32**(20): p. 4604-4608.

108. Cao, Z.Q., Q. Yu, H. Xue, G. Cheng, and S. Jiang, *Nanoparticles for Drug Delivery Prepared from Amphiphilic PLGA Zwitterionic Block Copolymers with Sharp Contrast in Polarity between Two Blocks.* Angewandte Chemie International Edition, 2010. **49**(22): p. 3771-3776.

109. Zhang, L., Z. Cao, Y. Li, J.R. Ella-Menye, T. Bai, and S. Jiang, *Softer Zwitterionic Nanogels for Longer Circulation and Lower Splenic Accumulation.* ACS Nano, 2012. **6**(8): p. 6681-6686.

110. Takeuchi, H., H. Kojima, H. Yamamoto, and Y. Kawashima, *Evaluation of circulation profiles of liposomes coated with hydrophilic polymers having different molecular weights in rats.* Journal of Controlled Release, 2001. **75**(1-2): p. 83-91.

111. Menon, J.U., S. Kona, A.S. Wadajkar, F. Desai, A. Vadla, and K.T. Nguyen, *Effects of surfactants on the properties of PLGA nanoparticles.* Journal of Biomedical Materials Research Part A, 2012. **100A**(8): p. 1998-2005.

112. Woodle, M.C., C.M. Engbers, and S. Zalipsky, *New Amphipatic Polymer Lipid Conjugates Forming Long-Circulating Reticuloendothelial System-Evading Liposomes.* Bioconjugate Chemistry, 1994. **5**(6): p. 493-496.

113. Torchilin, V.P., V.S. Trubetskoy, K.R. Whiteman, P. Caliceti, P. Ferruti, and F.M. Veronese, *New Synthetic Amphiphilic Polymers for Steric Protection of Liposomes in-Vivo.* Journal of Pharmaceutical Sciences, 1995. **84**(9): p. 1049-1053.

114. Ishihara, T., T. Maeda, H. Sakamoto, N. Takasaki, M. Shigyo, T. Ishida, H. Kiwada, Y. Mizushima, and T. Mizushima, *Evasion of the Accelerated Blood Clearance Phenomenon by Coating of Nanoparticles with Various Hydrophilic Polymers.* Biomacromolecules, 2010. **11**(10): p. 2700-2706.

115. Kaneda, Y., Y. Tsutsumi, Y. Yoshioka, H. Kamada, Y. Yamamoto, H. Kodaira, S. Tsunoda, T. Okamoto, Y. Mukai, H. Shibata, S. Nakagawa, and T. Mayumi, *The use of PVP as a polymeric carrier to improve the plasma half-life of drugs.* Biomaterials, 2004. **25**(16): p. 3259-3266.

116. Romberg, B., J.M. Metselaar, L. Baranyi, C.J. Snel, R. Bunger, W.E. Hennink, J. Szebeni, and G. Storm, *Poly(amino acid)s: Promising enzymatically degradable stealth coatings for liposomes.* International Journal of Pharmaceutics, 2007. **331**(2): p. 186-189.

117. Deierkauf, F.A., H. Beukers, M Deierkauf, and J.C. Riemersma, *Phagocytosis by Rabbit Polymorphonuclear Leukocytes - Effect of Albumin and Polyamino Acids on Latex Uptake.* Journal of Cellular Physiology, 1977. **92**(2): p. 169-175.

118. Romberg, B., C. Oussoren, C.J. Snel, W.E. Hennink, and G. Storm, *Effect of liposome characteristics and dose on the pharmacokinetics of liposomes coated with poly(amino acid)s.* Pharmaceutical Research, 2007. **24**(12): p. 2394-2401.

119. Arimura, H., Y. Ohya, and T. Ouchi, *The formation of biodegradable polymeric micelles from newly synthesized poly(aspartic acid)-block-polylactide AB-type diblock copolymers.* Macromolecular Rapid Communications, 2004. **25**(6): p. 743-747.

120. Arimura, H., Y. Ohya, and T. Ouchi, *Formation of core-shell type biodegradable polymeric micelles from amphiphilic poly(aspartic acid)-block-polylactide diblock copolymer.* Biomacromolecules, 2005. **6**(2): p. 720-725.

121. Deng, C., X. Chen, J. Sun, T. Lu, W. Wang, and X. Jing, *RGD peptide grafted biodegradable amphiphilic triblock copolymer poly(glutamic acid)-b-poly(L-*

lactide)-b-poly(glutamic acid): Synthesis and self-assembly. Journal of Polymer Science Part A: Polymer Chemistry, 2007. **45**(15): p. 3218-3230.

122. Deng, C., H. Tian, P. Zhang, J. Sun, X. Chen, and X. Jing, *Synthesis and characterization of RGD peptide grafted poly(ethylene glycol)-b-poly(L-lactide)-b-poly(L-glutamic acid) triblock copolymer.* Biomacromolecules, 2006. **7**(2): p. 590-596.

123. Liang, H.F., S.C. Chen, M.C. Chen, P.W. Lee, C.T. Chen, and HW. Sung, *Paclitaxel-loaded poly(gamma-glutamic acid)-poly(lactide) nanoparticles as a targeted drug delivery system against cultured HepG2 cells.* Bioconjugate Chemistry, 2006. **17**(2): p. 291-299.

124. Sun, J., X. Chen, T. Lu, S. Liu, H. Tian, Z. Guo, and X. Jing, *Formation of reversible shell cross-linked micelles from the biodegradable amphiphilic diblock copolymer poly(L-cysteine)-block-poly(L-lactide).* Langmuir, 2008. **24**(18): p. 10099-10106.

125. Deng, C., X. Chen, H. Yu, J. Sun, T. Lu, and X. Jing, *A biodegradable triblock copolymer poly(ethylene glycol)-b-poly(L-lactide)-b-poly(L-lysine): Synthesis, self-assembly and RGD peptide modification.* Polymer, 2007. **48**(1): p. 139-149.

126. Kean, T. and M. Thanou, *Biodegradation, biodistribution and toxicity of chitosan.* Advanced Drug Delivery Reviews, 2010. **62**(1): p. 3-11.

127. Li, H.B., R. Niu, J. Yang, J. Nie, and D. Yang, *Photocrosslinkable tissue adhesive based on dextran.* Carbohydrate Polymers, 2011. **86**(4): p. 1578-1585.

128. Lemarchand, C., R. Gref, and P. Couvreur, *Polysaccharide-decorated nanoparticles.* European Journal of Pharmaceutics and Biopharmaceutics, 2004. **58**(2): p. 327-341.

129. Gregoriadis, G., S. Jain, I. Papaioannou, and P. Laing, *Improving the therapeutic efficacy of peptides and proteins: A role for polysialic acids.* International Journal of Pharmaceutics, 2005. **300**(1-2): p. 125-130.

130. Srikrishna, G., N. Varki, and H.H. Freeze, *Carboxylated N-glycans in inflammation-mediated colon cancer.* Glycobiology, 2006. **16**(11): p. 1150-1150.

131. Rutishauser, U., *Polysialic acid at the cell surface: Biophysics in service of cell interactions and tissue plasticity.* Journal of Cellular Biochemistry, 1998. **70**(3): p. 304-312.

132. Muhlenhoff, M., M. Eckhardt, and R. Gerardy-Schahn, *Polysialic acid: three-dimensional structure, biosynthesis and function.* Current Opinion in Structural Biology, 1998. **8**(5): p. 558-564.

133. Jain, S., D.H. Hreczuk-Hirst, B. McCormack, M. Mital, A. Epenetos, P. Laing, and G. Gregoriadis, *Polysialylated insulin: synthesis, characterization and biological activity in vivo.* Biochimica Et Biophysica Acta: General Subjects, 2003. **1622**(1): p. 42-49.

134. Fernandes, A.I. and G. Gregoriadis, *Polysialylated asparaginase: preparation, activity and pharmacokinetics.* Biochimica Et Biophysica Acta: Protein Structure and Molecular Enzymology, 1997. **1341**(1): p. 26-34.

135. Ohyanagi, T., N. Nagahori, K. Shimawaki, H. Hinou, T. Yamashita, A. Sasaki, T. Jin, T. Iwanaga, M. Kinjo, and S. Nishimura, *Importance of Sialic Acid Residues Illuminated by Live Animal Imaging Using Phosphorylcholine Self-Assembled Monolayer-Coated Quantum Dots.* Journal of the American Chemical Society, 2011. **133**(32): p. 12507-12517.

136. Bondioli, L., L. Costantino, A. Ballestrazzi, D. Lucchesi, D. Boraschi, F. Pellati, S. Benvenuti, G. Tosi, and M.A. Vandelli, *PLGA nanoparticles surface decorated with the sialic acid, N-acetylneuraminic acid.* Biomaterials, 2010. **31**(12): p. 3395-3403.

137. Tosi, G., A.V. Vergoni, B. Ruozi, L. Bondioli, L. Badiali, F. Rivasi, L. Constantino, F. Forni, and M.A. Vandelli, *Sialic acid and glycopeptides conjugated PLGA nanoparticles for central nervous system targeting: In vivo pharmacological evidence and biodistribution.* Journal of Controlled Release, 2010. **145**(1): p. 49-57.

138. Surolia, A. and B.K. Bachhawat, *Monosialoganglioside liposome-entrapped enzyme uptake by hepatic cells.* Biochimica et Biophysica Acta, 1977. **497**(3): p. 760-765.

139. Allen, T.M. and A. Chonn, *Large Unilamellar Liposomes with Low Uptake into the Reticuloendothelial System.* FEBS Letters, 1987. **223**(1): p. 42-46.

140. Allen, T.M., C. Hansen, and J. Rutledge, *Liposomes with prolonged circulation times: factors affecting uptake by reticuloendothelial and other tissues.* Biochimica et Biophysica Acta, 1989. **981**(1): p. 27-35.

141. Gabizon, A. and D. Papahadjopoulos, *Liposome Formulations with Prolonged Circulation Time in Blood and Enhanced Uptake by Tumors.* Proceedings of the National Academy of Sciences USA, 1988. **85**(18): p. 6949-6953.

142. Chonn, A., S.C. Semple, and P.R. Cullis, *Association of blood proteins with large unilamellar liposomes in vivo. Relation to circulation lifetimes.* The Journal of Biological Chemistry, 1992. **267**(26): p. 18759-18765.

143. Liu, D., Y.K. Song, and F. Liu, *Antibody dependent, complement mediated liver uptake of liposomes containing GM1*. Pharmaceutical Research, 1995. **12**(11): p. 1775-1780.

144. Park, Y.S. and L. Huang, *Effect of chemically modified GM1 and neoglycolipid analogs of GM1 on liposome circulation time: evidence supporting the dysopsonin hypothesis.* Biochimica et Biophysica Acta, 1993. **1166**(1): p. 105-114.

145. Woodle, M.C., C.M. Engbers, and S. Zalipsky, *New amphipatic polymer-lipid conjugates forming long-circulating reticuloendothelial system-evading liposomes.* Bioconjugate Chemistry, 1994. **5**(6): p. 493-496.

146. Yamauchi, H., T. Yano, T. Kato, I. Tanaka, S. Nakabayashi, K. Higashi, S. Miyoshi, and H. Yamada, *Effects of Sialic-Acid Derivative on Long Circulation Time and Tumor Concentration of Liposomes.* International Journal of Pharmaceutics, 1995. **113**(2): p. 141-148.

147. Yamauchi, H., H. Kikuchi, K. Yachi, M. Sawada, M. Tomikawa, and S. Hirota, *Effects of Glycophorin and Ganglioside Gm3 on the Blood-Circulation and Tissue Distribution of Liposomes in Rats.* International Journal of Pharmaceutics, 1993. **90**(1): p. 73-79.

148. Michalek, M.T., E.G. Bremer, and C. Mold, *Effect of gangliosides on activation of the alternative pathway of human complement.* The Journal of Immunology, 1988. **140**(5): p. 1581-1587.

149. Oldenborg, P.A., A. Zheleznyak, Y.F. Fang, C.F. Lagenaur, H.D. Gresham, and F.P. Lindberg, *Role of CD47 as a marker of self on red blood cells.* Science, 2000. **288**(5473): p. 2051-2054.

150. Lindberg, F.P., D.M. Lublin, M.J. Telen, R.A. Veile, Y.E. Miller, H. Donis-Keller, and E.J. Brown, *Rh-related antigen CD47 is the signal-transducer integrin-associated protein.* The Journal of Biological Chemistry, 1994. **269**(3): p. 1567-1570.

151. Weiskopf, K., A.M. Ring, C.C. Ho, J.P. Volkmer, A.M. Levin, A.K. Volkmer, E. Ozkan, N.B. Fernhoff, M. van de Rijn, I.L. Weissman, and K.C. Garcia, *Engineered SIRPalpha variants as immunotherapeutic adjuvants to anticancer antibodies.* Science, 2013. **341**(6141): p. 88-91.

152. Tsai, R.K., P.L. Rodriguez, and D.E. Discher, *Self inhibition of phagocytosis: the affinity of 'marker of self' CD47 for SIRPalpha dictates potency of inhibition but only at low expression levels.* Blood Cells, Molecules and Diseases, 2010. **45**(1): p. 67-74.

153. Stachelek, S.J., M.J. Finley, I.S. Alferiev, F. Wang, R.K. Tsai, E.C. Eckells, N. Tomczyk, J.M. Connolly, D.E. Discher, D.M. Eckmann, and R.J. Levy, *The effect of CD47 modified polymer surfaces on inflammatory cell attachment and activation.* Biomaterials, 2011. **32**(19): p. 4317-4326.

154. Rodriguez, P.L., T. Harada, D.A. Christian, D.A. Pantano, R.K. Tsai, and D.E. Discher, *Minimal "Self" Peptides That Inhibit Phagocytic Clearance and Enhance Delivery of Nanoparticles.* Science, 2013. **339**(6122): p. 971-975.

155. Hu, C.M., L. Zhang, S. Aryal, C. Cheung, R.H. Fang, and L. Zhang, *Erythrocyte membrane-camouflaged polymeric nanoparticles as a biomimetic delivery platform.* Proceedings of the National Academy of Sciences USA, 2011. **108**(27): p. 10980-10985.

156. Feng, Z.D., L. Hensley, K.L. McKnight, F. Hu, V. Madden, L. Ping, S.H. Jeong, C. Walker, R.E. Lanford, and S.M. Lemon, *A pathogenic picornavirus acquires an envelope by hijacking cellular membranes.* Nature, 2013. **496**(7445): p. 367-371.

157. Ramakrishnaiah, V., C. Thumann, I. Fofana, F. Habersetzer, Q. Pan, P.E. de Ruiter, R. Willemsen, J.A. Demmers, V. Stalin Raj, G. Jenster, J. Kwekkeboom, H.W. Tilanus, B.L. Haagmans, T.F. Baumert, and L.J. van der Laan, *Exosome-mediated transmission of hepatitis C virus between human hepatoma Huh7.5 cells.* Proceedings of the National Academy of Sciences USA, 2013. **110**(32): p. 13109-13113.

158. Hu, C.M., R.H. Fang, B.T. Luk, K.N. Chen, C. Carpenter, W. Gao, K. Zhang, and L. Zhang, *'Marker-of-self' functionalization of nanoscale particles through a top-down cellular membrane coating approach.* Nanoscale, 2013. **5**(7): p. 2664-2668.

159. Owens, D.E., 3rd and N.A. Peppas, *Opsonization, biodistribution, and pharmacokinetics of polymeric nanoparticles.* International Journal of Pharmaceutics, 2006. **307**(1): p. 93-102.

160. Hu, C.M., R.H. Fang, and L. Zhang, *Erythrocyte-inspired delivery systems.* Advanced Healthcare Materials, 2012. **1**(5): p. 537-547.

161. Gao, W., C.M. Hu, R.H. Fang, B.T. Luk, J. Su, and L. Zhang, *Surface functionalization of gold nanoparticles with red blood cell membranes.* Advanced Materials, 2013. **25**(26): p. 3549-3553.

162. Parodi, A., N. Quattrocchi, A.L. van de Ven, C. Chiappini, M. Evangelopoulos, J.O. Martinez, B.S. Brown, S.Z. Khaled, I.K. Hazdi, M.V. Enzo, L. Isenhart, M. Ferrarri, and E. Tasciotti, *Synthetic nanoparticles functionalized with biomimetic leukocyte membranes possess cell-like functions.* Nature Nanotechnology, 2013. **8**(1): p. 61-68.

163. Aryal, S., C.M. Hu, R.H. Fang, D. Dehaini, C. Carpenter, D.E. Zhang, and L. Zhang, *Erythrocyte membrane-cloaked polymeric nanoparticles for controlled drug loading and release.* Nanomedicine, 2013. **8**(8): p. 1271-1280.

164. Fang, R.H., C.M. Hu, K.N. Chen, B.T. Luk, C.W. Carpenter, W. Gao, S. Li, D.E. Zhang, W. Lu, and L. Zhang, *Lipid-insertion enables targeting functionalization of erythrocyte membrane-cloaked nanoparticles.* Nanoscale, 2013. **5**(19): p. 8884-8888.

165. Hu, C.M., R.H. Fang, J. Copp, B.T. Luk, and L. Zhang, *A biomimetic nanosponge that absorbs pore-forming toxins.* Natre Nanotechnology, 2013. **8**(5): p. 336-340.

166. Lakhal, S. and M.J. Wood, *Exosome nanotechnology: an emerging paradigm shift in drug delivery: exploitation of exosome nanovesicles for systemic in vivo delivery of RNAi heralds new horizons for drug delivery across biological barriers.* Bioessays, 2011. **33**(10): p. 737-741.

167. Kulp, A. and M.J. Kuehn, *Biological functions and biogenesis of secreted bacterial outer membrane vesicles.* Annual Reviews of Microbiology, 2010. **64**: p. 163-184.

168. Lejeune, A., M. Moorjani, C. Gicquaud, J. Lacroix, P. Poyet, and R. Gaudreault, *Nanoerythrosome, a new derivative of erythrocyte ghost: preparation and antineoplastic potential as drug carrier for daunorubicin.* Anticancer Research, 1994. **14**(3A): p. 915-919.

169. Toledano Furman, N.E., Y. Lupu-Haber, T. Bronshtein, L. Kaneti, N. Letko, E. Weinstein, L. Baruch, and M. Machluf, *Reconstructed Stem Cell Nano-Ghosts: A Natural Tumor Targeting Platform.* Nano Letters, 2013. **13**(7): p. 3248-3255.

170. Tang, K., Y. Zhang, H. zhang, P. Xu, J. Liu, J. Ma, M. Lv, D. Li, F. Katirai, G.X. Shen, G. Zhang, Z.H. Fend, D. Ye, and B. Hang, *Delivery of chemotherapeutic drugs in tumour cell-derived microparticles.* Nature Communications, 2012. **3**: p. 1282.

Chapter 1, in full, is a reprint of the material as it appears in *Nanoscale*, 2014, Che-Ming Hu, Ronnie Fang, Brian Luk and Liangfang Zhang. The dissertation author was a major contributor and co-author of this paper. The remainder of this dissertation will focus on the development of novel biomimetic nanotherapeutics using a cellular membrane cloaking strategy to disguise polymeric nanoparticles for a variety of targeted therapies.

Chapter 2

Understanding the Fundamentals of Membrane Coating on Polymeric Nanoparticles

2.1 Interfacial Interactions between the Membrane and Core

2.1.1 Introduction

Recent advancement in biology and materials engineering has led to surging interest in bio-inspired nanodevices with biomimetic functionalities [1-3]. Exploiting the immunomodulatory self-marker proteins commonly found in cells for nanocarrier functionalization has bestowed unique anti-phagocytic properties and prolonged *in vivo* survival onto nanoparticles [4, 5]. Among bio-inspired nanocarriers, a recently developed RBC membrane-cloaked nanoparticle (RBC-NP) platform presents an intriguing system as it utilizes the RBC membrane content in its entirety for immune-evasive stealth camouflage [6, 7] and therapeutic purposes [8, 9]. Upon unilamellar membrane coating, RBC-NPs display self-marker proteins with a right-side-out orientation bias [10], which contributes to the prolonged *in vivo* circulation time of the platform. The unique structural features and properties of RBC-NPs raise curiosity concerning the biomembrane–particle interface that plays a significant role in enabling colloidal stability and preserving biomimetic functionalities of the platform. In this study, we dissect the RBC-NP system to shed light on the mechanisms that elegantly bridge synthetic polymeric particles with natural cellular membranes.

While the development of RBC-inspired drug carriers has focused primarily on mechano-mimicry [11-13] and protein functionalization [5], the present study introduces a different emphasis on surface glycans, which in fact represent the predominant moieties on cellular surfaces [14]. On RBCs, the dense glycan coatings,

known as glycocalyx, have significant implications in the stabilization and immune-evasive properties of the cells [15-19]. These complex polysaccharides serve as a hydrophilic coating, and stabilizing strategies using analogous sugar polymers can be found in many carbohydrate-functionalized nanoformulations [20-22]. The asymmetric membrane distribution of glycans, which reside exclusively on the extracellular side of RBCs, also make glycans a good indicator of membrane sidedness [23, 24]. In addition, the abundant, negatively charged sialyl residues at the glycan terminus bestow a charge asymmetry across cellular membranes [25], which can affect interfacial interactions between RBC membranes and synthetic polymeric particles through electrostatic interactions. Herein, we carry out a series of studies to examine several interfacial aspects of RBC-NPs, including completeness of membrane coverage, membrane sidedness on the nanoparticles, and the effects of polymeric particles' surface charge and surface curvature on the membrane cloaking process. These studies help scrutinize the RBC-NP platform from a colloidal science perspective and shed light on the implications of membrane glycans and nanoparticle properties on RBC-NP formation. The studies also provide pertinent information toward future translation of the RBC-NP platform as well as inspirations for both synthetic and naturally derived nanoparticle designs.

2.1.2 Experimental Methods

2.1.2.1 Preparation and Characterization of RBC-NPs

RBC membranes were derived from whole blood collected from male

imprinting control region (ICR) mice (Charles River Laboratories, Wilmington, MA). Whole blood was centrifuged and subjected to hemolysis by hypotonic treatment to isolate RBC membranes. The membranes were then bath sonicated for 3 min using an FS30D bath sonicator (Fisher Scientific, Waltham, MA) at a frequency of 42 kHz and a power of 100 W and subsequently extruded through a 100 nm polycarbonate porous membrane using an Avanti mini extruder to form RBC membrane vesicles. In parallel, poly(D,L-lactic-*co*-glycolic acid) (PLGA) polymeric cores were prepared using a 0.67 dL g^{-1} carboxy-terminated 50:50 PLGA polymer (LACTEL Absorbable Polymers, Birmingham, AL) through a solvent displacement method. PLGA was first dissolved in acetone at a concentration of 1 mg mL^{-1} and added dropwise to 3 mL of water. The mixture was then stirred in open air for 2 h and filtered using an Amicon Ultra-4 Centrifugal Filter with a molecular weight cutoff (MWCO) of 10,000 Da (Millipore, Billerica, MA). To fuse the RBC membrane vesicles with the PLGA cores, 1 mg of PLGA particles was mixed with RBC membranes derived from various amounts of mouse whole blood and extruded through a 100 nm polycarbonate porous membrane using an Avanti mini extruder. The hydrodynamic diameter, polydispersity index, and surface zeta potential of the resulting RBC-NPs were determined from three repeated experiments using dynamic light scattering (DLS) on a ZEN3600 Nano Zetasizer (Malvern Instruments, UK) at 25°C. Transmission electron microscopy (TEM) images were taken to examine the structure of the RBC-NPs. A drop of the RBC-NP solution at a concentration of 2 mg mL^{-1} was deposited onto a glow-discharged carbon-coated grid. After 5 min, the grid was rinsed with 10 drops of distilled water and a drop of 1%

uranyl acetate stain was added for negative staining. The grid was then dried and imaged using a Tecnai G2 Sphera (FEI, Hillsboro, OR) microscope.

2.1.2.2 Membrane Coverage Assay

Biotin-functionalized PLGA was prepared by conjugating amine–PEG_2–biotin to 0.67 dL g^{-1} carboxy-terminated PLGA (Thermo Scientific, Waltham, MA). 100 mg of PLGA was dissolved in 2.5 mL chloroform and activated with 5 mg of ethyl(dimethylaminopropyl) carbodiimide (EDC) and 5.5 mg of *N*-hydroxysuccinimide (NHS) (Thermo Scientific, Waltham, MA). Following 60 min of activation, a 3-to-1 molar excess of amine–PEG_2–biotin was added to the polymer solution along with 8 μL of*N*,*N*-diisopropylethylamine (Fisher Scientific, Waltham, MA). After overnight incubation under gentle stirring, the polymer was precipitated by adding the solution dropwise into 40 mL of −20°C methanol. Functionalized PLGA was pelleted through centrifugation at 3500 rpm for 5 min. The pelleted polymer was then dissolved in chloroform and further purified in −20°C methanol two more times. Following the last wash, the biotin-functionalized PLGA was dried in a vacuum and dissolved in acetone. For the preparation of biotin-functionalized PLGA particles, 1 mg mL^{-1} of PLGA solution containing 2% of biotin–PLGA was prepared in acetone and added dropwise to 3 mL of water. The mixture was then stirred in open air for 2 h and filtered using an Amicon Ultra-4 Centrifugal Filter with a MWCO of 10,000 Da (Millipore, Billerica, MA). Biotin functionalization on nanoparticle surfaces was confirmed by incubating 1 mL of 1 mg mL^{-1} biotinylated nanoparticles with 20 μg of

streptavidin (Invitrogen, Grand Island, NY) for 30 min. Particle aggregation induced by streptavidin–biotin interactions was monitored by DLS, using non-biotinylated PLGA particles as a negative control. The biotinylated PLGA particles were then used to examine the extent of particle surface coverage by RBC membranes. 1 mL of 1 mg mL^{-1} RBC-NPs prepared with different membrane-to-particle ratios were incubated with 20 μg of streptavidin for 30 min. The particle size was determined from three repeated experiments using DLS at 25 °C.

2.1.2.3 Membrane Sidedness Assay

RBC-NPs were first prepared with 100 nm PLGA cores and RBC membrane vesicles. For glycoprotein quantification, proteins exposed on the RBC-NP surfaces were trypsinized by incubating 1 mL of 1 mg mL^{-1} RBC-NPs with 5 μg of trypsin (G-Biosciences, St. Louis, MO) at room temperature for 2 h. Sialic acid removal from RBC-NPs was performed by incubating 1 mL of 1 mg mL^{-1} RBC-NPs in water with 100 units of sialidase (Roche Diagnostics, Indianapolis, IN) at room temperature for 2 h. The samples were then centrifuged at 200,000×*g* for 45 min using an Optima L-90K Ultracentrifuge (Beckman Coulter, Brea, CA), and the supernatant was collected and examined for glycoprotein and sialic acid content. To quantify glycoprotein, the supernatant was examined using a Glycoprotein Detection Reagent (Thermo Scientific) following the manufacturer's instructions. To quantify sialic acid, the supernatant was examined using a Sialic Acid Quantification Kit (Sigma-Aldrich, St. Louis, MO) following the manufacturer's instructions. Equivalent amounts of RBC

ghosts and bare PLGA cores were used as a positive and a negative control, respectively.

2.1.2.4 Stability Study of RBC-NPs

A series of RBC-NP formulations were prepared by coating 1 mg of PLGA cores with RBC membranes collected from 200 μL, 100 μL, 75 μL, 50 μL, 25 μL or 0 μL of mouse blood. Each formulation was then adjusted to 1× PBS buffer (pH = 7.4) and sonicated for 5 min using an FS30D bath sonicator (Fisher Scientific, Waltham, MA) at a frequency of 42 kHz and a power of 100 W to facilitate the aggregation process. After sonication, the hydrodynamic diameter of the particles was determined using DLS. Trypsinized RBC-NPs were prepared by incubating a stable RBC-NP formulation (100 μL blood per mg PLGA core) with 50 μg mL^{-1} trypsin (G-Biosciences, St. Louis, MO). Two hours following the trypsinization, the particle size was measured by DLS.

2.1.2.5 Preparation of Positively Charged Cores

To create positively charged polymeric cores, 100 nm PLGA nanoparticles prepared using the aforementioned protocol were mixed with 5% (w/w) polyethylenimine (PEI, molecular weight = 1800 Da) and bath sonicated for 5 min. The resulting nanoparticle solution was filtered using an Amicon Filter with a MWCO of 10,000 Da. The hydrodynamic size, polydispersity index, and surface zeta potential of the PEI-coated PLGA particles were characterized by DLS. 1 mg of the resulting positively charged nanoparticles was then mixed with RBC membrane vesicles

derived from 100 μL of whole blood and extruded through a 200 nm, 400 nm or 1000 nm polycarbonate porous membrane using an Avanti mini extruder. The particle size and surface zeta potential before and after RBC membrane coating were measured by DLS. The structure of the particles was examined using TEM after negative staining with uranyl acetate.

2.1.2.6 Preparation of RBC-NPs with Differently Sized Polymeric Cores

Differently sized PLGA cores between 65 and 340 nm in diameter were prepared by adjusting the polymer concentration, the solvent-to-water ratio, and the ionic content in the aqueous phase during the nanoprecipitation process. Specifically, to prepare 65 nm PLGA cores, 1 mL of 5 mg mL^{-1} PLGA dissolved in acetone was pipetted into 3 mL of water. 120 nm cores were made by pipetting 1 mL of 10 mg mL^{-1} PLGA dissolved in acetone into 3 mL of water. 200 nm cores were prepared by pipetting 1 mL of 10 mg mL^{-1} PLGA dissolved in acetone into 4 mL of 2.5× PBS. 340 nm cores were prepared by adding water dropwise into 1 mL of 3 mg mL^{-1}PLGA dissolved in acetone until cloudiness was observed in the solution. All formulations were then evaporated in a vacuum chamber overnight to remove excess acetone. The prepared cores were washed 3 times using Amicon Filters with a MWCO of 10,000 Da prior to coating with RBC membranes. A 10% excess of RBC membranes was added to each core type based on the theoretical membrane-to-polymer ratio for complete membrane coverage. For 65 nm cores, RBC membranes derived from 165 μL of blood were added and the mixture was extruded through a 100 nm porous

membrane. For 120 nm cores, RBC membranes derived from 75 μL of blood were added and the mixture was extruded through a 200 nm porous membrane. For 200 nm cores, RBC membranes derived from 40 μL of blood were added and the mixture was extruded through a 400 nm porous membrane. For 340 nm cores, RBC membranes derived from 23 μL of blood were added and the mixture was extruded through a 400 nm porous membrane. The particle size and surface zeta potential before and after RBC membrane coating were measured by DLS. The core–shell structure of the particles was examined using TEM after negative staining with uranyl acetate.

2.1.3 Results and Discussion

RBC-NPs were first examined for the completeness of the membrane coverage. An aggregation assay based on streptavidin–biotin cross-linking chemistry was implemented to examine whether polymeric surfaces were exposed. In the study, biotinylated PLGA nanoparticles were prepared, which readily aggregate upon direct exposure to free streptavidin in solution (Figure 2.1A). Carboxylated PLGA polymers were first functionalized with amine–PEG_2–biotin using EDC/NHS chemistry, and the resulting biotinylated PLGA polymers were mixed with carboxylated PLGA at a 1:50 ratio to form biotinylated polymeric nanoparticles. The biotin-conjugated polymers showed a negligible effect on the physicochemical properties of the PLGA cores, as both biotinylated and non-biotinylated particles were ∼100 nm in size and −45 mV in surface zeta potential. Upon mixing with free streptavidin, the biotinylated cores aggregated to approximately 2000 nm, whereas the non-biotinylated cores remained

similar in size, demonstrating a particle bridging mechanism that was specific to the strong streptavidin–biotin interaction. A slight size increase by ~10 nm was observed in the non-biotinylated cores upon mixing with streptavidin, which was likely due to the non-specific protein absorption on the particle surface.

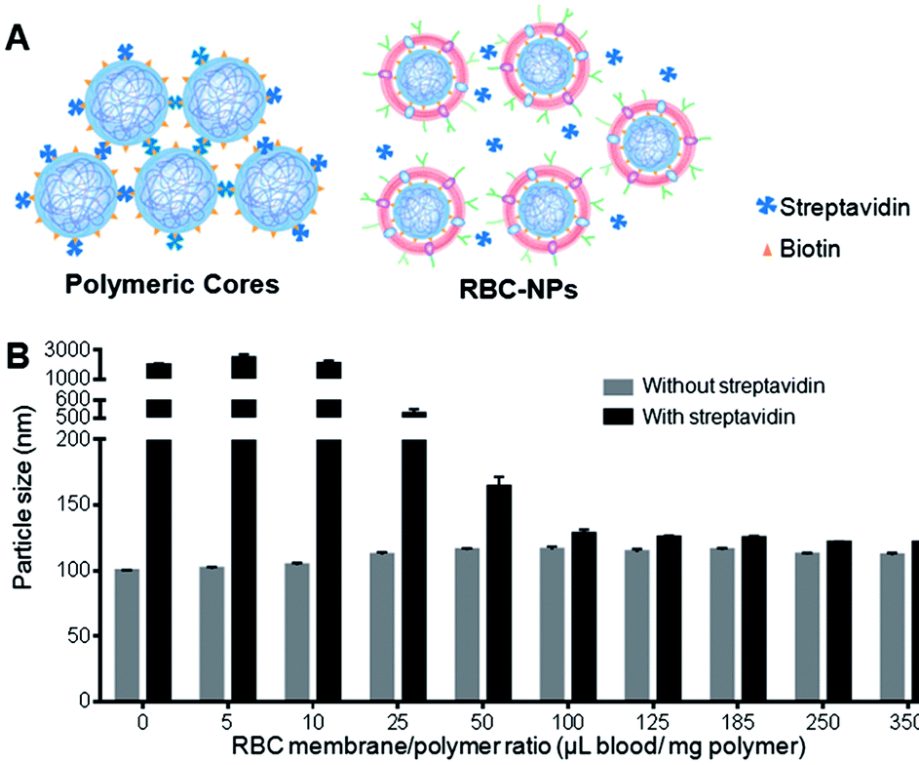

Figure 2.1 Determination of completeness of RBC membrane coating. (A) Schematic illustration shows the membrane coverage assay in which RBC membrane coating precludes the binding of free streptavidin to the biotin immobilized on the surface of polymeric cores. (B) Size change of RBC-NPs due to streptavidin–biotin cross-linking at various RBC membrane-to-polymer ratios. Error bars represent standard deviation (n = 3).

Given that bilayer membranes can preclude surface-attached biotin from interacting with the 60 kDa streptavidin, the completeness of RBC membrane coating was then evaluated using the biotinylated polymeric cores. Using a previously described extrusion process [6], the cores were coated with increasing amounts of RBC membrane content ranging from 0 to 350 μL of mouse blood per mg of polymer.

The coated cores were then mixed with streptavidin and monitored for particle size change. At low membrane-to-polymer ratios (below 25 μL mg^{-1}), significant aggregation was observed. However, as the membrane-to-polymer ratio increased to 100 μL mg^{-1} or higher, the addition of streptavidin failed to induce any considerable size increase among the biotinylated cores (Figure 2.1B). The preclusion of streptavidin-induced aggregation suggests that the particle surfaces were completely shielded, and 100 μL mg^{-1} was sufficient to fully coat all the nanoparticles present. Based on the particle surface area, RBC surface area, and RBC concentration in mouse blood, it was estimated that ~85 μL of mouse blood would be needed to derive enough RBC membrane material to completely coat 1 mg of 100 nm PLGA nanoparticles. The close match between the theoretical and the experimental membrane-to-polymer ratio for full coverage suggests a high membrane coating efficiency, which is consistent with a previous study that showed a high protein translocation yield through the membrane coating approach [10].

Owing to the asymmetric distribution of glycans on the extracellular side of cellular membranes, these glycans can be used as an indicator to quantitatively analyze the membrane sidedness on RBC-NPs. A trypsinization method was herein applied to examine the glycoprotein content on the outer surface of RBC-NPs [26]. In the study, RBC-NPs were first prepared with excess polymeric cores to ensure that all RBC membranes were occupied. RBC ghosts containing equivalent amounts of membrane content and bare polymeric cores were prepared as a positive control and a negative control, respectively. The samples were then trypsinized for 2 h and subjected to

ultracentrifugation at 200,000×*g* for 45 min. Since RBC bilayer membranes are impermeable to trypsin, membrane sidedness can be assessed by measuring the enzymatically removed glycoprotein content [26]. Detached glycoproteins were collected from the sample supernatant and quantified using a periodate-based glycoprotein detection assay (Figure 2.2A). Relative to the glycoprotein content in trypsinized RBC ghosts, trypsinized RBC-NPs yielded ~95% of the glycoprotein content in the sample supernatant (Figure 2.2B). This result indicates that the majority of surface glycoproteins on RBC-NPs were exposed to the trypsin treatment, corroborating a right-side-out membrane orientation that was previously observed by immunogold staining of surface proteins [10].

To further verify the membrane sidedness of RBC-NPs, a secondary assay was applied to quantify sialic acid, a characteristic carbohydrate terminus on RBC glycans. A sialidase enzyme was used to remove the terminal sialyl groups on the RBC-NPs (Figure 2.2A). Unlike the complete glycoprotein removal by trypsin, sialidase treatment only removed the terminal carbohydrate and did not affect the size of the RBC-NPs. The enzymatic activity, however, could be observed through surface zeta potential measurements as the removal of negatively charged sialic acid altered the surface charge of the RBC-NPs. Following 2 h of sialidase treatment, the zeta potential of RBC-NPs shifted from −23 mV to −0.6 mV, whereas that for bare nanoparticles remained largely unchanged, verifying the enzymatic removal of sialic acid. Following sialidase treatment and ultracentrifugation at 200,000×*g*, the sample

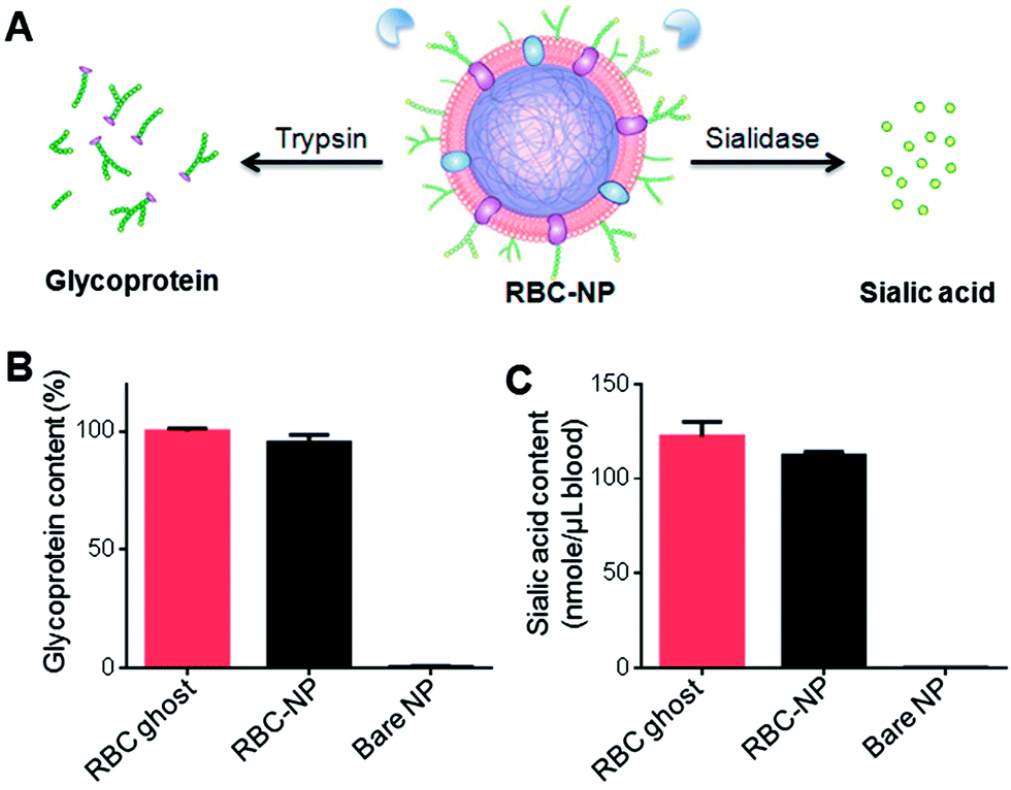

Figure 2.2 Quantification of glycoprotein and sialic acid on RBC-NPs to examine the sidedness of RBC membranes. (A) Schematic demonstrating the use of trypsin and sialidase to remove exoplasmic glycoprotein and sialic acid from RBC-NPs, respectively. (B) Comparison of the relative glycoprotein content recovered from equivalent amounts of RBC ghosts, RBC-NPs, and bare NPs after trypsinization (n= 3). (C) Comparison of the sialic acid content recovered from equivalent amounts of RBC ghosts, RBC-NPs, and bare NPs after sialidase treatment (n = 3).

supernatants were collected and assayed using a sialic acid quantification kit. It was found that per RBC membrane content derived from 1 mL of blood, 122±8 and 112±2 nmol of sialic acid was recovered from RBC ghosts and RBC-NPs, respectively (Figure 2.2C). The values are consistent with the reported sialic acid density on erythrocytes [27], and the close match in sialic acid recovery further supports the right-side-out-membrane orientation of the RBC-NPs. Based on the quantification result, it can also be estimated that at full coverage each RBC-NP with 100 nm in core diameter possesses ~43,500 sialyl moieties. This dense population of surface sialyl

moieties has strong implications on the RBC-NPs' properties as they are a key modulator of cellular interaction and immune activation and contribute to erythrocytes' *in vivo* survival [18, 19, 28].

Upon verification that the RBC membrane can completely envelop PLGA nanoparticles with a right-side-out membrane orientation, the stabilizing effect of the membrane coating was then evaluated. Carboxylated PLGA was used to prepare polymeric cores that were ~100 nm in diameter with a surface zeta potential of −45 mV. The cores were then extruded with various amounts of RBC membrane to form RBC-NPs. To test the stabilizing effect of RBC membranes, the particle solution was adjusted to 1× PBS (pH = 7.4), in which non-stabilized nanoparticles are known to aggregate owing to the charge screening effect by the ionic environment. Following brief sonication to agitate the sample solutions, the nanoparticle sizes were monitored using DLS. For the formulations containing 0, 25, 50, 75, 100, and 200 μL of RBC membrane per mg of PLGA core, the final particle sizes following sonication in PBS were 1965±152 nm, 850±84 nm, 395±51 nm, 135±2 nm, 117±1 nm, and 116±2 nm respectively (Figure 2.3A) The results reflect the increasing particle stability with higher RBC membrane content, and above 100 μL mg^{-1} of membrane-to-particle ratio, which is above the theoretical value for full particle coverage, the nanoparticles showed negligible size increase following sonication.

The stabilizing effect of RBC membranes can be attributed to the copious surface glycans present, which are highly hydrophilic and contribute to the steric

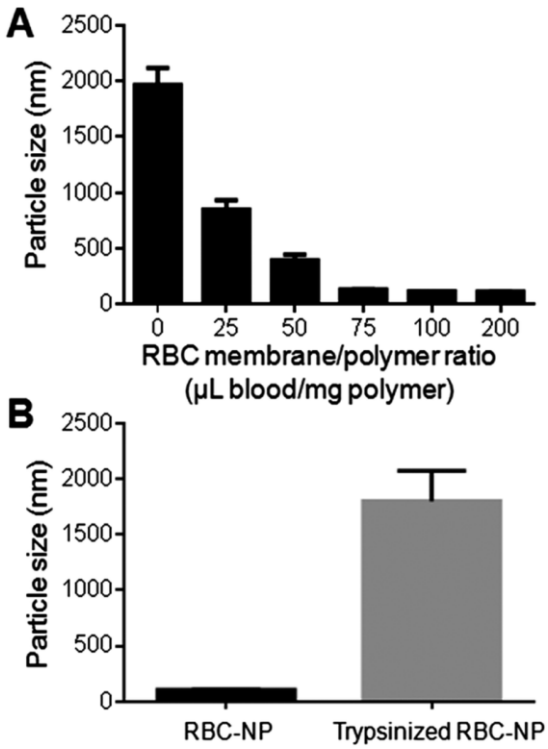

Figure 2.3 Stabilization of polymeric cores by RBC membrane cloaking. (A) Size of RBC-NPs prepared from different RBC membrane-to-polymer ratios. For a given amount of polymeric particles, the particles become more stable in PBS buffer with increasing RBC membrane content. Error bars represent standard deviation (*n*=3). (B) Sizes of stable RBC-NPs before and after trypsinization. Trypsinization resulted in the loss of particle stability (*n*=3).

stabilization of cells [15, 17]. To examine the role of these glycans in enabling colloidal stability, stabilized RBC-NPs (membrane-to-polymer ratio: 100 μL blood per mg polymer) were treated with trypsin, which enzymatically cleaves glycoproteins that serve to anchor the majority of RBC surface glycans. 2 h following trypsinization, significant RBC-NP aggregation was observed (Figure 2.3B). The loss of colloidal stability following trypsinization suggests that the phospholipid membrane bilayer alone is not sufficient to stabilize the particles, and that steric stabilization was enabled by the polysaccharides on RBC membranes. The stabilizing capability of hydrophilic glycans is not surprising, as synthetic polysaccharides have been commonly applied

for nanoparticle stabilization [20-22]. In the RBC-NP platform, polymeric nanoparticles are functionalized by naturally derived surface glycans. This glycan stabilization mechanism also provides an explanation to the efficient membrane cloaking process, in which unilamellar membrane coating readily occurs and yet multilamellar coating is not observed despite excess membrane materials; the non-stabilized polymeric surfaces with higher surface energy would readily interact with glycan-stabilized membranes to minimize the overall energy, whereas glycan-stabilized RBC-NP surfaces preclude further membrane interactions.

To further advance the understanding and development of cell membrane-cloaked nanoparticles, we examined effects of the nanoparticle core properties on the formation of the RBC-NPs. Since the electrostatic effect has shown a strong influence on lipid membrane interactions with a nanoparticle substrate [29], we investigated the use of positively and negatively charged polymeric cores for RBC-NP preparations. The negatively charged cores were prepared from carboxyl-terminated PLGA, and the positively charged cores were prepared by modifying carboxyl-terminated PLGA particles with polyethyleneimine (PEI). Upon mixing PLGA–COOH cores with 5% PEI solution, a change in the surface charge from −45 mV to +27 mV was observed with a negligible effect on the nanoparticle size. The two oppositely charged cores were then used to prepare RBC-NPs using the extrusion method.

Unlike the negatively charged cores, which were readily extruded with RBC membrane vesicles to form RBC-NPs, the positively charged cores formed observable aggregates upon mixture with the vesicles. Extruding the positively charged cores with

RBC membrane vesicles through 200, 400, and 1000 nm porous polycarbonate membranes resulted in significant membrane clogging that impeded the extrusion process. To better examine the membrane–particle interactions, the particle–membrane mixtures were visualized using transmission electron microscopy (TEM). The negatively charged cores formed consistent spherical particles with a core–shell structure (Figure 2.4A). The absence of aggregates in membranes mixed with negatively charged cores suggests a more subtle membrane–particle interaction that is less disruptive to the membrane structure and fluidity (Figure 2.4B). In contrast, the positively charged cores coalesced into large polydisperse aggregates with the membranes (Figure 2.4C). The aggregate formation can likely be attributed to the strong electrostatic interactions between positively charged cores and the negatively charged RBC membranes. Owing to the dense, negatively charged sialyl moieties on the extracellular membrane side, the strong affinity to positively charged nanoparticles could collapse the fluidic lipid bilayer and impede the local arrangement necessary for lipid coverage [30]. Bridging between cores and collapsed lipid membranes with opposite charges can therefore account for the observed aggregate formation (Figure 2.4D). While understanding the dynamics between the negatively charged cores and RBC membranes demands in-depth molecular analysis beyond the scope of the present study, we demonstrate that the negative surface charge is a major factor in enabling proper RBC-NP formation. The electrostatic repulsion between negatively charged particle surfaces and asymmetrically charged RBC membranes also provides a driving force that favors the right-side-out membrane orientation on the RBC-NPs.

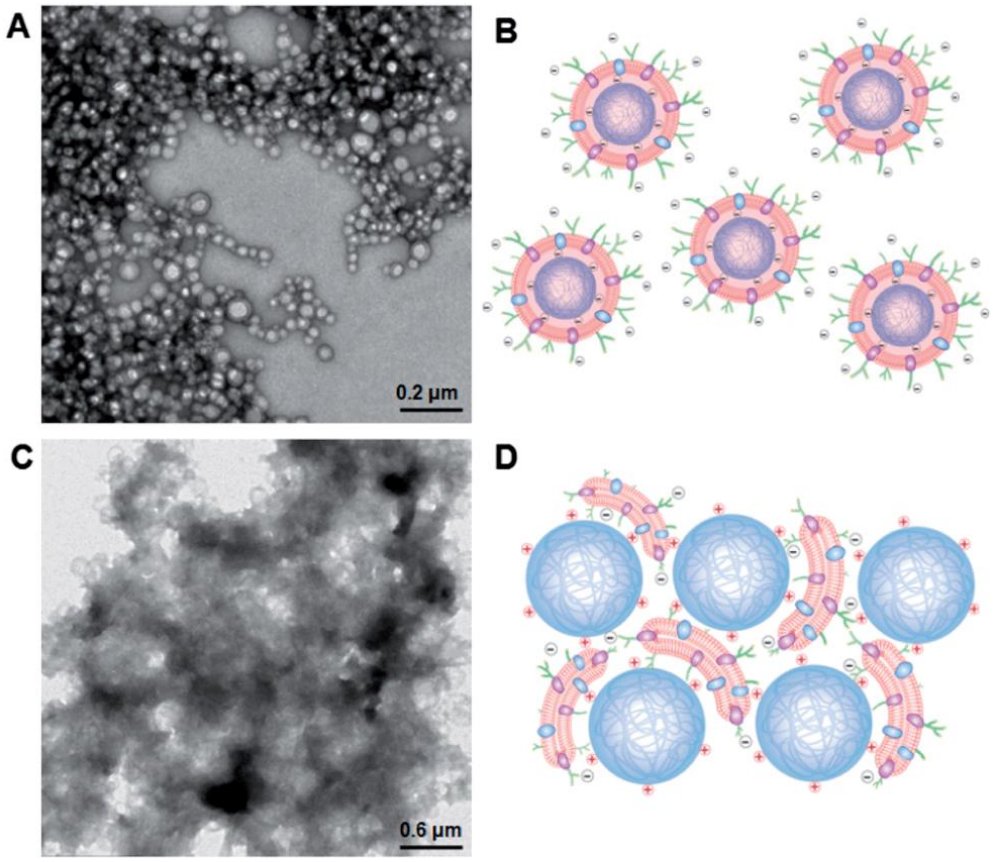

Figure 2.4 Effect of particles' surface charge on RBC membrane coating. (A) Representative transmission electron microscopy (TEM) image of negatively charged polymeric particles extruded with RBC membranes. (B) Schematic conceptualization of the electrostatic interaction between the negatively and asymmetrically charged RBC membranes with negatively charged polymeric cores. (C) Representative TEM image of positively charged polymeric cores extruded with RBC membranes. (D) Schematic conceptualization of the electrostatic interaction between negatively and asymmetrically charged RBC membranes with positively charged polymeric cores.

As lipid bilayer coating on nanoscale substrates can be influenced by the substrates' radius of curvature [31], or, alternatively speaking, the cores' size, we demonstrate the applicability of the RBC membrane cloaking process over a range of particle sizes that are relevant for nanomedicine applications. We prepared carboxyl-terminated PLGA cores of different diameters using variations of the solvent displacement method [32], creating unimodal nanoparticles that ranged from 65 nm to 340 nm. Each of these PLGA nanoparticle cores was extruded with the corresponding

amount of RBC membrane vesicles through a polycarbonate membrane with appropriate pore sizes to form RBC-NPs. For all the differently sized particles, RBC membrane coating resulted in an increase in size by 10–20 nm. The cloaking process also shifted the zeta potential of the particles from approximately −45 mV to −24 mV, which corresponds closely to the zeta potential of RBC membrane vesicles (Figure 2.5A). TEM visualization of particle cores 65, 120, 200, and 340 nm in diameter showed that uniform RBC membrane cloaks were broadly applied (Figure 2.5B). The flexibility of the membrane coating technique offers the freedom to functionalize a broad range of nanodevices with different sizes and geometries. The size of RBC-NPs can also be fine-tuned to match the need of specific medical applications.

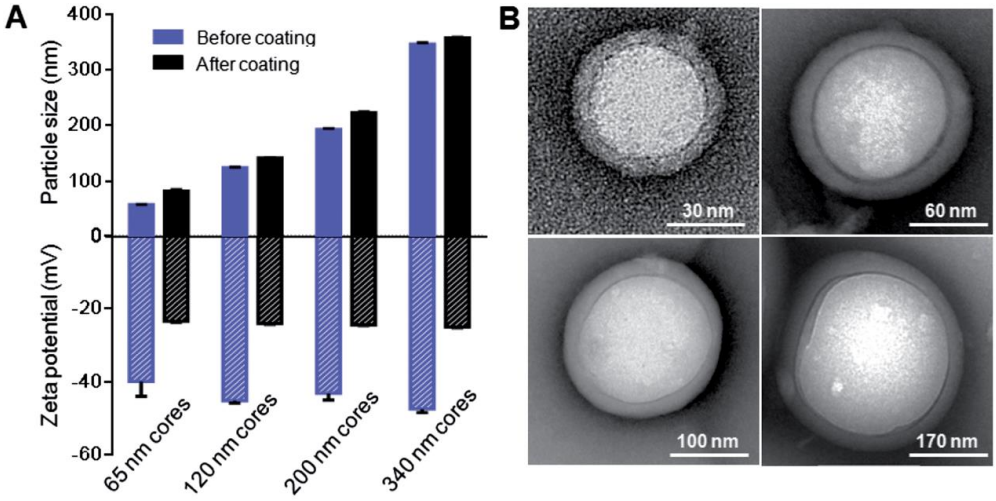

Figure 2.5 Effect of particles' surface curvature on RBC membrane coating. (A) Size and surface zeta potential of RBC-NPs with differently sized, negatively charged polymeric cores, both before and after RBC membrane coating. (B) Representative TEM images of RBC-NPs with differently sized polymeric cores.

By examining multiple interfacial aspects of RBC-NPs, the present study provides a better understanding of the platform. The particles were shown to be completely enveloped, suggesting a continuous membrane coating on the particle surfaces. The completeness of membrane coverage has significant implications as it

can shield the particles from external exposure, thereby minimizing the risk of complement activation and immunological responses typically associated with foreign materials. The RBC-NPs were also found to possess right-side-out oriented membrane coating, which exposes dense surface glycan contents to the aqueous environment and ensures the proper protein presentation on the particle surface [10]. The hydrophilic glycan layer also enhances the colloidal stability of RBC-NPs under ionic conditions, and its enzymatic removal by trypsin led to rapid particle aggregation. Taken together with previous findings that demonstrate the membrane and surface protein retention [6] and cargo encapsulation by the particles [33], the RBC-NPs can be considered a multifunctional nanoparticle system that integrates the steric stabilization of polysaccharides, the biological immunoevasive activities of membrane proteins, the cargo loading capacity of polymeric cores, and the anchoring and insulating functions of the lipid membranes, into a single, unified package. The present study also demonstrates RBC-NPs' size-tunability and enzyme-triggered particle destabilization. These features provide the platform with the opportunity to be tailored for specific delivery goals.

In addition to elucidating structural composition of RBC-NPs, the present study also extends the understanding of cell membrane–nanoparticle interaction that drives the membrane cloaking process. Both the surface glycans on RBC membranes and the physicochemical properties of nanoparticle cores were found to play a significant role in RBC-NP formation. With carboxy-terminated PLGA cores as nanoparticle substrates, the membrane cloaking process was highly efficient.

Achieving complete particle shielding and particle stabilization requires a membrane-to-polymer ratio closely matched to the theoretical value for complete particle coverage. This efficient cloaking process can be attributed to the glycan-driven colloidal stabilization of the polymeric particles, which renders the system energetically favorable. The asymmetrically distributed sialic acids, which bestow a negative charge to the extracellular membrane side, can also affect the membrane–particle interaction electrostatically. Rapid aggregation occurred upon the mixture of positively charged polymeric cores with RBC membranes, as strong electrostatic attractions resulted in membrane–particle bridging. In contrast, negatively charged cores readily form RBC-NPs with right-side-out membrane coating, which is likely aided by the repulsion between particle and extracellular membrane surfaces. As surface sialic acids and their associated membrane charge asymmetry are broadly present in biology [34, 35], such a membrane–particle interaction should be considered broadly in the development of cell membrane-functionalized nanodevices.

2.1.4 Conclusions

RBC-NPs present a unique nanocarrier platform that combines the immunomodulatory properties of natural cellular components with the cargo carrying capacity of polymeric nanoparticles. In the present study, we examined the platform's interfacial features and assessed the roles of RBC surface glycans and nanoparticle properties in RBC-NP formation. RBC-NPs are completely shielded by lipid membranes and are stabilized by surface glycans. The hydrophilic glycans and the

negatively charged sialic acid residues contribute to the structural organization of RBC-NPs, which possess a unilamellar, right-side-out membrane cloak. Owing to the inherent electrostatic properties of RBC membranes, positively charged nanoparticles did not yield proper RBC-NP formation. The membrane cloaking approach was successfully applied to nanoparticle substrates between 65 and 340 nm in diameter (the size range tested in this study), demonstrating the versatility of the camouflaging technique toward a variety of nanocarriers.

2.1.5 References

1. Yoo, J.W., D.J. Irvine, D.E. Discher, and S. Mitragotri, *Bio-inspired, bioengineered and biomimetic drug delivery carriers.* Nature Reviews Drug Discovery, 2011. **10**(7): p. 521-535.

2. Balmert, S.C. and S.R. Little, *Biomimetic delivery with micro- and nanoparticles.* Advanced Materials, 2012. **24**(28): p. 3757-3778.

3. Hu, C.M, R.H. Fang, B.T. Luk, and L. Zhang, *Polymeric nanotherapeutics: clinical development and advances in stealth functionalization strategies*. Nanoscale, 2014. **6**(1): p. 65-75.

4. Tsai, R.K., P.L. Rodriguez, and D.E. Discher, *Self inhibition of phagocytosis: the affinity of 'marker of self' CD47 for SIRPalpha dictates potency of inhibition but only at low expression levels*. Blood Cells, Molecules, and Diseases, 2010. **45**(1): p. 67-74.

5. Rodriguez, P.L, T. Harada, D.A. Christian, D.A. Pantano, R.K. Tsai, and D.E. Discher, *Minimal "Self" peptides that inhibit phagocytic clearance and enhance delivery of nanoparticles*, Science, 2013. **339**(6122): p. 971-975.

6. Hu, C.M., L. Zhang, S. Aryal, C. Cheung, R.H. Fang and L. Zhang, *Erythrocyte membrane-camouflaged polymeric nanoparticles as a biomimetic delivery platform.* Proceedings of the National Academy of Sciences USA, 2011. **108**(27): p. 10980-10985.

7. Gao, W., C.M. Hu, R.H. Fang, B.T Luk, J. Su, and L. Zhang, *Surface functionalization of gold nanoparticles with red blood cell membranes*. Advanced Materials, 2013. **25**(26): p. 3549-3553.

8. Hu, C.M., R.H. Fang, J.A. Copp, B.T. Luk, and L. Zhang, *A biomimetic nanosponge that absorbs pore-forming toxins*. Nature Nanotechnology, 2013. **8**(5): p. 336-340.

9. Fang, R.H., C.M. Hu, K.N. Chen, B.T. Luk, C.W. Carpenter, W. Gao, S. Li, D.E. Zhang, W. Lu, and L. Zhang, *Lipid-insertion enables targeting functionalization of erythrocyte membrane-cloaked nanoparticles*. Nanoscale, 2013. **5**(19): p. 8884-8888.

10. Hu, C.M., R.H. Fang, B.T. Luk, K.N. Chen, C.W. Carpenter, W. Gao, K. Zhang, and L. Zhang, *'Marker-of-self' functionalization of nanoscale particles through a top-down cellular membrane coating approach*. Nanoscale, 2013. **5**(7): p. 2664-2668.

11. Doshi, N., A.S. Zahr, S. Bhaskar, J. Lahann, and S. Mitragotri, *Red blood cell-mimicking synthetic biomaterial particles*. Proceedings of the National Academy of Sciences USA, 2009. **106**(51): p. 21495-21499.

12. Merkel, T.J., S.W. Jones, K.P. Herlihy, F.R. Kersey, A.R. Shields, M. Napier, J.C. Luft, H. Wu, W.C. Zamboni, A.Z. Wang, J.E. Bear, and J.M. DeSimone, *Using mechnobiological mimicry of red blood cells to extend circulation times of hydrogel microparticles*. Proceedings of the National Academy of Sciences USA, 2011. **108**(2): p. 586-591.

13. Hu, C.M., R.H. Fang, and L. Zhang, *Erythrocyte-inspired delivery systems*. Advanced Healthcare Materials, 2012. **1**(5): p. 537-547.

14. Mager, M.D., V. LaPointe, and M.M Stevens, *Exploring and exploiting chemistry at the cell surface*. Nature Chemistry, 2011. **3**(8), 582-589.

15. W. Evans and J. Graham, *Membrane Structure and Function*, Oxford University Press, New York, 1991, p. 1–86.

16. Eylar, E.H., M.A. Madoff, O.V. Brody, and J.L. Oncley, *The contribution of sialic acid to the surface charge of the erythrocyte*. Journal of Biological Chemistry, 1962. **237**(6): p. 1992-2000.

17. M. Fukuda, *Molecular Glycobiology*, Oxford University Press, New York, 1994, p. 1–52 .

18. R. Schauer, *Sialic acids as regulators of molecular and cellular interactions*. Current Opinion in Structural Biology, 2009. **19**(5): p. 507-514.

19. Kelm, S. and R. Schauer, *Sialic acids in molecular and cellular interactions*. International Review of Cytology, 1997. **175**: p. 137-240.

20. Raveendran, P., J. Fu, and S.L. Wallen, *Completely "green" synthesis and stabilization of metal nanoparticles*. Journal of the American Chemical Society, 2003. **125**(46): p. 13940-13941.

21. Cho, C.S., J.I. Jeong, T. Ishihara, R. Takei, J.U. Park, K.H. Park, A. Maruyama, and T. Akaike, *Simple preparation of nanoparticles coated with carbohydrate-carrying polymers*. Biomaterials, 1997. **18**(4): p. 323-326.

22. Lemarchand, C., R. Gref, and P. Couvreur, *Polysaccharide-decorated nanoparticles*. European Journal of Pharmaceutics and Biopharmaceutics, 2004. **58**(2): p. 327-341.

23. Rothman, J.E. and J. Lenard, *Membrane asymmetry*. Science, 1977. **195**(4280): p. 743-753.

24. Steck, T.L. and G. Dawson, *Topographical distribution of complex carbohydrates in the erythrocyte membrane*. Journal of Biological Chemistry, 1974. **249**(7): p. 2135-2142.

25. R. Winzler, *Red Cell Membrane*, Lippincott, Philadelphia, 1969, p. 157.

26. Heidrich, H.G. and G. Leutner, *two types of vesicles from the erythrocyte-ghost membrane differing in surface charge. Separation and characterization by preparative free-flow electrophoresis*. European Journal of Biochemistry, 1974. **41**(1): p. 37-43.

27. Miller, A., J.F. Sullivan, and J.H. Katz, *Sialic acid content of the erythrocyte and of an ascites tumor cell of the mouse*. Cancer Research, 1963. **23**: p. 485-490.

28. Durocher, J.R., R.C. Payne, and M.E. Conrad, *Role of Sialic acid in erythrocyte survival*. Blood, 1975. **45**(1): p. 11-20.

29. Mornet, S., O. Lambert, E. Duguet, and A. Brisson, *The formation of supported lipid bilayers on silica nanoparticles revealed by cryoelectron microscopy*. Nano Letters, 2005. **5**(2): p. 281-285.

30. Fischlechner, M., M. Zaulig, S. Meyer, I. Estrela-Lopis, L. Cuellar, J. Irigoyen, P. Pescador, M. Brumen, P. Messner, S. Moya, and E. Donath, *Lipid layers o polyelectrolyte multilayer supports*. Soft Matter, 2008. **4**: p. 2245-2258.

31. Roiter, Y., M. Ornatska, A.R. Rammohan, J. Balakrishnan, D.R. Heine, and S. Minko, Interaction of nanoparticles with lipid membrane. *Nano Letters*, 2008. **8**(3): p. 941-944.

32. Chan, J.M., L. Zhang, K.P. Yuet, G. Liao, J.W. Rhee, R. Langer, and O.C. Farokhzad, *PLGA-lecithin-PEG core-shell nanoaprticles for controlled drug delivery*. Biomaterials, 2009. **30**(8): p. 1627-1634.

33. Aryal, S., C.M. Hu, R.H. Fang, D. Dehaini, C.W. Carpenter, D.E. Zhang, and L. Zhang, *Erythrocyte membrane-cloaked polymeric naonparticles for controlled drug loading and release*. Nanomedicine, 2013. **8**(8): p. 1271-1280.

34. R. Schauer, *Chemistry, metabolism, and biological functions of sialic acids*. Advances in Carbohydrate Chemistry and Biochemistry, 1982. **40**: p. 131-234.

35. Glick, M.C., C.A. Comstock, M.A. Cohen, and L. Warren, *Membranes of animal cells. 8. Distribution of sialic acid, hexosamines and sialidase in the L cell*. Biochimica et Biophysica Acta, 1971. **233**: p. 247-257.

2.2 “Marker-of-Self” Functionalization

2.2.1 Introduction

Enabling active immune evasion through biomimetic surface functionalization presents an emerging stealth strategy for developing long-circulating delivery vehicles [1, 2]. The identification of CD47, a transmembrane protein that serves as a universal molecular ‘marker-of-self’, has led to its utilization in the growing development of bio-inspired, immune-evasive devices. Capable of inhibiting phagocytosis and conferring anti-inflammatory properties through interactions with signal regulatory protein alpha (SIRPα) expressed by macrophages, CD47 and its analogs have been found to contribute to the *in vivo* survival of red blood cells (RBCs) [3], cancer cells [4], and viruses [5]. Application of CD47 to modulate the immune responses against synthetic devices was first demonstrated with macrophages treated by purified recombinant, soluble CD47, which showed reduced uptake of colloidal emulsions [6]. Synthetic materials covalently conjugated with recombinant CD47 further advanced this biomimetic stealth approach, yielding polymeric microspheres [7] and implant surfaces with reduced affinity to inflammatory cells [8, 9]. On nanoscale particles, however, interfacing with native biological components through chemical conjugation of immunomodulatory proteins to particle surfaces can be difficult to manipulate. In particular, inconsistent protein surface density and randomized ligand orientations are notable issues that can greatly undermine the performance of the resulting nanocarriers.

Toward engineering nanocarriers that can actively suppress immune attack by macrophages, herein we demonstrate a robust 'top-down' approach to functionalizing nanoscale particles with native CD47 by cloaking sub-100 nm nanoparticles with cellular membranes derived directly from natural RBCs (Figure 2.6). The uniqueness of this membrane coating approach lies in its ability to functionalize nanoparticles with native immunomodulatory proteins including CD47 at an equivalent density to that on natural RBCs. In this study, we show direct evidence that the 'marker-of-self' proteins are transferred to the particle surfaces and present in the right-side-out orientation. A macrophage uptake study confirms the stealth functionality conferred

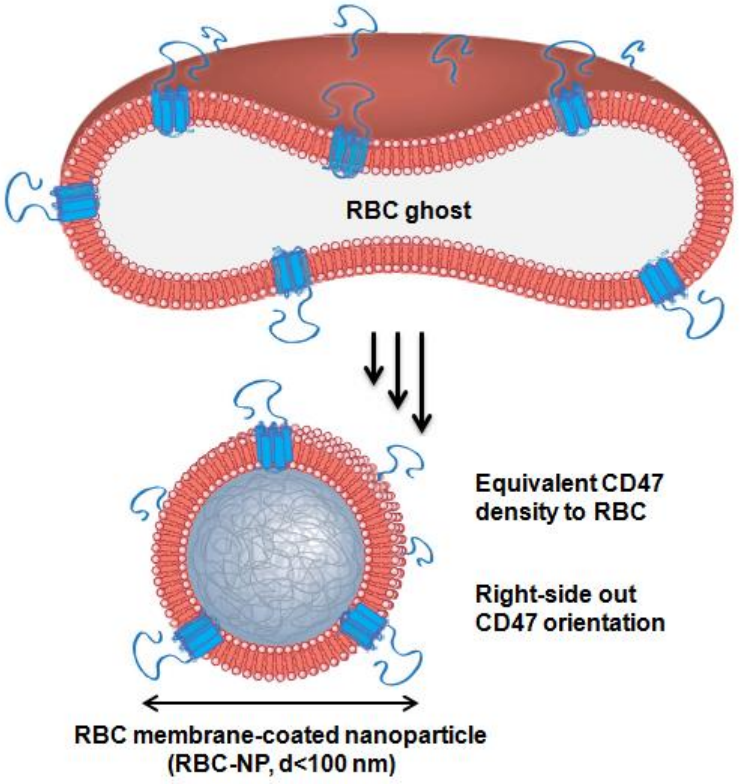

Figure 2.6 Controlled CD47 functionalization enabled by RBC membrane coating. The resulting RBC membrane-coated nanoparticle (RBC-NP) is expected to have a CD47 density equivalent to that on a natural RBC.

by the immunomodulatory proteins. Since cellular membranes anchor the many molecular tags that define cellular identities, attaching these membranes to nanoparticle surfaces provides unparalleled control over the functionalization of synthetic nanocarriers toward biomimicry.

2.2.2 Experimental Methods

2.2.2.1 Preparation of RBC Membrane-Coated NPs

RBCs were collected from 10 week-old male ICR mice (Charles River Laboratories) by centrifuging the whole blood at 2000 x g for 5 min, following which the supernatant and buffy coat were removed. Collected RBCs were then subject to hypotonic treatment to remove interior contents. The resulting RBC ghosts were extruded through 100 nm polycarbonate porous membranes using an extruder (Avanti Polar Lipids) to prepare RBC membrane-derived vesicles with a diameter of approximately 120 nm. Poly(lactic-co-glycolic acid) (PLGA) polymeric cores were prepared using 0.67 dL/g carboxy-terminated 50:50 PLGA polymer (LACTEL Absorbable Polymers) through a solvent displacement process, during which 1 mg of PLGA was dissolved in 200 μL of acetone and added drop-wise to 3 mL of water. Following solvent evaporation for 2 hr, the particles were washed using 10 kDa molecular weight cutoff (MWCO) Amicon Ultra-4 Centrifugal Filters (Millipore). The RBC-NPs were then prepared by fusing the RBC membrane-derived vesicles onto the PLGA particles by extruding the particles with the RBC membrane-derived vesicles through 100 nm polycarbonate porous membranes. The size and the zeta potential of

the resulting RBC-NPs were obtained from three dynamic light scattering (DLS) measurements using a Malvern ZEN 3600 Zetasizer, which showed an average hydrodynamic diameter of 70 and 85 nm before and after the extrusion process, respectively. The particle morphology was characterized using scanning electron microscopy (SEM). Samples for SEM imaging were prepared by dropping 5 μL of the RBC-NP solution onto a polished silicon wafer. After drying the droplet at room temperature overnight, the sample was coated with chromium and then imaged by SEM.

2.2.2.2 Identification of Membrane Proteins and CD47

RBC-NPs were isolated from free RBC membrane materials by ultracentrifugation at 14000 x g for 30 min. The resulting RBC-NPs were lyophilized, prepared in lithium dodecyl sulfate (LDS) sample loading buffer (Invitrogen), and separated on a 4-12% Bis-Tris 10-well minigel in MOPS running buffer using a Novex® Xcell SureLock Electrophoresis System (Invitrogen). For membrane protein identification, the gel was stained using SimplyBlue^{TM} SafeStain solution (Life Technologies) following the manufacturer's instructions and imaged using a gel imager. For CD47 identification, the resulting gel was transferred to a nitrocellulose membrane. The membrane was then stained with a primary rat anti-mouse CD47 antibody (BD Biosciences) and a secondary goat anti-rat IgG HRP conjugate (Millipore). The membrane was then subject to ECL western blotting substrate (Pierce) and developed with the Mini-Medical/90 Developer (ImageWorks).

2.2.2.3 Quantification of CD47 on RBC-NPs

The amount of CD47 retained on the RBC-NPs was quantified by comparing the CD47 protein intensity to protein standards prepared on the same western blotting membrane. The protein standards were prepared from predetermined volumes of blood, which yielded a positive linear correlation between the CD47 band intensity and the blood volume following western blotting. The band intensities were quantified through an image analysis with Adobe Photoshop software. A CD47 standard curve was then established by converting the blood volumes to their corresponding CD47 quantity, using an estimated concentration of mouse RBCs in the blood (10^{10}/mL) [10] and an average number of CD47 per mouse RBC (16,500 copies/cell) [11].

2.2.2.4 Transmission Electron Microscopy

A drop of the RBC-NP or bare PLGA nanoparticle (bare NP) solution (1 mg/mL) was deposited onto a glow-discharged carbon-coated grid. For immunostaining, the sample droplet was washed with 3 drops of 0.5 mg/mL rat anti-mouse CD47 antibody solution. For staining the intracellular sequence of CD47, an intracellular sequence specific rabbit anti-CD47 antibody (GeneTex). Following 30 sec of incubation, the sample was rinsed with 3 drops of either a goat anti-rat IgG gold conjugate (5 nm) solution (Canemco, Inc.) or a anti-rabbit IgG gold conjugate (5 nm) solution (Sigma-Aldrich) and then washed with 10 drops of distilled water. For negative staining, the particle sample droplet was washed with 10 drops of distilled water and stained with 1% uranyl acetate. These samples were then imaged using an

FEI Sphera Microscope at 200kV.

2.2.2.5 Macrophage Uptake Study

PLGA nanoparticles encapsulating 0.05% (w/w) 1,1'-dioctadecyl-3,3,3',3'-tetramethylindodicarbocyanine, 4-chlorobenzenesulfonate salt (DiD) dye (Life Technologies) were prepared for fluorescence quantification using flow cytometry. CD47-blocked RBC-NPs were prepared by incubating 1 mg of the DiD-loaded RBC-NPs with 400 μg of rat anti-mouse CD47 antibodies (BD Biosciences) for 1 hr. For the macrophage uptake study, J774 murine macrophage cells were cultured in DMEM media (Invitrogen) supplemented with 10% FBS (Sigma-Aldrich) and plated at a density of 10^5 cells/well on 12-well plates (BD Biosciences). On the day of the experiment, the cells were washed and cultured in fresh culture media. Bare PLGA nanoparticles (bare NPs), RBC-NPs, and CD47-blocked RBC-NPs were incubated at a concentration of 25 μg/mL with the macrophage cells at 37°C for 10 min. Non-internalized nanoparticles were washed away with PBS. The macrophage cells were then scraped off the plates and analyzed using flow cytometry. All flow cytometry studies were conducted on a FACSCanto II flow cytometer (BD Biosciences) and the resulting data was analyzed using FlowJo software from Tree Star. Thirty thousand events were collected per sample and gated using control cells that were not incubated with any nanoparticles. Histograms were plotted with fluorescence intensity as the x-axis using a biexponential scale. The mean fluorescence was plotted in a bar chart with error bars representing the standard error. Statistical analysis was performed based on

a two-tailed, unpaired t-test.

2.2.3 Results and Discussion

With five membrane-spanning regions, CD47 is an integral membrane protein firmly embedded in RBC membranes, exhibiting an IgV-like extracellular domain that helps maintain the RBCs' survival in the circulation [12]. While it was previously shown that RBC membrane coating associated nanoparticles with the majority of the membrane materials [13], it remained to be investigated whether these RBC membrane-coated nanoparticles (RBC-NPs) properly present the CD47 for immunomodulation. Verification of the protein, its density, and its orientation on the RBC-NP surfaces demands a molecular examination of these RBC-mimicking nanocarriers. To investigate the functionalization of native CD47 on RBC-NPs, 70 nm poly(lactic-co-glycolic acid) (PLGA) particles were first extruded with RBC membrane-derived vesicles following a previously described protocol [13]. Through scanning electron microscopy (SEM) visualization, a spherical morphology was observed for the resulting RBC-NPs (Figure 2.7A), and dynamic light scattering measurements showed a mean particle diameter of 85 ± 2 nm. The purified particles were then solubilized in a lithium dodecyl sulphate (LDS) sample loading buffer, following which the protein contents stripped from the nanoparticles were separated by SDS-PAGE. The resulting protein gel was subsequently subjected to western blotting using anti-CD47 antibody as the primary immunostain. The presence of CD47 on the RBC-NPs was confirmed by a distinct, single band at 50 kDa (Figure 2.7B),

which is the characteristic molecular weight of the CD47 protein self-marker [12].

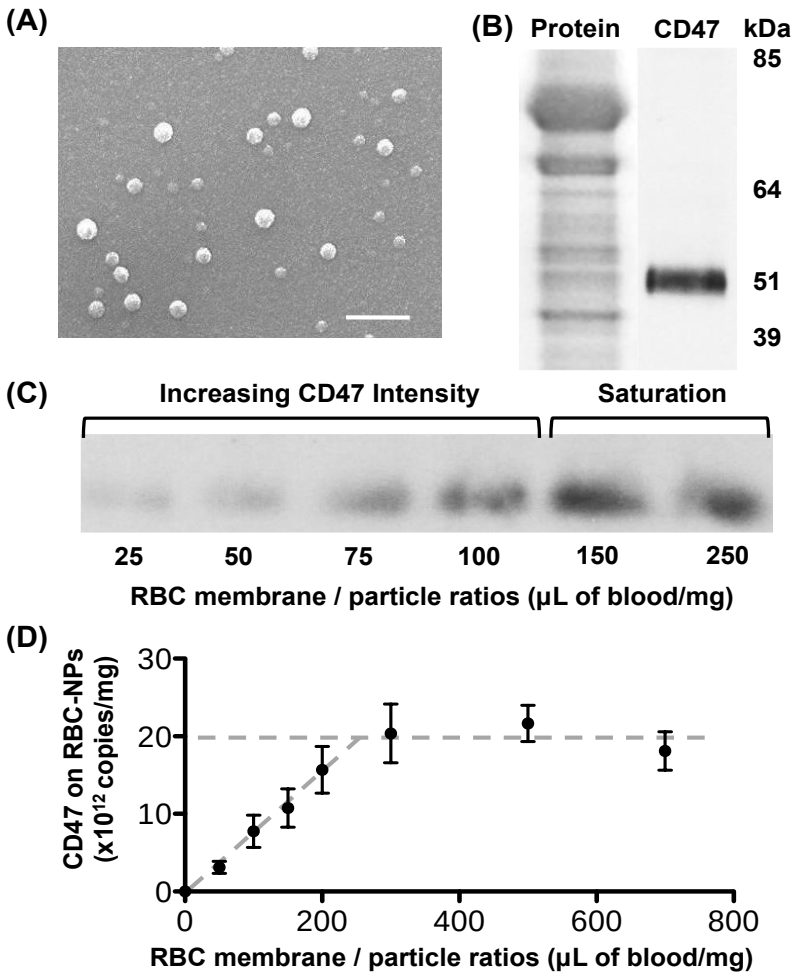

Figure 2.7 Characterization and quantification of CD47 on the RBC-NPs. (A) A representative scanning electron microscopy (SEM) image shows the spherical structure and morphology of the prepared RBC-NPs (scale bar = 250 nm). (B) Coomassie staining (left) and CD47 western blot (right) of the RBC-NPs' protein contents following SDS-PAGE separation. (C) Comparison of CD47 contents on the RBC-NPs prepared from different RBC membrane to polymer ratios. (D) Quantitative analysis of CD47 density on the RBC-NPs prepared from different RBC membrane to polymer ratios (n=5).

To further examine the extent of CD47 protein on the particle surfaces, the RBC-NPs prepared with different RBC membrane to polymeric particle ratios were collected and analysed for retained CD47 contents. An ultracentrifugation process was applied to isolate the resulting RBC-NPs from free RBC membranes, following which

protein contents on the nanoparticles was processed through SDS-PAGE and examined by western blotting analysis. Figure 2.7C shows the relative CD47 retention on the different particle formulations. As the RBC membrane to polymeric particle ratio increased from 25 to 150 μL of blood per mg of polymer, a corresponding increase in the CD47 intensity was observed. This positive correlation reflects the increasing particle functionalization by the increasing RBC membrane inputs, as more CD47 could be identified in the isolated nanoparticle samples. Saturation in CD47 band intensity was observed upon further raising the RBC membrane to polymer ratio above 150 μL/mg, which reflected the upper limit of CD47 functionalization achievable by the RBC membrane coating. To quantitatively analyze the protein density on the RBC-NPs, CD47 standards were prepared from predetermined volumes of blood, from which CD47 content was estimated based on the average CD47 number on a mouse RBC (16,500 copies per cell) [11] and the RBC concentration in mouse blood (10^{10} cells per mL of blood) [10]. Comparing the CD47 retention from the different RBC-NP formulations to the protein standards showed that the saturation level corresponded to approximately 2×10^{13} copies of CD47 per mg of polymeric particles (Figure 2.7D), yielding on average ~5 copies of CD47 per RBC-NP. To put the CD47 density into perspective, the surface area of the 85 nm RBC-NPs was calculated (~1×10^{11} μm^2/mg), from which a surface density of ~200 molecules of CD47 per μm^2 at saturation on the RBC-NPs can be derived. Given that natural RBCs possess 200~250 copies of CD47 per μm^2 [11, 14], the close match in the CD47 density on the RBC-NPs suggests that the membrane coating brought nearly all of

RBCs' CD47 content onto the sub-100 nm particles. The result reflects the robustness of the membrane functionalization technique, as most of the membrane proteins were retained within the cellular membranes throughout the particle preparation process.

It should also be noted that the RBC membrane to polymer ratio corresponding to the onset of CD47 saturation was in close match to the theoretical ratio for complete unilamellar particle coating. Based on surface area estimations, approximately 125 μL of blood is required to completely cover the surfaces of 1 mg of the 70 nm PLGA particles. Experimental observations showed that above the ratio of ~130 μL of blood/mg PLGA polymer, additional RBC membrane materials did not further functionalize the particles with CD47. As additional membrane materials in excess of complete unilamellar particle coverage were removed during the isolation of RBC-NPs, it can be inferred that the RBC membrane coating precluded further membrane interactions and that multilamellar membrane coating on the nanoparticles was unfavorable. To further investigate the RBC-NP formation under excessive RBC membrane to polymer ratios, RBC-NPs prepared with 250 μL of blood per mg of polymer were visualized under TEM. It was found that despite the availability of excess membrane materials in the samples, the nanoparticles were covered by a single, unilamellar coating of lipid membranes with a thickness of 6~8 nm, which is in agreement with the characteristic membrane thickness of RBCs [15]. Excess membranes remained in vesicular forms, which helped to explain the CD47 saturation on the RBC-NPs. In contrast to the unfavored multilamellar coating, unilamellar membrane coating on the RBC-NPs appeared to be highly efficient. By converting the

RBC membrane input in Figure 2.7D to its corresponding CD47 content, the resulting correlation showed that, below the CD47 saturation, approximately 92% of the input membrane proteins were utilized for particle functionalization. This observation suggests that the RBC membrane coating to the PLGA particle surfaces was a favorable process that readily took place. The high efficiency in translocating CD47 onto nanoparticle surfaces confers a unique advantage to the RBC membrane coating approach.

To verify that the CD47 functionalized RBC-NPs possessed the properly oriented self-markers for molecular interactions, the particle surfaces were examined for the presence of CD47's extracellular domains. Rat anti-CD47 antibodies specific to the CD47's extracellular region were applied to the RBC-NPs on a glow-discharged carbon-coated grid. Following 1 min of incubation, the sample was washed and subsequently incubated with anti-rat IgG gold conjugate, which labelled the anti-CD47 antibodies that were retained on the grid. The immunogold-labelled sample was then rinsed with water prior to visualization by transmission electron microscopy (TEM). Figure 2.8A shows the attachment of the electron-dense gold particles to multiple gray circular patterns 60-80 nm in diameter, which confirmed that the gold conjugates were attached to the RBC-NPs. A negative control prepared in the absence of the primary stain showed that the gold labelling was specific to the anti-CD47 antibodies. Together, these TEM results confirm the presence of right-side-out CD47 on the RBC-NPs. To further examine the presence of inside-out CD47 on the RBC-NPs, an antibody that specifically targets an intracellular sequence of CD47 was used.

Curiously, while the antibody bound to the CD47 on RBC-NPs in western blotting, it did not yield observable immune-gold staining on either RBC-NPs or bare nanoparticles under TEM. This result indicates the relative absence of intracellular CD47 sequences on the particle surfaces. Even though the immunostaining experiment provides a qualitative rather than a quantitative measure of the membrane sidedness on the RBC-NPs, it suggests that the right-side-out membrane orientation was dominant on the RBC-NPs. Given that the extracellular side of RBC membranes possess a strong negative charge owing to high abundance of sialiated moieties [16], it is likely that electrostatic effects favored the interactions between negatively charged polymeric cores and the less negatively charged intracellular side of the RBC membranes, giving rise to a right-side-out orientation bias. This orientation bias also helps explain the unilamellar coating on the RBC-NPs, which could result from the rich surface glycan content that precludes membrane-membrane interactions. Figure 2.8B provides a juxtaposition of magnified images of RBC-NPs and the corresponding bare PLGA nanoparticles under negative staining or immunostaining. It can be observed that, following the RBC membrane coating, the particles were bestowed with a unilamellar membrane shell containing CD47 that predominantly exposes their extracellular domains. The proper CD47 orientation is crucial for their molecular interactions.

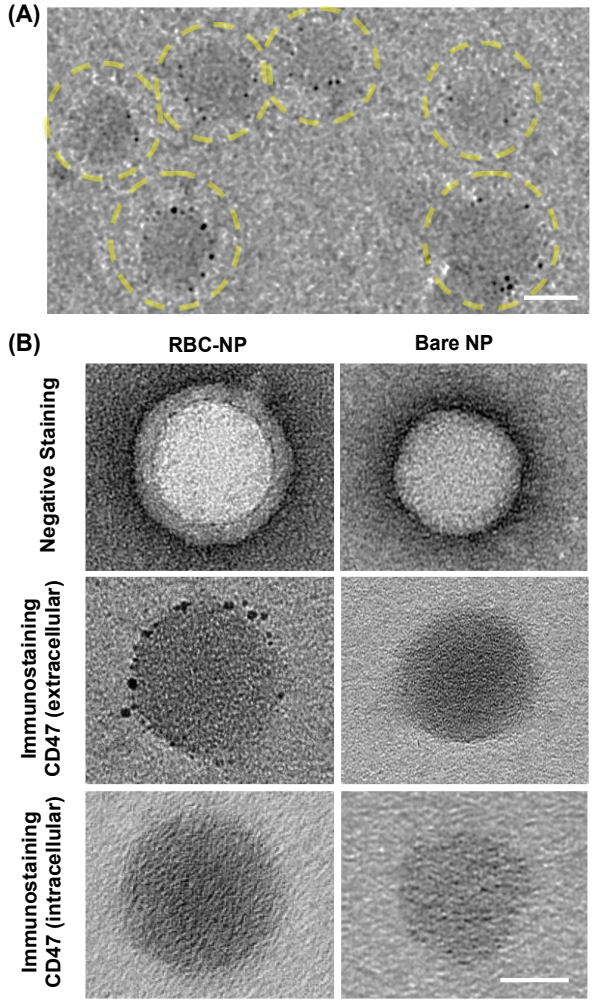

Figure 2.8 CD47 orientation on the RBC-NPs. (A) A representative transmission electron microscopy (TEM) image of the RBC-NPs under immunostaining, consisting of a primary stain by rat anti-mouse CD47 antibodies and a secondary stain by anti-rat IgG gold conjugates (scale bar = 50 nm). (B) Comparison of the RBC-NPs and the corresponding bare PLGA nanoparticles (bare NPs) and under negative staining with uranyl acetate or immunostaining with anti-CD47 antibodies that target either the extracellular or the intracellular protein domains. (scale bar = 30 nm).

Lastly, the immunomodulatory effect of the CD47 functionalized RBC-NPs was studied. Bare PLGA nanoparticles and RBC-NPs loaded with hydrophobic DiD fluorophores (excitation/emission = 644 nm/655 nm) were first incubated with J774 murine macrophage cells and examined for particle internalization. Following 10 min of incubation, the macrophage cells were washed and examined using flow cytometry,

which revealed that the RBC membrane coating rendered the particles less prone to the macrophage uptake, resulting in a 64% reduction in particle internalization (Figure 2.9). The reduced susceptibility to macrophage engulfment confirmed the translocation of immune-evasive functionality from RBCs to RBC-NPs and helped to explain the long *in vivo* circulation previously observed for the RBC-NPs [13]. To identify CD47's contribution to RBC-NPs' immune-evasive property, saturating amounts of anti-CD47 antibodies were applied to the RBC-NPs to block the right-side-out CD47 proteins. The antibody blocking was previously demonstrated to disrupt SIRPα signalling and increased macrophage engulfment of RBCs [17]. Similarly, depriving the particles of the molecular protection from phagocytosis resulted in an increase in particle internalization by 20%, which confirmed the immunomodulatory functionality conferred by the particle-bound CD47. Curiously,

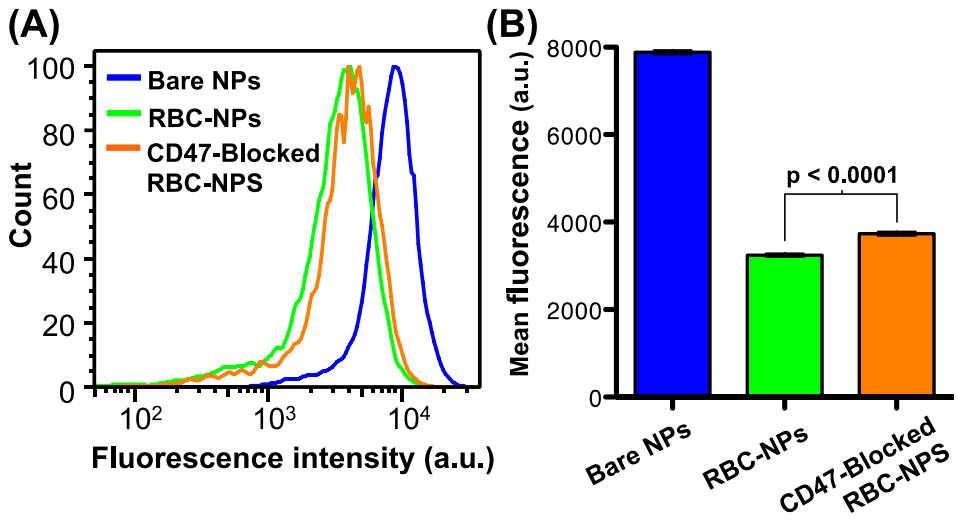

Figure 2.9 Inhibition of macrophage uptake. (A) Flow cytometry analysis of particle internalization by murine macrophage cells. The blue, green, and orange lines represent the bare PLGA nanoparticles (bare NPs), RBC-NPs, and CD47-blocked RBC-NPs, respectively. (B) Mean fluorescence intensity reflecting the overall particle uptake by the macrophage cells.

the CD47-blocked RBC-NPs remained significantly more “stealthy” than the bare PLGA nanoparticles. Given that RBCs have a variety of proteins and glycans on their surface, many of which have been identified to modulate their immunological properties [18, 19], other surface moieties in addition to CD47 on the RBC-NPs likely functioned collectively to inhibit the macrophage activity. Future studies are warranted to verify these other membrane moieties and to examine their implications in nanodevice functionalization.

2.2.4 Conclusions

In summary, RBC membrane coating was demonstrated to functionalize sub-100 nm substrates with native CD47, yielding nanoparticles with equivalent CD47 surface density to natural RBCs. Right-side-out CD47 proteins were identified on the particle surfaces, readily exposing their extracellular domain for molecular interactions. The immune-evasive property of the RBC-NPs, as indicated by their reduced susceptibility to macrophage uptake, further verified the presence of functional immunomodulatory proteins on the particle surfaces. These biomimetic nanocarriers have tremendous potential in drug delivery applications, as they provide the opportunity to actively inhibit the immune clearance of their therapeutic cargo, thereby improving drug pharmacokinetics and therapeutic efficacy. The in-depth examination of the RBC-NPs also provides an up-close look at the fusion process between RBC membranes and PLGA polymeric particles, which appears to favour the formation of unilamellar membrane coated particles with the right-side-out membrane

orientation. From synthesis and fabrication perspectives, the membrane coating technique contrasts with bottom-up functionalization schemes, which often employ chemical conjugation methods that can alter proteins' innate structures. The non-disruptive protein functionalization through the coating of natural cellular membranes presents a robust and versatile approach in interfacing synthetic materials with biological components, offering a compelling technique for the development of bio-inspired and biomimetic nanodevices.

2.2.5 References

1. Yoo, J.W., D.J. Irvine, D.E. Discher, and S. Mitragotri, *Bio-inspired, bioengineered and biomimetic drug delivery carriers.* Nature Reviews Drug Discovery, 2011. **10**(7): p. 521-535.

2. Balmert, S.C. and S.R. Little, *Biomimetic delivery with micro- and nanoparticles.* Advanced Materials, 2012. **24**(28): p. 3757-3778.

3. Oldenborg, P.A., A. Zheleznyak, Y.F. Fang, C.F. lagenaur, H.D. Greshan, and F.P. Lindberg, *Role of CD47 as a marker of self on red blood cells.* Science, 2000. **288**(5473): p. 2051-2054.

4. Jaiswal, S., C.H. Jamieson, W.W. Pang, C.Y. Park, M.P. Chao, R. Majeti, D. Traver, N. van Rooijen, and I.L. Weissman, *CD47 is upregulated on circulating hematopoietic stem cells and leukemia cells to avoid phagocytosis.* Cell, 2009. **138**(2): p. 271-285.

5. Cameron, C.M., J.W. Barrett, M. Mann, A. Lucas, and G. McFadden, *Myxoma virus M128L is expressed as a cell surface CD47-like virulence factor that contributes to the downregulation of macrophage activation in vivo.* Virology, 2005. **337**(1): p. 55-67.

6. Hsu, Y.C., M. Acuna, S.M. Tahara, and C.A. Peng, *Reduced phagocytosis of colloidal carriers using soluble CD47.* Pharmaceutical Research, 2003. **20**(10): p. 1539-1542.

7. Tsai, R.K., P.L. Rodriguez, and D.E. Discher, *Self inhibition of phagocytosis: the affinity of 'marker of self' CD47 for SIRPalpha dictates potency of*

inhibition but only at low expression levels. Blood Cells, Molecules, and Diseases, 2010. **45**(1): p. 67-74.

8. Finley, M.J., L. Rauova, I.S. Alferiev, J.W. Weisel, R.J. Levy, and S.J. Stachelek, *Diminished adhesion and activation of platelets and neutrophils with CD47 functionalized blood contacting surfaces.* Biomaterials, 2012. **33**(24): p. 5803-5811.

9. Stachelek, S.J., M.J. Finley, I.S. Alferiev, F. Wang, R.K. Tsai, E.C. Eckells, N. Tomczyk, J.M. Connolly, D.E. Discher, D.M. Eckmann, and R.J. Levy, *The effect of CD47 modified polymer surfaces on inflammatory cell attachment and activation.* Biomaterials, 2011. **32**(19): p. 4317-4326.

10. Russell, E.S., E.F. Neufeld, and C.T. Higgins, *Comparison of normal blood picture of young adults from 18 inbred strains of mice.* Proceedings of the Society for Experimental Biology and Medicine, 1951. **78**(3): p. 761-766.

11. Subramanian, S., R. Tsai, S. Sen, K.N. Dahl, and D.E. Discher, *Membrane mobility and clustering of Integrin Associated Protein (IAP, CD47)--major differences between mouse and man and implications for signaling.* Blood Cells, Molecules, and Diseases, 2006. **36**(3): p. 364-372.

12. Brown, E.J. and W.A. Frazier, *Integrin-associated protein (CD47) and its ligands.* Trends in Cell Biology, 2001. **11**(3): p. 130-135.

13. Hu, C.M., L. Zhang, S. Aryal, C. Cheung, R.H. Fang, and L. Zhang, *Erythrocyte membrane-camouflaged polymeric nanoparticles as a biomimetic delivery platform.* Proceedings of the National Academy of Sciences USA, 2011. **108**(27): p. 10980-10985.

14. Mouro-Chanteloup, I., J. Delaunay, P. Gane, V. Nicolas, M. Johansen, E.J. Brown, L.L. Peters, C.L. Van Kim, J.P. Cartron, and Y. Colin, *Evidence that the red cell skeleton protein 4.2 interacts with the Rh membrane complex member CD47.* Blood, 2003. **101**(1): p. 338-344.

15. Hochmuth, R.M., C.A. Evans, H.C. Wiles, and J.T. McCown, *Mechanical measurement of red cell membrane thickness.* Science, 1983. **220**(4592): p. 101-102.

16. Jan, K.M. and S. Chien, *Role of surface electric charge in red blood cell interactions.* The Journal of General Physiology, 1973. **61**(5): p. 638-654.

17. Oldenborg, P.A., H.D. Gresham, and F.P. Lindberg, *CD47-signal regulatory protein alpha (SIRPalpha) regulates Fcgamma and complement receptor-*

mediated phagocytosis. The Journal of Experimental Medicine, 2001. **193**(7): p. 855-862.

18. Hu, C.M., R.H. Fang, and L. Zhang, *Erythrocyte-Inspired Delivery Systems.* Advanced Healthcare Materials, 2012. **1**(5): p. 537-547.

19. Durocher, J.R., R.C. Payne, and M.E. Conrad, *Role of sialic acid in erythrocyte survival.* Blood, 1975. **45**(1): p. 11-20.

Chapter 2, in full, is a reprint of the material as it appears in *Nanoscale*, 2014, Brian Luk, Che-Ming Hu, Ronnie Fang, Diana Dehaini, Cody Carpenter, Weiwei Gao, and Liangfang Zhang; *Nanoscale*, 2013, Che-Ming Hu, Ronnie Fang, Brian Luk, Kevin Chen, Cody Carpenter, Weiwei Gao, Kang Zhang, and Liangfang Zhang.

Chapter 3

Cell Membrane-Coated Nanoparticles for Targeted Biomimetic Nanodelivery

3.1 Red Blood Cell Membrane-Cloaked Nanoparticles for Drug Delivery

3.1.1 Introduction

Nanoparticle-based drug delivery platforms are often tasked with navigating complex biological environments, and their performance can ultimately be governed by their ability to avoid nonspecific interactions while exhibiting a high degree of target selectivity [1-3]. As such, the facile incorporation of complex functionalities onto nanoparticle surfaces has long been desirable [4-7]. Recently, the direct use of naturally derived biomembrane as a coating material represents an emerging strategy for nanoparticle functionalization [8-10]. The faithful, right-side-out translocation of all membrane-bound moieties from the cell surface onto the surface of a nanoparticle can naturally bestow the nanoparticle with desirable properties such as long circulation, immune evasion, and targeting affinity without the need to explicitly engineer these functionalities from the bottom-up [11-13]. This cell membrane cloaking strategy has demonstrated utility for a variety of purposes, including biodetoxification [14-16], antibacterial vaccination [17, 18], antibiotic delivery [19], photothermal therapy [20], and cancer immunotherapy [13, 21]. Using this approach, an endless number of applications can be envisioned, as it should be possible to combine the membrane from any cell type with a variety of different nanoparticle core materials [22-25].

One cell type that has been widely explored as a source for membrane coating

is the red blood cell (RBC), which represents nature's own long circulating carrier. RBCs express a variety of immunomodulatory markers that enable the body to recognize them as self [26, 27], and functionalization of nanoparticles with RBC membrane has been proven to promote immune evasion and significantly enhance circulation residence time [10, 22]. These properties make RBC membrane-coated nanocarriers a truly appealing candidate for cancer drug delivery, which is a field that has long benefited from the use of long-circulating, lowly immunogenic nanocarriers [28, 29]. As more nanoparticle-based chemotherapies are being investigated in the clinic, a great deal of emphasis has been placed on safety and immunocompatibility [30, 31]. To this end, RBC membrane-coated polymeric nanoparticles (denoted RBC-NP), consisting of a poly(lactic-*co*-glycolic acid) (PLGA) core and an RBC membrane shell, represent a promising delivery system due to their combination of high drug carrying capacity along with an inherently biocompatible membrane coating [32]. Here, we demonstrate that RBC-NP can be effectively used to deliver a model chemotherapeutic drug, doxorubicin (DOX), in a mouse model of lymphoma. We study the ability of the drug-loaded nanoparticles to control tumor growth while concurrently assessing their ability to eliminate the toxicities commonly associated with free drug administration. Further, the short- and long-term immune effects of the RBC-NP upon systemic administration are studied as well.

3.1.2 Experimental Methods

3.1.2.1 Preparation of RBC-NP and RBC-NP(DOX)

Whole blood was collected from C57BL/6 mice (Harlan Sprague Dawley) and collected by centrifugation at 500 × g for 10 min. RBC membrane vesicles were then prepared using a sonication approach. PLGA polymeric cores loaded with DOX were prepared with carboxy-terminated 50:50 PLGA polymer (LACTEL Absorbable Polymers) using a double emulsion process. DOX was dissolved in 25 μL of 500 mM Tris-HCl at pH 8 as the inner phase, and sonicated with 500 μL of PLGA in dichloromethane (DCM) at 10 mg/mL. The solution was then added to 5 mL of 10 mM Tris-HCl at pH 8 and sonicated again. This final solution was then added to an additional 10 mL of 10 mM Tris-HCl at pH 8 and allowed to evaporate for at least 4 h with stirring. Empty PLGA cores were prepared in the same fashion, but without DOX in the inner phase. RBC-NP were prepared by fusing RBC membrane vesicles on preformed PLGA cores using a previously established protocol [15]. The size and zeta potential of the RBC-NP were obtained from three dynamic light scattering (DLS) measurements using a Malvern ZEN 3600 Zetasizer. Transmission electron microscopy (TEM) was used to characterize the morphology of RBC-NP. Briefly, a drop of RBC-NP solution (1 mg/mL) was deposited onto a glow-discharged carbon-coated TEM grid, followed by washing with 10 drops of distilled water and staining with 1 wt% uranyl acetate. An FEI Sphera Microscope operating at 200 kV was used to image the sample. The DOX loading was evaluated by measuring its fluorescence (excitation at 480 nm; emission at 580 nm). Drug release was studied by dialyzing samples against phosphate buffered saline (PBS) buffer (1 X, pH = 7.4) using Slide-A-Lyzer MINI Dialysis Cups (Thermo Scientific) with a molecular weight cut-off of 10

kDa.

3.1.2.2 *In Vitro* Cytotoxicity and Uptake

EL4 cells (American Type Culture Collection) were plated at 5,000 cells per well. Free DOX and RBC-NP(DOX) at varying drug concentrations were incubated with the cells for 72 h at 37 °C and 5% CO_2, after which an XTT Cell Proliferation Kit (Roche Diagnostics) was used to assess cell viability. DOX uptake was assessed by incubating 100,000 EL4 cells with varying concentrations of free DOX or RBC-NP(DOX) for 1 h at 37 °C. After 1 h, the samples were washed and fixed with 10% formalin for analysis. Flow cytometry was used to measure the DOX signal in the cells using a Becton Dickinson FACSCanto II.

3.1.2.3 *In Vivo* Antitumor Efficacy

75,000 EL4 cells were implanted subcutaneously into the right flank of 6-week-old male C57BL/6 mice. The tumors were allowed to grow for 9 days. RBC-NP(DOX), free DOX, empty RBC-NP, or sucrose was administered every other day starting from day 9 post-implantation of the tumor cells for 2 weeks (n = 5 per group). Where applicable, 200 μL of each respective formulation was administered intravenously via tail vein injection at a concentration equivalent to 3 mg/kg DOX, which was found to be the maximum tolerated dose of the drug. Tumor dimensions and mouse weights were measured every other day beginning on day 8 post-implantation and every 3 days beginning on day 35. Tumor volume was calculated

using the equation $V = \frac{\pi}{6} LW^2$, where V is volume, L is length, and W is width. Survival was pre-defined as tumor size < 2000 mm^3 prior to the initiation of the study.

3.1.2.4 *In Vivo* Safety Studies

To examine the effect of RBC-NP(DOX) on normal physiological parameters, 200 μL of sucrose, RBC-NP(DOX), or free DOX at 3 mg/kg of drug was injected intravenously into the tail vein of C57BL/6 mice (n = 3 per group). Whole blood was collected into heparinized tubes before and 24 h after injection. Hematological parameters (RBC count, platelet count, hemoglobin, hematocrit, white blood cell count, neutrophil count, lymphocyte count, and monocyte count) were evaluated using a Drew Scientific Hemavet 950 FS Multi-Species Hematology System. To evaluate serum chemistry, blood was collected and allowed to clot for 4 h at room temperature. Samples were then centrifuged at 7000 × g, and 300 μL of serum was collected. Serum chemistry components were measured using the SEAL AutoAnalyzer 3 HR.

3.1.2.5 *In Vivo* Immunogenicity Studies

To examine the safety of the RBC-NP platform, 200 μL of RBC-NP at a particle dosing of 30 mg/kg was injected intravenously into the tail vein of C57BL/6 mice; additional mice were administered isotonic sucrose solution or a mixture of lipopolysaccharide (10 μg/kg) and D-galactosamine (100 mg/kg) (n = 3 per group). Blood was collected 6 h post-injection and the plasma was separated. An IL-6 ELISA kit (Biolegend) was used to measure the levels of IL-6 following the manufacturer's

protocol. To study the anti-RBC IgG and IgM titers, blood was collected at day 30 post-challenge from tumor-bearing mice administered with RBC-NP in the above antitumor efficacy study (n = 5). In the study, mice were injected with RBC-NP at a particle dosing of 30 mg/kg every other day for 2 weeks starting from day 9 post-challenge. Plasma was separated from whole blood. To measure anti-RBC titers, RBCs in PBS were coated onto Costar 96 well plates (Corning) at 10^6 RBCs per well. The collected plasma was used as the primary immunostain. Goat anti-mouse IgG-HRP (Biolegend) or goat anti-mouse IgM-HRP (Santa Cruz Biotechnology) was used as the secondary antibody for detecting the presence of autoantibodies against RBCs, and TMB substrate (Thermo Scientific) was used to develop the plate.

3.1.3 Results and Discussion

Empty or DOX-loaded PLGA nanoparticles were prepared using a double emulsion method. RBC membrane derived from the blood of C57BL/6 mice was coated onto the polymeric cores using a sonication approach as previously described [15]. The general structure of the resulting nanoparticles is depicted in Figure 3.1A with the DOX loaded inside the PLGA core and the RBC membrane coating, with all its associated proteins, forming the outer layer. Drug loading into the PLGA cores could be controlled by varying the initial input concentration of DOX (Figure 3.1B). By increasing the input of DOX, loading of the drug was also increased, and a saturation level was reached at approximately 40 wt% (DOX weight/PLGA weight) drug input, corresponding to approximately 10 wt% loading. As the drug input

concentration was increased, the encapsulation efficiency decreased markedly, dropping from 50% efficiency at an input of 10 wt% down to 20% efficiency at the maximal tested input of 50 wt%. A formulation approaching the saturation loading level of 10 wt% DOX was used for subsequent *in vitro* and *in vivo* studies.

Coating of 140 nm empty or DOX-loaded PLGA cores with RBC membranes resulted in a size increase to approximately 155 nm and an increase in zeta potential of approximately 15 mV, from ~-45 mV to -30 mV (Figure 3.1C). This is consistent with previous findings, as the membrane layer adds to the hydrodynamic size, while the membrane coating, which is less negatively charged than the core, shields the highly negative carboxyl groups present on the surface of the core [13]. The core-shell structure of the drug-loaded RBC-NP, herein denoted RBC-NP(DOX), was confirmed by visualization using transmission electron microscopy (TEM) with uranyl acetate negative staining (Figure 3.1D). Morphologically, the drug-loaded RBC-NP are similar in appearance to unloaded PLGA coated with the same membrane, suggesting that drug-loaded RBC-NP of varying sizes can easily be fabricated to meet the requirements of future applications [12]. The resulting RBC-NP(DOX) demonstrated sustained release over time (Figure 3.1E); approximately 80% of the encapsulated drug was released over the course of 7 days, with the majority of the release occurring within the first 72 h. This observed prolonged release is due in part to the RBC membrane coating acting as a diffusional barrier for DOX release, a phenomenon that has been previously reported [32, 33].

To evaluate whether the drug encapsulated within the RBC-NP(DOX) could

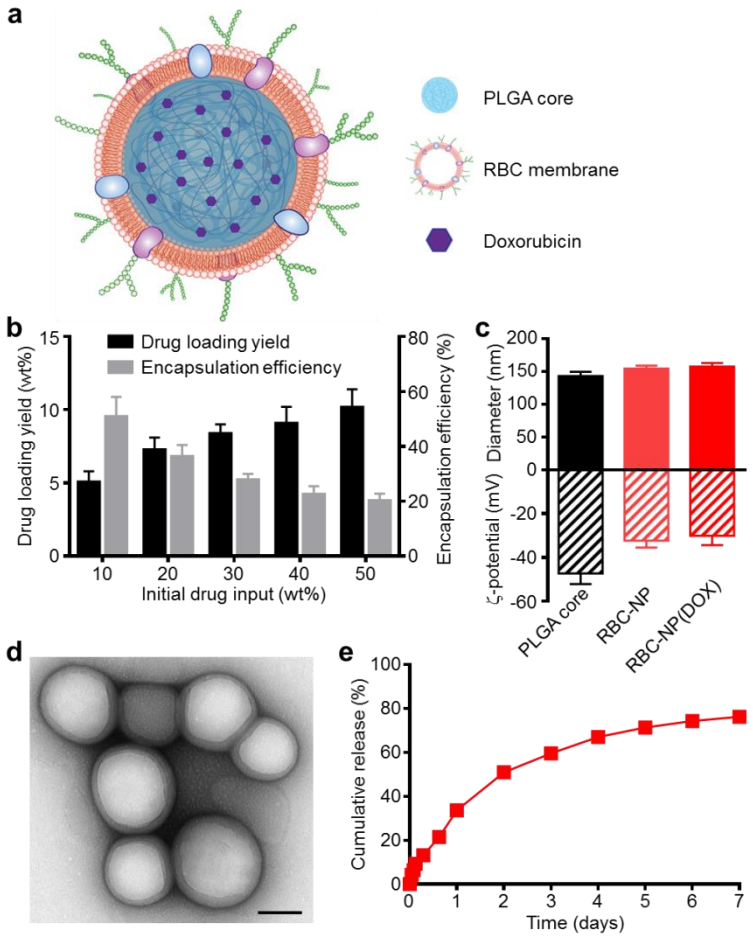

Figure 3.1 Physicochemical characterization and drug loading of RBC-NPs. (A) Schematic of doxorubicin (DOX)-loaded RBC-NP, denoted "RBC-NP(DOX)". (B) Loading yield and loading efficiency of DOX into PLGA nanoparticles at various initial drug inputs. (C) Dynamic light scattering (DLS) measurements of the size and surface zeta potential of bare PLGA core, RBC-NP, and RBC-NP(DOX) with a drug loading yield of 10 wt%. (D) Transmission electron microscopy (TEM) visualization of RBC-NP(DOX) with uranyl acetate negative staining (scale bar = 100 nm). (E) Cumulative release profile of DOX from RBC-NP(DOX) with 10 wt% DOX loading yield over a period of 7 days.

retain its tumor killing activity, an *in vitro* cytotoxicity test was conducted. It was shown that RBC-NP(DOX) exhibited cytotoxicity when incubated together with EL4 mouse lymphoma cells for 72 h *in vitro* (Figure 3.2A). Under the conditions tested, the nanoparticle formulation had an apparent drug IC_{50} of 5.6 ng/mL. Free DOX demonstrated slightly better efficacy against EL4 tumor cells *in vitro* compared with

RBC-NP(DOX) with an IC_{50} of 1.4 ng/mL. This difference can be rationalized by the fact that, at the 72 h conclusion of the experiment, there was still incomplete release of drug from RBC-NP(DOX). Additionally, free DOX can easily diffuse into the cancer cells, making it extremely potent over extended incubation periods, especially given that the EL4 cell line is not inherently DOX-resistant [34]. While RBC-NP(DOX) and free DOX showed similar activity over longer incubation periods, encapsulated DOX showed enhanced uptake by EL4 cells after a short, 1 h incubation (Figure 3.2B). The observed difference in intracellular localization is likely due to the fact that nanoparticles are taken up via active mechanisms such as endocytosis [35], enabling a higher capacity for transport across the cellular membrane compared with pure diffusion. This effect can be further enhanced with active targeting ligands, which can be introduced onto the surface of RBC-NP [36]. These observations indicate that encapsulating DOX into RBC-NP has the potential to facilitate quick uptake of the drug by tumor cells and slow release in a sustained manner over time.

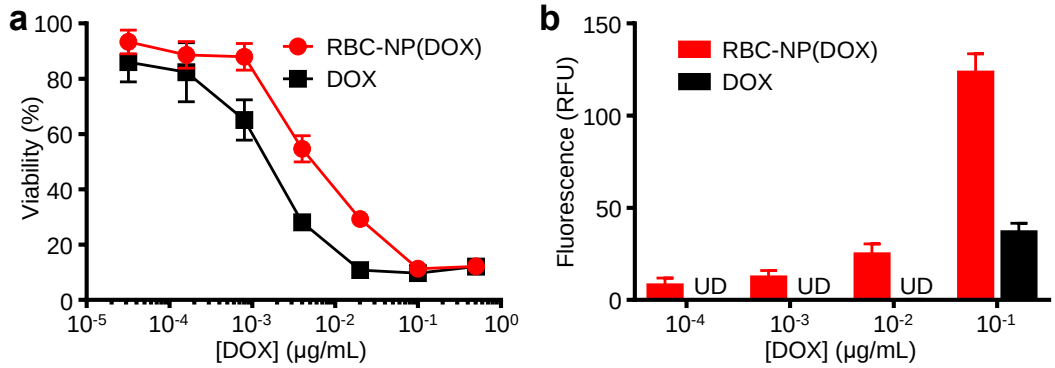

Figure 3.2 *In vitro* antitumor efficacy and uptake. (A) *In vitro* cytotoxicity of RBC-NP(DOX) in comparison with free DOX against EL4 murine lymphoma cells after 72 h of incubation. (B) Uptake of DOX by EL4 cells after 1 h incubation with either RBC-NP(DOX) or free DOX.

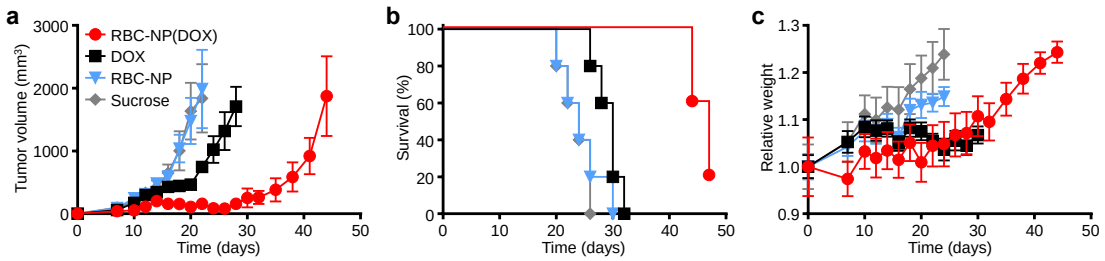

Figure 3.3 *In vivo* treatment of solid tumors. (A) Tumor growth inhibition in mice treated with RBC-NP(DOX), free DOX, RBC-NP, or isotonic sucrose by tail vein injection (n=5). Treatment was initiated 9 days post-challenge, and mice were administered formulations every other day for 2 weeks. (B) Survival of mice treated with RBC-NP(DOX), free DOX, RBC-NP, or isotonic sucrose. (C) Relative weights of tumor-bearing mice treated with RBC-NP(DOX), free DOX, RBC-NP, or isotonic sucrose. Values were normalized within each group using the measurements on day 0.

To determine the ability of drug-loaded RBC-NP to function as effective therapy against tumor growth *in vivo*, we analyzed long-term tumor burden in a murine lymphoma model. EL4 cells were implanted subcutaneously into the right flank of C57BL/6 mice and were first allowed to develop for 9 days, after which tumor-bearing mice were treated every other day with RBC-NP(DOX), free DOX, empty RBC-NP, or isotonic sucrose at a drug dosage of 3 mg of DOX per kg of body weight (3 mg/kg) (Figure 3.3A). The dosing was determined to be just under the maximum tolerated dose for 6-week-old male C57BL/6 mice, designated as the dose at which the mouse body weight decreases 10% (data not shown). Isotonic sucrose and RBC-NP treatment alone did not affect tumor growth. Mice treated with free DOX exhibited marginal control of tumor growth, extending median survival by 6 days compared with no treatment. The RBC-NP(DOX) treatment group showed the most significant efficacy in terms of tumor growth inhibition, with the median survival nearly doubling from 24 days for the control group to 47 days for the treated group (Figure 3.3B). Though not an actively targeted formulation, it is believed that RBC-

NP(DOX) was able to accumulate at the tumor site via the enhanced permeation and retention (EPR) effect [37, 38], thereby substantially increasing the local drug concentration at the tumor site. It should be noted that it was not until treatment ceased on day 23 post-implantation that the tumor growth kinetics started to accelerate. During this period, mice treated by RBC-NP(DOX) showed no appreciable decrease in weight, a global parameter of formulation safety (Figure 3.3C). It should also be noted that, for the free DOX treatment group, the observed steady weight kinetics reflects an increase in tumor burden, which indicates an appreciable toxic effect. Mice treated with RBC-NP(DOX) continued to increase in weight despite minimal tumor burden during the treatment period, suggesting that, in future explorations, the nanoparticle formulation can be further increased to exert an even more potent antitumor effect.

Next, we evaluated the safety profile of RBC-NP(DOX) in order to assess the formulation's potential as a clinically translatable drug delivery platform. Isotonic sucrose, RBC-NP(DOX), or free DOX was administered at a drug dosage of 3 mg/kg, and whole blood was collected prior to injection and 24 h post-injection. Hematological parameters largely showed no difference between the sucrose, RBC-NP(DOX), and free DOX treatment groups (Figure 3.4A-D). RBC, platelet, hemoglobin, and hematocrit quantifications were all normal 24 h after injection. Free DOX, however, is known to have myelosuppressing effects, which can lead to severe complications in the clinic such as neutropenic fever, infections, hemorrhage, and even death [39]. This was reflected in the white blood cell (WBC) quantifications

(Figure 3.4E-H). When free DOX was administered, the mice suffered a significant decrease in WBC count. This decrease in overall WBC count was seen across different leukocyte subsets, with the sharpest reduction occurring in the number of lymphocytes. The RBC-NP(DOX) formulation was able to stably sequester the drug, delivering it for potent tumor control with no observable myelosuppression, which is often the dose-limiting toxic side effect of DOX in a clinical setting.

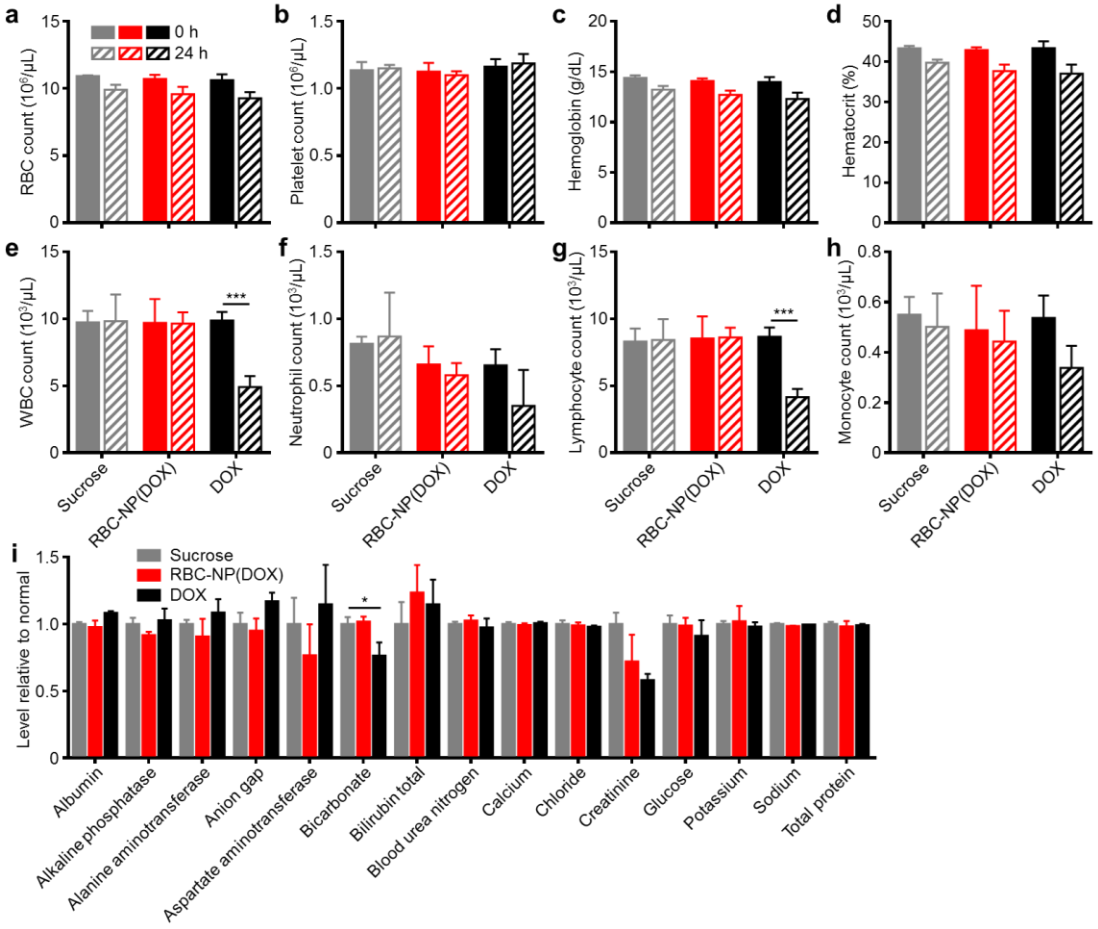

Figure 3.4 *In vivo* safety studies of RBC-NP(DOX). (A) RBC count, (B) platelet count, (C) hemoglobin quantification, (D) hematocrit, (E) white blood cell count, (F) neutrophil count, (G) lymphocyte count, and (H) monocyte count in mice before and 24 h after injection of sucrose, RBC-NP(DOX) or free DOX. (I) Comprehensive serum chemistry panel conducted on mice intravenously injected with isotonic sucrose, RBC-NP(DOX), or free DOX. Serum was collected 24 h post-injection (n = 3 for all experiments; $*P \leq 0.05$; $***P \leq 0.001$).

Additionally, RBC-NP(DOX) did not elicit any adverse physiological effects based on a comprehensive chemistry panel of mouse serum (Figure 3.4I). The creatinine levels for mice treated with free DOX were significantly decreased, possibly indicating increased activity of the kidneys to remove excess free drug. Of potential note are the decrease in bicarbonate and concurrent increase in anion gap for mice treated with free DOX only. These results, when taken together, can indicate a shift towards acidosis, which can be an early sign of kidney failure. Furthermore, RBC-NP(DOX) treatment did not result in any increase in serum alanine aminotransferase (ALT) or aspartate aminotransferase (AST) levels, suggesting that RBC-NP(DOX) administration does not induce liver injury. As is the case with most nanoparticle formulations, RBC-NPs are cleared by the liver [22], so it is important that the DOX-loaded RBC-NPs do not induce any acute hepatic damage. Compared with free DOX, RBC-NP(DOX) demonstrated a lack of acute systemic abnormalities after administration of a therapeutic dose, thereby underscoring the biocompatibility and safety of RBC-NP as a drug carrier.

To further evaluate the translatability of RBC-NP as a cancer drug carrier, we investigated the immunological implications of RBC-NP administration. RBC-NP did not induce elevated serum levels of interleukin-6 (IL-6), which indicates lack of an acute systemic inflammatory response against the nanocarrier (Figure 3.5A). Nanoscale drug delivery vehicles must also not induce any long-term immune responses, the lack of which helps to preserve functionality of the particles upon repeated injections [40]. Multiple administrations of RBC-NP induced no detectable

serum IgM or IgG titers against RBCs after 30 days (Figure 3.5B,C), indicating that RBC-NPs can be used *in vivo* repeatedly without reduction in their abilities to function as a drug delivery vehicle. Additionally, the lack of antibody titers against RBCs reveals that no autoimmunity against self-RBCs is developed as a result of repeated RBC-NP injections. Taken together, these results demonstrate that RBC-NP themselves produce no significant acute or long-term immunological responses as a delivery vehicle, highlighting the "self" nature of the RBC-NP platform. Thus, RBC-NP can serve as an effective option for drug delivery to overcome the limitations of traditional chemotherapy.

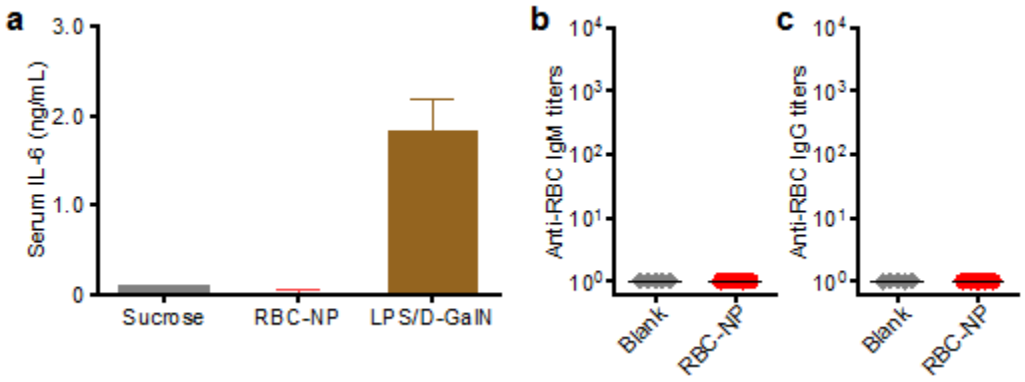

Figure 3.5 *In vivo* immunogenicity of RBC-NP. (A) Serum analysis of interleukin-6 (IL-6) production in mice administered with isotonic sucrose, RBC-NP, or lipopolysaccharide with D-galactosamine (LPS/D-GalN) as a positive control (n = 3). (B) anti-RBC IgM and (C) anti-RBC IgG titers produced in mice receiving repeated dosing of RBC-NP (n = 5). Tumor-bearing mice were administered with RBC-NP every other day starting from day 9 post-implantation of the tumor cells for 2 weeks and blood was collected on day 30 post-implantation for titer analyses.

The focus of these studies as a whole was to evaluate a biocompatible nanoparticle drug delivery agent with clinical translation potential to treat solid tumors with enhanced efficacy. Therapeutic nanocarriers must be safe for use *in vivo*. Previous nanoparticle studies on bare materials such as carbon nanotubes [41, 42],

iron nanoparticles [43], and titanium dioxide [44], have shown adverse responses indicative of material toxicity. RBC-NP(DOX), employing a highly generalizable membrane cloaking approach, was able to deliver a toxic chemotherapy drug payload to the tumor site and significantly prolong survival without any acute increases in myelosuppression, systemic immune response, or abnormal blood chemistry parameters. Furthermore, early mortality and toxicity from high DOX dosages were not observed during long-term and repetitive treatment with RBC-NP(DOX).

3.1.4 Conclusions

The studies described here indicate that the RBC-NP platform is able to unite several important drug delivery properties into a single system. Of great importance, RBC-NP with its natural membrane coating, demonstrated good biocompatibility and did not elicit immune reactions. Furthermore, the versatility of the inner polymeric core provides opportunities to deliver a wide variety of therapeutics (i.e. hydrophilic/hydrophobic small molecules, proteins, nucleic acids, etc.) [45]. Although translating RBC-NP to human use remains to be investigated, large-scale synthesis of the particles should be feasible given the existing infrastructure for blood collection and transfusion as well as the maturing development of polymeric therapeutics [46]. Ultimately, the safety and biocompatibility of RBC-NP paired with its efficacy against solid tumors reveal that this platform possesses many of the requisite characteristics for a clinically translatable drug delivery system. The results presented here provide a promising foundation for continued development and future clinical tests of the RBC-

NP platform.

3.1.5 References

1. Desai, N., *Challenges in development of nanoparticle-based therapeutics*. American Association of Pharmaceutical Scientists Journal, 2012. **14**(2): p. 282-295.

2. Mitragotri, S., P.A. Burke, and R. Langer, *Overcoming the challenges in administering biopharmaceuticals: formulation and delivery strategies*. Nature Reviews Drug Discovery, 2014. **13**(9): p. 655-672.

3. De Jong, W.H. and P.J. Borm, *Drug delivery and nanoparticles: applications and hazards*. International Journal of Nanomedicine, 2008. **3**(2): p. 133-149.

4. Jiang, S., K.Y. Win, S. Liu, C.P. Teng, Y. Zheng, and M.Y. Han, *Surface-functionalized nanoparticles for biosensing and imaging-guided therapeutics*. Nanoscale, 2013. **5**(8): p. 3127-3148.

5. Mout, R., D.F. Moyano, S. Rana, and V.M. Rotello, *Surface functionalization of nanoparticles for nanomedicine*. Chemical Society Reviews, 2012. **41**(7): p. 2539-2544.

6. Sperling, R.A. and W.J. Parak, *Surface modification, functionalization and bioconjugation of colloidal inorganic nanoparticles*. Philosophical Transactions of the Royal Society A Mathematical, Physical and Engineering Sciences, 2010. **368**(1915): p. 1333-1383.

7. Hu, C.M., R.H. Fang, B.T. Luk, and L. Zhang, *Polymeric nanotherapeutics: clinical development and advances in stealth functionalization strategies*. Nanoscale, 2014. **6**(1): 65-75.

8. Yoo, J.W., D.J. Irvine, D.E. Discher, and S. Mitragotri, *Bio-inspired, bioengineered and biomimetic drug delivery carriers*. Nature Reviews Drug Discovery, 2011. **10**(7): p. 521-535.

9. Fang, R.H., C.M. Hu, and L. Zhang, *Nanoparticles disguised as red blood cells to evade the immune system*. Expert Opinion on Biological Therapy, 2012. **12**(4): p. 385-389.

10. Hu, C.M., R.H. Fang, and L. Zhang, *Erythrocyte-inspired delivery systems*. Advanced Healthcare Materials, 2012. **1**(5): p. 537-547.

11. Hu, C.M., R.H. Fang, B.T. Luk, K.N. Chen, C.W. Carpenter, W. Gao, K. Zhang, and L. Zhang, *'Marker-of-self' functionalization of nanoscale particles through a top-down cellular membrane coating approach*. Nanoscale, 2013. **5**(7): p. 2664-2668.

12. Luk, B.T., C.M. Hu, R.H. Fang, D. Dehaini, C. Carpenter, W. Gao, and L. Zhang, *Interfacial interactions between natural RBC membranes and synthetic polymeric nanoparticles*. Nanoscale, 2014. **6**(5): p. 2730-2737.

13. Fang, R.H., C.M. Hu, B.T. Luk, W. Gao, J.A. Copp, Y. Tai, D.E. O'Connor, and L. Zhang, *Cancer cell membrane-coated nanoparticles for anticancer vaccination and drug delivery*. Nano Letters, 2014. **14**(4): p. 2181-2188.

14. Hu C.M., R.H. Fang, J.A. Copp, B.T. Luk, and L. Zhang, *A biomimetic nanosponge that absorbs pore-forming toxins*. Nature Nanotechnology, 2013. **8**(5): p. 336-340.

15. Copp J.A., R.H. Fang, B.T. Luk, C.M. Hu, W. Gao, K. Zhang, and L. Zhang, *Clearance of pathological antibodies using biomimetic nanoparticles*. Proceedings of the National Academy of Sciences USA, 2014. **111**(37): p. 13481-13486.

16. Pang, Z., C.M. Hu, R.H. Fang, B.T. Luk, W. Gao, F. Wang, et al. *Detoxification of organophosphate poisoning using nanoparticle bioscavengers*. ACS Nano, 2015. **9**(6): p. 6450-6458.

17. Gao, W., R.H. Fang, S. Thamphiwatana, B.T. Luk, J. Li , P. Angsantikul, et al. *Modulating antibacterial immunity via bacterial membrane-coated nanoparticles*. Nano Letters, 2015, **15**(2): p. 1403-1409.

18. Hu, C.M., R.H. Fang, B.T. Luk, and L. Zhang, *Nanoparticle-detained toxins for safe and effective vaccination*. Nature Nanotechnology, 2013. **8**(12): p. 933-938.

19. Hu, C.M., R.H. Fang, K.C. Wang, B.T. Luk, S. Thamphiwatana, D. Dehaini, et al. *Nanoparticle biointerfacing by platelet membrane cloaking*. Nature, 2015. **526**(7571): p. 118-121.

20. Piao, J.G., L. Wang, F. Gao, Y.Z. You, Y. Xiong, and L. Yang, *Erythrocyte membrane is an alternative coating to polyethylene glycol for prolonging the circulation lifetime of gold nanocages for photothermal therapy.* ACS Nano, 2014. **8**(10): p. 10414-10425.

21. Guo, Y., D. Wang, Q. Song, T. Wu, X. Zhuang, Y. Bao, et al. *Erythrocyte membrane-enveloped polymeric nanoparticles as nanovaccine for induction of antitumor immunity against melanoma*. ACS Nano, 2015. **9**(7): p. 6918-6933.

22. Hu, C.M., L. Zhang, S. Aryal, C. Cheung, R.H. Fang, and L. Zhang, *Erythrocyte membrane-camouflaged polymeric nanoparticles as a biomimetic delivery platform.* Proceedings of the National Academy of Sciences USA, 2011. **108**(27): p. 10980-10985.

23. Gao, W., C.M. Hu, R.H. Fang, B.T. Luk, J. Su, and L. Zhang. *Surface functionalization of gold nanoparticles with red blood cell membranes*. Advanced Materials, 2013. **25**(26): p. 3549-3553.

24. Zhang, J., W. Gao, R.H. Fang, A. Dong, and L. Zhang, *Synthesis of nanogels via cell membrane-templated polymerization*. Small, 2015. **11**(34): p. 4309-4313.

25. Parodi, A., N. Quattrocchi, A.L. van de Ven, C. Chiappini, M. Evangelopoulos, J.O. Martinez, et al. *Synthetic nanoparticles functionalized with biomimetic leukocyte membranes possess cell-like functions*. Nature Nanotechnology, 2013. **8**(1): p. 61-68.

26. Oldenborg, P.A., A. Zheleznyak, Y.F. Fang, C.F. lagenaur, H.D. Greshan, and F.P. Lindberg, *Role of CD47 as a marker of self on red blood cells.* Science, 2000. **288**(5473): p. 2051-2054.

27. Rodriguez, P.L, T. Harada, D.A. Christian, D.A. Pantano, R.K. Tsai, and D.E. Discher, *Minimal "Self" peptides that inhibit phagocytic clearance and enhance delivery of nanoparticles*, Science, 2013. **339**(6122): p. 971-975.

28. Davis, M.E., Z.G. Chen, and D.M. Shin, *Nanoparticle therapeutics: an emerging treatment modality for cancer*. Nature Reviews Drug Discovery, 2008. **7**(9): p. 771-782.

29. Peer, D., J.M. Karp, S. Hong, O.C. Farokhzad, R. Margalit, and R. Langer, *Nanocarriers as an emerging platform for cancer therapy.* Nature Nanotechnology, 2007. **2**(12): p. 751-760.

30. Ishida, T., R. Maeda, M. Ichihara, K. Irimura, and H. Kiwada, *Accelerated clearance of PEGylated liposomes in rats after repeated injections*. Journal of Controlled Release, 2003. **88**(1): p. 35-42.

31. Knop, K., R. Hoogenboom, D. Fischer, and U.S. Schubert, *Poly(ethylene glycol) in drug delivery: pros and cons as well as potential alternatives*. Angewandte Chemie International Edition, 2010. **49**(36): p. 6288-6308.

32. Aryal, S., C.M. Hu, R.H. Fang, D. Dehaini, C.W. Carpenter, D.E. Zhang, and L. Zhang, *Erythrocyte membrane-cloaked polymeric naonparticles for controlled drug loading and release*. Nanomedicine, 2013. **8**(8): p. 1271-1280.

33. Zhang, L., J.M. Chan, F.X. Gu, J.W. Rhee, A.Z. Wang, A.F. Radovic-Moreno, et al. *Self-assembled lipid-polymer hybrid nanoparticles: a robust drug delivery platform*. ACS Nano, 2008, **2**(8): p. 1696-1702.

34. Maccubbin, D.L., K.R. Wing, K.F. Mace, R.L. Ho, M.J. Ehrke, and E. Mihich, *Adriamycin-induced modulation of host defenses in tumor-bearing mice*. Cancer Research, 1992. **52**(13): p. 3572-3576.

35. Iversen, T.G., T. Skotland, and K. Sandvig, *Endocytosis and intracellular transport of nanoparticles: present knowledge and need for future studies*. Nano Today, 2011. **6**(2): p. 176-185.

36. Fang, R.H., C.M. Hu, K.N. Chen, B.T. Luk, C.W. Carpenter, W. Gao, et al. *Lipid-insertion enables targeting functionalization of erythrocyte membrane-cloaked nanoparticles*. Nanoscale, 2013. **5**(19): 8884-8888.

37. Matsumura, Y. and H. Maeda, *A new concept for macromolecular therapeutics in cancer chemotherapy: mechanism of tumoritropic accumulation of proteins and antitumor agent smancs*. Cancer Research, 1986. **46**(12): p. 6387-6392.

38. Maeda, H., *Macromulecular therapeutics in cancer treatment: the EPR effect and beyond*. Journal of Controlled Release, 2012. **164**(3): p. 138-144.

39. Rostad, M.E., *Current strategies for managing myelosuppression in patients with cancer*. Oncology Nursing Forum, 1991. **18**(2 Suppl): p. 7-15.

40. Rao, L., L.L. Bu, J.H. Xu, B. Cai, G.T. Yu, X. Yu, et al. *Red blood cell membrane as a biomimetic nanocoating for prolonged circulation time and reduced accelerated blood clearance*. Small, 2015. **11**(46): p. 6225-6236.

41. Kam, N.W., M. O'Connell, J.A. Wisdom, and H. Dai, *Carbon nanotubes as multifunctional biological transporters and near-infrared agents for selective cancer cell destruction*. Proceedings of the Naitonal Academy of Sciences USA, 2005. **102**(33): p. 11600-11605.

42. Monteiro-Riviere, N.A., R.J. Nemanich, A.O. Inman, Y.Y. Wang, and J.E. Riviere, *Multi-walled carbon nanotube interactions with human epidermal keratinocytes*. Toxicology Letters, 2005. **155**(3): p. 377-384.

43. Pisanic, T.R., J.D. Blackwell, V.I. Shubayev, R.R. Finones, and S. Jin, *Nanotoxicity of iron oxide nanoparticle internalization in growing neurons.* Biomaterials, 2007. **28**(16): p. 2572-2581.

44. Warheit, D.B., T.R. Webb, K.L. Reed, S. Frerichs, and C.M. Sayes, *Pulmonary toxicity study in rats with three forms of ultrafine-TiO2 particles: differential responses related to surface properties*. Toxicology, 2007. **230**(1): p. 90-104.

45. Luk, B.T. and L. Zhang, *Current advances in polymer-based nanotheranostics for cancer treatment and diagnosis*. ACS Applied Materials amd Interfaces, 2014. **6**(24): 21859-21873.

46. Hrkach, J., D. Von Hoff, A.M. Mukkaram, E. Andrianova, J. Auer, T. Campbell, et al. *Preclinical development and clinical translation of a PSMA-targeted docetaxel nanoparticle with a differentiated pharmacological profile*. Science Translational Medicine, 2012. **4**(128): p. 128ra39.

3.2 Functionalization of Targeting Ligands to RBC Membrane-Cloaked Nanoparticles

3.2.1 Introduction

A major goal in engineering nanocarriers for systemic drug delivery is to achieve long circulation half-lives [1], as increased residence time in the bloodstream can improve the pharmacokinetic profile of therapeutic cargoes and allow a greater chance for the nanocarriers to reach the desired location through either passive [2, 3] or active [4-6] targeting mechanisms. Ongoing search for new and effective ways to construct long-circulating nanoparticles has introduced numerous stealth functionalization strategies. While the use of synthetic polymers represents the current golden standard for prolonging particle residence time in circulation, recent efforts have drawn inspiration from nature to bestow immune-evasive properties on nanoparticles [7, 8]. Bridging the complex surface biochemistry of nature's carriers, RBCs, with the versatile cargo-carrying capacity of polymeric nanoparticles, an RBC membrane-cloaked nanoparticle (RBC-NP) platform represents a new class of bio-inspired nanocarriers with long-circulating capability [9, 10]. In this system, a top-down approach is used to coat polymeric nanoparticles with natural RBC membranes, which possess a litany of immunomodulatory proteins responsible for RBCs' extraordinarily long survival in circulation [11-14]. This membrane cloak acts to camouflage the nanoparticle *in vivo* to evade immune attacks [9]. Consisting entirely

of biocompatible and biodegradable materials, the RBC-NPs have significant potential for drug delivery applications.

In applying RBC-NPs for disease treatments, particularly against cancers, target-selectivity is a desirable feature that promises minimization of off-target side effects [15-19]. Cancer targeting has been made possible by carrier functionalization with ligands that target overexpressed tumor antigens, and numerous chemical conjugation techniques employing carboxyl-, amine-, or sulfhydryl-based chemistry have been used to decorate synthetic nanocarriers with targeting ligands [20-26]. In the case of biologically derived carriers such as RBC-NPs, however, the presence of biological components on the particle surfaces demands a non-disruptive functionalization strategy since the immune evasion capabilities of cellular membranes is predicated upon having fully functional proteins. In order to address the issue of chemical denaturation, we report a lipid-insertion approach to functionalizing RBC-NPs that exploits the fluidity of bilayered RBC lipid membranes and precludes RBC membrane exposure to chemical reactions. As shown in Figure 3.6, targeting moieties

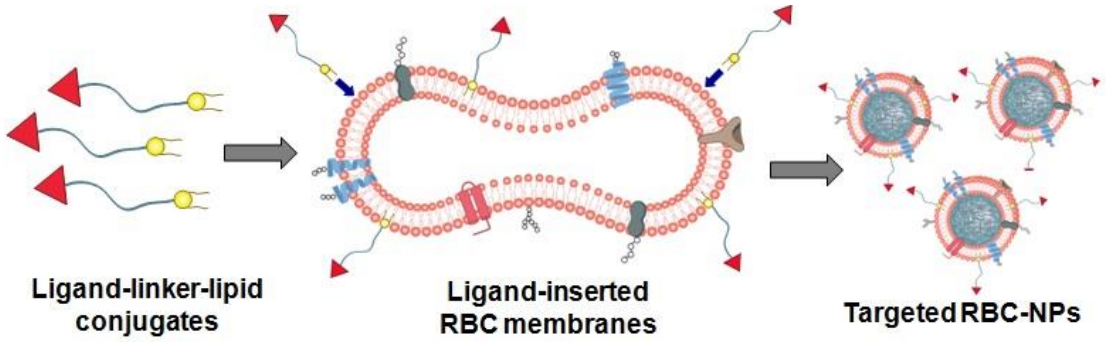

Figure 3.6 Schematic of the preparation of RBC-NPs with targeting ability. Ligand-linker-lipid conjugates are synthesized and then inserted into RBC membrane ghosts. The resulting ligand-functionalized RBC membranes are used to coat polymeric cores to form targeted RBC-NPs.

are incorporated onto RBC membranes through the aid of lipid tethers. The physical insertion of ligand-linker-lipid conjugates into the RBC membranes produces functionalized RBC membranes without damaging the existing surface proteins. Using two differently sized ligands, a small molecule folate (MW ~ 441 Da) and a nucleolin-targeting aptamer AS1411 (MW ~ 9,000 Da), we demonstrate that the lipid-insertion technique can be applied to targeting ligands of different length scales. Following preparation of RBC-NPs with the functionalized RBC membranes, their receptor-specific targeting ability is verified in model cancer cell lines *in vitro*.

3.2.2 Experimental Methods

3.2.2.1 Synthesis of Ligand-Linker-Lipid Conjugates

1,2-distearoyl-*sn*-glycero-3-phosphoethanol amine conjugated to polyethylene glycol 2000 with fluorescein isothiocyanate (FITC-PEG-lipid) was purchased from Nanocs (New York, NY). 1,2-distearoyl-*sn*-glycero-3-phosphoethanolamine-N-[folate(polyethylene glycol)-2000] (folate-PEG-lipid) was purchased from Avanti Polar Lipids (Alabaster, AL). AS1411 aptamer, with the sequence of GGT GGT GGT GGT TGT GGT GGT GGT GG, was custom synthesized by Integrated DNA Technologies (San Diego, CA) with a 3' thiol modifier. 1,2-distearoyl-*sn*-glycero-3-phosphoethanolamine-N-[maleimide(polyethylene glycol)-2000] (maleimide-PEG-lipid) was purchased from Avanti Polar Lipids. For the synthesis of AS1411-PEG-lipid, the aptamer was suspended at 1 mg/mL in a buffer consisting of 10 mM Tris pH 8.0 (Cellgro) and 0.1 mM ethylenediaminetetraacetic acid (EDTA) (USB Corporation)

with a 100× molar excess of tris[2-carboxyethyl] phosphine (TCEP) (Millipore) to reduce the disulfide bond of the thiol modifier. The solution was allowed to incubate for 4 hr at room temperature before washing the aptamer in the same reducing solution 3 times using a 10 kDa molecular weight cutoff Amicon Ultra-4 centrifuge filter (Millipore). The reduced aptamer was then incubated overnight with an equimolar amount of maleimide-PEG-lipid before washing again 3 times in water.

3.2.2.2 Preparation of Ligand-Inserted RBC Ghosts

Whole blood was obtained from 10 week-old male ICR mice (Charles River Laboratories) via cardiac puncture using syringes preconditioned with heparin (Sigma Aldrich) and EDTA. All animal experiments were reviewed, approved and performed under the regulatory supervision of The University of California, San Diego's institutional biosafety program and the Institutional Animal Care and Use Committee (IACUC). RBCs were extracted from the collected blood by centrifuging at 800 × g for 5 min at 4°C and washed 3 times in cold phosphate buffered solution (PBS) (Invitrogen). The buffy coat was removed in the process. The washed RBCs were then lysed in 0.25× PBS, and the ghosts were separated by collecting the pink pellet after centrifuging at 800 × g for 5 min at 4°C. The pellet was then resuspended in water and incubated with ligand-PEG-lipid (ligand = FITC, folate, or AS1411) for 30 min to form ligand-inserted RBC ghosts. All samples were then washed by pelleting at 800 × g for 5 min at 4°C before further use.

3.2.2.3 Characterization of Ligand-Inserted RBC Ghosts

To quantify ligand incorporation onto RBC ghosts, different amounts of FITC-PEG-lipid were incubated with RBC ghosts derived from 1 mL of mouse blood for 30 min. The total fluorescence of the solution was first quantified to obtain a value for the initial input. The ghosts were then washed 3 times and resuspended to the original volume. Another fluorescence reading was taken to determine the amount of ligand retained on the RBC ghosts relative to the initial input. For flow cytometry measurements, 40 μg of FITC-PEG-lipid was added into RBC ghosts derived from 1 mL of blood while plain RBC ghosts were used as a negative control. The samples were run on a FACSCanto II flow cytometer from Becton, Dickinson, and Company (Franklin Lakes, NJ) and the resulting data was analyzed using FlowJo software from Tree Star (Ashland, OR). Fluorescence imaging studies were conducted by dropping the FITC-modified RBC ghosts on a poly-L-lysine coated slide from Polysciences (Warrington, PA) and imaged using a 60X oil immersion objective on a DeltaVision Deconvolution Scanning Fluorescence Microscope from Applied Precision (Issaquah, WA).

3.2.2.4 Synthesis of Ligand-Functionalized RBC-NPs

The synthesis of ligand-functionalized RBC-NPs was adapted from a previously published protocol [9]. Briefly, RBC ghosts derived from 1 mL of blood that were functionalized with 40 μg of FITC-PEG-lipid were extruded serially through a 400 nm and then 100 nm polycarbonate membranes using a mini extruder (Avanti Polar Lipids). Polymeric cores of about 70 nm in diameter were prepared via the

nanoprecipitation of 0.67dL/g carboxyl-terminated poly($_{D,L}$-lactic-*co*-glycolic acid) (PLGA) (LACTEL Absorbable Polymers). The ligand-inserted membrane vesicles and the polymeric cores were then extruded together at a ratio of 1 mL of blood worth of vesicles to 1 mg of cores through a 100 nm polycarbonate membrane to form the final RBC-NPs. To measure average particle size and zeta potential, functionalized and non-functionalized RBC-NPs were suspended at 1 mg/mL in clear disposable capillary cells (DTS1061) from Malvern and measured by DLS using a Zetasizer (ZEN3600) from Malvern (United Kingdom). All measurements were taken at a backscattering angle of 173° and were performed in triplicate. The morphology of the particles were imaged by scanning electron microscopy (SEM) using an XL30 ESEM from FEI/Phillips (Hillsboro, OR) at a beam intensity of 20 kV. Samples were prepared at 1 μg/mL and 5 μL drops were dried onto silicon wafers. The samples were then coated with iridium at 85 mA for 7 sec on a K575X Sputter Coater from Emitech (Fall River, MA) followed by SEM imaging.

3.2.2.5 Colocalization Studies of Functionalized RBC-NPs

KB cells (ATCC: #CCL-17) were maintained in folate free RPMI 1640 (Gibco) supplemented with 10% fetal bovine serum (Hyclone) and penicillin-streptomycin (Gibco). Before the experiment, cultures were detached with 0.25% trypsin-EDTA (Gibco) and plated onto 8-chamber Labtek II slides (Nunclon) at 80% confluency. After allowing the cells to adhere overnight, they were incubated with RBC-NPs, of which the polymeric core was loaded with 0.05 wt% 1,1′-dioctadecyl-

3,3,3′,3′-tetramethylindo dicarbocyanine (DiD) (Invitrogen) and the RBC membrane shell contained FITC (40 μg FITC-PEG-lipid per 1 mL of blood worth of RBC ghosts). The cells were incubated with the RBC-NPs at a concentration of 0.25 mg/mL for 2 hr. The cells were then washed with media and allowed to incubate for another 4 hr before fixing with 10% formalin (Millipore) and mounted with DAPI-containing Vectashield® (Invitrogen). Imaging was done using a 60X oil immersion objective on an Applied Precision DeltaVision Deconvolution Scanning Fluorescence Microscope.

3.2.2.6 Cellular Uptake Studies

All flow cytometry studies were conducted on a FACSCanto II flow cytometer (Becton Dickinson) and the resulting data was analyzed using FlowJo software (Tree Star). 10,000 events were collected per sample and gated using control cells with no RBC-NP incubation. Histograms were plotted with fluorescence intensity on the x-axis using a biexponential scale. All imaging studies were conducted using a 20X objective on a DeltaVision Deconvolution Scanning Fluorescence Microscope from Applied Precision.

Both KB Cells (ATCC: #CCL-17) and A549 cells (ATCC: #CCL-185) were maintained as described above in supplemented folate-free RPMI (Gibco). Folate-functionalized particles with 0.05 wt% DiD loaded into the polymeric cores were prepared using folate-PEG-lipid at a ratio of 20 μg folate-PEG-lipid per 1 mL of blood worth of RBC ghosts. Cells were plated at a density of 10^5 cells per well on 12-well plates (Becton Dickinson) for flow cytometry or at 80% confluency on 8-chamber

Labtek II slides (Nunclon) for fluorescence imaging and were allowed to adhere overnight before use. Folate-functionalized and non-targeted particles were incubated at a concentration of 250 μg per 1 mL of media. For samples with free folate, the concentration was adjusted to 1 mM using a 100 mM stock solution of folate in PBS (Gibco) 10 min before incubation with nanoparticles. All samples were incubated for 30 min, washed 3 times with media, and incubated in fresh media for another 30 minutes. For flow cytometry, cells were detached with trypsin EDTA (Gibco), washed with PBS (Gibco), and taken for analysis. For fluorescence imaging, the chambers were gently washed with PBS, fixed with 10% formalin (Millipore), and mounted with DAPI-containing Vectashield® (Invitrogen).

MCF-7 Cells (ATCC: #HTB-22) were maintained in DMEM (Gibco) supplemented with 10% fetal bovine serum (Hyclone) and penicillin-streptomycin (Gibco). AS1411-functionalized particles with 0.05 wt% DiD loaded into the polymeric cores were prepared using AS1411-PEG-lipid at a ratio of 100 μg AS1411-PEG-lipid per 1 mL of blood worth of RBC ghosts. Cells were plated at a density of 10^5 cells per well on 12-well plates (Becton Dickinson) for flow cytometry or at 80% confluency on 8-chamber Labtek II slides (Nunclon) for fluorescence imaging and were allowed to adhere overnight before use. AS1411-functionalized and non-targeted particles were incubated at a concentration of 250 μg per 1 mL of media. For the sample with free AS1411, 100 μg AS1411 in 10 μL PBS (Gibco) was added 10 min before incubation with nanoparticles. All samples were incubated for 30 min and then washed 3 times with media followed by incubating for another 30 minutes. For flow

cytometry, cells were detached with trypsin EDTA (Gibco), washed with PBS (Gibco), and taken for analysis. For fluorescence imaging, the chambers were gently washed with PBS, fixed with 10% formalin (Millipore), and mounted with DAPI-containing Vectashield® (Invitrogen).

3.2.2.7 Cytotoxicity Study

Human umbilical vein endothelial cells (HUVECs) (Cell Applications) were maintained in endothelial cell growth medium (Cell Applications). Before the experiment, the cells were detached and plated at a density of 5000 cells per well in a 96-well plate and allowed to attach overnight. Both unmodified and folate-functionalized RBC-NPs were prepared as previously described and serially diluted 3X starting from a concentration of 2 mg/mL. The samples were added to an equal volume of media in each well and allowed to incubate for 16 hr. Each sample was done in triplicate. The wells were then washed with media and allowed to incubate for another 48 hr. To conduct the cytotoxicity assay, all solution was removed from the wells and 100 μL of 3-(4,5-dimethylthiazol-2-yl)-2,5-diphenyltetrazolium bromide (MTT) (Invitrogen) in PBS was added to each well at a concentration of 0.5 mg/mL. After a 3 hr incubation at 37°C, the solution was removed and the crystals were solubilized with 100 μL of dimethyl sulfoxide (DMSO) (Sigma Aldrich) and the plate was allowed to incubate for another 20 m. The data was analyzed after reading the absorbance at 540 nm.

3.2.3 Results and Discussion

To demonstrate that lipid-tethered ligands can be spontaneously incorporated onto RBC membranes, a FITC-linker-lipid (excitation/emission = 495/519 nm) conjugate was used for a proof-of-concept test, where FITC was linked to a lipid molecule through a short polyethylene glycol chain (MW ~ 2,000 Da). In the study, 40 μg of FITC-PEG-lipid was first incubated with emptied red blood cells (RBC ghosts) collected from 1 mL of whole mouse blood for 30 min. The RBC ghosts were then centrifuged, washed with PBS, reconstituted, and examined using flow cytometric analysis (Figure 3.7A). Compared to unmodified RBC ghosts, modified membrane ghosts had significantly higher signal under the FITC channel. Visualization by fluorescence microscopy further confirmed the localization of the lipid-tethered FITC on the RBC membranes, as the microscopy image displays strong FITC signals outlining the exterior of the RBC ghosts (Figure 3.7B). To characterize the lipid-insertion efficiency and saturation, varying amounts of FITC-PEG-lipid were incubated with the membrane ghosts followed by membrane purification through centrifugation. Fluorescence quantification showed that the retained FITC fluorescence increased with the initial FITC-PEG-lipid input (Figure 3.7C). Saturation was observed as the retained FITC-PEG-lipid approached a plateau at approximately 40 μg per mL of RBCs. Based on the RBC concentration and the molecular weight of the ligand, it is estimated that each RBC ghost contains about 800,000 FITC-PEG-lipid. Figure 3.7C also demonstrates adjustability of ligand density on the membranes by controlling the lipid-tethered ligand input.

Upon confirming the incorporation of FITC onto the RBC ghosts, the

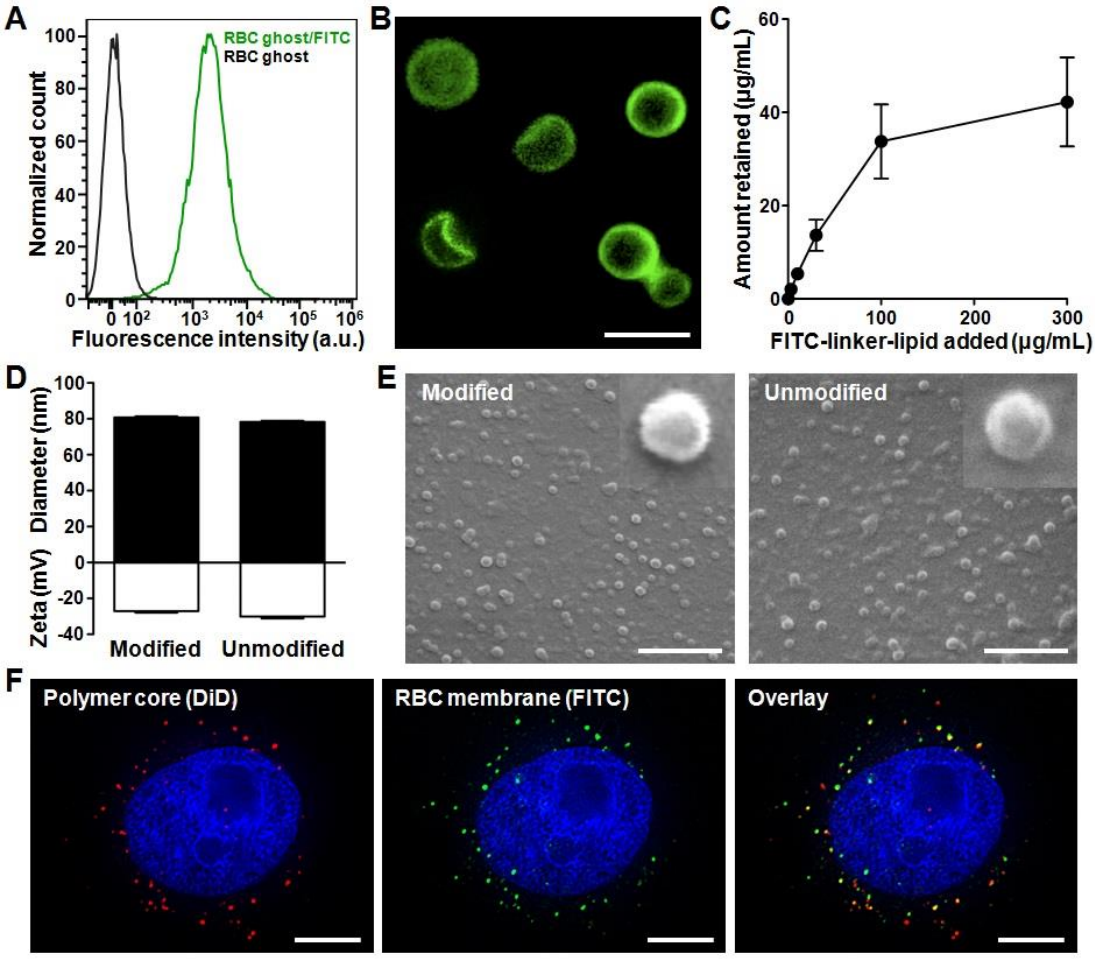

Figure 3.7 Lipid-insertion enables modification of RBC-NPs with FITC. (A) Flow cytometry histograms of plain RBC ghosts (black) and RBC ghosts incorporated with FITC-linker-lipid (green). (B) Fluorescence microscopy visualization of RBC ghosts modified with FITC (green). Scale bar = 8 μm. (C) FITC-linker-lipid was incubated with RBC ghosts derived from 1 mL of mouse blood. The amount of FITC-linker-lipid incorporated onto the RBC ghosts was then quantified after 30 min of incubation and plotted against the initial input. (D) Physicochemical characterizations (size and zeta potential) of both FITC-modified and unmodified RBC-NPs. (E) SEM images of FITC-modified and unmodified RBC-NPs. Insets represent a single particle with a size of ~80 nm. Scale bars = 500 nm. (F) Colocalization of the polymeric core (red) and the FITC-modified RBC membrane shell (green) upon intracellular uptake by KB cells. Cellular nuclei were stained with DAPI (blue). Scale bars = 8 μm.

membrane materials were then used to prepare FITC-modified RBC-NPs. Following a previously reported protocol [9], the FITC-modified RBC membrane ghosts were extruded to form ~100 nm vesicles, which were then mixed and extruded with 70 nm

PLGA particles to generate FITC-modified RBC-NPs. For comparison, RBC-NPs coated with unmodified RBC membranes were also prepared. Characterization of the two particles by dynamic light scattering (DLS) showed similar physicochemical properties between the FITC-modified and unmodified RBC-NPs (Figure 3.7D). Both particles were approximately 80 nm in mean diameter and under -25 mV in zeta potential. Scanning electron microscopy (SEM) further demonstrated the similarity between the two particle types (Figure 3.7E), both of which were spherical in morphology and exhibited monodisperse population distributions. To confirm the colocalization of lipid-tethered ligands with the polymeric cores, an *in vitro* fluorescence colocalization study was conducted by loading DiD dye (excitation/emission = 644/663 nm) into the polymeric cores. Following cellular uptake, significant overlap was observed between the DiD-specific red punctates and the FITC-specific green punctates (Figure 3.7F). The colocalization pattern confirms the presence of lipid-tethered FITC on the surface of the polymeric cores, demonstrating successful preparation of ligand-modified RBC-NPs.

After validating the lipid-insertion method for RBC-NP functionalization using lipid-tethered fluorescent probes, particle modification with cancer-targeting ligands was explored. A small molecule ligand, folate (MW ~ 441 Da), which has similar molecular weight as FITC, was first examined. Folate-functionalized nanocarriers have broad applicability as folate receptors are overexpressed on several types of cancers [27]. Upon receptor-mediated binding, folate-functionalized nanocarriers can deliver their cargoes intracellularly through an endocytic uptake pathway. The benefit

of folate-induced cancer targeting has been demonstrated on several nanocarrier platforms [28, 29], and thus its incorporation onto RBC-NPs can improve the particles' utility in cancer drug delivery.

To prepare folate-functionalized RBC-NPs, a commercially available folate-PEG-lipid conjugate was used (Figure 3.8A). Folate-functionalized RBC-NPs were prepared using RBC ghosts inserted with folate-PEG-lipid. Since the targeting ability of folate-functionalized nanoparticles has already been well-established, the KB cell line, a model cancer cell line overexpressing the folate receptor that is commonly used to evaluate folate targeting [30-32], was used to confirm successful functionalization of the RBC-NPs. To assess for folate-mediated differential uptake, the cells were cultured in folate-free media and incubated with folate-functionalized RBC-NPs, non-targeted RBC-NPs, or folate-functionalized RBC-NPs together with 1 mM of free folate. The cells from each sample were then detached, washed, and analyzed using flow cytometry (Figure 3.8B,C). Compared to the non-targeted RBC-NPs, the particles functionalized with folate ligand resulted in an 8-fold increase in cellular uptake. Conjoint incubation with folate-functionalized RBC-NPs and 1 mM of free folate yielded a similar level of cellular uptake as compared to non-targeted RBC-NPs, which indicates that the increased uptake of folate-functionalized RBC-NPs was receptor-specific. Fluorescence microscopy visualization of particle uptake further confirmed the results observed from flow cytometry. As shown in Figure 3.8D, fluorescence from the DiD dye encapsulated inside the particles was only observed in cells incubated with folate-functionalized RBC-NPs in the absence of free folate

molecules. To demonstrate that the targeting effects were exclusive to cells overexpressing the folate receptor, a negative cancer cell line [33], A549, was incubated with either unmodified or folate-functionalized RBC-NPs. No increased uptake was observed for the targeted nanoparticles compared to the unmodified nanoparticles using both flow cytometry and fluorescence imaging. Important to note also is that no cytotoxicity was observed for the RBC-NPs when incubated with human umbilical vein endothelial cells (HUVECs), a normal cell line, at the

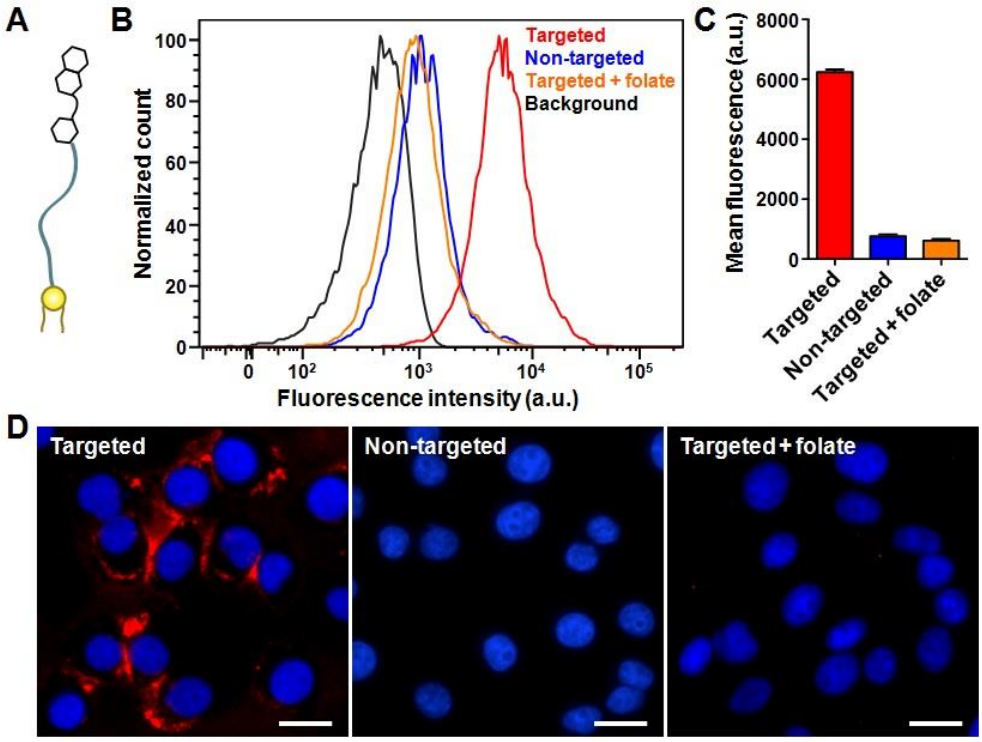

Figure 3.8 Lipid-insertion enables targeting functionalization with folate. (A) Schematic representation of folate-linker-lipid. (B) Flow cytometry histograms of KB cells alone (black) and the cells incubated with folate-functionalized RBC-NPs (red), non-targeted RBC-NPs (blue), and folate-functionalized RBC-NPs together with free folate (orange). (C) Quantification of the mean fluorescence intensity of the histograms in (B). (D) Fluorescence microscopy of KB cells incubated with folate-functionalized RBC-NPs, non-targeted RBC-NPs, and folate-functionalized RBC-NPs together with free folate. A fluorescent probe DiD was loaded inside the RBC-NPs for visualization (red) and cellular nuclei were stained with DAPI (blue). Scale bars = 25 μm.

concentrations used in these studies. Overall, the results confirm the receptor-specific

targeting capability of folate-functionalized RBC-NPs.

To demonstrate that the lipid-insertion method can be applied to targeting ligands of different length scales, a nucleolin-targeting oligonucleotide, AS1411 aptamer (MW ~ 9,000 Da), was also tested for particle functionalization. Oligonucleotide-based targeting agents, or aptamers, are a versatile class of ligands that can be customized against specific receptors through affinity screening [34]. AS1411, a 26-mer DNA aptamer with the sequence GGT GGT GGT GGT TGT GGT GGT GGT GG, has shown targeting capability against several cancer cell types owing to frequent overexpression of surface nucleolin on cancerous cells [35-37]. The ligand has also been applied for the preparation of cancer-targeted nanoparticles [38, 39], thus its integration onto the RBC-NPs would greatly benefit the utility of the platform. To incorporate aptamers onto RBC-NPs via lipid-insertion, a lipid-tethered AS1411 was first prepared. AS1411 aptamers containing a 3' thiol modifier was reduced using tris[2-carboxyethyl]phosphine (TCEP) and conjugated to lipid-PEG-maleimide via maleimide-sulfhydryl chemistry (Figure 3.9A). After purification, the AS1411-PEG-lipid conjugates were used to prepare RBC-NPs following the aforementioned procedures. In a cellular uptake study using a surface nucleolin expressing breast cancer cell line, MCF-7 [35], differential targeting was observed. Flow cytometry analysis revealed that the targeted nanoparticles induced a two-fold increase in cellular uptake as compared to the non-targeted RBC-NPs (Figure 3.9B,C). The uptake enhancement by the targeted nanoparticles was also confirmed to be receptor-specific, as blocking by free AS1411 reduced the particle uptake to the level of the non-targeted

nanoparticles. Fluorescence imaging corroborated the flow cytometry results with the AS1411-fuctionalized RBC-NP showing much greater uptake than the non-targeted and blocked samples (Figure 3.9D). The results demonstrate that the lipid-insertion method can be applied to relatively large targeting ligands (e.g., MW ~ 9,000 Da) with a molecular weight larger than that of the lipid anchor (MW ~ 748 Da).

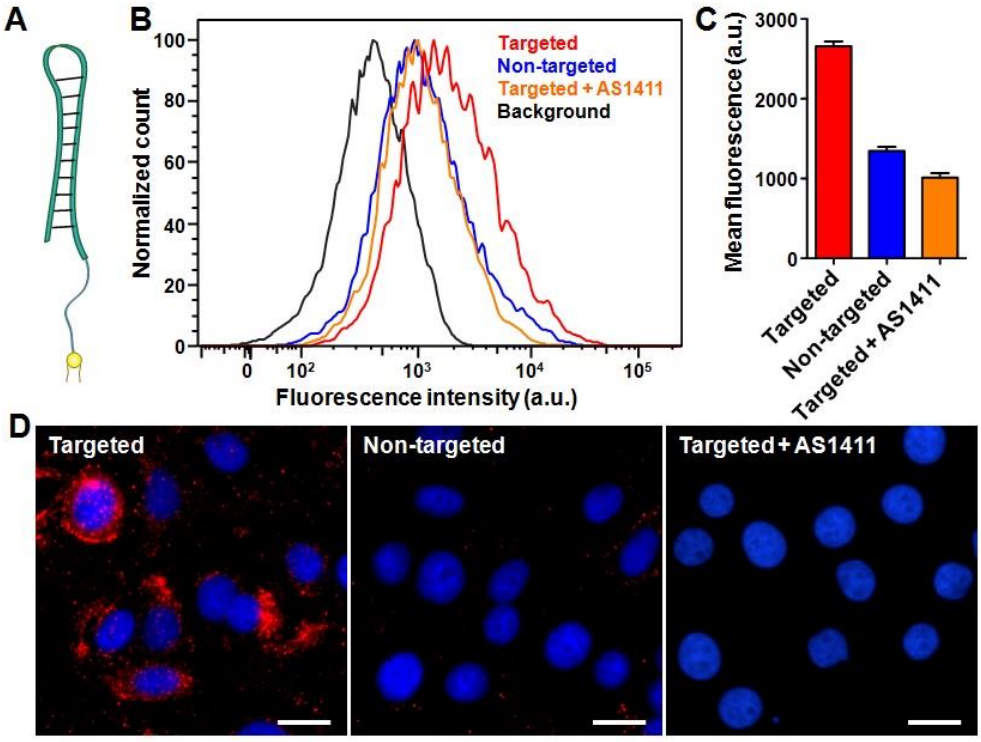

Figure 3.9 Lipid-insertion enables targeting functionalization with AS1411 aptamer. (A) Schematic representation of AS1411-linker-lipid. (B) Flow cytometry histograms of MCF-7 cells alone (black) and the cells incubated with AS1411-functionalized RBC-NPs (red), non-targeted RBC-NPs (blue), and AS1411-functionalized RBC-NPs together with free AS1411 aptamer (orange). (C) Quantification of the mean fluorescence intensity of the histograms in (B). (D) Fluorescence microscopy of MCF-7 cells incubated with AS1411-functionalized RBC-NPs, non-targeted RBC-NPs, and AS1411-functionalized RBC-NPs together with free AS1411. A fluorescent probe DiD was loaded inside the RBC-NPs for visualization (red) and cellular nuclei were stained with DAPI (blue). Scale bars = 25 μm.

3.2.4 Conclusions

In summary, by employing a lipid-insertion technique for the functionalization of biological membrane, targeted RBC-NPs were successfully prepared with two different types of targeting ligands. Through the aid of lipid tethers and the dynamic conformation of membrane bilayers, targeting ligands can be spontaneously incorporated onto the RBC-NP platform without exposing the biological membranes to chemical reactions. The robustness and simplicity of this functionalization scheme can enable a wide array of functionalized RBC-NPs for specific disease treatments. In addition, the technique can be generalized to help improve the applicability of emerging biologically inspired nanocarriers possessing complex surface chemistry. The capability to control and adjust ligand density through the lipid-insertion technique also provides versatility for platform optimization. Future studies are warranted to examine the *in vivo* implications of ligand functionalization on RBC-NPs. The targeted RBC-NPs reported in the present work possess significant potential for cancer treatments as they integrate nature's immune-evasive moieties with cancer-binding ligands.

3.2.5 References

1. Li, S.D. and L. Huang, *Pharmacokinetics and biodistribution of nanoparticles.* Molecular Pharmaceutics, 2008. **5**(4): p. 496-504.

2. Maeda, H., J. Wu, T. Sawa, Y. Matsumura, and K. Hori, *Tumor vascular permeability and the EPR effect in macromolecular therapeutics: a review*. Journal of Controlled Release, 2000. **65**(1-2): p. 271-284.

3. Iyer, A.K., G. Khaled, J. Fang, and H. Maeda, *Exploiting the enhanced permeability and retention effect for tumor targeting.* Drug Discovery Today, 2006. **11**(17-18): p. 812-818.

4. Singh, R. and J.W. Lillard, Jr., *Nanoparticle-based targeted drug delivery.* Experimentla and Molecular Pathology, 2009. **86**(3): p. 215-223.

5. Emerich, D.F. and C.G. Thanos, *Targeted nanoparticle-based drug delivery and diagnosis.* Journal of Drug Targeting, 2007. **15**(3): p. 163-183.

6. Brannon-Peppas, L. and J.O. Blanchette, *Nanoparticle and targeted systems for cancer therapy.* Advanced Drug Delivery Reviews, 2004. **56**(11): p. 1649-1659.

7. Fang, R.H., C.M.J. Hu, and L.F. Zhang, *Nanoparticles disguised as red blood cells to evade the immune system.* Expert Opinion Biological Therapy, 2012. **12**(4): p. 385-389.

8. Hu, C.M., R.H. Fang, and L. Zhang, *Erythrocyte-inspired delivery systems.* Advanced Healthcare Materials, 2012. **1**(5): p. 537-547.

9. Hu, C.M.J., L. Zhang, S. Aryal, C. Cheung, R.H. Fang, and L. Zhang, *Erythrocyte membrane-camouflaged polymeric nanoparticles as a biomimetic delivery platform.* Proceedings of the National Academy of Sciences USA, 2011. **108**(27): p. 10980-10985.

10. Hu, C.M.J., R.H. Fang, J. Copp, B.T. Luk, and L. Zhang, *A biomimetic toxin nanosponge*. Nature Nanotechnology, 2013. **8**(5): p. 336-340.

11. Kim, D.D. and W.C. Song, *Membrane complement regulatory proteins.* Clinical Immunology, 2006. **118**(2-3): p. 127-136.

12. Oldenborg, P.A., A. Zheleznyak, Y.F. Fang, C.F. Lagenaur, H.D. Greshan, and F.P. Lindberg, *Role of CD47 as a marker of self on red blood cells.* Science, 2000. **288**(5473): p. 2051-2054.

13. Tsai, R.K. and D.E. Discher, *Inhibition of "self" engulfment through deactivation of myosin-II at the phagocytic synapse between human cells.* The Journal of Cell Biology, 2008. **180**(5): p. 989-1003.

14. Tsai, R.K., P.L. Rodriguez, and D.E. Discher, *Self inhibition of phagocytosis: The affinity of 'marker of self' CD47 for SIRP alpha dictates potency of inhibition but only at low expression levels.* Blood Cells, Molecules, and Diseases, 2010. **45**(1): p. 67-74.

15. Farokhzad, O.C. and R. Langer, *Nanomedicine: developing smarter therapeutic and diagnostic modalities.* Advanced Drug Delivery Reviews, 2006. **58**(14): p. 1456-1459.

16. Davis, M.E., Z. Chen, and D.M. Shin, *Nanoparticle therapeutics: an emerging treatment modality for cancer.* Nature Reviews Drug Discovery, 2008. **7**(9): p. 771-782.

17. Peer, D., J.M. Karp, S. Hong, O.C. Farokhzad, R. Margalit, and R. Langer, *Nanocarriers as an emerging platform for cancer therapy.* Nature Nanotechnology, 2007. **2**(12): p. 751-760.

18. Wagner, V., A. Dullaart, A.K. Bock, and A. Zweck, *The emerging nanomedicine landscape.* Nature Biotechnology, 2006. **24**(10): p. 1211-1217.

19. Zhang, L., F.X. Gu, J.M. Chang, A.Z. Wang, R.S. Langer, and O.C. Farokhzad, *Nanoparticles in medicine: therapeutic applications and developments.* Clinical Pharmacology & Therapeutics, 2008. **83**(5): p. 761-769.

20. Bahadur, K.C.R., B. Thapa, and P.S. Xu, *pH and Redox Dual Responsive Nanoparticle for Nuclear Targeted Drug Delivery.* Molecular Pharmaceutics, 2012. **9**(9): p. 2719-2729.

21. Bartczak, D. and A.G. Kanaras, *Preparation of Peptide-Functionalized Gold Nanoparticles Using One Pot EDC/Sulfo-NHS Coupling.* Langmuir, 2011. **27**(16): p. 10119-10123.

22. Chen, T., I. Ocsoy, Q. Yuan, R. Wang, M. You, Z. Zhao, E. Song, X. Zhang, and W. Tan, *One-Step Facile Surface Engineering of Hydrophobic Nanocrystals with Designer Molecular Recognition.* Journal of the American Chemical Society, 2012. **134**(32): p. 13164-13167.

23. Hu, C.M.J., S. Kaushal, H.S. Tran Cao, S. Aryal, M. Sartor, S. Esener, M. Bouvet, and L. Zhang, *Half-Antibody Functionalized Lipid-Polymer Hybrid Nanoparticles for Targeted Drug Delivery to Carcinoembryonic Antigen Presenting Pancreatic Cancer Cells.* Molecular Pharmaceutics, 2010. **7**(3): p. 914-920.

24. Jin, E.L., B. Zhang, X. Sun, Z. Zhou, X. Ma, Q. Sun, J. Tang, Y. Shen, E. Van Kirk, W.J. Murdoch, and M. Radosz, *Acid-Active Cell-Penetrating Peptides for in Vivo Tumor-Targeted Drug Delivery.* Journal of the American Chemical Society, 2013. **135**(2): p. 933-940.

25. Kamphuis, M.M.J., A.P. Johnston, G.K. Such, H.H. Dam, R.A. Evans, E.C. nice, J.K. Heath, and F. Caruso, *Targeting of Cancer Cells Using Click-*

Functionalized Polymer Capsules. Journal of the American Chemical Society, 2010. **132**(45): p. 15881-15883.

26. Wang, J., S. Tian, R.A. Petros, M.E. Napier, and J.M. DeSimone, *The Complex Role of Multivalency in Nanoparticles Targeting the Transferrin Receptor for Cancer Therapies.* Journal of the American Chemical Society, 2010. **132**(32): p. 11306-11313.

27. Sudimack, J. and R.J. Lee, *Targeted drug delivery via the folate receptor.* Advanced Drug Delivery Reviews, 2000. **41**(2): p. 147-162.

28. Pan, X. and R.J. Lee, *Tumour-selective drug delivery via folate receptor-targeted liposomes.* Expert Opinion on Drug Delivery, 2004. **1**(1): p. 7-17.

29. Byrne, J.D., T. Betancourt, and L. Brannon-Peppas, *Active targeting schemes for nanoparticle systems in cancer therapeutics.* Advanced Drug Delivery Reviews, 2008. **60**(15): p. 1615-1626.

30. Lee, R.J. and P.S. Low, *Delivery of Liposomes into Cultured Kb Cells Via Folate Receptor-Mediated Endocytosis.* The Journal of Biological Chemistry, 1994. **269**(5): p. 3198-3204.

31. Lee, R.J. and P.S. Low, *Folate-Mediated Tumor-Cell Targeting of Liposome-Entrapped Doxorubicin in-Vitro.* Biochimica et Biophysica Acta - Biomembranes, 1995. **1233**(2): p. 134-144.

32. Wang, S., R.J. Lee, G. Cauchon, D.G. Gorenstein, and P.S. Low, *Delivery of Antisense Oligodeoxyribonucleotides against the Human Epidermal Growth-Factor Receptor into Cultured Kb Cells with Liposomes Conjugated to Folate Via Polyethylene-Glycol.* Proceedings of the National Academy of Sciences USA, 1995. **92**(8): p. 3318-3322.

33 Yoo, H.S. and T.G. Park, *Folate-receptor-targeted delivery of doxorubicin nano-aggregates stabilized by doxorubicin-PEG-folate conjugate*. Journal of Controlled Release, 2004. **100**(2): p. 247-256.

34. Mayer, G., M.S. Ahmed, A. Dolf, E. Endl, P.A. Knolle, and M. Famulok, *Fluorescence-activated cell sorting for aptamer SELEX with cell mixtures.* Nature Protocols, 2010. **5**(12): p. 1993-2004.

35. Soundararajan, S., W. Chen, E.K. Spicer, N. Courtenay-Luck, and D.J. Fernandes, *The nucleolin targeting aptamer AS1411 destabilizes bcl-2 messenger RNA in human breast cancer cells.* Cancer Research, 2008. **68**(7): p. 2358-2365.

36. Mongelard, F. and P. Bouvet, *AS-1411, a guanosine-rich oligonucleotide aptamer targeting nucleolin for the potential treatment of cancer, including acute myeloid leukemia.* Current Opinion in Molecular Therapeutics, 2010. **12**(1): p. 107-114.

37. Soundararajan, S., L. Wang, V. Sridharan, W. Chen, N. Courtenay-Luck, D. Jones, E.K. Spicer, and D.J. Fernandes, *Plasma Membrane Nucleolin Is a Receptor for the Anticancer Aptamer AS1411 in MV4-11 Leukemia Cells.* Molecular Pharmacology, 2009. **76**(5): p. 984-991.

38. Aravind, A., P. Jeyamohan, R. Nair, S. Veeranarayanan, Y. Nagaoka, Y. Yoshida, T. Maekawa, and D.S. Kumar, *AS1411 aptamer tagged PLGA-lecithin-PEG nanoparticles for tumor cell targeting and drug delivery.* Biotechnology and Bioengineering, 2012. **109**(11): p. 2920-2931.

39. Hwang, D.W., H.Y. Ko, J.H. Lee, H. Kang, S.H. Ryu, I.C. Song, D.S. Lee, and S. Kim, *A Nucleolin-Targeted Multimodal Nanoparticle Imaging Probe for Tracking Cancer Cells Using an Aptamer.* Journal of Nuclear Medicine, 2010. **51**(1): p. 98-105.

3.3 Platelet Membrane-Cloaked Nanoparticles for Targeted Drug Delivery

3.3.1 Introduction

Development of functional nanoparticles can be encumbered by unanticipated material properties and biological events, which can negatively impact nanoparticle effectiveness in complex, physiologically relevant systems [1-3]. Despite the advances in bottom-up nanoengineering and surface chemistry, reductionist functionalization approaches remain inadequate in replicating the complex interfaces present in nature and cannot avoid exposure of foreign materials. Here we report on the preparation of polymeric nanoparticles enclosed in the plasma membrane of human platelets, which are a unique population of cellular fragments that adhere to a variety of disease-relevant substrates [4-7]. The resulting nanoparticles possess a right-side-out unilamellar membrane coating functionalized with immunomodulatory and adhesion antigens associated with platelets. As compared to uncoated particles, the platelet membrane-cloaked nanoparticles have reduced cellular uptake by macrophage-like cells and are absent of particle-induced complement activation in autologous human plasma. The cloaked nanoparticles also display platelet-mimicking properties such as selective adhesion to damaged human and rodent vasculatures as well as enhanced binding to platelet-adhering pathogens. In an experimental rat model of coronary restenosis and a mouse model of systemic bacterial infection, docetaxel and

vancomycin, respectively, show enhanced therapeutic efficacy when delivered by the platelet-mimetic nanoparticles. The multifaceted biointerfacing enabled by the platelet membrane cloaking method provides a new approach in developing functional nanoparticles for disease-targeted delivery.

Owing to their role as circulating sentinels for vascular damage as well as for invasive microorganisms, platelets have inspired the design of many functional nanocarriers [8-13]. The multitude of platelet functions stems from a unique set of surface moieties responsible for immune evasion [14, 15], subendothelium adhesion [5, 16], and pathogen interactions [6, 7]. By adopting a recently developed cell membrane cloaking technique [17-19], we demonstrate the preparation of platelet membrane-cloaked nanoparticles (PNPs) consisting of a biodegradable polymeric nanoparticle core shielded entirely in the plasma membrane of human platelets. Several inherent platelet properties, including immunocompatibility, binding to injured vasculature, and pathogen adhesion, as well as their therapeutic implications, were studied.

3.3.2 Experimental Methods

3.3.2.1 Human Platelet Isolation and Platelet Membrane Derivation

Human type O^- blood anti-coagulated with 1.5 mg mL^{-1} EDTA was purchased from BioreclamationIVT and processed for platelet collection approximately 16 h after blood collection. Unless otherwise stated, platelets derived from this commercial blood source were used in this study. Fresh human type O^- blood was also collected

with dipotassium EDTA-treated or lithium heparin-treated blood collection tubes (Becton, Dickinson and Company) under the approval of the Institutional Review Board (IRB) at the University of California, San Diego. Patients consented to use of their blood samples for this study prior to collection. The freshly drawn blood was processed for platelet collection approximately 30 min following blood draw. In addition, in-dated human type O^- platelet rich plasma (PRP) in acid-citrate-dextrose (ACD) was purchased from the San Diego Blood Bank. Samples not originally drawn in EDTA were adjusted to a concentration of 5 mM EDTA prior to platelet collection. To isolate platelets, the blood and plasma samples were centrifuged at 100 × g for 20 min at room temperature to separate red blood cells and white blood cells. The resulting PRP was then centrifuged at 100 × g for 20 min to remove remaining blood cells. PBS buffer containing 1 mM of EDTA and 2 μM of prostaglandin E1 (PGE1, Sigma Aldrich) was added to the purified PRP to prevent platelet activation. Platelets were then pelleted by centrifugation at 800 × g for 20 min at room temperature, following which the supernatant was discarded and the platelets were resuspended in PBS containing 1 mM of EDTA and mixed with protease inhibitor tablets (Pierce). 1.5 mL aliquots of platelet solution containing ~ 3 x 10^9 platelets were prepared and used to cloak 1 mg of PLGA nanoparticles.

Platelet membrane was derived by a repeated freeze-thaw process. Aliquots of platelet suspensions were first frozen at -80 °C, thawed at room temperature, and pelleted by centrifugation at 4000 × g for 3 min. Following three repeated washes with PBS solution mixed with protease inhibitor tablets, the pelleted platelet membranes

were suspended in water and sonicated in a capped glass vial for 5 min using a Fisher Scientific FS30D bath sonicator at a frequency of 42 kHz and a power of 100 W. The presence of platelet membrane vesicles was verified by size measurement using dynamic light scattering (DLS) and morphological examination by transmission electron microscopy (TEM).

3.3.2.2 Platelet Membrane-Cloaked Nanoparticle (PNP) Preparation and Characterization

100 nm polymeric cores were prepared using 0.67 dL g^{-1} carboxyl-terminated 50:50 poly(lactic-*co*-glycolic) acid (PLGA) (LACTEL Absorbable Polymers) in a nanoprecipitation process. 1 mL of 10 mg mL^{-1} PLGA solution in acetone was added dropwise to 3 mL of water. For fluorescently labeled nanoformulations, 1,1'-dioctadecyl-3,3,3',3'-tetramethylindodicarbocyanine perchlorate (DiD, ex = 644 nm/em = 665 nm, Life Technologies) was loaded into the polymeric cores at 0.1 wt%. The mixture was then stirred in open air for 1 h and placed in vacuum for another 3 h. The resulting nanoparticle solution was filtered with 10 kDa MWCO Amicon Ultra-4 Centrifugal Filters (Millipore). Platelet membrane cloaking was then accomplished by dispersing and fusing platelet membrane vesicles with PLGA particles via sonication using an FS30D bath sonicator at a frequency of 42 kHz and a power of 100 W for 2 min. The size and the surface zeta potential of the replicate PNP samples (n=3) were obtained by DLS measurements using a Malvern ZEN 3600 Zetasizer. PBS stability was examined by mixing 1 mg mL^{-1} of PNPs in water with 2X PBS at a 1:1 volume

ratio. Storability of PNPs was examined by suspending PNPs in 10% sucrose. The nanoparticle solutions were subject to either a freeze-thaw cycle or lyophilization followed by resuspension. The resulting particle solution was then monitored for particle size using DLS. The structure of PNPs was examined with TEM following negative staining with 1 wt% uranyl acetate using an FEI 200 kV Sphera microscope. RBCNPs were prepared using the same polymeric cores and RBC membranes of equivalent total surface area to the platelet membranes using a previously described protocol[16]. The RBCNPs were characterized using DLS and had similar size and zeta potential as the PNPs.

Docetaxel-loaded PLGA nanoparticle cores were prepared via a nanoprecipitation process. 10 wt% docetaxel was added to 5 mg PLGA in acetone and precipitated dropwise into 3 mL water. The solvent was evaporated as described above and free docetaxel was removed via repeated wash steps. Vancomycin-loaded nanoparticles were synthesized using a double emulsion process. The inner aqueous phase consisted of 25 μL of vancomycin (Sigma Aldrich) dissolved in 1 M NaOH at 200 mg mL^{-1}. The outer phase consisted of 500 μL of PLGA polymer dissolved in dichloromethane at 50 mg mL^{-1}. The first emulsion was formed via sonication at 70% power pulsed (2 sec on/1 sec off) for 2 min on a Fisher Scientific 150E Sonic Dismembrator. The resulting emulsion was then emulsified in aqueous solution under the same dispersion setting. The final w/o/w emulsion was added to 10 mL of water and the solvent was evaporated in a fume food under gentle stirring for 3 h. The particles were collected via centrifugation at 80,000 × g in a Beckman Coulter Optima

L-90K Ultracentrifuge. The particles were washed and resuspended in water. Upon preparation of drug-loaded PLGA cores, cell membrane coating was performed by adding the appropriate surface area equivalent of either platelet or RBC membrane followed by 3 min of sonication in a Fisher Scientific FS30D Bath Sonicator. Particle size, polydispersity (PDI), and surface zeta potential were characterized using DLS. Drug loading yield and release rate of replicate samples (n=3) were quantified by high performance liquid chromatography (HPLC). Drug release was determined by dialyzing 500 μL of particle solution at a concentration of 2.67 mg mL^{-1} in PBS using 3.5K MWCO Slide-A-Lyzers (Thermo Scientific).

3.3.2.3 Examination of Platelet Membrane Proteins

PNPs were purified from unbound proteins or membrane fragments via centrifugation at 16,000 × g in 10% sucrose. Platelet-rich plasma, platelets, platelet membrane vesicles, and PNPs were then normalized to equivalent overall protein concentration using a Pierce BCA Protein Assay Kit (Life Technologies). To examine the effect of different platelet derivation protocols on the membrane protein expression, platelets collected from commercial blood anti-coagulated in EDTA, freshly drawn blood anti-coagulated in EDTA or heparin, and transfusion-grade PRP in ACD were prepared in parallel. All platelets were processed using the aforementioned platelet membrane derivation protocol for PNP preparation. The samples containing equivalent total proteins were then lyophilized, prepared in lithium dodecyl sulfate (LDS) sample loading buffer (Invitrogen), and separated on a 4-12%

Bis-Tris 17-well minigel in MOPS running buffer using a Novex® Xcell SureLock Electrophoresis System (Life Technologies). For membrane protein visualization, the gel was stained using SimplyBlue^{TM} SafeStain solution (Life Technologies) following the manufacturer's instructions and imaged using a gel imager. Identification of key membrane proteins via western blotting was performed using primary antibodies including mouse anti-human CD47 (eBioscience, B6H12), mouse anti-human CD55 (Biolegend, JS11), mouse anti-human CD59 (Biolegend, p282 (H19)), mouse anti-human αIIb subunit (Biolegend, HIP8), rat anti-human integrin α2 subunit (R&D Systems, 430907), rabbit anti-human integrin α5 subunit (Abgent, AP12204c), mouse anti-human integrin α6 subunit (Abgent, AM1828a), mouse anti-human integrin β1 subunit (R&D Systems, 4B7R), mouse anti-human β3 subunit (Biolegend, VI-PL2), mouse anti-human GPIbα (R&D Systems, 486805), mouse anti-human GPIV (R&D Systems, 877346), mouse anti-human GPV (Santa Cruz Biotech, G-11), rat anti-human GPVI (EMD Millipore, 8E9), rabbit anti-human GPIX (Santa Cruz Biotech, A-9), and mouse anti-human CLEC-2 (Genetex, 8J24). A goat anti-mouse IgG-HRP conjugate (Biolegend, Poly4053), a goat anti-rat IgG-HRP conjugate (Biolegend, Poly4054), or a donkey anti-rabbit IgG-HRP conjugate (Biolegend, Poly4064) was used for secondary staining based on the isotype of the primary antibody. MagicMark XP western protein standard (Invitrogen) was used as a molecular weight ladder. The nitrocellulose membrane was then incubated with ECL western blotting substrate (Pierce) and developed with the Mini-Medical/90 Developer (ImageWorks).

3.3.2.4 Examination of Protein Sidedness of PNPs

For immunogold staining, a drop of the PNP solution (1 mg mL^{-1}) was deposited onto a glow-discharged carbon-coated grid. The grid was then washed 3 times with PBS, blocked with 1% BSA for 15 min, and stained with 0.5 mg mL^{-1} of anti-CD47 targeted to either the intracellular or extracellular domain of the protein. Following 1 h of incubation, the samples were rinsed with PBS containing 1% BSA for 6 times and stained with anti-rabbit IgG gold conjugate (5 nm) solution (Sigma Aldrich) for another hour. Following 6 times of PBS washing, the samples were fixed with 1% glutaraldehyde in PBS for 5 min and washed with water for 6 times. The sample grids were subsequently stained with 2% vanadium solution (Abcam) and visualized using an FEI 200 kV Sphera microscope.

3.3.2.5 Platelet Aggregation Assay

Platelets, platelet membrane vesicles, and PNPs of equivalent membrane content were prepared and examined for platelet-activating molecules, including thrombin, ADP, and thromboxane, using a SensoLyte 520 Thrombin Activity Assay Kit (AnaSpec), ADP Colorimetric/Fluorometric Assay Kit (Sigma Aldrich), and Thromboxane B2 (TXB_2) ELISA Kit (Enzo Life Sciences), respectively, based on the manufacturers' instructions. Each sample was assayed in replicate (n=3).

Aggregation of platelets in the presence of PNPs was assessed using a spectrophotometric method. 1 mL aliquot of platelet rich plasma (PRP) was first prepared from human whole blood with sodium citrate as the anti-coagulant. The plasma was then loaded into a cuvette followed by addition of 500 μL of 2 mg mL^{-1}

PNPs in PBS solution. As negative and positive controls, the PRP was mixed with 500 μL of PBS or 500 μL of PBS containing 0.5 IU mL^{-1} of human thrombin (Sigma Aldrich), respectively. The cuvettes were immediately placed in a TeCan Infinite M200 reader and monitored for change in absorbance at 650 nm over time, and platelet aggregation was observed based on the reduction of turbidity.

3.3.2.6 Collagen Binding Study

Collagen type IV derived from human placenta (Sigma Aldrich) was reconstituted to a concentration of 2.0 mg mL^{-1} in 0.25% acetic acid. 200 μL of the collagen solution was then added to a 96-well assay plate and incubated overnight at 4 °C. Prior to the collagen binding study, the plate was blocked with 2% BSA and washed three times with PBS. For the collagen binding study, 100 μL of 1 mg mL^{-1} DiD-loaded nanoformulations in water were added into replicate wells (n=6) of collagen-coated or non-collagen-coated plates. Following 30 sec of incubation, the plates were washed three times. Retained nanoparticles were then dissolved with 100 μL of DMSO for fluorescence quantification using a TeCan Infinite M200 reader.

3.3.2.7 Differential Adhesion to Endothelial and Collagen Surfaces

Collagen type IV was coated on 8-well Lab-Tek II chamber slides (Nunclon) as described above. The collagen-coated chamber slides were used to seed primary HUVECs obtained from the American Type Culture Collection and cultured in HUVEC Culture Medium (Sigma Aldrich) supplemented with 10% fetal bovine serum for 24 h. The cells were then incubated with 1 mg mL^{-1} DiD-loaded PNPs in PBS at

4°C for 30 sec. Next the cells were washed with PBS three times and fixed with tissue fixative (Millipore) for 30 min at room temperature. Fluorescence staining was done with 4'6-diamidino-2-phenylinodle (DAPI, Life Technologies) for the nuclei and 22-(n-(7-nitrobenz-2-oxa-1,3-diazol-4-yl)amino)-23,24-bisnor-5-cholen-3β-ol (NBD cholesterol, Life Technologies) for the cytosol before mounting the cells in ProLong Gold antifade reagent (Life Technologies) and imaged using a DeltaVision deconvolution scanning fluorescence microscope. Z-stacks were collected at 0.25 μm intervals over 10 μm. The images were deconvolved and superimposed. DiD fluorescence signal over collagen and endothelial surfaces as defined by the boundaries of NBD fluorescence were analyzed using ImageJ. PNP retention over collagen and endothelial surfaces was quantified based on distinct images (n=10) in which the average fluorescence per unit area was analyzed.

3.3.2.8 Cellular Uptake Study with Macrophage-like Cells

THP-1 cells were obtained directly from the American Type Culture Collection and used without further testing. They were maintained in RPMI 1640 media (Life Technologies) supplemented with 10% FBS (Sigma Aldrich). THP-1 cells were differentiated in 100 ng mL^{-1} phorbol myristate acetate (PMA, Sigma Aldrich) for 48 h and differentiation was visually confirmed by cellular attachment to petri dishes. For the cellular uptake study, the differentiated macrophage-like cells were incubated in replicate wells (n=3) with DiD-loaded PNPs, anti-CD47 blocked PNPs, and bare NPs at 100 μg mL^{-1} in culture media. Following 30 min of incubation at 37

°C, the macrophage-like cells were scraped off the petri dish and washed three times in PBS to remove non-internalized particles. Flow cytometry was performed to examine nanoparticle uptake by the macrophage-like cells. All flow cytometry studies were conducted on a FACSCanto II flow cytometer (BD Biosciences) and the data was analyzed using FlowJo software from Tree Star. The mean fluorescence was plotted in a bar chart with error bars representing the standard error. Statistical analysis was performed based on a two-tailed, unpaired t-test.

3.3.2.9 Complement Activation Study

To assess complement system activation, two complement split products (C4d and Bb) were analyzed using enzyme-linked immunosorbent assay kits (Quidel Corporation). The nanoparticles were incubated in replicate aliquots (n=4) of human serum at a volume ratio of 1:5 in a shaking incubator (80 rpm) at 37 °C for 1 h. The reaction was then stopped by adding 60 volumes of PBS containing 0.05% Tween-20 and 0.035% ProClin 300. Complement system activation of the nanoparticles was assayed following the manufacturer's instructions, and zymosan was used as a positive control.

3.3.2.10 PNP Adherence to Human Carotid Artery

Human umbilical cord was collected under the approval of the Institutional Review Board (IRB) at the University of California, San Diego, and human carotid arteries were collected under the approval of the IRB at the University of Southern California. Patients consented to use of their samples for this study prior to collection.

To derive decellularized arterial extracellular matrix (ECM), human arteries were carefully dissected from the umbilical cord and removed from the surrounding Wharton's jelly, and subsequently incubated in 2% sodium dodecyl sulfate (SDS, Sigma Aldrich) for 72 h. The decellularized tissue was then rinsed with PBS and incubated in PBS solution containing 200 μg mL^{-1} PNPs for 30 sec. The sample was then transferred to PBS solution and rinsed extensively prior to examination by scanning electron microscopy (SEM). A control decellularized arterial tissue sample without PNP incubation was prepared and visualized for comparison.

To examine PNP binding on denuded vascular walls, approximately 2 mm thick fresh human carotid artery sections were dissected and placed in normal saline on ice and transported immediately to the laboratory for a PNP binding study. To create the vascular characteristics of damaged arteries, an excised artery sample was surgically scraped on its luminal side with forceps to remove the endothelial layer. Successful denudation was confirmed via microscopy visualization. Prior to the nanoparticle binding experiment, both damaged and non-damaged artery samples were rinsed with PBS solution. The PNP binding experiment was performed by incubating the arterial samples in PBS solution containing 200 μg mL^{-1} of DiD-loaded PNPs for 30 sec. The samples were then transferred to PBS solution and rinsed extensively prior to visualization by fluorescence microscopy. Endogenous tissue components such as collagen and elastin were identified based on their autofluorescence, which excites and emits maximally at 300~500 nm and was captured using a FITC filter. DiD fluorescence was captured using a Cy5 filter to examine the deposition of PNPs. The

arterial samples were imaged via a cross-sectional view of a histological section and a top-down view on the luminal side. The images were normalized to a reference illumination image for proper comparison.

3.3.2.11 Pharmacokinetics, Biodistribution and Safety of PNPs in a Rat Model of Angioplasty-Induced Arterial Denudation

All animal experiments were performed in accordance with NIH guidelines and approved by the Animal Care Committee of the University of California, San Diego. For the pharmacokinetics study, adult male Sprague-Dawley rats weighing 300-350 g (Harlan Laboratories) were administered with DiD-labeled PNPs and their blood was collected at specific time points via tail-vein blood sampling for fluorescence quantification. For the safety study, rats were injected with 1 mL of 5 mg mL^{-1} of PNPs on day 0 and day 5 followed by blood collection on day 10 for comprehensive metabolic panel analysis. Rats receiving equivalent PBS injections were prepared as a control.

For the biodistribution and vasculature-targeting studies, adult male Sprague-Dawley rats weighing 300-350 g (Harlan Laboratories) were subjected to carotid balloon injury. In brief, the animals were anesthetized with intraperitoneal ketamine (Pfizer) at 100 mg kg^{-1} and xylazine (Lloyd Laboratories) at 10 mg kg^{-1}. A ventral mid-line incision (~2 cm) was made in the neck, and the left common carotid artery and carotid bifurcation was exposed by blunt dissection. Proximal of left carotid artery, inner carotid artery and external carotid artery were temporarily clamped to

avoid excessive blood loss during the induction of the 2F Fogarty arterial embolectomy catheter (Edwards Lifesciences). The catheter was introduced into left carotid artery through an arteriotomy on the external carotid artery. The catheter was slowly inflated to a determined volume (0.02 mL) and withdrawn with rotation for 3 times to denude endothelium. The wound was later closed with 4-0 sutures.

Following the wound closure, rats were injected intravenously with 1 mL of 5 mg mL^{-1} DiD-loaded PNPs in 10% sucrose. At specified time points following the injection, animals were euthanized by CO_2 inhalation. After perfusion with PBS, organs including heart, lung, liver, spleen, kidney, gut, blood, and aortic branch including both the left and right carotid arteries were carefully collected and homogenized for biodistribution analysis. The overall PNP distribution at the aortic branch was visualized using Keyence BZ-X700 fluorescence microscope. To examine the local distribution of PNP, damaged and undamaged arteries were cut longitudinally and stained with DAPI solution. En face examination was done on the luminal surfaces of denuded and intact area for the binding of PNPs. Sequences of images along z-axis (0.5 μm per section) from the intima to media layers of the carotid arteries were acquired with and Olympus ix81 fluorescence microscope. The 3D reconstruction of arterial wall from multisectional images was performed using Image J. To analyze the PNP retention, damaged and undamaged arteries collected at specified time points were homogenized, and their respective fluorescence was normalized to the liver fluorescence for comparison. All replicates represent different rats subjected to the same treatment (n=6).

3.3.2.12 Treatment of Experimental Coronary Restenosis

Sprague-Dawley rats following angioplasty-induced arterial denudation were randomly placed into groups. The nanoparticle treatment group was injected intravenously with 1 mL of 5 mg mL^{-1} docetaxel-loaded PNPs in 10% sucrose at a docetaxel dose of 0.3 mg kg^{-1} on day 0 and day 5. As controls, animals receiving PBS, free docetaxel, and empty PNPs were prepared. On day 14, animals were euthanized with an overdose of ketamine-xylazine cocktail and perfused with PBS and 4% paraformaldehyde (PFA) at a pressure of 120-140 mm Hg. Segments of left and right carotid arteries were carefully dissected out, and the PFA-fixed carotid arteries were embedded with Tissue-Tek OCT compound (VWR International) in a tissue base mold and slowly submerged into pre-chilled 2-methyl butane until frozen completely. The frozen tissue block was then immediately stored at -80°C until sectioning. Serial sectioning (15 μm per section) was performed with a Cyrotome cryostat machine (Leica), and the tissue sections were placed on polylysine-treated glass slides. Tissue sections on slides were dried at room temperature for 30 min before staining. For immunohistochemistry, frozen sections on slides were first washed with PBS to remove residual OCT medium and then subjected to standard hematoxylin and eosin (H&E) staining. Areas of intima and media were analyzed using Image J. Luminal obliteration is defined as the intima area / the area within the internal elastic lamina. Statistical analysis was performed using one-way ANOVA. Sample sizes were estimated prior to the study to give statistically interpretable data. Studies were done

in a non-blinded fashion. All replicates represent different rats subjected to the same treatment (n=6).

3.3.2.13 Staphylococcus aureus (MRSA252) Bacteria Adherence Study

MRSA252 obtained from the American Type Culture Collection was cultured on tryptic soy broth (TSB) agar (Becton, Dickinson and Company) overnight at 37 °C. A single colony was inoculated in TSB medium at 37 °C in a rotary shaker. Overnight culture was refreshed in TSB medium at 1:100 dilution at 37 °C under shaking for another 3 h until OD_{600} of the culture medium reached approximately 1.0 (logarithmic growth phase). The bacteria were harvested by centrifugation at 5,000 × g for 10 min and then washed with sterile PBS twice and then fixed with 10% formalin for 1 h. The fixed bacteria were washed with sterile PBS and suspended in 10% sucrose to a concentration of 1×10^8 CFU mL^{-1}. For the nanoparticle adhesion study, aliquots of 0.8 mL of 1×10^8 CFU mL^{-1} MRSA252 were mixed with 1.2 mL of 200 μg mL^{-1} DiD-loaded PNPs, RBCNPs, or bare NPs in 10% sucrose for 10 min at room temperature. The bacteria were then isolated from unbound nanoparticles by repeated centrifugal washes in sucrose solution at 5,000 × g. The purified bacteria were then suspended in 10% sucrose for replicate measurements (n=3) by flow cytometric analysis and SEM imaging.

3.3.2.14 Antimicrobial Efficacy Study

For *in vitro* antimicrobial efficacy study, 5×10^6 CFU of MRSA252 was mixed with 500 μL of 20 mg mL^{-1} nanoparticles (4 wt% vancomycin loading) in saline. As

controls, equivalent amount of bacteria was incubated in either PBS or free vancomycin (0.8 mg mL^{-1}). Following 10 min of incubation, bacteria were isolated from the solution via centrifugation at 2500 × g for 5 min. The collected bacteria pellet was resuspended with 500 μL of TSB culture medium and incubated for 5 h. The resulting samples were serially diluted in PBS and spotted on TSB agar plates. Following 24 h of culturing, the colonies were counted to determine the bacteria count in each sample. Replicates represent separate bacterial aliquots incubated with the same formulation (n=3).

For *in vivo* antimicrobial efficacy study, vancomycin-loaded PNPs (PNP-Vanc) and vancomycin-loaded RBCNPs (RBCNP-Vanc) were suspended in 10% sucrose solution at 31.25 mg mL^{-1} (4 wt% vancomycin loading). An equivalent concentration of free vancomycin (1.25 mg mL^{-1}) was also suspended in 10% sucrose. Male CD-1 mice (Harlan Laboratories) weighing ~25 g were challenged intravenously with 6 x 10^6 CFU of MRSA252 suspended in 100 μL of PBS. 30 min following the bacteria injection, mice were randomly placed into separate groups and injected with 200 μL of PNP-Vanc, RBCNP-Vanc, free vancomycin (daily dosage: 10 mg kg^{-1} vancomycin), or PBS. To compare to the clinical dosing of vancomycin, a control group treated with twice daily dosing of 30 mg kg^{-1} free vancomycin was prepared (total daily dosage: 60 mg kg^{-1} vancomycin). The mice received their corresponding treatments from day 0 to 2. On day 3, blood was collected from the submandibular vein. The mice were then sacrificed, perfused with PBS, and their organs were collected. The organs were homogenized using a Biospec Mini Beadbeater in 1 mL of

PBS for 1 min, serially diluted in PBS by 10-fold, and plated onto agar plates with spotting volume of 50 μL. Following 48 h of culture, bacterial colonies were counted to determine the bacterial load in each organ. Under the given experimental conditions, the detection limit was determined to be approximately 20 CFU per organ. Data points on the X-axis represent samples with no detectable bacterial colony. It was confirmed that samples prepared from unchallenged mice had no detectable colonies. The data was tested for normal distribution via the Shapiro-Wilk test. For blood and heart, which contained non-normal distributions, statistical analysis was performed using Kruskal-Wallis test. For the other organs, in which all groups were normally distributed and variance criteria were met, statistical analysis was performed using one-way ANOVA. Grubbs' test was used to detect and remove statistical outliers. Sample sizes were estimated prior to the study to give statistically interpretable data. Studies were done in a non-blinded fashion. Replicates represent different mice subjected to the same treatment (n=14).

3.3.3 Results and Discussion

PNPs were prepared by fusing plasma membranes derived from human platelets with 100 nm poly(lactic-*co*-glycolic acid) (PLGA) nanoparticles. Prior to platelet collection, blood and plasma samples were mixed with EDTA, which prevents platelet aggregation by deactivating fibrinogen-binding integrin αIIbβ3 [20]. Platelets were then processed for nanoparticle membrane cloaking. Physicochemical characterizations revealed that the final PNPs were approximately 15 nm larger than

the uncoated PLGA nanoparticles (bare NPs) and possessed an equivalent surface charge to that of platelet and platelet membrane-derived vesicles (platelet vesicles) (Figure 3.10A). Transmission electron microscopy (TEM) visualization of platelet vesicles and PNPs showed the formation of distinctive nanoparticulates and consistent unilamellar membrane coatings over the polymeric cores (Figure 3.10B). Improved colloidal stability was observed with the PNPs compared to bare NPs (Figure 3.10C), which is attributable to the stabilizing effect by the plasma membrane's hydrophilic surface glycans [21]. Translocation of platelet membrane protein content, including immunomodulatory proteins, CD47, CD55, and CD59 [14, 15], integrin components, αIIb, α2, α5, α6, β1, and β3, and other transmembrane proteins, GPIbα, GPIV, GPV, GPVI, GPIX, and CLEC-2 [5, 16] , onto the nanoparticles was examined via western blotting (Figure 3.20D). Platelets derived from multiple protocols were prepared in parallel for comparison, and it was observed that the PNP preparation resulted in membrane protein retention and enrichment very similar across the different platelet sources. Notably, platelets derived from blood treated with heparin, an anticoagulant that inactivates thrombin rather than platelets, showed evidence of higher platelet activation including increased GPIbα cleavage and CLEC-2 oligomerization [22]. Using blood anticoagulated with EDTA as the platelet source, a right-side-out membrane orientation on the PNPs was verified via both immunogold staining and flow cytometric analysis with antibodies targeting either the intracellular or extracellular domain of CD47 (Figure 3.10E). Pro-thrombotic, platelet-activating molecules such as thrombin, ADP, and thromboxane were removed in the PNP

formulation (Figure 3.10F-H), thereby permitting PNP administration with little risk of a thrombotic response (Figure 3.10I).

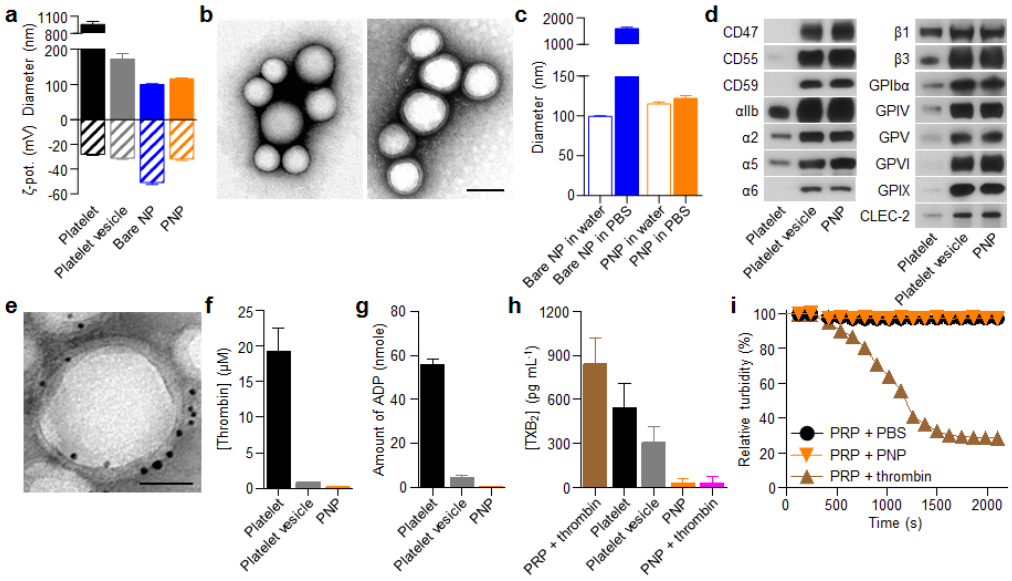

Figure 3.10 Preparation and characterization of PNPs. (a) Physicochemical characterization of platelets, platelet vesicles, bare NPs, and PNPs (n=3). ζ-pot., surface charge. (b) TEM images of bare NPs (left) and PNPs (right) negatively stained with uranyl acetate. Scale bar, 100nm. (c) Particle diameter of bare NPs and PNPs in water and in 1x PBS (n=3). (d) Representative protein bands resolved using western blotting. (e) TEM image of PNPs primary-stained with extracellular-domain-specific anti-CD47, and secondary-stained by an immunogold conjugate. Scale bar, 40 nm. (f–h) Platelet-activating contents including thrombin (f), ADP (g) and thromboxane (TXB2, h) in platelets, platelet vesicles, and PNPs were quantified (n=3). i, Platelet aggregation assay in which citrate-stabilized platelet rich plasma (PRP) was mixed with PBS, PNPs, or thrombin followed by spectroscopic examination of solution turbidity. All bars represent means±s.d.

PNPs' platelet-mimicking functionalities were first studied via the particles' binding to human type IV collagen, a primary subendothelial component [23]. Fluorescently labeled PNPs, along with bare NPs and red blood cell membrane-cloaked nanoparticles (RBCNPs), were incubated on collagen-coated plates. The platelet membrane cloak significantly enhanced particle retention as compared to bare NPs and RBCNPs (Figure 3.11A), indicating that the collagen adhesion was membrane type specific. Reduced PNP retention on non-collagen coated plates and in

the presence of anti-GPVI antibodies supports a specific collagen/platelet membrane interaction attributable to the presence of membrane glycoprotein receptors for collagen [16]. Further examination of PNP's differential binding to endothelial and collagen surfaces was performed using collagen-coated tissue culture slides seeded with human umbilical vein endothelial cells (HUVECs). PNPs adhered primarily outside of areas encompassed by the cells (Figure 3.11B). In addition, the PNPs were incubated with the extracellular matrix derived from decellularized human umbilical cord arteries. Following PBS washes, scanning electron microscopy (SEM) revealed a significant number of PNPs remaining on the fibrous structures on the luminal side of the artery (Figure 3.11C).

Examination of PNPs' immunocompatibility was conducted using differentiated human THP-1 macrophage-like cells. The platelet membrane cloaking reduced particle internalization in a CD47-specific manner [24], as blocking by anti-CD47 antibodies increased the cellular uptake (Figure 3.11D). The PNPs were further investigated for their interactions with the complement system based on quantifications of C4d and Bb split products. Following incubation in human plasma, complement activation was observed with bare NPs, reflecting their susceptibility to opsonization as well as the spontaneous reaction between C3 thioesters and the hydroxyl groups on the PLGA particles [25]. In contrast, an equal amount of PNPs mixed with autologous plasma showed no observable complement activation (Figure 3.11E,F). This suppression of the complement system can be attributed to membrane-bound complement regulator proteins such as CD55 and CD59 [26]. The lack of

complement activation by the PNPs also attests to the completeness of the membrane cloaking, which shields the polymeric cores from plasma exposure and minimizes the risk of anaphylatoxin generation frequently associated with injectable nanocarriers [27].

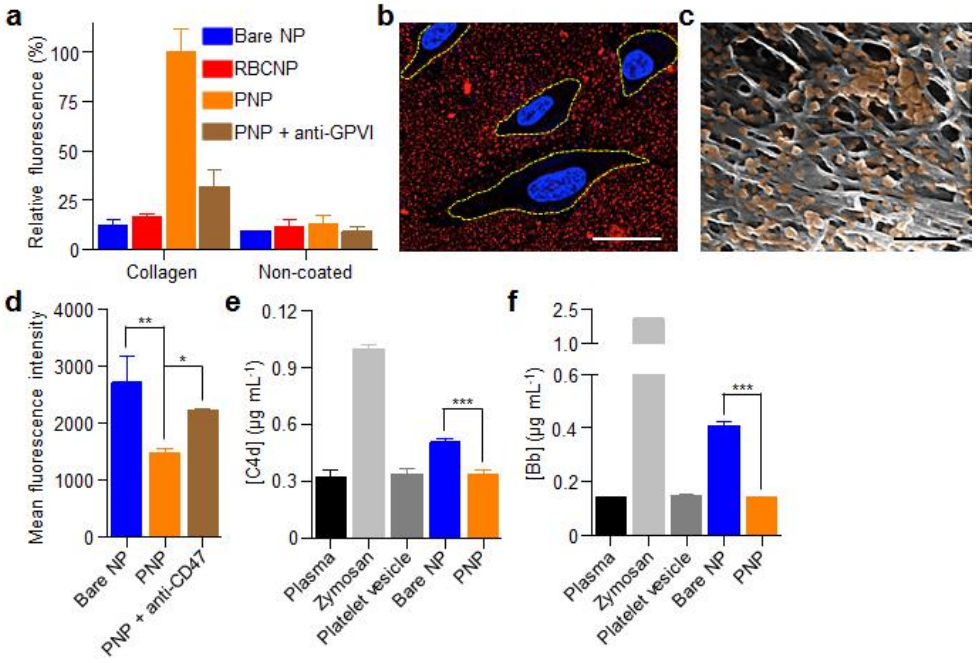

Figure 3.11 Collagen binding and immunocompatibility. (a) Fluorescence quantification of nanoparticle retention on collagen-coated and non-coated plates (n=6). (b) Localization of PNPs (stained in red) on collagen-coated tissue culture slides seeded with HUVECs (nuclei stained in blue). Cellular periphery is outlined based on cytosolic staining. Scale bar, 10 μm. (c) A pseudocolored SEM image of the extracellular matrix of a decellularized human umbilical cord artery following PNP incubation (PNPs colored in orange). Scale bar = 500 nm. (d) Flow cytometric analysis of nanoparticle uptake by human THP-1 macrophage-like cells (n=3). (e) Classical complement activation measured by C4d split products and (f) alternative complement activation measured by Bb split products for bare NPs, platelet vesicles, and PNPs in autologous human plasma (n=4). Zymosan and untreated plasma are used as positive and negative controls respectively. All bars represent means ± SD. *P ≤ 0.05, **P ≤ 0.01, ***P ≤ 0.001.

The PNP's therapeutic potential was first examined by assessing their selective adherence to damaged vasculatures. A segment of the human carotid artery was surgically scraped to expose the subendothelial matrix (Figure 3.12A). The intact and

damaged artery samples were subsequently incubated with fluorescently labeled PNPs for 30 sec followed by repeated PBS washes. The resulting arterial cross-sections and en face visualizations revealed that the denuded artery was more prone to PNP adhesion than the intact artery (Fig. 3.12B,C). In Figure 3.12C, it can also be observed that PNPs preferentially bind to the edges of the intact artery, where subendothelium was exposed upon tissue incision. This selective PNP adhesion was further validated in a rat model of angioplasty-induced arterial injury. Pharmacokinetic analyses and biodistribution studies showed that >90% of the PNPs were distributed to tissues 30 min after intravenous injection, with liver and spleen being the primary distribution organs. A comprehensive blood chemistry panel analysis revealed that the PNPs did not inflict observable adverse effects in the rats. Selective particle binding to the denuded artery was observed upon examination of the aortic branch 2 h following PNP administration (Figure 3.12D). The PNPs were localized on the luminal side above the smooth muscle layer (Figure 3.12E), and retention at the injury site lasted for at least 5 days (Figure 3.12F). In a rat model of coronary restenosis, therapeutic relevance of platelet-mimicking delivery was examined using docetaxel-loaded PNPs (PNP-Dtxl). PNP-Dtxl treatment on day 0 and 5 at 0.3 mg kg^{-1} of docetaxel dosing potently inhibited neointima growth in balloon-denuded rats as evidenced by the arterial cross-sections collected on day 14 (Figure 3.12G,H). To quantitatively evaluate the vascular remodeling, intima-to-media ratio (I/M) and luminal obliteration were calculated. As compared to free docetaxel, which resulted in an I/M of 0.76±0.18 and a luminal obliteration of 33.6%, PNP-Dtxl yielded significantly lower values of

0.18±0.06 and 8.0%, respectively ($P \leq 0.0001$) (Figure 3.12I-J). These results demonstrate the benefit of PNP-directed delivery in improving drug localization to diseased vasculatures.

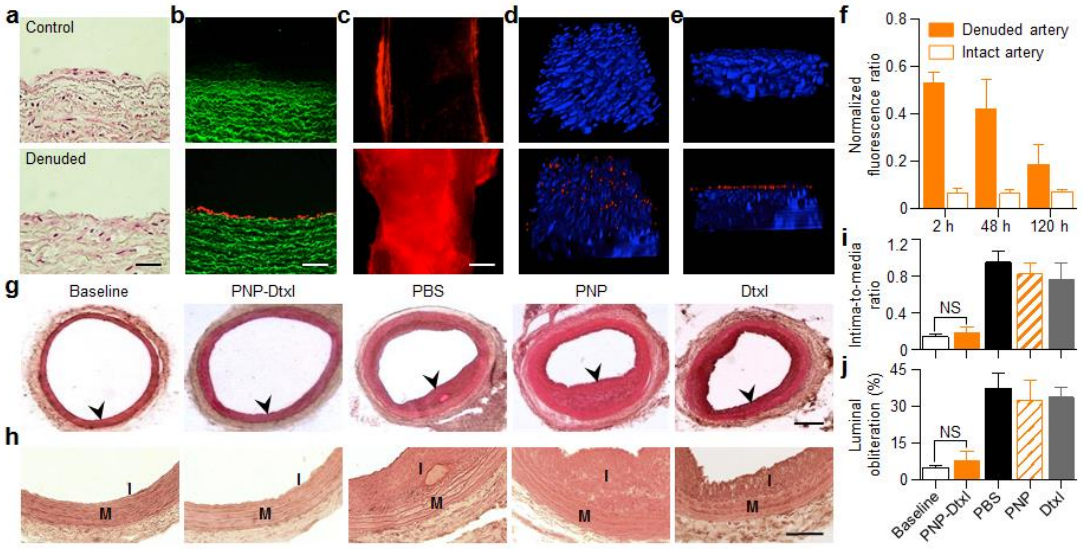

Figure 3.12 Adherence to damaged human and rodent vasculatures. (a) H&E-stained cross-sections of undamaged (top) and damaged (bottom) human carotid arteries. Scale bar, 200 μm. (b) Fluorescence images of the cross-section (scale bar, 200 μm) and (c) the luminal side (scale bar, 500 μm) of undamaged (top) and damaged (bottom) arteries following PNP incubation (tissue in green and PNPs in red). (d,e) 3D reconstructed images of intact (top) and balloon-denuded (bottom) arterial walls from multisectional images following intravenous administration of PNPs in rats (cell nuclei in blue and PNPs in red). Dimensions: 152.5 μm x 116 μm x 41 μm. (f) Retention of PNPs at the denuded and the intact arteries over 120 h following PNP administration (n=6). (g) Representative H&E-stained arterial cross-sections from different treatment groups in a rat model of coronary restenosis. Scale bar, 200 μm (h) Zoomed-in H&E-stained arterial cross-sections highlight the different vascular remodeling from the different treatment groups. I, intima; M, media. Scale bar, 100 μm. (i,j) Quantitative analysis of intima-to-media area ratio and luminal obliteration from the different treatment groups (n=6). All bars represent means ± SD. NS = no statistical significance.

We further examined the therapeutic potential of PNPs against platelet-adhering pathogens. Opportunistic bacteria including several strains of staphylococci and streptococci exploit platelets via both direct and indirect adherence mechanisms for tissue localization and immune evasion [6]. To demonstrate that PNPs can exploit the inherent bacterial adherence mechanism for targeted antibiotics delivery,

MRSA252, a strain of methicillin-resistant *Staphylococcus aureus* expressing a serine-rich adhesin for platelets (SraP) [28], was used as a model pathogen for particle adhesion study. Following 10 min of incubation between formalin-fixed MRSA252 and different nanoformulations, the collected bacteria showed preferential binding by PNPs (Figure 3.13A), exhibiting a 12-fold increase in PNP retention as compared to bare NPs (Figure 3.13B). This adherence was membrane-specific as RBCNPs showed lower retention than PNPs. The therapeutic potential of PNPs was further evaluated using vancomycin-loaded formulations. In an *in vitro* antimicrobial study, live MRSA252 bacteria were briefly incubated with free vancomycin, vancomycin-loaded RBCNPs (RBCNP-Vanc), or vancomycin-loaded PNPs (PNP-Vanc) followed by a subsequent wash and culturing in fresh media. The PNP-Vanc formulation showed statistically significant improvement in MRSA252 reduction that corroborates the targeting effect of the particles (Figure 3.13C). An *in vivo* antimicrobial efficacy study was further conducted using a mouse model of systemic MRSA252 infection. Mice systemically challenged with 6×10^6 CFU MRSA252 received once daily intravenous treatment of free vancomycin, RBCNP-Vanc, or PNP-Vanc for 3 days at 10 mg kg^{-1} of vancomycin. A control group of high-dose vancomycin treatment in which infected mice received a therapeutic concentration of vancomycin at 30 mg kg^{-1} twice daily was conducted in parallel. 24 h following the last treatment, bacterial enumeration at the primary infection organs showed that the PNP-Vanc resulted in the lowest mean bacterial counts across all organs (Figure 3.13D-I). Statistical analyses revealed significance between PNP-Vanc and free vancomycin at equivalent dosage in

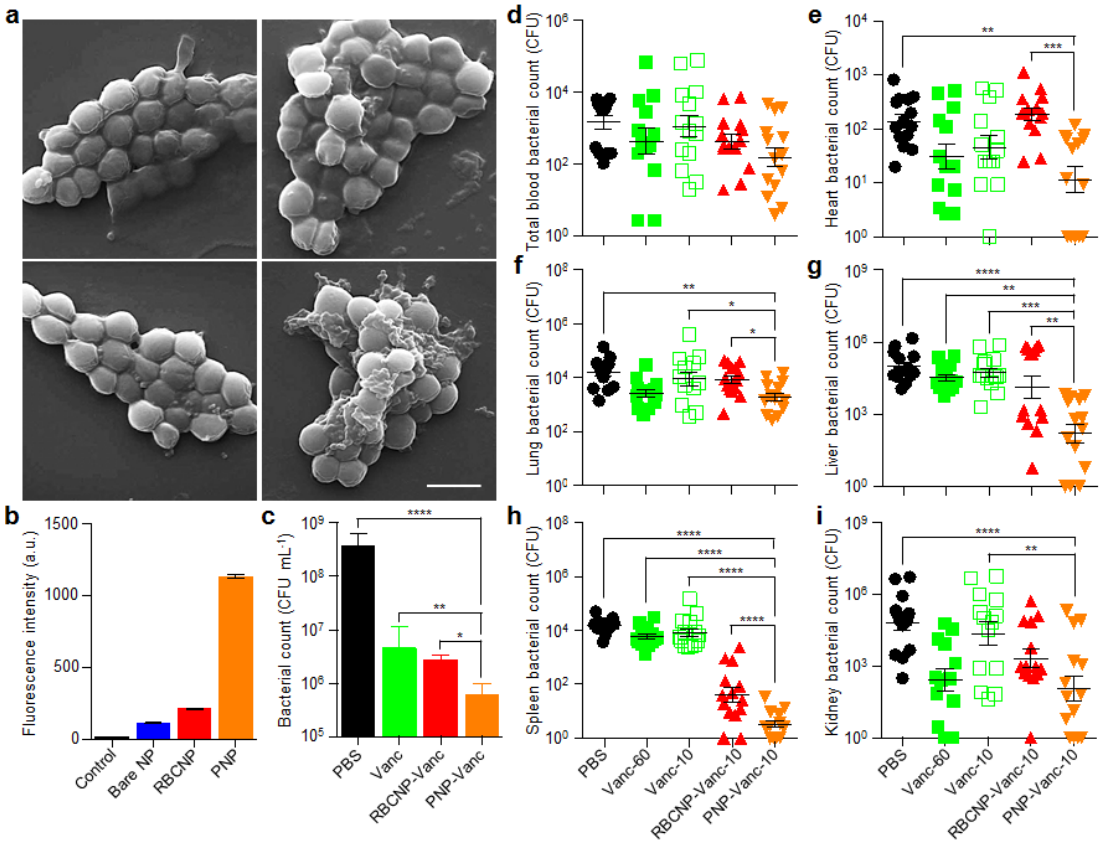

Figure 3.13 Binding to platelet-adhering pathogens. (a) SEM images of MRSA252 bacteria following incubation with PBS (top left), bare NPs (top right), RBCNPs (bottom left), and PNPs (bottom right). Scale bar, 1 μm. (b) Normalized fluorescence intensity of DiD-loaded nanoformulations retained on MRSA252 based on flow cytometric analysis. Bars represent means ± SD (n=3). (c) *In vitro* antimicrobial efficacy of free vancomycin, vancomycin-loaded RBCNPs (RBCNP-Vanc), and vancomycin-loaded PNPs (PNP-Vanc). Bars represent means ± SD (n=3). (d-i) *In vivo* antimicrobial efficacy of free vancomycin at 10 mg kg^{-1} (Vanc-10), RBCNP-Vanc-10, and PNP-Vanc-10, and free vancomycin at 6 times the dosing (Vanc-60, 60 mg kg^{-1}) was examined in a mouse model of systemic infection with MRSA252. Following 3 days of treatments, bacterial loads in different organs including (d) blood, (e) heart, (f) lung, (g) liver, (h) spleen, and (i) kidney were quantified. Bars represent means ± SEM (n=14). *P ≤ 0.05, **P ≤ 0.01, ***P ≤ 0.001, ****P ≤ 0.0001.

the lung, liver, spleen, and kidney. In comparison to free vancomycin at 6-fold the dosage, PNP-Vanc showed significantly better antimicrobial efficacy in the liver and spleen while being at least equally effective in the blood, heart, lung, and kidney. Notably, as compared to RBCNP-Vanc, PNP-Vanc showed significantly higher potency in the heart, lung, liver, and spleen, reflecting membrane-specific modulation

of nanoparticle performance. The study validates the feasibility of harnessing biomembrane interfaces to improve infectious disease treatment.

3.3.4 Conclusions

The vast medical relevance of platelets has inspired many platelet-mimicking systems that target dysfunctional vasculature in cardiovascular diseases [8, 9], traumas [10, 11, 13], cancers [12], and acute inflammations [29]. The present PNP platform exploits platelet membrane in its entirety to enable biomimetic interactions with proteins, cells, tissues, and microorganisms. Toward translation, the platform would benefit from existing infrastructures and logistics for transfusion medicine, polymeric nanotherapeutics, and cell-derived pharmaceutics. Prior works on the cell membrane cloaking approach demonstrated high cloaking efficiency [30] and viable storage [18] upon platform optimization. By employing large-scale purification and dispersion techniques commonly applied to biologics, reliable platelet membrane derivation and PNP production can be envisioned.

3.3.5 References

1. Pelaz, B., G. Charron, C. Pfeiffer, Y. Zhao, J.M. de la Fuente, X.J. Liang, W.J. Parak, and P. Del Pino, *Interfacing engineered nanoparticles with biological systems: anticipating adverse nanobio interactions*. Small, 2013. **9**(9-10): p. 1573-1584.

2. Salvati, A., A.S. Pitek, M.P. Monopoli, K. Prapainop, F.B. Bombelli, D.R. Hristov, P.M. Kelly, C. Aberg, E. Mahon, and K.A. Dawson, *Transferrin-functionalized nanoparticles lose their targeting capabilities when a biomolecule corona adsorbs on the surface*. Nature Nanotechnology, 2013. **8**(2): p. 137-143.

3. Tenzer, S., D. Docter, J. Kuharev, A. Musyanovych, V. Fetz, R. Hecht, F. Schlenk, *et al.*, *Rapid formation of plasma protein corona critically affects nanoparticle pathophysiology*. Nature Nanotechnology, 2013. **8**(10): p. 772-781.

4. Born, G.V.R. and M.J. Cross, *The aggregation of blood platelets*. Journal of Physiology, 1963. **168**(1): p. 178-195.

5. Kieffer, N. and D.R. Phillips, *Platelet membrane-glycoproteins: functions in cellular interactions*. Annual Review of Cell Biology, 1990. **6**: p. 329-357.

6. Fitzgerald, J.R., T.J. Foster, and D. Cox, *The interaction of bacterial pathogens with platelets*. Nature Reviews Microbiology, 2006. **4**(6): p. 445-457.

7. Yeaman, M. R., *Platelets in defense against bacterial pathogens*. Cellular and Molecular Life Sciences, 2010. **67**(4): p. 525-544.

8. Peters, D., M. Kastantin, V.R. Kotamraju, P.P. Karmali, K. Gujraty, M. Tirrell, and E. Ruoslahti, *Targeting atherosclerosis by using modular, multifunctional micelles*. Proceedings of the National Academy of Sciences USA, 2009. **106**(24): p. 9815-9819.

9. Chan, J.M., L. Zhang, R. Tong, D. Ghosh, W. Gao, G. Liao, *et al.*, *Spatiotemporal controlled delivery of nanoparticles to injured vasculature*. Proceedings of the National Academy of Sciences USA, 2010. **107**(5): p. 2213-2218.

10. Bertram, J.P., C.A. Williams, R. Robinson, S.S. Segal, N.T. Flynn and E.B. Lavik, *Intravenous hemostat: nanotechnology to halt bleeding*. Science Translational Medicine, 2009. **1**(11): p. 11ra22.

11. Modery-Pawlowski, C.L., L.L. Tian, V. Pan, K.R. McCrae, S. Matrigotri, and A. Sen Gupta, *Approaches to synthetic platelet analogs*. Biomaterials, 2013. **34**(2): p. 526-541.

12. Simberg, D., T. Duza, J.H. Park, M. Essler, J. Pilch, L. Zhang, *et al. Biomimetic amplification of nanoparticle homing to tumors*. Proceedings of the National Academy of Sciences USA, 2007. **104**(3): p. 932-936.

13. Anselmo, A.C., C.L. Modery-Pawlowski, S. Menegatti, S. Kumar, D.R. Vogus, L.L. Tian, *et al.*, *Platelet-like nanoparticles: mimicking shape,*

flexibility, and surface biology of platelets to target vascular injuries. ACS Nano, 2014. **8**(11): p. 11243-11253.

14. Olsson, M., P. Bruhns, W.A. Frazier, J.V. Ravetch, and P.A. Oldenborg, *Platelet homeostasis is regulated by platelet expression of CD47 under normal conditions and in passive immune thrombocytopenia*. Blood, 2005. **105**(9): p. 3577-3582.

15. Sims, P.J., S.A. Rollins, and T. Wiedmer, *Regulatory control of complement on blood platelets: modulation of platelet procoagulant responses by a membrane inhibitor of the C5b-9 Complex.* Journal of Biological Chemistry, 1989. **264**(32): p. 19228-19235.

16. Nieswandt, B. and S.P. Watson, *Platelet-collagen interaction: is GPVI the central receptor?* Blood, 2003. **102**(2): p. 449-461.

17. Hu, C. M., L. Zhang, S. Aryal, C. Cheung, R.H. Fang, and L. Zhang, *Erythrocyte membrane-camouflaged polymeric nanoparticles as a biomimetic delivery platform*. Proceedings of the National Academy of Sciences, 2011. **108**(27): p. 10980-10985.

18. Hu, C.M., R.H. Fang, J. Copp, B.T. Luk, and L. Zhang, *A biomimetic nanosponge that absorbs pore-forming toxins*. Nature Nanotechnology, 2013. **8**(5): p. 336-340.

19. Hu, C.M., R.H. Fang, B.T. Luk, and L. Zhang, Nanoparticle-detained toxins for safe and effective vaccination. Nature Nanotechnology, 2013. **8**(12): p. 933-938.

20. Gachet, C., D. Hanau, D. Spehner, C. Birsson, J.C. Garaud, D.A. Schmitt, P. Ohlmann, and J.P. Cazenave, *Alpha IIb beta 3 integrin dissociation induced by EDTA results in morphological changes of the platelet surface-connected canalicular system with differential location of the two separate subunits*. Journal of Cell Biology, 1993. **120**(4): p. 1021-1030.

21. Luk, B.T, C.M. Hu, R.H. Fang, D. Dehaini, C. Carpenter, W. Gao, and L. Zhang, *Interfacial interactions between natural RBC membranes and synthetic polymeric nanoparticles*. Nanoscale, 2013. **6**(5): p. 2730-2737.

22. Hughes, C.E., A.Y. Pollitt, J. More, J.A. Eble, M.G. Tomlinson, J.H. Hartwig, *et al.*, *CLEC-2 activates Syk through dimerization*. Blood, 2010. **115**(14): p. 2947-2955.

23. Kalluri, R. *Basement membranes: structure, assembly and role in tumour angiogenesis*. Nature Rev. Cancer, 2003. **3**(6): p. 422-433.

24. Rodriguez, P.L., T. Harada, D.A. Christian, P.A. Pantano, R.K. Tsai, and D.E. Discher, *Minimal "self" peptides that inhibit phagocytic clearance and enhance delivery of nanoparticles*. Science, 2013. **339**(6122): p. 971-975.

25. Law, S.K.A. and A.W. Dodds, *The internal thioester and the covalent binding properties of the complement proteins C3 and C4*. Protein Science, 1997. **6**(2): p. 263-274.

26. Terstappen, L.W.M.M. M., Nguyen, H.M. Lazarus, and M.E. Medof, *Expression of the DAF (CD55) and CD59 antigens during normal hematopoietic-cell differentiation*. Journal of Leukocyte Biology, 1992. **52**(6): p. 652-660.

27. Andersen, A.J., S.H. Hashemi, T.L. Andresen, A.C. Hunter, and S.M. Moghimi, *Complement: alive and kicking nanomedicines*. Journal of Biomedical Nanotechnology, 2009. **5**(4): p. 364-372.

28. Siboo, I.R., H.F. Chambers, and P.M. Sullam, *Role of SraP, a serine-rich surface protein of Staphylococcus aureus, in binding to human platelets*. Infection and Immunity, 2005. **73**(4): p. 2273-2280.

29. Kamaly, N, G. Fredman, M. Subramanian, S. Gadde, A. Pesic, L. Cheung, *et al., Development and in vivo efficacy of targeted polymeric inflammation-resolving nanoparticles*. Proceedings of the National Academy of Sciences USA, 2013. **110**(16): p. 6506-6511.

30. Hu, C.M., R.H. Fang, B.T. Luk, K.N. Chen, C. Carpenter, W. Gao, K. Zhang, and L. Zhang, *'Marker-of-self' functionalization of nanoscale particles through a top-down cellular membrane coating approach*. Nanoscale, 2013. **5**(7): p. 2664-2668.

Chapter 3, in full, is a reprint of the material as it appears in *Theranostics*, 2016, Brian Luk, Ronnie Fang, Che-Ming Hu, Jonathan Copp, Soracha Thamphiwatana, Diana Dehaini, Weiwei Gao, Kang Zhang, Shulin Li, and Liangfang Zhang; *Nanoscale*, 2013, Ronnie Fang, Che-Ming Hu, Kevin Chen, Brian Luk, Cody Carpenter, Weiwe Gao, Shulin Li, Dong-Er Zhang, Weiyue Lu, and Liangfang Zhang; and *Nature*, 2015, Che-Ming Hu, Ronnie Fang, Kuei-Chun Wang, Brian Luk, Soracha Thamphiwatana, Diana Dehaini, Phu Nguyen, Pavimol Angsantikul, Cindy Wen, Ashley Kroll, Cody Carpenter, Manikantan Ramesh, Vivian Qu, Sherrina Patel, Jie Zhu, William Shi, Florence Hofman, Thomas Chen, Weiwei Gao, Kang Zhang, Shu Chien, and Liangfang Zhang. The dissertation author was either the primary investigator or a major contributor and co-author of these papers.

Chapter 4

Cell Membrane-Coated Nanoparticles as "Nanosponges" for Biodetoxification

4.1 Clearance of Pore-Forming Toxins

4.1.1 A Biomimetic Nanosponge that Absorbs Pore-forming Toxins

4.1.1.1 Introduction

Detoxification treatments offer the potential to cleanse the body of virulence factors that underlie numerous health threats including bacterial infections, venomous injuries, and biological weaponry. Particularly, toxin-targeted anti-virulence therapy is emerging as a compelling strategy against infectious diseases [1, 2]. Existing detoxification platforms such as anti-sera [3], monoclonal antibodies [4], small-molecule inhibitors [5, 6], and molecularly imprinted polymers [7] target toxins' molecular structures and thereby require toxin-specific custom synthesis for different disease treatments. Here we show a biomimetic toxin nanosponge that targets the membrane-disrupting mechanism of pore-forming toxins (PFTs) and functions as a toxin decoy *in vivo*. Consisting of polymeric nanoparticle-supported RBC membranes, these easily fabricated nanosponges readily take in the membrane-damaging toxins and divert them away from their cellular targets. In a mouse model, the nanosponges markedly reduce the toxicity of staphylococcal alpha-hemolysin (α-toxin) and thus improve the survival rate of toxin-challenged mice. This biologically inspired toxin nanosponge presents a new paradigm in detoxification treatments that has the potential to treat a variety of PFT-induced injuries and diseases.

PFTs are one of the most common protein toxins found in nature [8, 9]. These toxins disrupt cells by forming pores in cellular membranes and altering their

permeability. In bacterial infections, the attack by PFTs constitutes a major virulence mechanism [9]. It has been demonstrated that the inhibition of the pore-forming α-toxin can reduce the severity of *Staphylococcus aureus* infections [10], and similar PFT-targeted strategies have shown therapeutic potential against other pathogens including *Escherichia coli* [11], *Listeria monocytogenes* [12], *Bacillus anthracis* [13], and *Streptococcus pneumonia* [14]. Aside from their roles in bacterial pathogenesis, PFTs are commonly employed in venomous attacks by animals including sea anemones, scorpions, and snakes [15]. Over 80 families of PFTs have been identified, displaying diverse molecular structures and distinctive epitopic targets [16]. Despite these differences, the functional similarity among these toxins in perforating cellular membranes provides the design cue for an action mechanism-targeted detoxification platform with a broad applicability.

4.1.1.2 Experimental Methods

4.1.1.2.1 Preparation of Toxin Nanosponges

RBC membrane vesicles were prepared through an extrusion approach using fresh RBCs collected from 6 week-old male ICR mice (Charles River Laboratories). PLGA polymeric cores were prepared using 0.67 dL/g carboxy-terminated 50:50 PLGA polymer (LACTEL Absorbable Polymers) through a solvent displacement process. The nanosponges were then prepared by fusing the RBC membrane vesicles onto the PLGA nanoparticles following a published protocol. The size of the nanosponges was 85 nm as obtained from three dynamic light scattering (DLS)

measurements using a Malvern ZEN 3600 Zetasizer. The morphology of the toxin-bound nanosponges was visualized using transmission electron microscopy (TEM). Briefly, 100 μg of nanosponges was incubated with 3 μg of *Staphylococcus aureus* α-toxin (Sigma Aldrich) for 15 min. A drop of the nanosponge/toxin solution (1 mg/mL) was deposited onto a glow-discharged carbon-coated grid, followed by washing with 10 drops of distilled water and staining with 1% uranyl acetate. The sample was then imaged using an FEI Sphera Microscope at 200kV. For preparing human RBC nanosponges, the RBCs were collected from whole human blood (Bioreclamation).

For lyophilization, nanosponges were prepared in 5% sucrose solution. The samples were subsequently frozen in a -80°C freezer. The frozen samples were then freeze-dried in a benchtop freeze dryer (Laboconco) overnight. Reconstitution of the lyophilized samples was performed by solubilizing the samples in water. Following reconstitution, the nanosponges were characterized for particle size, particle morphology, and neutralization capacity using DLS, TEM, and an RBC hemolysis assay, respectively.

4.1.1.2.2 Preparation of Control Nanoparticles

The PLGA nanoparticles, coated with polyethylene glycol (PEG, M_w=2000), were prepared via a nanoprecipitaton method. The liposomes consisting of 80 wt% of Egg PC (Avanti Polar Lipids) and 20 wt% of DSPE-PEG (2000)-carboxylic acid (Avanti Polar Lipids) were prepared via an extrusion method. The RBC membrane vesicles were prepared following the aforementioned protocol. Measured by DLS, the

hydrodynamic diameters of the resulting PLGA nanoparticles, liposomes, and RBC membrane vesicles were 90, 105, and 120 nm, respectively.

4.1.1.2.3 *In Vitro* Toxin Neutralization and Retention

200 μL of PBS (1X, pH = 7.2) solution containing 1 mg/mL of nanosponges, PLGA nanoparticles, liposomes, RBC membrane vesicles, or 250 μg/mL of sheep anti-α-toxin polyclonal antibodies (abcam) was prepared. 3 μg of α-toxin was then incubated with the respective formulations for 30 min, followed by addition into 1.8 mL of 5% purified mouse RBCs in PBS. After an additional 30 min of incubation, each sample was spun down at 14,000 rpm in a Beckman Coulter Microfuge® 22R Centrifuge for 10 min. The absorbance of hemoglobin in the supernatant was measured at 540 nm using a Tecan Infinite M200 Multiplate Reader to determine the degree of RBC lysis. All experiments were performed in triplicate. For the toxin retention study, the samples containing the nanoformulations and the α-toxin were filtered through a Sepharose® CL-4B size-exclusion column to remove unbound toxin, lyophilized and prepared in SDS sample buffer (Invitrogen), and then separated on a 4-12% Bis-Tris 10-well minigel in MOPS running buffer using a Novex® XCell SureLock Electrophoresis System (Invitrogen). The samples were run at 200 V for 50 min, and the polyacrylamide gel was then stained in SimplyBlue (Invitrogen) overnight for visualization. To quantify the retention of α-toxin, the band intensity at 34 kDa was analyzed by ImageJ and compared to a standard curve consisting of 0.3, 1, 3, and 9 μg of pure α-toxin.

4.1.1.2.4 *In Vitro* Toxin Absorption Study

200 μL of 1 mg/mL nanosponges in PBS was incubated with different amounts of α-toxin, streptolysin-O, and melittin for 30 min followed by incubation with 1.8 mL of 5% purified mouse RBCs for 30 min. Each sample was then spun down at 14,000 rpm for 10 min. The absorbance of the hemoglobin in the supernatant was measured at 540 nm to determine the degree of RBC lysis. As controls, solutions containing the same concentrations of the respective toxins without the nanosponges were tested in parallel. All experiments were performed in triplicate.

4.1.1.2.5 Cellular Uptake of Nanosponges

10 μg of DMPE-rhodamine B (Avanti Polar Lipids) was incorporated into RBC ghosts collected from 1 mL of whole blood prior to preparing RBC membrane vesicles and the nanosponges. For the fluorescence imaging studies, the fluorescent nanosponges and RBC membrane vesicles were incubated with human umbilical vein endothelial cells (HUVEC) (ATCC #CRL-1730) at a concentration of 300 μg/mL in Medium 199 (Gibco) for 1 hr. The media was then aspirated and the cells were incubated in fresh media for additional 1 hr. Following the second incubation period, the cells were washed with PBS, fixed with 10% formalin (Millipore), mounted with DAPI-containing Vectashield® (Invitrogen), and imaged using a 60X oil immersion objective on an Applied Precision DeltaVision Deconvolution Scanning Fluorescence Microscope.

4.1.1.2.6 Cellular Cytotoxicity of Sequestered Toxins

Human umbilical vein endothelial cells (HUVECs) were seeded in a 96-well plate in Medium 199 at a density of $2x10^4$ cells per well. To prepare the samples, nanosponges of different concentrations were incubated with varied amounts of α-toxin, streptolysin-O, and melittin for 30 min. The samples were then added to the cells for 24 hr, following which the cells were washed and incubated in fresh media for 48 hr. Cell viability was then assayed using an MTT kit (Invitrogen) following the manufacturer's instruction. In the conjoint mixture study, corresponding amounts of nanosponges were first added to HUVECs and α-toxin was subsequently added to the cultures, followed by a cell viability test (n=6).

4.1.1.2.7 *In Vivo* Subcutaneous Toxin Neutralization

12 μg/mL of α-toxin was incubated with 0.67 mg/mL of nanosponges, PEG-PLGA nanoparticles, or RBC membrane vesicles in PBS for 15 min. A volume of 150 μL of the mixture was then injected subcutaneously into the flank region of 6 week-old female nu/nu nude mice (Charles River Laboratories). At day 3 after the injections the mice were imaged. Skin and muscles samples were cut at 5 μm and stained with hematoxylin and eosin (H&E) for histological analyses. On-site neutralization of α-toxin by the nanosponges was conducted by subcutaneously injecting 50 μL of 36 μg/mL of α-toxin solution, which was immediately followed by a 100 μL injection of 2 mg/mL nanosponges. The mice were imaged 3 days later for visualization of skin lesion formation.

4.1.1.2.8 *In Vivo* Systemic Toxin Neutralization

Nanosponges, RBC membrane vesicles, and PEG-PLGA nanoparticles at a concentration 20 mg/mL and α-toxin at a concentration of 60 μg/mL were prepared beforehand in deionized water. For the pre-inoculation studies, 6 week-old male ICR mice were injected intravenously through the tail vein with 80 mg/kg (dose per body weight) of the nanoformulation followed by a 75 μg/kg injection of α-toxin 2 min later. For the post-inoculation studies, the mice were injected first with 75 μg/kg of α-toxin followed by 80 mg/kg of the nanoformulation 2 min later. The no treatment group was injected with 75 μg/kg of α-toxin solution only. The sample size for each group was 9 mice. The statistic *p* values were obtained using the log-rank test.

4.1.1.2.9 Biodistribution of Nanosponge/α-Toxin Complex

200 μg of nanosponges containing 0.05% (w/w) DiD probe (Invitrogen) in the polymeric cores was prepared and incubated with 3 μg of α-toxin. The mixture was subsequently filtered in a Sepharose® CL-4B column to purify out the unbound toxin. For the biodistribution study, 6 week-old male ICR mice were sacrificed 24 hr after intravenous injection of the fluorescent nanosponge/toxin complex via the tail vein. The liver, spleen, kidneys, lung, heart and blood were collected and homogenized. The fluorescence of the homogenate at 670 nm with an excitation wavelength of 630 nm was read using a Tecan Infinite M200 Multiplate Reader. The resulting signal was then multiplied by the corresponding organ weight to obtain the total organ fluorescence and the relative distribution of the nanosponge/toxin complex in each organ was calculated (n = 6). For the hepatotoxicity study, one group of mice was

sacrificed on day 3 following the injection of the toxin-bound nanosponges and another group was sacrificed on day 7. The livers were collected, sectioned, and stained with H&E for histological analyses.

4.1.1.3 Results and Discussion

In this study, a toxin nanosponge is constructed with a polymeric core wrapped in natural RBC bilayer membranes (Figure 4.1A). The RBC membrane shell provides an ideal mimicry to absorb a wide range of PFTs regardless of their molecular

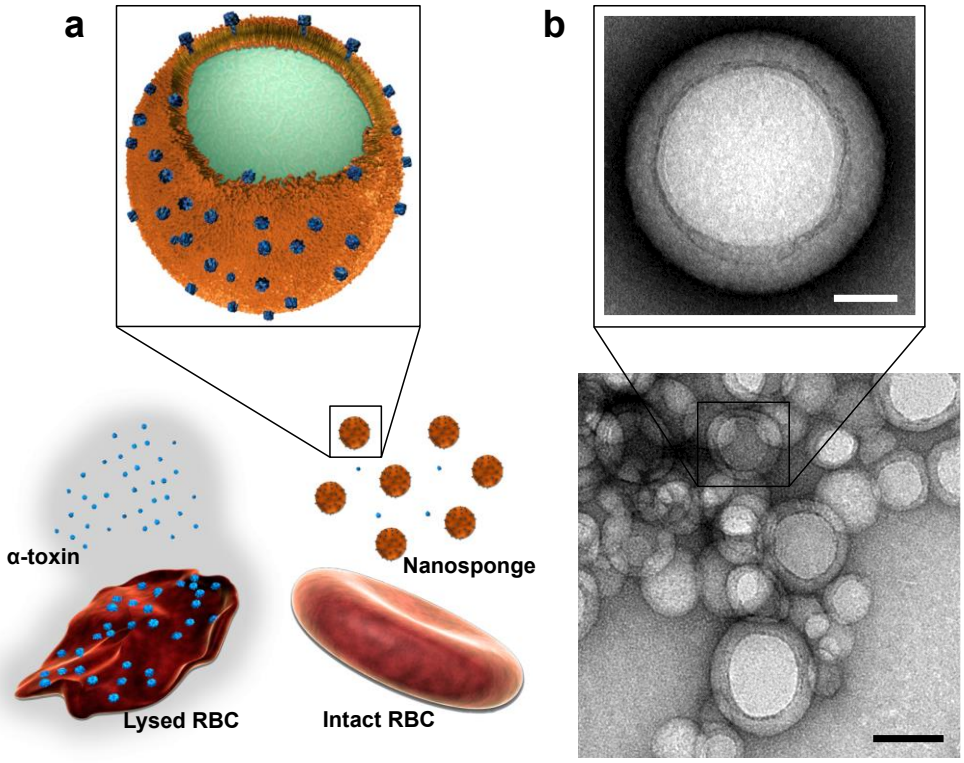

Figure 4.1 Nanosponge schematic and actual structures. (A) Schematic structure of toxin nanosponges and their mechanism of neutralizing pore-forming toxins (PFTs). The nanosponges consist of substrate-supported RBC bilayer membranes into which PFTs can incorporate. After being absorbed and arrested by the nanosponges, the PFTs are diverted away from their cellular targets, thereby avoiding target cells and preventing toxin-mediated hemolysis. (B) TEM visualization of nanosponges mixed with α-toxin (scale bar = 80 nm) and the zoomed-in view of a single toxin-absorbed nanosponge (scale bar = 20 nm). The nanosponge is comprised of a PLGA polymeric core and an RBC membrane shell. The sample was negatively stained with uranyl acetate prior to TEM imaging.

structures. Meanwhile, the inner polymeric core stabilizes the RBC membrane shell to enable prolonged systemic circulation essential for absorbing toxins in the bloodstream. The nanosponges were prepared by fusing RBC membrane vesicles onto poly(lactic-*co*-glycolic acid) (PLGA) nanoparticles through an extrusion approach [17]. Under transmission electron microscopy, the resulting nanosponges exhibited a core-shell structure approximately 85 nm in diameter (Figure 4.1B).

To test the nanosponges' ability to neutralize PFTs, α-toxin was mixed with the nanosponges and then added to purified mouse RBCs. Equivalent amounts of PLGA nanoparticles (coated with PEG for stability), liposomes (coated with PEG for stability), and RBC membrane vesicles of comparable particle sizes were tested in parallel as controls. As shown in Figure 4.2A, the nanosponge sample was noticeably different from the other samples, exhibiting a clear supernatant that indicated the RBCs were undamaged. The degree of hemolysis was quantified by measuring the absorbance of the released hemoglobin in the supernatant at 540 nm (Figure 4.2B). A positive control sample containing anti-α-toxin antibodies verified that the observed hemolysis was toxin-specific. The capability of the nanosponges to absorb toxins was further examined by measuring the RBC hemolysis at varying amounts of α-toxin and fixed nanosponge content (Figure 4.2D). Experiments with streptolysin-O (a pore-forming exotoxin produced by *Streptococcus pyogenes* [18]) and melittin (a membrane-disrupting peptide in bee venom [19]) showed similar patterns of reduced RBC hemolysis by the nanosponges, demonstrating the platform's applicability against different types of membrane-targeted toxins.

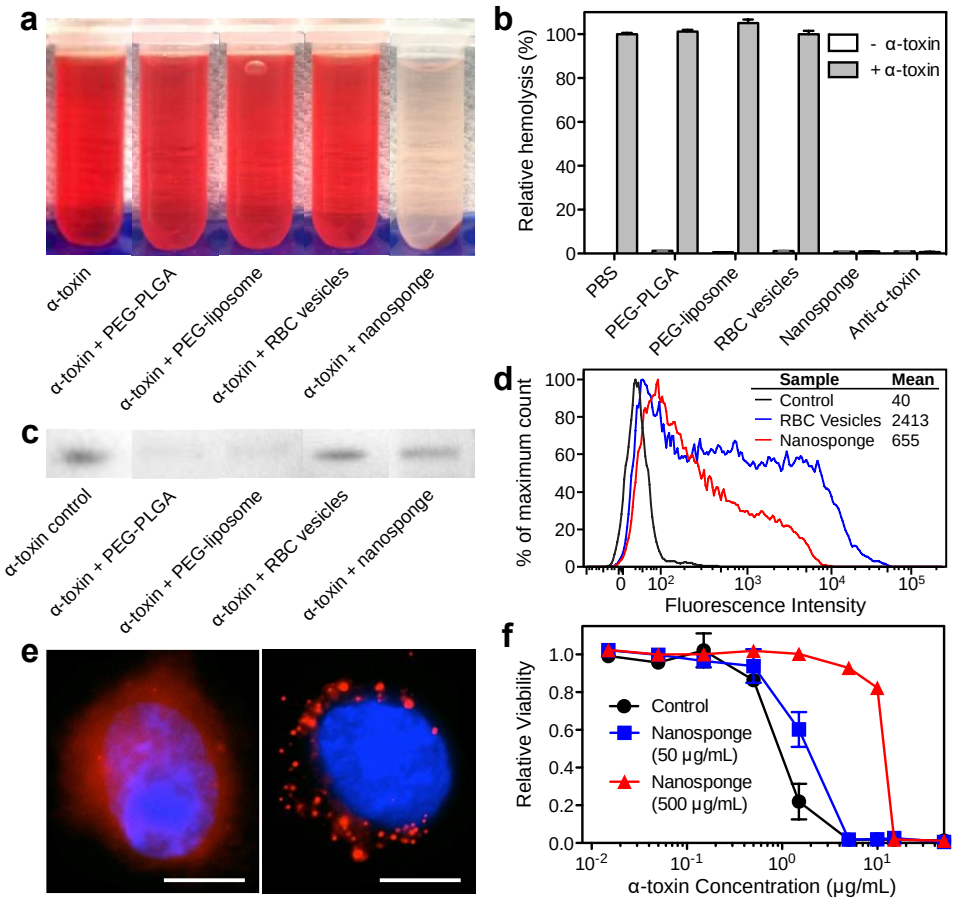

Figure 4.2 *In vitro* characterizations. (A) Centrifuged RBCs after incubation with α-toxin mixed in PBS, PLGA nanoparticle, liposome, RBC membrane vesicle, or nanosponge solution. (B) Quantification of the RBC hemolysis of samples in (A) by measuring the absorbance of the hemoglobin in the supernatant. Anti-α-toxin was used as a positive control. Each sample was examined in the absence of α-toxin to verify that the formulations did not induce hemolysis themselves. (C) SDS-PAGE to examine toxin absorption and retention by the nanoformulations. The same amount of free α-toxin was used as a reference. (D) Hemolytic activity of varying amounts of α-toxin with or without mixing with 200 μg of nanosponges. (E) Cellular uptake of RBC membrane vesicles (left) and toxin nanosponges (right) by cells (scale bar = 5 μm). (F) Dose-dependent neutralization of α-toxin's toxicity against HUVECs by nanosponges.

Next the nanoformulation/α-toxin mixtures were filtered through a column to separate out free-floating, unbound toxin. Given α-toxin's tendency to spontaneously incorporate into erythrocyte membranes [20], the nanosponges and the RBC membrane vesicles were expected to absorb and retain the toxin after being run through the filtration column. Following SDS-PAGE analysis, it was found that the

nanosponges and the RBC membrane vesicles retained 90.2% and 95.3% of the α-toxin respectively (Figure 4.2C). In comparison, the toxin protein band was almost nonexistent in the PLGA nanoparticle and liposome samples, which suggested that their PEG coating precluded protein interactions. The purified α-toxin-bound nanosponges and RBC membrane vesicles were subsequently examined for their hemolytic activities. It was found that the nanosponges showed no hemolytic activity whereas the RBC membrane vesicles went on to lyse the RBCs.

The fact that the RBC membrane vesicles were able to absorb α-toxin but failed to reduce its hemolytic activity highlights the role of the polymeric cores in the nanosponges. A cellular uptake study was conducted to better understand the disparity between their neutralization capabilities. Fluorescence microscopy of the nanoformulations with fluorescently doped membranes portrayed their different fates upon incubation with human umbilical vein endothelial cells (HUVECs) (Figure 4.2E). In the sample with RBC membrane vesicles, broadly distributed fluorescence was cast over the entire cellular area, which can be explained by the fusion of these nanoscale, unstable RBC vesicles with the cellular membranes [21]. In contrast, the nanosponges showed up within the intracellular region as distinct punctates similar to those often seen in the endocytosis of nanoparticles [22]. These findings help to justify the observed hemolysis results; the RBC membrane vesicles with bound α-toxin likely fused with RBCs and thus failed to deter the toxin's hemolytic activity. The nanosponges, however, were able to not only arrest but also lock in the toxins to keep them away from other RBC membranes.

To examine whether the nanosponges can detoxify α-toxin and render it harmless to cellular targets, cellular cytotoxicity was studied using HUVECs. It was shown that α-toxin's toxicity against the cells was significantly reduced upon both pre-mixing with nanosponges (Figure 4.2F) and conjointly mixing with nanosponges. Similar detoxification properties of the nanosponges were observed with other PFT types including streptolysin-O and melittin. The virulence neutralization by the nanosponges was likely due to both toxin diversion from cellular membranes and enhanced endolysosomal digestion of the absorbed toxin protein following the endocytic uptake observed in Figure 4.2E. Based upon these experimental cytotoxicity results and the physicochemical characteristics of the nanosponges and the toxins, it was estimated that each nanosponge was able to neutralize approximately 85 α-toxin, 30 streptolysin-O, or 850 melittin monomers.

The ability of the nanosponges to neutralize α-toxin was further demonstrated *in vivo* by subcutaneous injection of α-toxin or α-toxin/nanosponge mixture beneath the right flank skin of mice. 72 hr after the injection of 150 μL of free α-toxin (12 μg/mL in PBS), severe skin lesions were induced with demonstrable edema and inflammation (Figure 4.3A) and closer examination of the skin tissue showed necrosis, apoptosis, and inflammatory infiltrate of neutrophils with dermal edema (Figure 4.3B). Moreover, the toxin damaged the underlying muscle tissue as evidenced by interfibril edema, tears on muscles fibers, and a significant number of extravasating neutrophils from the surrounding vasculature (Figure 4.3C). However, mixing 100 μg of the nanosponges with the injected amount of α-toxin (toxin-to-nanosponge ratio ≈ 70:1)

appeared to neutralize the toxin, as there was no observable damage on the mice (Figure 4.3D). The tissue samples showed normal epithelial structures in skin histology and intact fibrous structures with no visible infiltrate in the muscle histology (Figure 4.3E,F). In contrast, PEG-PLGA nanoparticles and RBC membrane vesicles failed to prevent the toxin damage in the skin.

Finally, the systemic detoxification efficacy of the nanosponges was

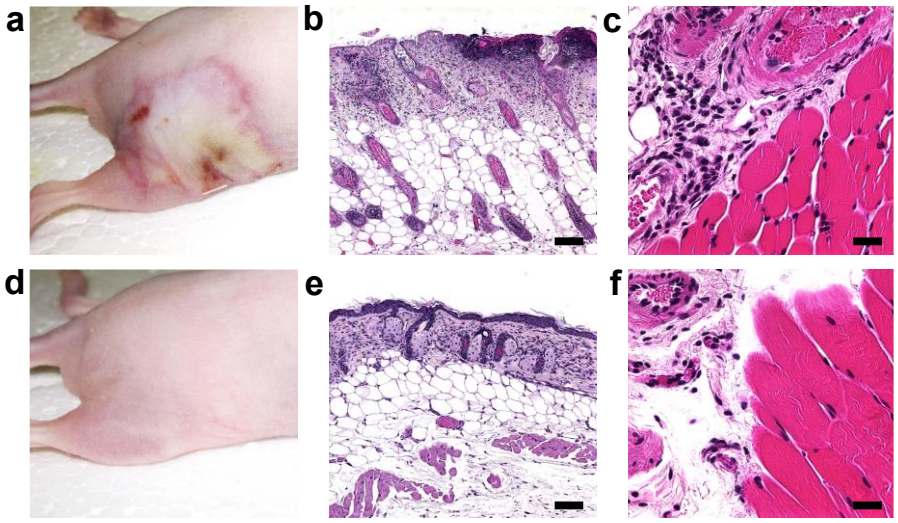

Figure 4.3 *In vivo* toxin neutralization capacities. Mice injected with α-toxin alone: (A) skin lesions occurred 3 days following the injection; (B) histological sectioning with hematoxylin and eosin staining revealed inflammatory infiltrate, apoptosis, necrosis and edema in the epidermis (scale bar = 80 μm); (C) tears on muscle fibers, interfibril edema, and extravasation of neutrophils from surrounding vasculature indicated damage of the muscle (scale bar = 20 μm). Mice injected with α-toxin/nanosponge: Dd) no skin lesion occurred; (E) no abnormality was observed in the epidermis (scale bar = 80 μm); (F) normal muscle fiber structures and the lack of inflammatory signs indicated no muscle damage (scale bar = 20 μm).

investigated. A bolus lethal dose of α-toxin (75 μg/kg), known to induce acute death in mice [23], was injected into mice through a tail vein. In the two experimental settings, 80 mg/kg of the nanosponges was injected either 2 min before or 2 min after the toxin injection. Note that a separate study verified that such a nanosponge dose was well tolerated by mice. Figure 4.4A and 4.4B show that mice without any treatments had a

100% mortality rate within 6 hr following the α-toxin injection. In the group treated with nanosponge pre-inoculation, the mortality rate was reduced markedly to 11% ($p<0.0001$, n=9). In contrast, pre-inoculation with PEG-PLGA nanoparticles and RBC membrane vesicles failed to improve the survival rate of the toxin-challenged mice (Figure 4.4A). In the post-inoculation treatment groups, the nanosponge injection remained beneficial to the overall survival, yielding a 56% mortality rate ($p=0.0091$, n=9), whereas the control formulations showed no survival advantage (Figure 4.4B). It

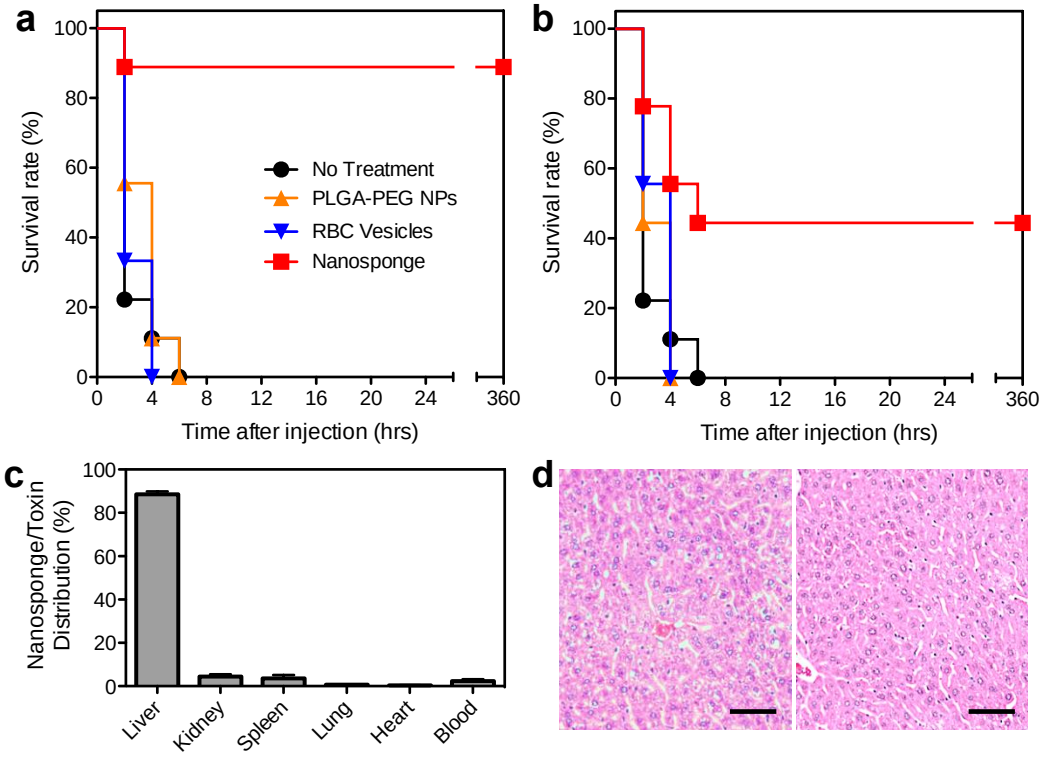

Figure 4.4 *In vivo* detoxification efficacies. Survival rates of mice over a 15-day period following an intravenous injection of 75 μg/kg α-toxin; 80 mg/kg of nanosponges, RBC vesicles, or PEG-PLGA nanoparticles were administered intravenously 2 min either before (A) or after (B) the toxin injection. All injections were performed through the intravenous route via the tail vein (n = 9). (C) Biodistribution of α-toxin-bound nanosponges 24 hr after intravenous injection into mice (n = 6). (D) Liver histology with hematoxylin and eosin staining showing normal hepatocytes with no tissue damage on day 3 (left) and day 7 (right) following the injection of α-toxin-bound nanosponges.

should be noted that in both of the nanosponge treatment groups, no additional death

occurred past the 6 hr mark, suggesting that the absorbed toxin was detoxified rather than merely having its toxicity delayed.

To elucidate the *in vivo* fate of the nanosponge-sequestered toxin, the biodistribution of the toxin-bound nanosponges was studied, which revealed that they accumulated primarily in the liver (Figure 4.4C). Liver biopsies on day 3 and day 7 following the intravenous injection of the toxin-bound nanosponges were performed to investigate the potential effect of the sequestered toxin upon liver accumulation. Examination of the liver sections revealed normal hepatocytes supplied by blood vessels with no inclusion of Kupffer cells in the sinusoids (Figure 4.4D). The lack of liver tissue damage suggests that the sequestered toxin was safely metabolized, likely through ingestion by hepatic macrophages.

4.1.1.4 Conclusions

Through the use of a rationally designed nanostructure, detoxification of α-toxin was achieved in this study. As α-toxin in the circulation can promote blood coagulation, systemic inflammation, and endothelial dysfunction by attacking platelets [24], monocytes [25], and endothelial cells [26], the nanosponges offer the potential to reduce toxin burden and relieve disease symptoms associated with the toxin [27]. The function of these nanosponges as an *in vivo* toxin decoy can be distinguished from the current paradigm of detoxification treatments, where toxin antagonists rely primarily on structure-specific epitopic binding. The nanosponges address a common membrane-disrupting mechanism shared by a broad range of PFT proteins and thus

have the potential to treat a variety of PFT-induced injuries and diseases. Moreover, the platform poses little risk of complication upon administration, as it is comprised entirely of biocompatible and biodegradable materials. The nanosponge platform introduces a unique strategy in injectable nanocarriers for biodetoxification [28], and as PFTs are one of the most common forms of toxin, the nanosponges have tremendous therapeutic implications in clinics.

4.1.1.5 References

1. Clatworthy, A.E., E. Pierson, and D.T. Hung, *Targeting virulence: a new paradigm for antimicrobial therapy.* Nature Chemical Biology, 2007. **3**(9): p. 541-548.

2. Rasko, D.A. and V. Sperandio, *Anti-virulence strategies to combat bacteria-mediated disease.* Nature Reviews Drug Discovery, 2010. **9**(2): p. 117-128.

3. Beghini, D.G., S. Hernandez-Oliveria, L. Rodrigues-Simoni, J.C. Novello, S. Hyslop, and S. Marangoni, *Anti-sera raised in rabbits against crotoxin and phospholipase A2 from Crotalus durissus cascavella venom neutralize the neurotoxicity of the venom and crotoxin.* Toxicon, 2004. **44**(2): p. 141-148.

4. Chen, Z., M. Moayeri, H. Zhao, D. Crown, S.H. Leppla, and R.H. Purcell, *Potent neutralization of anthrax edema toxin by a humanized monoclonal antibody that competes with calmodulin for edema factor binding.* Proceedings of the National Academy of Sciences USA, 2009. **106**(32): p. 13487-13492.

5. McCormick, C.C., A.R. Caballero, C.L. Balzli, A. Tang, and R.J. O'Callaghan, *Chemical inhibition of alpha-toxin, a key corneal virulence factor of Staphylococcus aureus.* Investigative Ophthalmology & Visual Science, 2009. **50**(6): p. 2848-2854.

6. Hung, D.T., E.A. Shakhnovich, E. Pierson, and J.J. Mekalanos, *Small-molecule inhibitor of Vibrio cholerae virulence and intestinal colonization.* Science, 2005. **310**(5748): p. 670-674.

7. Hoshino, Y., H. Koide, K. Furuya, W.W. Haberaecker 3rd, S.H. Lee, T. Kodama, H. Kanazawa, N. Oku, and K.J. Shea, *The rational design of a synthetic polymer nanoparticle that neutralizes a toxic peptide in vivo.*

Proceedings of the National Academy of Sciences USA, 2012. **109**(1): p. 33-38.

8. Gilbert, R.J., *Pore-forming toxins.* Cellular and Molecular Life Sciences, 2002. **59**(5): p. 832-844.

9. Rosado, C.J., S. Kondos, T.E. Bull, M.J. Kuiper, R.H. Law, A.M. Buckle, I. Voskoboinik, P.I. Bird, J.A. Trapani, J.C. Whisstock, and M.A. Dunstone, *The MACPF/CDC family of pore-forming toxins.* Cellular Microbiology, 2008. **10**(9): p. 1765-1774.

10. Shoham, M., *Antivirulence agents against MRSA.* Future Medicinal Chemistry, 2011. **3**(7): p. 775-777.

11. O'Hanley, P., G. Lalonde, and G. Ji, *Alpha-hemolysin contributes to the pathogenicity of piliated digalactoside-binding Escherichia coli in the kidney: efficacy of an alpha-hemolysin vaccine in preventing renal injury in the BALB/c mouse model of pyelonephritis.* Infection and Immunity, 1991. **59**(3): p. 1153-1161.

12. Edelson, B.T. and E.R. Unanue, *Intracellular antibody neutralizes Listeria growth.* Immunity, 2001. **14**(5): p. 503-512.

13. Nakouzi, A., J. Rivera, R.F. Rest, and A. Casadevall, *Passive administration of monoclonal antibodies to anthrolysin O prolong survival in mice lethally infected with Bacillus anthracis.* BMC Microbiology, 2008. **8**: p. 159.

14. Kirkham, L.A., A.R. Kerr, G.R. Douce, G.K. Paterson, D.A. Dilts, D.F. Liu, and T.J. Mitchell, *Construction and immunological characterization of a novel nontoxic protective pneumolysin mutant for use in future pneumococcal vaccines.* Infection and Immunity, 2006. **74**(1): p. 586-593.

15. Andreeva-Kovalevskaya Zh, I., A.S. Solonin, E.V. Sineva, and V.I. Ternovsky, *Pore-forming proteins and adaptation of living organisms to environmental conditions.* Biochemistry (Moscow), 2008. **73**(13): p. 1473-1492.

16. Bayley, H., *Membrane-protein structure: Piercing insights.* Nature, 2009. **459**(7247): p. 651-652.

17. Hu, C.M., L. Zhang, S. Aryal, C. Cheung, R.H. Fang, and L. Zhang, *Erythrocyte membrane-camouflaged polymeric nanoparticles as a biomimetic delivery platform.* Proceedings of the National Academy of Sciences USA, 2011. **108**(27): p. 10980-10985.

18. Bhakdi, S., J. Tranum-Jensen, and A. Sziegoleit, *Mechanism of membrane damage by streptolysin-O.* Infection and Immunity, 1985. **47**(1): p. 52-60.

19. Dempsey, C.E., *The actions of melittin on membranes.* Biochimica et Biophysica Acta, 1990. **1031**(2): p. 143-161.

20. Klainer, A.S., M.A. Madoff, L.Z. Cooper, and L. Weinstein, *Staphylococcal Alpha-Hemolysin: Detection on the Erythrocyte Membrane by Immunofluorescence.* Science, 1964. **145**(3633): p. 714-715.

21. Moorjani, M., A. Lejeune, C. Gicquaud, J. Lacroix, P. Poyet, and R.C. Gaudreault, *Nanoerythrosomes, a new derivative of erythrocyte ghost II: identification of the mechanism of action.* Anticancer Research, 1996. **16**(5A): p. 2831-2836.

22. Gao, W., R. Langer, and O.C. Farokhzad, *Poly(ethylene glycol) with Observable Shedding.* Angew Chem Int Ed, 2010. **49**(37): p. 6567-6571.

23. Gill, D.M., *Bacterial toxins: a table of lethal amounts.* Microbiological Reviews, 1982. **46**(1): p. 86-94.

24. Bhakdi, S., M. Muhly, U. Mannhardt, F. Hugo, K. Klapettek, C. Mueller-Eckhardy, and L. Roka, *Staphylococcal alpha toxin promotes blood coagulation via attack on human platelets.* The Journal of Experimental Medicine, 1988. **168**(2): p. 527-542.

25. Bhakdi, S., M. Muhly, S. Korom, and F. Hugo, *Release of interleukin-1 beta associated with potent cytocidal action of staphylococcal alpha-toxin on human monocytes.* Infection and Immunity, 1989. **57**(11): p. 3512-3519.

26. Powers, M.E., H.K. Kim, Y. Wang, and J. Bubeck Wardenburg, *ADAM10 mediates vascular injury induced by Staphylococcus aureus alpha-hemolysin.* The Journal of Infectious Diseases, 2012. **206**(3): p. 352-356.

27. Adhikari, R.P., A.O. Ajao, M.J. Aman, H. Karauzum, J. Sarwar, A.D. Kydecker, J.K. Johnson, C. Nguyen, W.H. Chen, and M.C. Roghmann, *Lower Antibody Levels to Staphylococcus aureus Exotoxins Are Associated With Sepsis in Hospitalized Adults With Invasive S. aureus Infections.* The Journal of Infectious Diseases, 2012. **206**(6): p. 915-923.

28. Leroux, J.C., *Injectable nanocarriers for biodetoxification.* Nature Nanotechnology, 2007. **2**(11): p. 679-684.

4.1.2 Hydrogel Retaining Nanosponges for Local Treatment of MRSA

4.1.2.1 Introduction

Targeting virulence factors such as bacterial toxins represents an attractive antimicrobial approach with potential advantages of expanding the repertoire of bacterial targets, preserving the host endogenous microbiome, and lowering selective pressure for resistance development [1, 2]. Among various toxins, pore-forming toxins (PFTs) are the most common class of bacterial protein toxins and constitute important bacterial virulence factors [3]. These toxins disrupt cells by forming pores on cellular membranes and altering their permeability for bioactivity [4]. However, the majority of current toxin targeting strategies, such as antisera [5], monoclonal antibodies [6, 7], small-molecule inhibitors [8, 9], and molecularly imprinted polymers [10], relies primarily on structure-specific epitopic binding and custom synthesis is required to match specific toxins. As a result, the enormous diversity of PFTs presents a serious challenge to devise an effective detoxification platform against bacterial infections. To address this challenge, a unique red blood cell (RBC) membrane–coated nanoparticle system has been recently developed by wrapping intact RBC membrane onto polymeric nanoparticles (denoted as “nanosponges”) for broad detoxification applications [11, 12]. The term “nanosponges” is used to describe the unique capability of the RBC membrane–coated nanoparticles for nonspecifically “soaking up” a broad spectrum of PFTs. Different from existing detoxification strategies, the nanosponges target the membrane-disrupting mechanism common to PFTs, thereby

offering an all-purpose toxin decoy strategy to absorb various types of PFTs regardless of their molecular structures [12].

Meanwhile, on the front of nanotechnology development, therapeutic nanoparticles are increasingly combined with other biomaterials to form hybrid nanostructures for improved therapeutic index. Particularly, loading nanoparticles into hydrogels has received much attention [13]. Hydrogels are hydrophilic 3D polymer networks with extensive uses in tissue engineering and drug delivery. With appropriate compositions, hydrogels can not only preserve the structural integrity and the functionalities of the contained nanoparticles but also offer additional engineering flexibility to improve the therapeutic efficacy. For example, biopolymers were linked together by selective adsorption to nanoparticles, forming self-assembled hydrogels with shear-thinning and self-healing properties [14]. Modifying hydrogel composition has also allowed for controllable nanoparticle release and tunable viscoelasticity suitable for topical applications [15, 16]. Hydrogels made from responsive polymer matrices have also been attempted to load nanoparticles for controlled releases triggered by environmental cues such as pH, ionic strength, and temperature [17, 18]. Recently, polymeric nanoparticles were also loaded into liver lobule-mimicking hydrogel for toxin entrapment [19]. Inspired by the numerous advantages of hydrogels in retaining nanoparticles and enhancing their properties, herein, we report on an advanced hybrid nanoformulation that integrates toxin nanosponge with hydrogel for local treatment of bacterial infection. Such nanosponge–hydrogel formulation judiciously integrates two distinct materials into one robust hybrid system with unique

physicochemical and biological properties that either one of the two building blocks cannot achieve independently.

Among various bacterial pathogens, *Staphylococcus aureus* is a prominent Gram-positive bacterium and the leading cause for a vast range of human skin and wound infections [20, 21]. Over the past a few decades, *S. aureus* has experienced several waves of antibiotic resistance and now displays broad resistance to the entire β-lactam class of antibiotics, including penicillins, cephalosporins, and carbapenems [22]. To keep up the pace of antibiotic resistance, new antibiotics including vancomycin, linezolid, tedezolid, daptomycin, ceftaroline, and tigecycline have been developed and introduced in recent years. However, the emergence of resistant *S. aureus* strains, especially toward vancomycin, has significantly increased [23]. Currently, virulent strains of methicillin-resistant *S. aureus* (MRSA) have become increasingly prevalent, imposing a paramount clinical challenge that threatens public health [24-26]. Collectively, these facts underscore the undisputed and urgent need to develop new and effective therapeutic approaches for MRSA treatment. Notably, MRSA infections are commonly localized to skin and soft tissues [27]. In these infections, a critical element of virulence results from a diverse arsenal of PFTs secreted by the bacteria, which attack the host cells [28]. These distinctive features of MRSA infections make the nanosponge–hydrogel hybrid formulation an attractive treatment strategy against such infections (Figure 4.5A). The hydrogel composition can be optimized to effectively retain nanosponges within its matrix without compromising toxin transport for neutralization. In this study, we confirm the *in vitro*

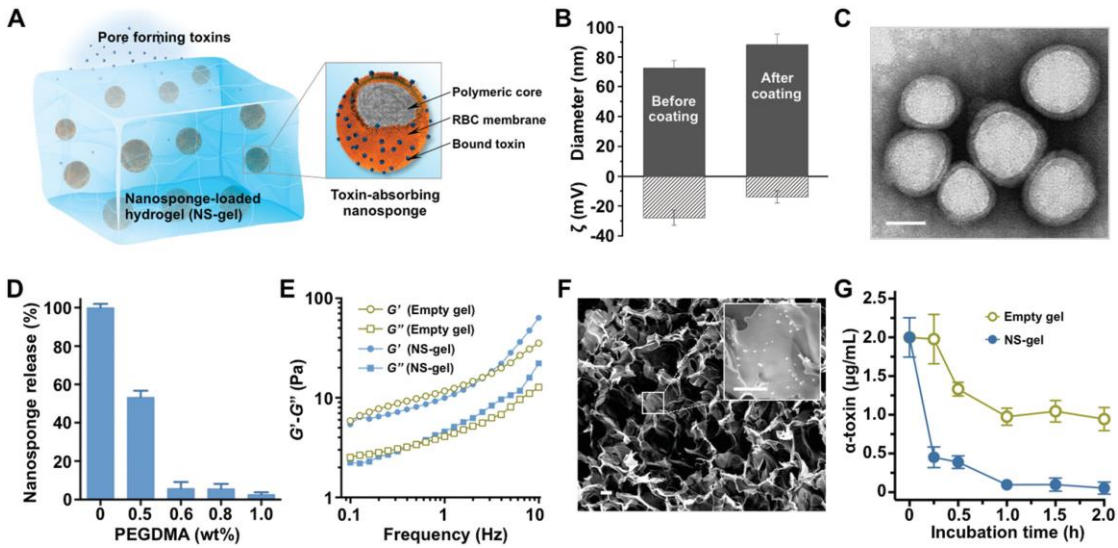

Figure 4.5 Formulation and characterization of nanosponge-loaded hydrogel (NS-gel). (A) Schematic illustration of a hydrogel retaining toxin-absorbing nanosponges for local treatment of methicillin-resistant *Staphylococcus aureus* (MRSA) infection. The toxin nanosponge was constructed with a polymeric core wrapped in natural red blood cell (RBC) bilayer membrane and was subsequently embedded into an acrylamide-based hydrogel. (B) Hydrodynamic size (diameter, nm) and surface zeta potential (ζ , mV) of PLGA polymeric cores before and after RBC membrane coating measured by dynamic light scattering (DLS). (C) A representative transmission electron microscopy (TEM) image showing the spherical core–shell structure of the nanosponges under negative staining with uranyl acetate. The scale bar represents 50 nm. (D) Release of the toxin nanosponge from hydrogels made with different crosslinker concentrations. Error bars represent the standard deviations (n = 3). (E) Rheological characterization of the hydrogel (0.6 wt% crosslinker) either without nanosponges (open markers) or loaded with 2 mg mL^{-1} nanosponges (solid markers). The storage modulus G' and loss modulus G'' were plotted logarithmically against frequency (0.1–10 Hz at 37°C). (F) A representative scanning electron microscopy (SEM) image of the NS-gel. The scale bar represents 1 μm. (G) Absorption of α-toxin was studied by incubating 1 mL α-toxin solution (2 μg mL^{-1} in PBS) with 1 mL NS-gel or empty gel. The concentrations of α-toxin in the supernatant at different incubation times were quantified using ELISA. Error bars represent standard deviations (n = 3).

and *in vivo* toxin neutralization capabilities of the nanosponge–hydrogel formulation. When injected *in situ*, the hydrogel can effectively retain nanosponges at the injection sites, a property favoring toxin absorption. In a subcutaneous MRSA mouse model, the hybrid formulation shows significant antivirulence therapeutic efficacy, evidenced by the markedly reduced MRSA skin lesion development. Overall, we demonstrate the potential of the nanosponge-loaded hydrogel (denoted as "NS-gel") as a new and effective detoxification strategy for the treatment of localized MRSA infection.

4.1.2.2 Experimental Methods

4.1.2.2.1 Preparation of Nanosponges

The nanosponge was prepared following previously described methods [11, 12]. Briefly, PLGA polymeric nanoparticles with a diameter of about 70 nm were prepared with 0.67 dL g^{-1} of carboxy-terminated 50:50 PLGA polymer (LACTEL Absorbable Polymers) through a nanoprecipitation process. Specifically, the PLGA polymer was first dissolved in acetone at a concentration of 10 mg mL^{-1}. Then 1 mL of the solution was added to 3 mL of deionized water. The mixture was then stirred in open air for 1 h and placed in vacuum for another 3 h. The resulting nanoparticle solution was filtered using an Amicon Ultra-4 centrifugal filter with a molecular weight cutoff of 10 kDa (Millipore). To prepare fluorescently labeled nanosponges, 0.1 wt% DiD (excitation/emission = 644/665 nm; Life Technologies) was added to the polymers prior to PLGA nanoparticle synthesis. RBC membrane coating was then completed by fusing RBC membrane–derived vesicles with PLGA nanoparticles via sonication using an FS30D bath sonicator at a frequency of 42 kHz and a power of 100 W for 2 min. Dynamic light scattering (DLS) measurements on the resulting nanosponges (Malvern ZEN 3600 Zetasizer) showed an average hydrodynamic diameter of about 73 and 88 nm before and after the membrane coating process, respectively. The core–shell structure of the nanosponge was confirmed by using TEM (FEI 200 kV Sphera microscope).

4.1.2.2.2 Preparation of NS-Gel:

Acrylamide (used as the monomer), PEGDMA (used as the crosslinker), TEMED, and ammonium persulfate (both used as initiators) were purchased from Sigma-Aldrich. For empty hydrogel, the final concentrations of acrylamide, ammonium persulfate, and TEMED were kept constant at 40 mg mL^{-1}, 1 mg mL^{-1}, and 1 μL mL^{-1}, respectively, while PEGDMA concentration was tested in the range of 0%–1% w/w. The liquid mixture was vortexed for 1 min and then placed in a vacuum chamber at room temperature for 2 h to allow complete gelation to occur. For NS-gel, nanosponges with a final concentration of 2 mg mL^{-1} were mixed in the aforementioned chemicals followed by gelation.

To measure the nanosponge release rate from the hydrogel, DiD dye–labeled nanosponges were used to prepare NS-gels at different PEGDMA concentrations. Then 0.5 mL NS-gel was submerged into 50 mL PBS. The mixture was incubated at 37 °C for 24 h and the DiD signal from the supernatant was measured. The rheological analysis was carried out at 37°C on a strain-controlled AR-G2 rheometer with 22 mm diameter parallel-plate geometry (TA Instruments Inc., New Castle, DE). Oscillatory rheological measurements were performed in the linear viscoelastic regime. The strain was kept at 0.1% and a dynamic frequency sweep from 0.1 to 10 rad s^{-1} was conducted to measure the storage modulus G' and loss modulus G''. To study hydrogel morphology, NS-gel was lyophilized and the flakes of the gel were placed on a silicon wafer. The samples were coated with iridium and then examined with SEM. Absorption of α-toxin by NS-gel was examined by incubating 2 mL α-toxin (2 μg mL^{-1}) with 0.5 mL NS-gel at 37°C for 24 h. Empty hydrogel was used as a control

group. At 4, 8, and 24 h time points, α-toxin concentration in the supernatants was quantified with ELISA (R&D Systems, Inc., Minneapolis, MN).

4.1.2.2.3 *In Vitro* α-Toxin Neutralization

To evaluate α-toxin neutralization by NS-gel in vitro, a hemolytic assay was conducted. Briefly, 3 μL of α-toxin solution (1 mg mL^{-1}) was mixed with 0.5 mL NS-gel, empty hydrogel, and PBS, respectively. Then 1 mL of 5% purified mouse RBCs was added to the top of each sample, followed by incubation at 37 °C for 1 h. Then the samples were carefully centrifuged. The extent of RBC lysis was quantified by measuring the absorption of the supernatants at 540 nm. To neutralize toxins in bacterial supernatant, MRSA culture (from an overnight culture of 1×10^9 CFU mL^{-1} of MRSA252) was used to dissolve the chemicals for the hydrogel preparation. All experiments were performed in triplicate.

4.1.2.2.4 Live Whole-Body Imaging of Mice

Prior to the study, the backs of the mice (six week old male ICR mice from Charles River Laboratories, $n = 3$) were carefully shaved. Then 50 μL DiD-labeled NS-gel was injected subcutaneously to the left flanks of the mice. As a control, nanosponges suspended in PBS (2 mg mL^{-1}, 50 μL) were injected subcutaneously to the right flanks the same mice. At the designated time points (0, 6, 24, and 48 h), mice were anesthetized with isoflurane and imaged with a Xenogen IVIS 200 system. Fluorescence intensities were quantified and normalized across the time points. Heat maps were overlaid on bright field images. All animal experiments followed protocols

that were reviewed, approved and performed under the regulatory supervision of the University of California, San Diego's institutional biosafety program and the Institutional Animal Care and Use Committee (IACUC).

4.1.2.2.5 *In Vivo* α-Toxin Neutralization

Neutralization of α-toxin by the NS-gel was conducted by subcutaneously injecting 50 μL of 40 μg mL^{-1} of α-toxin solution into the flank region of 6 week old male ICR mice (Charles River Laboratories, $n = 3$), immediately followed by injecting 100 μL empty gel or NS-gel into the same region. After 72 h the mice were imaged. Then the mice were sacrificed and the skin and muscle samples were removed. The tissues were frozen, cut, and then stained with hematoxylin and eosin (H&E) for histological analysis.

4.1.2.2.6 *In Vivo* Detoxification Efficacy against Localized MRSA Infection

To evaluate *in vivo* detoxification efficacy of the NS-gel against MRSA infection, an MRSA subcutaneous infection mouse model was used. Briefly, prior to the study, the backs of 18 ICR mice (6 week old male, Charles River Laboratories) were carefully shaved. Then 1×10^9 CFU of MRSA 252 suspended in 50 μL PBS were injected subcutaneously into the flank region. Then the mice were randomly divided into two groups ($n = 9$). For the treatment group, 0.2 mL NS-gel was injected into the infection region. For the control group, the empty gel instead of NS-gel was injected. The lesion of each mouse was carefully monitored. The lesion was

photographed and the lesion size was measured from the photography by using Image J.

4.1.2.3 Results and Discussion

The preparation of NS-gel was divided into two steps. In the first step, we prepared nanosponges by mechanically extruding purified mouse RBC membrane with poly(lactic-*co*-glycolic acid)(PLGA) polymeric cores. Following membrane fusion, the diameter of the nanoparticles increased from 72.7±0.2 to 88.4±0.3 nm, corresponding to the addition of a bilayered RBC membrane onto the polymeric cores. Meanwhile, the surface zeta potential changed from −27.7±1.1 to −13.9±0.9 mV, which was likely due to charge screening by RBC membranes (Figure 4.5B). The samples were then stained with uranyl acetate and visualized by transmission electron microscopy (TEM). Figure 4.5C shows that all nanosponges had a spherical core-shell structure, in which the PLGA core was wrapped by a thin shell. Collectively, these results confirmed the successful coating of RBC membranes onto the PLGA cores [11, 29]. In the second step, we mixed preformed nanosponges with acrylamide as the monomer and poly(ethylene glycol) dimethacrylate (PEGDMA) as the crosslinker. Hydrogelation was initiated by adding ammonium persulfate and tetramethylethylenediamine (TEMED), and allowed to proceed for 12 h at room temperature [16].

The hydrogel composition was optimized for effective nanosponge retention while maintaining a low viscosity suitable for injection. To this end, we first labeled

the nanosponges with 1,1′-dioctadecyl-3,3,3′,3′-tetramethylindodicarbocyanine, 4-chlorobenzenesulfonate salt (DiD) (excitation/emission = 644 nm/655 nm), a hydrophobic fluorophore with negligible leakage from PLGA polymer matrix [11, 30]. Then we fixed the concentrations of nanosponges, acrylamide, ammonium persulfate, and TEMED as 2 mg mL^{-1} (PLGA content), 40 mg mL^{-1}, 1 mg mL^{-1}, and 1 μL mL^{-1}, respectively, but varied PEGDMA concentrations and accordingly examined the nanosponge release from the corresponding hydrogels. As shown in Figure 4.1.2.1D, the accumulated release of nanosponge over 24 h decreased abruptly from ≈53% at 0.5 (w/v)% crosslinker concentration to no more than 5% at 0.6 (w/v)%, suggesting that the latter PEGDMA concentration was adequate in forming a hydrogel for effectively retaining nanosponges. This crosslinker concentration was used to prepare NS-gel for the following studies.

The NS-gel was further characterized with dynamic rheological measurements of the storage modulus (*G ′*) and the loss modulus (*G ″*) as a function of frequency (Figure 4.5E). In the study, *G ′* exceeded *G ″* over the entire frequency range, a clear viscoelastic behavior indicating the formation of a hydrogel network [16. We observed slightly higher values of *G′* and *G″* at high frequencies for the NS-gel formulation as compared to those of the empty hydrogel (without nanosponges), likely due to adhesive interactions between the nanosponges and the acrylamide polymer matrix [15, 31]. Nevertheless, *G ′* and *G ″* values measured from NS-gel were generally close to those measured from the empty hydrogel, suggesting a minor effect of the loaded nanosponges on the gel's rheological characteristics. We then freeze-dried the NS-gel

and observed its structure under scanning electron microscope (SEM). The sample showed characteristic porous sponge-like structures with some irregular lamellar features (Figure 4.5F). At a higher magnification, nanosponge particles with a diameter of ≈90 nm embedded within the hydrogel were also observed (Figure 4.5F, inset).

We then compared the ability of the NS-gel in absorbing α-toxin to that of the empty gel. When α-toxin solution was added to the empty gel of an equal volume, a gradual decrease of toxin concentration was observed within the first 1 h of incubation until it reached ≈50% of the original concentration (Figure 4.5G). No further decrease of the toxin concentration was observed with prolonged incubation time, suggesting a slow diffusion process of α-toxin into the hydrogel network until equilibrium was reached. In contrast, when α-toxin solution was incubated with the NS-gel, a sharp decrease of toxin concentration was observed within the first 30 min of incubation. After 1 h, no more than 5% of the initial toxin was left in the solution. Such significantly increased ability of the NS-gel in absorbing α-toxin suggests its potential for detoxification applications.

To test the ability of the NS-gel to neutralize PFTs, we used a hemolytic assay where α-toxin was mixed with the NS-gel and then added to purified mouse RBCs [12]. PBS and the empty gel were tested in parallel as controls. As shown in Figure 4.6A, NS-gel sample showed a clear supernatant, suggesting the RBCs were undamaged. In contrast, noticeable differences were observed with other samples, which showed significant RBC lysis. The degree of hemolysis was quantified by

measuring the absorbance of the released hemoglobin in the supernatant at 540 nm (Figure 4.6B). The capability of the NS-gel to absorb toxins secreted by MRSA bacteria was further examined by mixing the NS-gel with MRSA culture medium known to contain multiple virulent PFTs [32, 33]. As shown in Figure 4.6C,D, a similar reduction of RBC hemolysis by the NS-gel was observed as compared to the control groups, demonstrating the NS-gel's applicability in neutralizing multiple types of RBC membrane-targeted PFTs secreted by the bacteria.

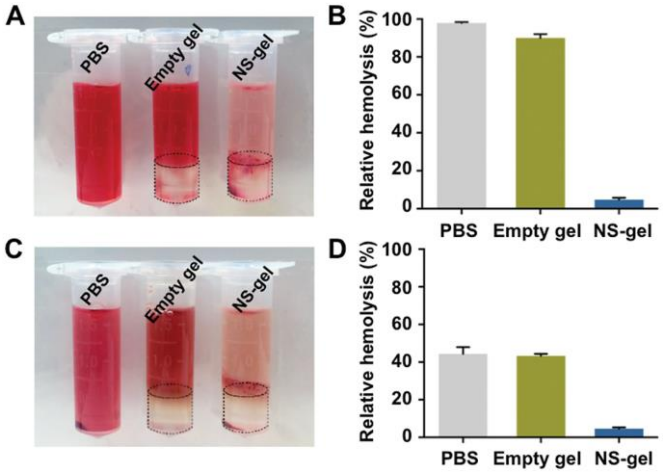

Figure 4.6 *In vitro* toxin neutralization. (A) Centrifuged RBCs after incubation with α-toxin mixed in PBS, empty gel, and NS-gel, respectively. (B) Hemolysis quantification of the samples in (A). (C) Centrifuged RBCs after incubation with MRSA-culturing medium mixed with PBS, empty gel, and NS-gel, respectively. (D) Hemolysis quantification of the samples in (D). Error bars represent standard deviations (n = 3).

Next, we evaluated the retention of the nanosponges by the hydrogel upon in vivo administration. In the study, we formulated the NS-gel with DiD-labeled nanosponges and injected the NS-gel subcutaneously to the left flank of the mice. As a control, the same amount of nanosponges suspended in PBS was injected to the right flank of the same mice. For both groups, the whole body imaging revealed the confinement of fluorescence at the injection sites within 48 h (Figure 4.7A). However,

a more rapid decay of fluorescence intensity was observed at the site injected with nanosponges suspended in PBS, indicating a faster loss of nanoparticles through diffusion to surrounding tissues. Quantification of the fluorescence intensity showed that nearly 80% of the free nanosponges diffused away from the injection site within 2 h. In contrast, the NS-gel had negligible loss of the nanosponge payloads within the initial 2 h and only lost ≈20% of the total nanosponge during the 48 h testing period (Figure 4.7B). This study, together with the previous *in vitro* nanosponge release results (Figure 4.5D), clearly demonstrated the prolonged retention of the nanosponges conferred by the hydrogel formulation. These results further indicate that the NS-gel could be a competent formulation for the treatment of local bacterial infection, in which the pathogens reside on a localized area of a tissue.

The ability of the NS-gel to neutralize α-toxin was further examined in vivo by subcutaneous injection of α-toxin (50 μL at a concentration of 40 μg mL^{-1} in PBS) immediately followed by injecting empty gel or NS-gel (100 μL), respectively, beneath the right flank skin of mice. For the mice treated with empty gel, 72 h after the injection obvious skin lesions were induced with demonstrable edema and inflammation (Figure 4.8A). Closer examination of the skin tissue showed typical indications of toxin-induced damages, including necrosis, apoptosis, and inflammatory infiltrate of neutrophils with dermal edema (Figure 4.8B) [12, 34]. Moreover, the toxin damaged the underlying muscle tissue, as indicated by interfibril edema, tears on muscles fibers, and a significant number of extravasating neutrophils from the surrounding vasculature (Figure 4.8C) [12]. However, mice treated with NS-gel

showed no observable damage on the skin (Figure 4.8D). The tissue samples showed normal epithelial structures in skin histology (Figure 4.8E) and intact fibrous structures with no visible infiltrate in muscle histology (Figure 4.8F).

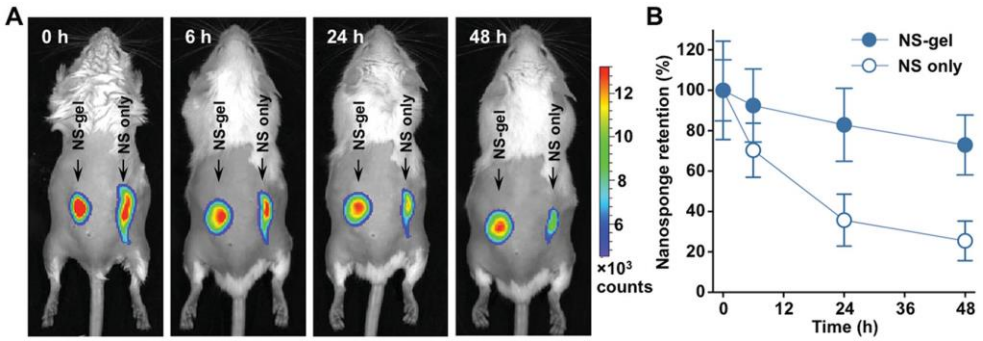

Figure 4.7 *In vivo* nanosponge retention by hydrogel. Nanosponges labeled with DiD fluorescent dye was used to formulate NS-gel, which was then injected subcutaneously under the loose skin over the left flank of the mice. Free suspended nanosponges (without hydrogel) were injected as a control group at the right flank of the same mice. (A) Fluorescence images taken at different time points show the retention of the nanosponges under mouse skin. (B) Quantification of the fluorescence intensity as observed in (A). All images are representative of three mice per group and the error bars represent the standard deviation (n = 3).

Finally, we proceeded to examine the *in vivo* anti-MRSA efficacy of the NS-gel. To establish a subcutaneous MRSA infection model, we injected 1×10^9 CFU MRSA bacteria under the flank skin of each ICR mouse [34]. The infected mice were randomly divided into two groups (n = 9) and then injected at the infection sites with the NS-gel and empty gel, respectively. Herein, to evaluate therapeutic efficacy, we chose to compare the size of MRSA-induced skin lesion observable on the superficial layer of the epidermis, a common index reflecting the severity of the infection [34-36]. After 24 h, mice in both groups developed visible skin lesions but the size difference was nonsignificant (Figure 4.9). At 48 h, the lesion sizes increased in both groups; however, the mice treated with the NS-gel showed a significantly smaller skin lesion when compared to those treated with the empty gel. At 72 and 96 h, the lesion sizes

continued to increase in both groups as the infection continued to progress. The lesion size of the NS-gel treated group remained significantly smaller than that of the group treated with the empty gel. As toxin neutralization by the nanosponges is dependent on both the dosage and dosing frequency, which need to be further optimized in order to completely eradicate MRSA-induced skin lesion. Nevertheless, a superior efficacy observed with the NS-gel demonstrates its potential as an effective local treatment regimen against MRSA infection.

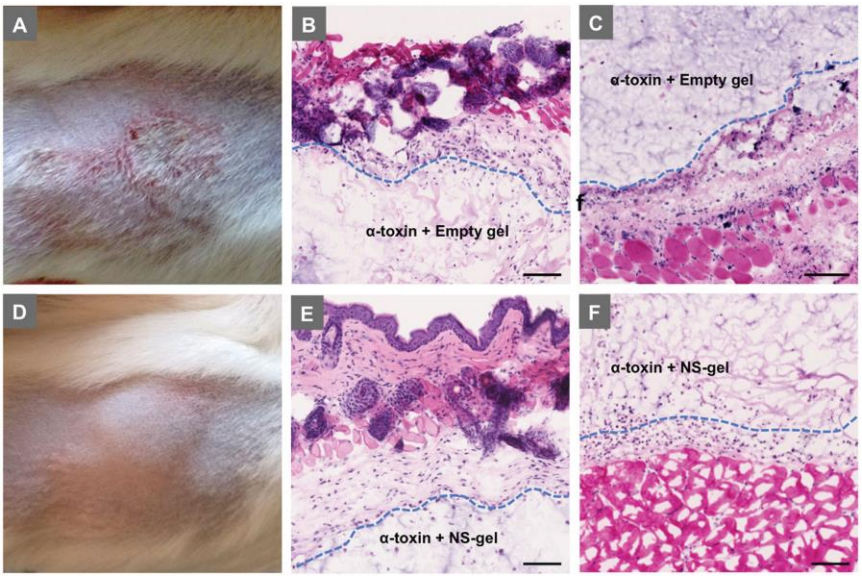

Figure 4.8 *In vivo* toxin neutralization. (A-C) Mice injected with α-toxin followed by empty gel. Dashed lines depict tissue-hydrogel boundary. (A) Skin lesions occurred 72 h following toxin injection. (B) Hematoxylin and eosin (H&E) stained histological sections revealed inflammatory infiltrate, apoptosis, necrosis, and edema in the epidermis. (C) Tears on muscle fibers, interfibril edema, and extravasation of neutrophils from surrounding vasculature indicate muscular damage. (D–F) Mice injected with α-toxin followed by NS-gel. D) No skin lesion occurred. E) No abnormality was observed in the epidermis. (F) Normal muscle structure was observed. Scale bar = 50 μm, n = 6 for each group.

Previously, we reported that RBC membrane–coated nanoparticles (i.e., nanosponges) were effective in neutralizing PFTs including α-toxin, streptolysin-O, and melittin [12]. The current study took this platform one important step further by directly demonstrating its effectiveness in treating MRSA infection in a mouse model.

This advancement is enabled by the combined advantages of the nanosponges and the hydrogel: while the nanosponges absorbing and diverting PFTs away from the cellular targets, the hydrogel retained nanosponges at the infection sites, promoting localized toxin neutralization for better therapeutic efficacy. The observed antivirulence efficacy reflects the synergy of such combination. With improved versatility and functionality, such advanced hybrid materials are expected to offer a practical and reliable formulation that facilitates downstream preclinical and clinical tests.

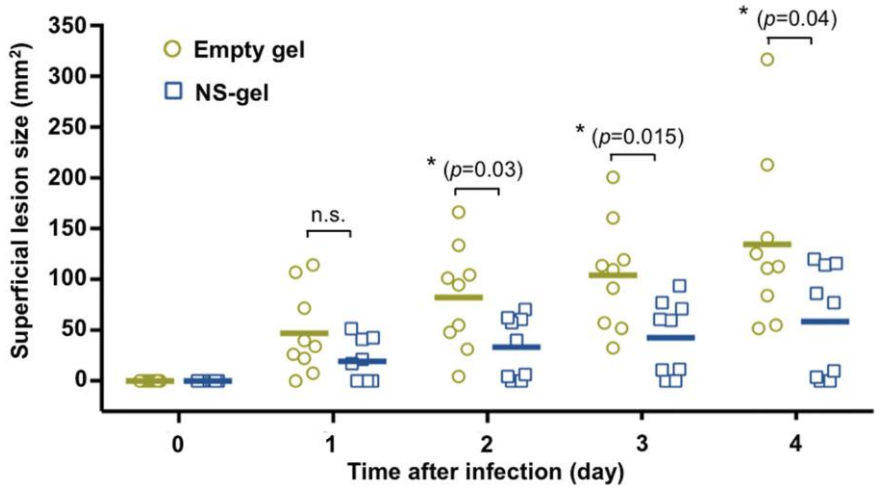

Figure 4.9 *In vivo* treatment of MRSA infection. 1×10^9 CFU of MRSA 252 was mixed with 0.2 mL of 2 mg mL^{-1} NS-gel or empty gels, followed by subcutaneous injection under the loose skin on the backs of the mice (n = 9 per group). Skin lesions were monitored and photographed on day 1–4 after the injections and the lesion sizes were measured. Bars represent median values. * $P < 0.05$, n.s.: not significant.

The rapid technological developments in nanotechnology and biomaterials provide a promising potential for engineering advanced materials through hybridization [37, 38]. On one hand, nanoparticle platforms are gaining an increasing attention for broad-spectrum toxin neutralization [39, 40]. For example, we have recently extended the nanosponges to neutralize other chemical and biological molecules that target RBCs such as pathological antibodies driving prevalent

autoimmune diseases [30]. Meanwhile, cell membrane coating technology has also been increasingly explored to functionalize various types of nanoparticles, including those made from gold [41, 42], silica [43], and gelatin [44], opening unprecedented capability to harness natural functionalities for innovative therapeutics. On the other hand, the technological advance has also led to the development of hydrogels featuring highly interactive, integrative, and biocompatible characteristics for increasingly advanced drug delivery and tissue engineering applications [37, 45-47]. Integrating hydrogel with nanosponges, or cell membrane–coated nanoparticles in general, is anticipated to result in advanced materials that harness the advantages of each building material. We believe that this design strategy will open unique opportunities for a wide range of therapeutic applications.

4.1.2.4 Conclusions

In summary, we have developed an advanced hybrid material that integrates a unique toxin-absorbing nanosponge with hydrogel for antivirulence treatment of local bacterial infection. The nanosponges were made by wrapping intact RBC membrane onto polymeric nanoparticles made from PLGA, followed by loading into hydrogels. The hydrogel composition was optimized to effectively retain nanosponges within its matrix without compromising toxin transport for neutralization. Following subcutaneous injection to mice, nanosponges were effectively retained at the injection sites. In an MRSA subcutaneous mouse model, we have demonstrated for the first time that mice treated with the nanosponge–hydrogel hybrid show markedly reduced

MRSA skin lesion development. These results collectively indicate that the nanosponge–hydrogel hybrid formulation represents a new and effective detoxification strategy for the treatment of localized bacterial infection. Given the critical roles played by pore-forming toxins in pathogenesis of a wide range of bacteria, we expect the nanosponge-hydrogel formulation to be capable for treatment of infectious diseases caused by various types of bacteria. More importantly, no antibiotics are involved in this new treatment, which is therefore unlikely to be affected by the existing bacterial antibiotic resistance mechanisms and will not exert selective pressure to bacteria for developing new resistance.

4.1.2.5 References

1. Clatworthy, A.E., E. Pierson, and D.T. Hung, *Targeting virulence: a new paradigm for antimicrobial therapy*. Nature Chemical Biology, 2007. **3**(9): p. 541-548.

2. Rasko, D.A. and V. Sperandio, *Anti-virulence strategies to combat bacteria-mediated disease*. Nature Reviews Drug Discovery, 2010. **9**(2): p. 117-128.

3. Los, F.C., T.M. Randis, R.V. Aroian, and A.J. Ratner, *Role of pore-forming toxins in bacterial infectious diseases*. Microbiology and Molecular Biology Reviews, 2013. **77**(2): p. 173-207.

4. Gilbert, R.J., *Pore-forming toxins*. Cellular and Molecular Life Sciences, 2002. **59**(5): p. 832-844.

5. Beghini, D.G,. S. Hernandez-Oliveira, L. Rodrigues-Simioni, J.C. Novello, S. Hyslop, and S. Marangoni, *Anti-sera raised in rabbits against crotoxin and phospholipase A2 from Crotalus durissus cascavella venom neutralize the neurotoxicity of the venom and crotoxin*. Toxicon, 2004. **44**(2): p. 141-148.

6. Cheng, L.W., T.D. Henderson II, S. Patfield, L. H. Stanker, and X. He, *Mouse in vivo neutralization of Escherichia coli Shiga toxin 2 with monoclonal antibodies*. Toxins, 2013. **5**(10): p. 1845-1858.

7. Oganesyan, V., L. Peng, M.M. Damschroder, L. Cheng, A. Sadowska, C. Tkaczyk, B.R. Sellman, H. Wu, and W.F. Dall'Acqua, *Mechanisms of neutralization of a human anti-α-toxin antibody*. Journal of Biological Chemistry, 2014. **289**(43): p. 29874-29880.

8. Hung, D.T., E.A. Shakhnovich, E. Pierson, and J.J. Mekalanos, *Small-molecule inhibitor of Vibrio cholerae virulence and intestinal colonization.* Science, 2005. **310**(5748): p. 670-674.

9. McCormick, C.C., A.R. Caballero, C.L. Balzli, A. Tang, and R.J. O'Callaghan, *Chemical inhibition of alpha-toxin, a key corneal virulence factor of Staphylococcus aureus*. Investigative Ophthalmology & Visual Science, 2009**.** **50**(6): p. 2848-2854.

10. Hoshino, Y., H. Koide, K. Furuya, W.W. Haberaecker III, S.H. Lee, T. Kodama, H. Kanazawa, N. Oku, and K.J. Shea, *The rational design of a synthetic polymer nanoparticle that neutralizes a toxic peptide in vivo*. Proceedings of the National Academy of Sciences USA, 2012. **109**(1): p. 33-38.

11. Hu, C.M., L. Zhang, S. Aryal, C. Cheung, R.H. Fang, and L. Zhang, *Erythrocyte membrane-camouflaged polymeric nanoparticles as a biomimetic delivery platform.* Proceedings of the National Academy of Sciences USA, 2011. **108**(27): p. 10980-10985.

12. Hu, C.M., R.H. Fang, J. Copp, B.T. Luk, and L. Zhang, *A biomimetic nanosponge that absorbs pore-forming toxins*. Nature Nanotechnology, 2013. **8**(5): p. 336-340.

13. Schexnailder, P. and G. Schmidt, *Nanocomposite polymer hydrogels*. Colloid and Polymer Science, 2009. **287**(1): p. 1-11.

14. Appel, E.A., M.W. Tibbitt, M.J. Webber, B.A. Mattix, O. Veiseh, and R. Langer, *Self-assembled hydrogels utilizing polymer-nanoparticle interactions.* Nature Communications, 2015. **6**: p. 6295.

15. Sekine, Y., Y. Moritani, T. Ikeda-Fukazawa, Y. Sasaki, and K. Akiyoshi, *A hybrid hydrogel biomaterial by nanogel engineering: bottom-up design with nanogel and liposome building blocks to develop a multidrug delivery system.* Advanced Healthcare Materials, 2012. **1**(6): p. 722-728.

16. Gao, W., D. Vecchio, J. Li, J. Zhu, Q. Zhang, V. Fu, J. Li, S. Thamphiwatana, D. Lu, and L. Zhang, *Hydrogel containing nanoparticle-stabilized liposomes for topical antimicrobial delivery*. ACS Nano, 2014. **8**(3): p. 2900-2907.

17. Ramanan, R.M., P. Chellamuthu, L.P. Tang, and K.T. Nguyen, *Development of a temperature-sensitive composite hydrogel for drug delivery applications*. Biotechnology Progress, 2006. **22**(1): p. 118-125.

18. Xiang, Y. and D. Chen, *Preparation of a novel pH-responsive silver nanoparticle/poly(HEMA-PEGMA-MAA) composite hydrogel*. European Polymer Journal, 2007. **43**(10): p. 4178-4187.

19. Gou, M., X. Qu, W. Zhu, M. Xiang, J. Yang, K. Zhang, Y. Wei, and S. Chen, *Bio-inspired detoxification using 3D-printed hydrogel nanocomposites*. Nature Communications, 2014. **5**: p. 3774.

20. Kuehnert, M.J., D. Kruszon-Moran, H.A. Hill, G. McQuillan, S.K. McAllister, G. Fosheim, *et al.*, *Prevalence of Staphylococcus aureus nasal colonization in the United States, 2001-2002*. Journal of Infectious Diseases, 2006. **193**(2): p. 172-179.

21. Singer, A.J. and D.A. Talan, *Management of skin abscesses in the era of methicillin-resistant Staphylococcus aureus*. New England Journal of Medicine, 2014. **370**(11): p. 1039-1047.

22. Chambers, H.F. and F.R. DeLeo, *Waves of resistance: Staphylococcus aureus in the antibiotic era*. Nature Reviews Microbiology, 2009. **7**(9): p. 629-641.

23. Weigel, L.M., D.B. Clewell, S.R. Gill , N.C. Clark, L.K. McDougal, S.E. Flannagan, *et al.*, *Genetic analysis of a high-level vancomycin-resistant isolate of Staphylococcus aureus*. Science, 2003. **302**(5650): p. 1569-1571.

24. Hiramatsu, K., N. Aritaka, H. Hanaki, S. Kawasaki, Y. Hosoda, S. Hori, *et al.*, *Dissemination in Japanese hospitals of strains of Staphylococcus aureus heterogeneously resistant to vancomycin*. Lancet, 1997. **350**(9092): p. 1670-1673.

25. Klevens, R.M., J.R. Edwards, F.C. Tenover, L.C. McDonald, T. Horan, and R. Gaynes, *Change sin the epidemiology of methicillin-resistant Staphylococcus aureus in intensive care units in US hospitals, 1992-2003.* Clinical Infectious Diseases, 2006. **42**(3): p. 389-391.

26. McKenna, M., *Vaccine development: man vs MRSA.* Nature, 2012. **482**(7383): p. 23-25.

27. Gordon, R.J. and F.D. Lowy, *Pathogenesis of methicillin-resistant Staphylococcus aureus infection*. Clinical Infectious Diseases, 2008. **46**(Suppl. 5): p. S350-S359.

28. Gorwitz, R.J., *Understanding the success of methicillin-resistant Staphylococcus aureus strains causing epidemic disease in the community*. Journal of Infectious Diseases, 2008. **197**(2): p. 179-182.

29. Hu, C.M. and L. Zhang, *Nanotoxoid vaccines*. Nano Today, 2014. **9**(4): p. 401-404.

30. Copp, J.A., R.H. Fang, B.T. Luk, C.M. Hu, W. Gao, K. Zhang, and L. Zhang, *Clearance of pathological antibodies using biomimetic nanoparticles*. Proceedings of the National Academy of Sciences USA, 2014. **111**(37): p. 13481-13486.

31. Thevenot, C., A. Khoukh, S. Reynaud, J. Desbrieres, and B. Grassl, *Kinetic aspects, rheological properties and mechanoelectricla effects of hydrogels composed of polyacrylamide and polystyrene nanoparticles*. Soft Matter, 2007. **3**(4): p. 437-447.

32. Wang, R., K.R. Braughton, D. Kretschmer, T.H. Bach, S.Y. Queck, M. Li, *et al., Identification of novel cytolytic peptides as key virulence determinants of rcommunity-associated MRSA*. Nature Medicine, 2007. **13**(12): p. 1510-1514.

33. Li, M., G.Y. Cheung, J. Hu, D. Wang, H.S. Joo, F.R. DeLeo, and M. Otto, *Comparative analysis of virulence and toxin expression of global community-associated methicillin-resistant Staphylococcus aureus strains*. Journal of Infectious Diseases, 2010. **202**(12): p. 1866-1876.

34. Yeaman, M.R., S.G. Filler, S. Chaili, K. Barr, H. Wang, D. Kupferwasser, *et al., Mechanisms of NDV-3 vaccine efficacy in MRSA skin versus invasive infection*. Proceedings of the National Academy of Sciences USA, 2014. **111**(51): p. E5555-E5563.

35. Guo, Y., R.I. Ramos, J.S. Cho, N.P. Donegan, A.L. Cheung, and L.S. Miller, *In vivo bioluminescence imaging to evaluate systemic and topical antibiotics against community-acquired methicillin-resistant Staphylococcus aureus-infected skin wounds in mice*. Antimicrobial Agents and Chemotherapy, 2013. **57**(2): p. 855-863.

36. Das, D., P.M. Tulkens, P. Mehra, E. Fang, and P. Prokocimer, *Tedizolid phosphate for the management of acute bacterial skin and skin structure infections: safety summary*. Clinical Infectious Diseases, 2014. **58**(Suppl 1): p. S51-S57.

37. Kopecek, J. and J. Yang, *Smart self-assembled hybrid hydrogel biomaterials*. Angewandte Chemie (International Edition, English), 2012. **51**(30): p. 7396-7417.

38. Kanie, K., R. Kurimoto, M. Ebara, N. Idota, Y. Narita, H. Honda, and R. Kato, Journal of Tissue Engineering and Regenerative Medicine, 2014. **8**: p. 220.

39. Forster, V., R.D. Signorell, M. Roveri, and J.C. Leroux, *Liposome-supported peritoneal dialysis for detoxification of drugs and endogenous metabolites.* Science Translational Medicine, 2014. **6**(258): p. 258ra141.

40. Weisman, A., Y.A. Chen, Y. Hoshino, H. Zhang, and K. Shea, *Engineering nanoparticle antitoxins utilizing aromatic interactions*. Biomacromolecules, 2014. **15**(9): p. 3290-3295.

41. Gao, W., C.M. Hu, R.H. Fang, B.T. Luk, J. Su, and L. Zhang, *Surface functionalization of gold nanoparticles with red blood cell membranes*. Advanced Materials, 2013. **25**(26): p. 3549-3553.

42. Piao, J.G., L. Wang, F. Gao, Y.Z. You, Y. Xiong, and L. Yang, *Erythrocyte membrane is an alternative coating to polyethylene glycol for prolonging the circulation lifetime of gold nanocages for photothermal therapy*. ACS Nano, 2014. **8**(10): p. 10414-10425.

43. Parodi, A., N. Quattrocchi, A.L. van de Ven, C. Chiappini, M. Evangelopoulos, J.O. Martinez,*et al.*, *Synthetic nanoparticles functionalized with biomimetic leukocyte membranes possess cell-like functions*. Nature Nanotechnology, 2013. **8**(1): p. 61-68.

44. Li, L.L., J.H. Xu, G.B. Qi, X. Zhao, F. Yu, and H. Wang, *Core-shell supramolecular gelatin nanoparticles for adaptive and "on-demand" antibiotic delivery*. ACS Nano, 2014. **8**(5): p. 4975-4983.

45. Burdick, J.A. and W.L. Murphy, *Moving from static to dynamic complexity in hydrogel design*. Nature Communications, 2012. **3**: p. 1269.

46. Li, Y., J. Rodrigues, and H. Tomas, *Injectable and biodegradable hydrogels: gelation, biodegradation and biomedical applications.* Chemical Society Reviews, 2012. **41**(6): p. 2193-2221.

47. Hoffman, A.S., *Hydrogels for biomedical applications*. Advanced Drug Delivery Reviews, 2012. **64**(Suppl 1): p. 18-23.

4.2 Clearance of Toxic Organophosphates

4.2.1 Introduction

Organophosphate poisoning is caused by exposure to organophosphorus compounds (OPs), which irreversibly inactivate acetylcholinesterase (AChE) by phosphorylating the serine hydroxyl residue on AChE and lead to the accumulation of acetylcholine (ACh) in the body. Such accumulation disrupts cholinergic synaptic transmissions and can lead to various neurotoxic effects, including death in severe cases. OPs are one of the most common causes of poisoning worldwide and are frequently used in suicide attempts. There is an estimated 750,000 to 3 million global cases of OP poisonings per year, with hundreds of thousands of annual fatalities [1, 2]. Because of their strong toxicity to humans, many OPs are applied in chemical warfare, serving as the primary ingredients in multiple nerve agents including sarin, tabun, soman, and VX. Typically, these nerve agents take effect within 1–10 min of exposure and can cause acute lethality within 15–30 min [3]. Combined with their ease of production, highly toxic OPs represent a great threat to both military and civilian populations [4]. Effective treatment of OP poisoning is of significant value to public health.

Removal of OPs from the body is difficult because they can easily enter circulation *via* several routes, including inhalation, ingestion, and dermal absorption. Current antidotes for OP poisoning consist of a pretreatment with carbamates to protect AChE from inhibition by OP compounds and post-exposure treatments with

anticholinergic drugs [5], which serve to counteract the effects of excess ACh. Atropine is the most widely used antidote against OP poisoning in conjunction with pralidoxime or other pyridinium oximes (such as trimedoxime and obidoxime) for AChE reactivation [6]. However, these treatments are associated with serious side effects and can be difficult to administer. Recent meta-analyses indicate that the use of "-oximes" appears to be of no benefit and can potentially be detrimental [7, 8]. In addition, it can be difficult to achieve a sufficient level of atropinization [9], as a high dose of the muscarinic antagonist is needed to block the action of over-accumulated peripheral ACh following AChE inactivation. Enzyme bioscavengers such as human serum butyrylcholinesterase (BChE) and human paraoxonase 1 (PON1) have been explored as treatment options to react and hydrolyze OPs before they can reach their physiological targets [10-12]. However, large-scale production of these recombinant proteins remains a hurdle in their translation [13]. Clinical treatment of OP poisoning may thus benefit from alternative strategies that can effectively deactivate the compounds in the bloodstream.

The activities of serum cholinesterases in the blood, which include both AChE and BChE, are the most widely used markers for diagnosing OP poisoning [14]. Whereas BChE exists primarily as a freely soluble form in the plasma, AChE is a membrane-anchored protein observed commonly on red blood cell (RBC) membranes, neuromuscular junctions, and cholinergic brain synapses. Recent advances in nanotechnology, particularly in cell-membrane-cloaked nanoparticles, have provided an opportunity for the membrane-bound AChE to be exploited for biomedical

applications. It has been demonstrated that the cell-membrane-cloaking approach enables membrane proteins to be controllably anchored and displayed in a right-side-out manner on nanoscale particulates [15-17], and the resulting biomimetic nanoparticles have been used for various biomedical functions, including bioscavenger applications for absorbing protein toxins and autoreactive immune factors [15, 18]. It is conceivable that the platform may permit the systemic administration of cell-membrane-associated AChE to intercept toxic OPs in the bloodstream. To demonstrate OP detoxification using the biomimetic nanoparticles, herein, we prepared RBC membrane-cloaked nanoparticles (denoted "RBC-NPs") to exploit the RBC's surface AChE for OP scavenging (Figure 4.10). Dichlorvos (DDVP), one of the most widely used compounds in organophosphorus pesticides, is used as a model OP in this study. We showed that following cell membrane cloaking the RBC-NPs retain the membrane-bound AChE as well as their enzymatic activity. The biomimetic nanoparticles were applied as an OP scavenger to help maintain endogenous cholinesterase activity following OP exposure.

4.2.2 Experimental Methods

4.2.2.1 Preparation of RBC-NPs and Characterization

RBC-NPs were prepared as previously described [19]. Briefly, 100 nm PLGA polymeric cores were prepared by a nanoprecipitation method. First, 0.67 dL/g carboxy-terminated 50:50 PLGA (LACTEL Absorbable Polymers) was dissolved in

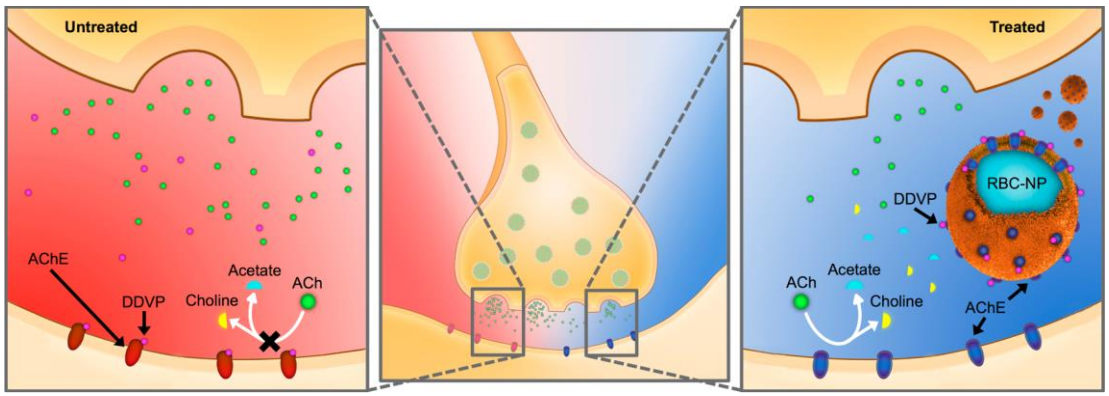

Figure 4.10 Schematic of RBC-NPs as anti-OP bioscavengers for treating OP poisoning. An idealized depiction of a neuronal synapse (center) under two opposing conditions. With no treatment (left), dichlorvos (DDVP), a model OP, irreversibly binds acetylcholinesterase (AChE), preventing the breakdown of acetylcholine (ACh) into choline and acetate. When RBC-NPs are introduced (right), they scavenge free DDVP molecules in circulation, preserving the ability of endogenous AChE at the synapse to perform the function of breaking down ACh.

acetone at a concentration of 10 mg/mL. One milliliter of the PLGA solution was added rapidly to 2 mL of water and then placed in a vacuum to accelerate acetone evaporation. The resulting nanoparticle solution was mixed with CD-1 mouse RBC membrane vesicles and sonicated for 2 min using an FS30D bath sonicator at a power of 100 W. The fluorescence-labeled RBC-NPs were prepared using the same method except that 1,1′-dioctadecyl-3,3,3′,3′-tetramethylindodicarbocyanine perchlorate (DiD; excitation/emission = 644/665 nm; Life Technologies) was incorporated into the polymer solution at a concentration of 10 μg/mL during the nanoparticle core preparation. Note that all stated concentration values for RBC-NPs refer to the concentration of the PLGA polymer in the nanoparticle formulation. The RBC-NP/DDVP complex was prepared by mixing 100 μL of RBC-NPs (5 mg/mL) with 10 μL of DDVP (1 mg/mL) for 15 min. Particle size and ζ-potential of RBC-NPs and RBC-NP/DDVP complexes were determined by DLS measurements using a Malvern ZEN 3600 Zetasizer, which showed an average hydrodynamic diameter of 123 and

130 nm, respectively. The morphology of the RBC-NP/DDVP was examined with TEM after being stained with 1 wt % uranyl acetate [16]. As a control, DSPE-PEG(2000)-coated lipid–PLGA hybrid nanoparticles (PLGA-PEG NPs) were prepared through a nanoprecipitation method following a previously published protocol [35]. As another control, PEGylated liposomes (PEG-liposomes) consisting of 80 wt % of egg PC and 20 wt % of DSPE-PEG(2000)-methoxy (Avanti Polar Lipids) were prepared by a film hydration method as previously described [36]. Measured by DLS, the diameters of the PLGA-PEG NPs and PEG-liposomes were 117 and 105 nm, respectively.

4.2.2.2 Western Blotting of AChE and AChE Activity in RBC-NPs

RBC ghosts and RBC-NPs were prepared in SDS sample buffer (Invitrogen), and the total protein content in the samples was quantified by a Pierce BCA protein assay kit (Thermo). The samples were then resolved on a NuPAGE Novex 4–12% Bis-Tris 12-well gel in MOPS running buffer using the Novex SureLock X-cell electrophoresis system (Invitrogen). The samples were run at 165 V for 45 min. The proteins on the resulting polyacrylamide gel were then transferred to Protran pure nitrocellulose transfer and immobilization membrane (PerkinElmer) at 15 V for 30 min. After blocking with 5% fresh milk in PBST for 2 h at room temperature, the nitrocellulose membrane was incubated with monoclonal mouse anti-AChE (1:2000 diluted in 5% fresh milk in PBST; Abgent) overnight at 4 °C. After being washed with PBST three times, the nitrocellulose membrane was then incubated with goat anti-

mouse IgG HRP conjugate (1:2000 diluted in 5% fresh milk in PBST; Millipore) for 2 h at room temperature. Afterward, the stained nitrocellulose membrane was subjected to ECL Western blotting substrate (Pierce) for 1 min and developed with a Mini-Medical/90 Developer (ImageWorks). Total blotting intensity was analyzed by ImageJ software to compare the AChE content between RBC-NPs and RBC ghosts. AChE activity in RBC-NPs and RBC ghosts was measured with an Amplex Red ACh/AChE assay kit (Invitrogen) using electric eel AChE as the standard.

4.2.2.3 DDVP Removal by RBC-NPs

To investigate the DDVP absorption and removal capability of RBC-NPs, 100 μL of PBS (1×, pH = 7.2) solution containing 4 or 1 mg/mL of RBC-NPs was incubated with 10 μL of different concentrations of DDVP for 30 min. Each sample was then spun down at 14 000 rpm in a Beckman Coulter microfuge 22R centrifuge for 10 min to pellet the nanoparticles. The free DDVP content in the supernatant was determined by using an HPLC system (Agilent 1100) with an analytical column (150 mm × 4.6 mm; pore size 5 μm; ZORBAX SB-C18; Agilent) at room temperature. The mobile phase consisted of a mixture of acetonitrile and water (50:50, v/v) at a flow rate of 1.0 mL/min. The sample injection volume was 10 μL, and the detector wavelength was 215 nm. The DDVP removal was calculated with the formula: DDVP removal (%) = (1 – DDVP in supernatant/total DDVP input) × 100%. All experiments were performed in triplicate. DDVP removal was plotted and fitted with the binding-saturation equation in GraphPad Prism. To investigate the effect of RBC-NP

concentration on DDVP removal, 10 μL of PBS (1×, pH = 7.2) solution containing 5 μg of DDVP was incubated with 100 μL of solution containing different concentrations of RBC-NPs for 30 min. Each sample was treated as described above, and DDVP removal was calculated, plotted with DDVP concentration, and fitted with the binding-saturation equation. To compare the removal capability of different nanoformulations, 100 μL of PBS (1×, pH = 7.2) solution containing 4 mg/mL of RBC-NPs, PLGA-PEG NPs, or PEG-liposomes was incubated with 10 μL of solution containing 5 μg of DDVP for 30 min. Each sample was processed and analyzed as described above, and the DDVP removal was calculated.

4.2.2.4 *In Vitro* Anti-OP Effect by RBC-NPs

In vitro anti-OP effect by RBC-NPs was investigated based on the AChE activity on RBC ghosts following co-incubation with RBC-NPs and DDVP. Briefly, 100 μL of PBS (1×, pH = 7.2) solution containing 2 μL of RBC ghosts and different concentrations of RBC-NPs was incubated with different concentrations of DDVP for 30 min. Each sample then was centrifuged at 2000 rpm in a Beckman Coulter microfuge 22R centrifuge for 10 min to selectively spin down the RBC ghosts, leaving RBC-NPs and DDVP in the supernatant. After the supernatant was discarded, the pellet of RBC ghosts was suspended in 10 μL of PBS and their AChE activity was measured by an Amplex Red ACh/AChE assay kit (Invitrogen). To compare the AChE protection effect by different nanoformulations, 100 μL of PBS (1×, pH = 7.2) solution containing 4 mg/mL of RBC-NPs, PLGA-PEG NPs, or PEG-liposomes was

incubated with 10 μL of solution containing 5 μg of DDVP for 30 min. Each sample was spun down at 14 000 rpm in a Beckman Coulter microfuge 22R centrifuge for 10 min to remove the nanoformulations. The supernatant was added to 2 μL of RBC ghosts and incubated for 30 min. AChE activity on the isolated RBC ghosts was measured as described above.

4.2.2.5 *In Vivo* OP Detoxification of Intravenously Administered DDVP

All animal experiments were performed in accordance with NIH guidelines and approved by the Institutional Animal Care and Use Committee (IACUC) of the University of California, San Diego. Animals were housed in a dedicated facility and were provided food/water *ad libitum*. RBC-NPs and PLGA-PEG NPs at a concentration 25 mg/mL suspended in 10% sucrose were first prepared. Six-week-old male CD-1 mice (Harlan Laboratories) were randomized to three groups of 10 mice. Each group of mice was intravenously administered with DDVP at a dose of 10 mg/kg through the tail vein. The treatment group received a tail vein intravenous injection of 200 mg/kg of nanoformulation immediately following the DDVP injection. The no treatment group was injected with DDVP only. Survival after DDVP injection was recorded, and statistical significance was determined using the log-rank test. For the no treatment group and the PLGA-PEG NP group, 50 μL of blood was collected by cardiac puncture immediately after death. For the RBC-NP group, 50 μL of blood was collected 1 h after DDVP injection by submandibular puncture. RBC ghosts were then derived from the collected blood based on a previously described protocol,(16) and the

AChE activity of 10 μL of RBC ghosts was measured and compared to that of normal mice.

4.2.2.6 *In Vivo* OP Detoxification of Orally Administered DDVP

RBC-NPs and PLGA-PEG NPs at a concentration 25 mg/mL suspended in 10% sucrose were first prepared. Six-week-old male CD-1 mice were placed into three groups of 10 mice. Each group of mice was orally administered with DDVP at a dose of 150 mg/kg. The treatment group received a tail vein intravenous injection of 200 mg/kg of nanoformulation immediately after DDVP administration. The no treatment group was administered with DDVP only. Survival after DDVP administration was recorded, and statistical significance was determined using the log-rank test. For mice suffering from acute death and the PLGA-PEG NP group, 50 μL of blood was collected by cardiac puncture immediately after death. For surviving mice, 50 μL of blood was collected 1 h after DDVP administration by submandibular puncture. RBC ghosts were derived as previously described [16], and the AChE activity of 10 μL of RBC ghosts was measured to compare with that of normal mice.

4.2.2.7 RBC AChE Activity Recovery after RBC-NP Treatment

After mice were challenged by intravenous or oral DDVP administration and treated with RBCNPs, 50 μL of blood was collected on day 0, day 2, and day 4. RBC ghosts were derived from the collected blood, and the AChE activity of 10 μL of RBC ghosts was measured to monitor the recovery of AChE activity following RBC-NP treatment. Statistical significance was determined by a two-tailed *t* test.

4.2.2.8 Biodistribution of the RBC-NP/DDVP Complex

RBC-NP/DDVP complex was first prepared by mixing 5 mg of DiD-labeled RBC-NPs with 250 μg of DDVP. The mixture was subsequently filtered through a Sepharose CL-4B column to remove unbound DDVP. For the biodistribution study, 6-week-old male CD-1 mice were sacrificed 24 h after intravenous injection of the fluorescent RBC-NP/DDVP complex *via* the tail vein. The heart, liver, spleen, kidneys, lung, brain, and blood were collected and homogenized. The fluorescence of the homogenate at 665 nm with an excitation wavelength of 640 nm was read using a Tecan Infinite M200 multiplate reader. The resulting signal was then multiplied by the corresponding organ weight to obtain the total organ fluorescence, and the relative distribution of the RBCNP/DDVP complex in each organ was calculated (n = 6). For the hepatotoxicity study, one group of mice was sacrificed on day 3 following the injection of the RBC-NP/DDVP complex and another group was sacrificed on day 7. The livers were collected, sectioned, and stained with H&E for histological analyses.

4.2.3 Results and Discussion

RBC-NPs were prepared according to a previously reported protocol in which purified RBC membranes were coated onto 100 nm poly(lactic-*co*-glycolic acid) (PLGA) polymeric cores *via* a sonication approach. To investigate the retention of AChE in the resulting RBC-NPs, Western blotting was conducted on RBC ghosts and RBC-NPs of equivalent membrane content. It was shown that following staining with anti-AChE antibodies RBC-NPs had banding patterns similar to those of RBC ghosts,

including bands that correspond to monomers, dimers, and tetramers of the protein (Figure 4.11A). Total blotting intensity analyzed by ImageJ demonstrated that there was no statistically significant difference in the total blotting intensity between RBC ghosts and RBC-NPs, indicating efficient translocation of membrane proteins onto the nanoparticle substrates (Figure 4.11B). Further examination of AChE activity showed that RBC-NPs and RBC ghosts had largely similar AChE activity (Figure 4.2.2C). These results indicate that, after nanoparticle preparation, there was minimal loss of membrane-associated AChE content and little alteration in AChE enzyme activity, which is consistent with previous findings that demonstrated preservation of surface protein functionality on these cell-membrane-cloaked nanoparticles [16, 19]. Given the well-studied reactivity between OPs and AChE, we then examined the effect of DDVP on the physicochemical properties of the RBC-NPs. Transmission electron microscopy (TEM) revealed that following mixing with DDVP the RBC-NPs retained a core/shell structure that corresponds to unilamellar membrane coatings over the nanoparticle (Figure 4.11D). In addition, dynamic light scattering (DLS) measurements showed that RBC-NPs remained similar in size following DDVP exposure (Figure 4.11E), indicating that the DDVP reaction had little effect on the RBC-NPs' structure and stability. An increase in the particles' ζ-potential was observed following incubation with DDVP (Figure 4.11F), which can likely be attributed to the surface charge shielding effect by the bound DDVP molecules.

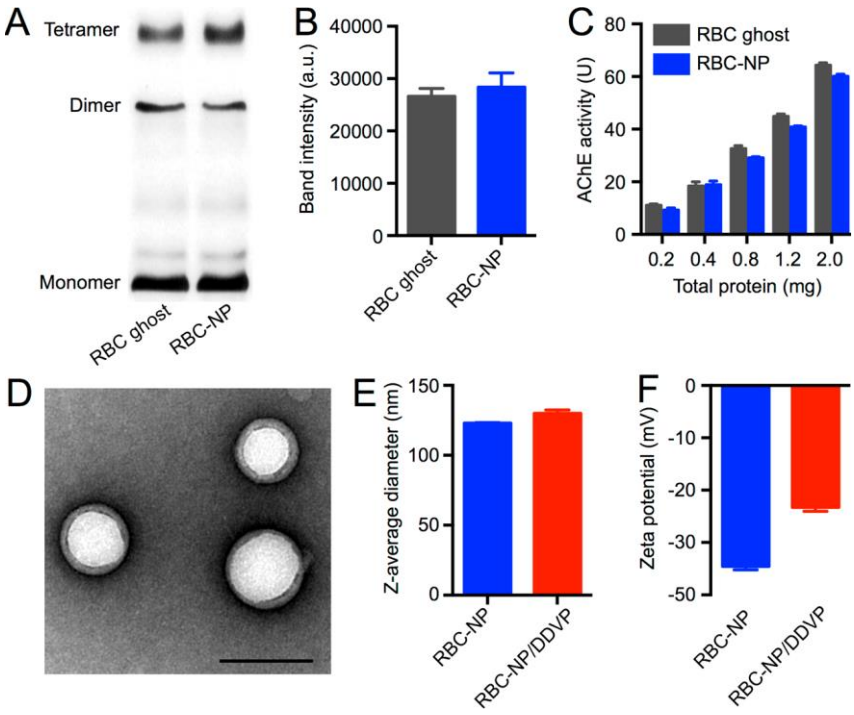

Figure 4.11 *In vitro* characterization of RBC-NPs and RBC-NP/DDVP complexes. (A) Western blotting showing that RBC ghosts and RBC-NPs have similar blotting patterns following anti-AChE staining. (B) Quantification of Western blot band intensity showing that RBC ghosts and RBC-NPs contain equivalent amounts of AChE, indicating little loss of membrane-bound AChE during the RBC-NP preparation. (C) AChE activity test showing that RBC-NPs and RBC ghosts prepared from equivalent membrane content have similar AChE activity. (D) TEM image demonstrating the core/shell structure of the RBC-NP/DDVP complex. Scale bar = 100 nm. (E) Size and (F) surface ζ-potential of the RBC-NP and RBC-NP/DDVP complexes. All error bars represent standard error of mean.

To investigate the ability of RBC-NPs to scavenge OPs, 0.4 and 0.1 mg of the particles suspended in 100 μL of aqueous solution was incubated with different concentrations of DDVP ranging from approximately 1 μg/mL to 1 mg/mL for 30 min. Following nanoparticle removal *via* centrifugation, the amount of nanoparticle-associated DDVP was quantified by measuring the remaining DDVP concentration in the supernatant *via* high-performance liquid chromatography (HPLC). It can be observed that RBC-NP/DDVP association occurs in a concentration-dependent manner (Figure 4.12A). A 4-fold increase in RBC-NP concentration correlated well

with the observed right shift in absorption capacity, reflecting the 1:1 stoichiometry behind the covalent interaction between Ops and AChE. We also titrated RBC-NPs in a reaction mixture with 100 μL of aqueous solution and 5 μg of DDVP (Figure 4.12B). It was observed that to absorb 50% or 2.5 μg of DDVP approximately 32 μg of RBC-NPs was needed. A saturation level was reached as the RBC-NP concentration was increased above 1 mg/mL. To evaluate the specificity of DDVP removal by RBC-NPs, different nanoformulations, including 0.4 mg of RBC-NPs, PEGylated PLGA NPs (PLGA-PEG NPs), and PEG-liposomes, were incubated with 5 μg of DDVP for 30 min (Figure 4.12C). Almost all DDVP was removed by the RBC-NPs, whereas PLGA-PEG NPs and PEG-liposomes showed little DDVP removal, indicating that only RBC-NPs have the capacity to remove DDVP. Furthermore, *in vitro* AChE protection efficacy was evaluated by co-incubating RBC ghosts with increasing concentrations of DDVP in the presence of RBC-NPs (Figure 4.12D). Following 30 min of incubation, the RBC ghosts were isolated from the reaction mixtures and examined for AChE activity. It was observed that the DDVP concentrations required to inhibit 50% of the AChE activity on the RBC ghosts were 10, 43, and 312 μg/mL for the mixtures containing 0, 1, and 4 mg/mL of RBC-NPs, respectively. The increased retention of AChE activity on RBC ghosts validated the scavenging effect of RBC-NPs. Comparison of different nanocarriers' anti-OP effect was performed using 4 mg/mL of PLGA-PEG NPs, PEG-liposomes, and RBC-NPs incubated with 5 μg of DDVP and 2% of RBC ghosts in 100 μL of reaction mixture (Figure 4.12E). Following 30 min of incubation, isolated RBC ghosts were analyzed for their AChE

activity. The RBC-NP group showed AChE activity retention on the RBC ghosts significantly higher than that on the other nanoformulations. Approximately 90% of RBC ghosts' AChE activity was preserved in the presence of RBC-NPs, corroborating the receptor-specific anti-OP effect enabled by the biomimetic nanoparticles.

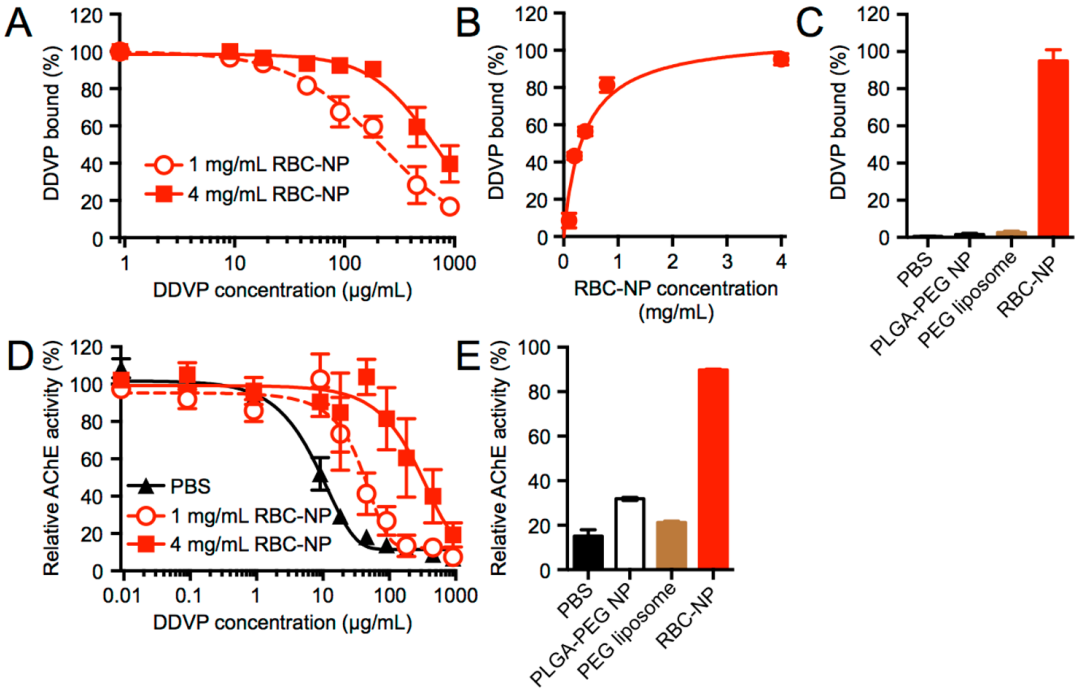

Figure 4.12 *In vitro* neutralization of DDVP by RBC-NPs. (A) DDVP removal by different amounts of RBC-NPs was analyzed by titrating the concentration of DDVP in the reaction mixtures. (B) Kinetics of DDVP absorption and removal were investigated by incubating DDVP with different concentrations of RBC-NPs for 30 min. (C) DDVP absorption and removal by different nanoformulations (PLGA-PEG NPs, PEG-liposomes, and RBC-NPs) were analyzed by incubating DDVP with the respective nanoformulations for 30 min. (D) RBC ghost AChE activity in the presence of different concentrations of RBC-NPs following incubation with varying levels of DDVP for 30 min. Higher RBC-NP content conferred higher in vitro anti-OP effect. (E) RBC ghost AChE activity in the presence of different nanoformulations (PLGA-PEG NPs, PEG-liposomes, and RBC-NPs) following incubation with DDVP for 30 min. Co-incubation with RBC-NPs resulted in the highest AChE activity retention on the RBC ghosts. All error bars represent standard error of mean.

To examine the potential of RBC-NPs to detoxify DDVP *in vivo*, we used a mouse model of OP poisoning with either intravenous or oral administrations of DDVP. For intravenous DDVP administration, which obviated absorption variability,

a lethal dose of DDVP (10 mg/kg) capable of inducing acute death in mice was injected *via* the tail vein. Mice in the treatment group received an intravenous injection of RBC-NPs or PLGA-PEG NPs at a dose of 200 mg/kg. It was shown that the mice without any treatment had a 100% mortality rate within 7 min after DDVP injection (Figure 4.13A). In the group treated with RBC-NPs, all mice survived the lethal DDVP challenge ($n = 10$, $p < 0.0001$). In contrast, PLGA-PEG NPs failed to improve the survival rate of the DDVP-challenged mice, and there was no significant difference in survival between the PLGA-PEG NP-treated group and the nontreatment group ($p = 0.3800$). Assaying the circulatory RBC AChE activity following the DDVP challenge and treatments further demonstrated that RBC-NPs significantly preserved RBC AChE activity as compared to the PLGA-PEG NP group ($p < 0.0001$) and the nontreatment group ($p < 0.0001$) (Figure 4.13B), whereas no statistical significance was observed in the circulatory RBC AChE activity between the PLGA-PEG NP-treated group and the nontreatment group ($p = 0.0652$). For the oral DDVP challenge, a scenario that models real-world exposure, mice were orally administered with a lethal dose of DDVP (150 mg/kg). Mice in the treatment group received an intravenous injection of RBC-NP or PLGA-PEG NP at a dose 200 mg/kg. It was shown that 90% of mice without any treatment died within 11 min after DDVP administration (Figure 4.13C). RBC-NP treatment remained beneficial to the overall survival with a 100% survival rate ($p < 0.0001$, $n = 10$), whereas PLGA-PEG NP treatment showed no survival advantage ($p = 0.8989$). The RBC AChE levels for the orally DDVP-challenged mice were consistent with the intravenously challenged ones.

Whereas RBC-NP treatment resulted in significant RBC AChE activity retention in circulation as compared to the nontreatment group ($p < 0.0001$), no statistical significance in AChE activity was observed between the nontreatment group and the PLGA-PEG NP treatment group ($p = 0.1479$) (Figure 4.13D).

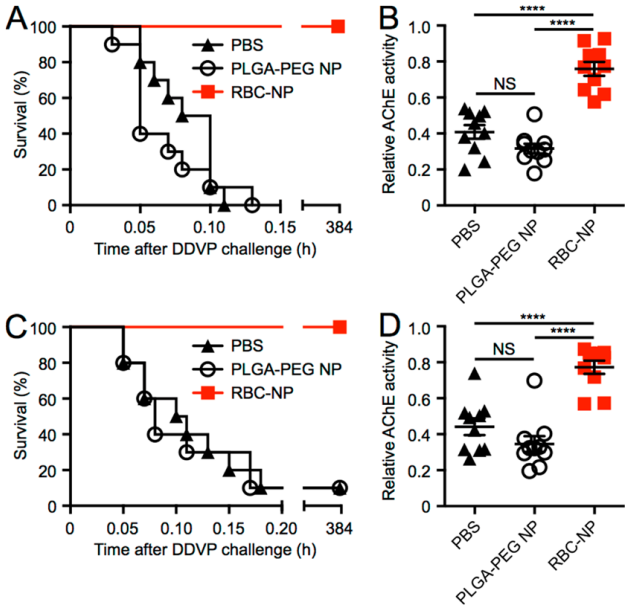

Figure 4.13 *In vivo* neutralization of DDVP by RBC-NPs. (A) Survival curve of mice over 16 days and (B) relative RBC AChE activity of mice following intravenous administration of 200 mg/kg of RBC-NPs or PLGA-PEG NPs immediately after an intravenous injection of DDVP at a lethal dose (10 mg/kg) (n = 10). (C) Survival curve of mice over 16 days and (D) relative RBC AChE activity of mice following administration of 200 mg/kg of RBC-NPs or PLGA-PEG NPs immediately after oral administration of DDVP at a lethal dose (150 mg/kg) (n = 10). All error bars represent standard error of mean. ****$p \leq 0.0001$, NS = no statistical significance.

Recovery following DDVP poisoning was also investigated using circulatory RBC AChE activity as a marker (Figure 4.14A,B). It was shown that, by day 4, the RBC AChE activity returned to normal levels in those mice treated with RBC-NPs. This indicates the eventual clearance of OPs and the replenishment of cholinesterase content in circulation. To examine the *in vivo* fate of DDVP detoxified by RBC-NPs, the biodistribution of the RBC-NPs loaded with DDVP was studied. It was shown that

the RBC-NP/DDVP complexes accumulated primarily in the liver (Figure 4.14C). Hematoxylin and eosin (H&E) stained liver histology on days 3 and 7 following the administration of RBC-NP/DDVP revealed normal hepatocytes supplied by blood vessels with no inclusion of Kupffer cells in the sinusoids (Figure 4.14D). The lack of liver tissue damage suggests that the sequestered DDVP was safely metabolized, showing minimal residual toxicity upon tissue distribution.

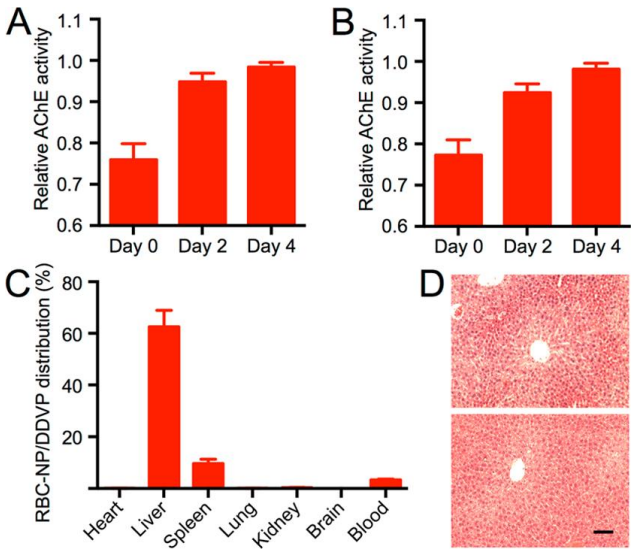

Figure 4.14 RBC AChE activity recovery following OP detoxification by RBC-NPs. (A) Relative RBC AChE activity recovered over a span of 4 days after the mice were challenged intravenouslywithDDVP(10mg/kg) and immediately treated with RBC-NPs (200 mg/kg) (n = 10). (B) Relative RBC AChE activity recovered over a span of 4 days after mice were challenged orally with DDVP (150 mg/kg) and immediately treated with RBC-NPs (200mg/kg) (n = 10). (C) Biodistribution of RBC-NP/DDVP complexes 24 h after intravenous injection. (D) Hematoxylin and eosin (H&E) stained liver histology showed no tissue damage on day 3 (top) and day 7 (bottom) following RBC-NP/DDVP complex injections. Each image is representative of five examined sections. Scale bar = 150 μm. All error bars represent standard error of mean.

OP poisoning remains a major public health issue as it is associated with high morbidity and mortality rates. Highly toxic OPs are considered one of the most dangerous chemical warfare agents and greatly threaten the safety of both military and civilian populations. OPs induce their acute toxicological effects through inhibition of

AChE, which leads to an accumulation of ACh at synapses followed by overstimulation of cholinergic receptors and the disruption of neurotransmission. Deaths can occur within a few minutes after serious OP poisoning, which are generally due to respiratory failures mediated by several mechanisms. Paralysis of respiratory muscles resulting from failure of nicotinic ACh receptors is a primary cause of OP-induced lethality, and overstimulation of peripheral muscarinic receptors can also lead to choking due to excessive bronchorrhea and bronchoconstriction. Brain damage is another severe effect of OP intoxication as hydrophobic OPs readily cross the blood–brain barrier to exert their effects on the central nervous system. Therefore, anti-OP therapy needs to prevent OPs' pathophysiological effects in a direct and effective manner.

Currently, treatment of OP poisoning remains challenging [20]. Very few therapeutic options have been developed since the 1950s and 1970s, when anticholinergic drugs, carbamate-based pretreatment, pyridinium oximes, and benzodiazepines were introduced as anti-OP countermeasures in emergency situations [21]. Research on medical intervention against OP poisoning has been relatively static, with atropine, a standard antidote in the 1940s, remaining the primary anti-OP treatment. It is the only universally accepted treatment for muscarinic symptoms such as miosis, bronchospasm, vomiting, increased sweating, diarrhea, and urinary incontinence. However, despite its acceptance, there is no universal guideline on its administration and dosing. Under-dosing can delay optimal atropinization, resulting in death from central respiratory depression, hypoxia, and hypotension. Conversely,

overdosing may lead to excessive anticholinergic toxicity, which can be fatal in severe cases [22]. Oximes are a unique class of anti-OP countermeasures, as they remove nerve agents from inhibited AChE to reactivate its activity. However, the efficacy of oxime therapy is still in debate. AChE inhibition by several nerve agents (*e.g.*, tabun and soman) has been shown to be irreversible despite the application of clinically used oxime, as cholinesterases undergo rapid conversion into a nonreactivatable form upon phosphorylation [23]. Despite extensive research and development, there is not a single, broadspectrum oxime suitable for antidotal treatment against all OP agents [24].

Bioscavenger therapy has more recently emerged as a medical countermeasure to detoxify OPs in the bloodstream. These scavengers can be either stoichiometric (mole-to-mole neutralization) or catalytic (facilitating OP hydrolysis). PON-1, for instance, is the leading catalytic bioscavenger under development [10, 12]. PON-1 is a calcium-dependent enzyme that hydrolyzes numerous OPs at a high efficiency [25]. Intravenous administration of purified PON-1 has been shown to protect guinea pigs against sarin and soman [26, 27]. However, there are limitations regarding large-scale production and use of PON-1 as a therapeutic candidate. These include difficulties in producing recombinant PON-1 using microbial expression systems, low hydrolytic activity of wildtype PON-1 toward certain substrates, and low storage stability of the purified enzyme. HuBChE is another leading bioscavenger candidate. It is estimated that 200 mg of these stoichiometric anti-OP scavengers can protect a human against two times the LD50 dose of soman [28]. Animal studies in guinea pigs revealed that

administration of large doses of HuBChE confer protection against up to 5.5 times the LD50 of soman or 8 times the LD50 of VX [29]. However, the lack of an affordable source of the enzyme remains a major hurdle in its translation. HuBChE isolation from human blood is economically prohibitive, and alternative production strategies using transgenic organisms pose immunogenicity concerns. Among other anti-OP candidates, AChE represents a promising bioscavenger with higher stereoselectivity than BuChE. Human AChE has been shown to more efficiently scavenge VX agents as compared to human HuBChE [30, 31]. Unfortunately, development of AChE as a stoichiometric bioscavenger has been discontinued due to similar translational challenges [21]. Given this landscape, alternative strategies in developing OP bioscavengers can be of great therapeutic impact.

Nanoparticles have been developed rapidly over the past years due to their great potential in drug delivery. More recently, nanoparticles have been applied to remove toxins or chemicals from blood for biodetoxification [32, 33]. To this end, little work has been done to apply nanoparticles as antidotes against OP poisoning. Here, we demonstrated that nanoparticles engineered with a biomimetic surface could be applied to intercept the binding between OPs and endogenous AChE, thereby reducing the severity of OP poisoning. Through the coating of cellular membranes, polymeric nanoparticles were successfully functionalized with enzymatically active membrane-bound proteins. The RBC-NPs demonstrated herein largely retained the content and functions of AChE on natural RBCs. These biomimetic nanoparticles were previously demonstrated to possess numerous cell-like functionalities, including

long systemic circulation [16] and spontaneous interactions with membrane-active pathogenic factors [15, 18]. The present study validates the potential of RBC-NPs as a novel form of anti-OP bioscavenger. The therapeutic potential of RBCNPs was demonstrated using mouse models of OP poisoning *via* both intravenous and oral OP challenges. It was shown that the mortality rate was sharply reduced after treatment of RBC-NPs. In contrast, equivalent doses of PLGA-PEG NPs of analogous physicochemical properties failed to improve the survival rate of the DDVP-challenged mice, thereby reaffirming the unique functionality of RBC-NPs in anti-OP applications. Unlike existing anti-OP therapies that compete with ACh or block ACh receptors, the RBC-NPs function as an OP decoy and are thus less likely to induce anticholinergic side effects including ventricular fibrillation, dizziness, nausea, blurred vision, loss of balance, dilated pupils, photophobia, dry mouth, and extreme confusion. The entirely biocompatible and biodegradable nature of the platform also minimizes safety concerns associated with nanomaterial administration.

Toward future translation, the RBC-NP platform may present production advantages over other experimental bioscavenger platforms as purified RBCs are readily available in blood transfusion practices. It can be envisioned that blood-type-matched RBC-NPs may be administered to poisoned subjects for OP neutralization with minimal concerns of immunogenicity. In addition, as both nucleated and non-nucleated mammalian cell membranes have been demonstrated for the preparation of cell-membrane-cloaked nanoparticles [16, 34], other biomimetic nanoparticles with specific surface receptors may be prepared for different biodetoxification purposes.

The unique bioscavenger approach using cell-membrane-cloaked nanoparticles may open a door to novel strategies in removing biological and chemical toxicants.

4.2.4 Conclusions

OP poisoning presents a major medical issue in the intensive care unit, and the acute nature of the poisoning demands effective therapeutic interventions. In this study, using DDVP as a model toxic agent, treatment of OP poisoning was demonstrated using RBC-NPs, which were capable of scavenging organophosphate compounds owing to the expression of functional membrane-bound acetylcholinesterase. The approach was shown to preserve endogenous RBC AChE activity *in vivo*, thereby validating its application in systemic OP neutralization. Rescue of mice following lethal OP toxin challenge was demonstrated using this nanoparticle bioscavenger approach, and the treated mice showed full AChE activity recovery and no observable liver injury following the treatment. As the platform consists of entirely biocompatible and biodegradable materials, the biomimetic nanoparticles offer a promising strategy in treating acute OP poisoning resulting from exposure to a wide array of chemicals used in domestic, industrial, and military settings.

4.2.5 References

1. Gunnell, D., M. Eddleston, M.R. Phillips, and F. Konradsen, *The global distribution of fatal pesticide self-poisoning: systematic review*. BMC Public Health, 2007. **7**: p. 357.

2. Eddleston, M., D. Gunnell, A. Karunaratne, D. de Silva, M.H. Sheriff, and N.A. Buckley, *Epidemiology of intentional self-poisoning in rural Sri Lanka*. British Journal of Psychiatry, 2005. **187**: p. 583–584.

3. Gupta, R.C., *Handbook of Toxicology of Chemical Warfare Agents*, Elsevier: London, 2009.

4. Yanagisawa, N., H. Morita, and T. Nakajima, *Sarin experiences in Japan: acute toxicity and long-term effects*. Journal of Neurological Sciences, 2006. **249**(1): p. 76–85.

5. Elsinghorst, P.W. F. Worek, H. Thiermann, and T. Wille, *Drug development for the management of organophosphorus poisoning*. Expert Opinion on Drug Discovery, 2013. **8**(12): p. 1467–1477.

6. Jokanovic, M., and M. Prostran, *Pyridinium oximes as cholinesterase reactivators. Structure-activity relationship and efficacy in the treatment of poisoning with organophosphorus compounds*. Current Medicinal Chemistry, 2009. **16**(17): p. 2177–2188.

7. Balali-Mood, M. and M. Shariat, *Treatment of organophosphate poisoning. Experience of nerve agents and acute pesticide poisoning on the effects of oximes*. Journal of Physiology, Paris, 1998. **92**(5-6): 375–378.

8. Rahimi, R., S. Nikfar, and M. Abdollahi, *Increased morbidity and mortality in acute human organophosphate-poisoned patients treated by oximes: a meta-analysis of clinical trials.* Human & Experimental Toxicology, 2006. **25**(3): p. 157–162.

9. Karakus, A., M.M. Celik, M. Karcioglu, K. Tuzcu, E.S. Erden, and C. Zeren, *Cases of organophosphate poisoning treated with high-dose of atropine in an intensive care unit and the novel treatment approaches.* Toxicology and Industrial Health, 2012. **30**(5): p. 421–425.

10. Nachon, F., X. Brazzolotto, M. Trovaslet, and P. Masson, *Progress in the development of enzyme-based nerve agent bioscavengers*. Chemico-Biological Interactions, 2013. **206**(3): p. 536–544.

11. Ceron, J.J., F. Tecles, and A. Tvarijonaviciute, *Serum paraoxonase 1 (PON1) measurement: an update*. BMC Veterinary Research, 2014. **10**: p. 74.

12. Rochu, D., E. Chabriere, and P. Masson, *Human paraoxonase: a promising approach for pre-treatment and therapy of organophosphorus poisoning.* Toxicology, 2007. **233**(1-3): p. 47–59.

13. Doctor, B.P. and A. Saxena, *Bioscavengers for the protection of humans against organophosphate toxicity*. Chemico-Biological Interactions, 2005. **157-158**: p. 167–171.

14. Worek, F., M. Koller, H. Thiermann, and L. Szinicz, *Diagnostic Aspects of Organophosphate Poisoning*. Toxicology, 2005. **214**(3): p. 182–189.

15. Hu, C.M., R.H. Fang, J. Copp, B.T. Luk, and L. Zhang, *A biomimetic nanosponge that absorbs pore-forming toxins*. Nature Nanotechnology, 2013. **8**(5): p. 336–340.

16. Hu, C.M., L. Zhang, S. Aryal, C. Cheung, R.H. Fang, and L. Zhang, *Erythrocyte membrane-camouflaged polymeric nanoparticles as a biomimetic delivery platform.* Proceedings of the National Academy of Sciences USA, 2011. **108**(27): p. 10980–10985.

17. Hu, C.M., R.H. Fang, B.T. Luk, and L. Zhang, *Nanoparticle-detained toxins for safe and effective vaccination*. Nature Nanotechnology, 2013. **8**(12): p. 933–938.

18. Copp, J.A., R.H. Fang, B.T. Luk, C.M. Hu, W. Gao, K. Zhang, and L. Zhang, *Clearance of pathological antibodies using biomimetic nanoparticles*. Proceedings of the National Academy of Sciences USA, 2014. **111**(37): p. 13481–13486.

19. Hu, C.M., R.H. Fang, B.T. Luk, K.N. Chen, C. Carpenter, W. Gao, K. Zhang, and L. Zhang, *'Marker-of-self' functionalization of nanoscale particles through a top-down cellular membrane coating approach*. Nanoscale, 2013. **5**(7): p. 2664–2668.

20. Hrabetz, H., H. Thiermann, N. Felgenhauer, T. Zilker, B. Haller, J. Nahrig, B. Saugel, and F. Eyer, *Organophosphate poisoning in the developed world:aA single centre experience from here to the millennium*. Chemico-Biological Interactions, 2013. **206**(3): p. 561–568.

21. Masson, P., *Evolution of and perspectives on therapeutic approaches to nerve agent poisoning*. Toxicology Letters, 2011. **206**(1): p. 5–13.

22. Eddleston, M., N.A. Buckley, H. Checketts, L. Senarathna, F. Mohamed, M.H. Sheriff, and A. Dawson, *Speed of initial atropinisation in significant organophosphorus pesticide poisoning--a systematic comparison of recommended regimens*. Journal of Toxicology. Clinical. Toxicology, 2004. **42**(6): p. 865–875.

23. Thiermann, H., F. Worek, and K. Kehe, *Limitations and challenges in treatment of acute chemical warfare agent poisoning*. Chemico-Biological Interactions, 2013. **206**(3): p. 435–443.

24. Kassa, J., K. Musilek, J.Z. Karasova, K. Kuca, and J. Bajgar, *Two possibilities how to increase the efficacy of antidotal treatment of nerve agent poisonings*. Mini Reviews in Medicinal Chemistry, 2012. **12**(1): p. 24–34.

25. Masson, P. and D. Rochu, *Catalytic bioscavengers against toxic esters, an alternative approach for prophylaxis and treatments of poisonings*. Acta Naturae, 2009. **1**(1): p. 68–79.

26. Valiyaveettil, M., Y. Alamneh, P. Rezk, L. Biggemann, M.W. Perkins, A.M. Sciuto, B.P. Doctor, and M.P. Nambiar, *Protective efficacy of catalytic bioscavenger, paraoxonase 1 against sarin and soman exposure in guinea pigs*. Biochemical Pharmacology, 2011. **81**(6): p. 800–809.

27. Valiyaveettil, M., Y.A. Alamneh, B.P. Doctor, and M.P. Nambiar, *Crossroads in the evaluation of paraoxonase 1 for protection against nerve agent and organophosphate toxicity*. Toxicology Letters, 2012. **210**(1): p. 87–94.

28. Ashani, Y. and S. Pistinner, *Estimation of the upper limit of human butyrylcholinesterase dose required for protection against organophosphates toxicity: a mathematically based toxicokinetic model*. Toxicological Sciences, 2004. **77**(2): p. 358–367.

29. Saxena, A., W. Sun, J.M. Fedorko, I. Koplovitz, and B.P. Doctor, *Prophylaxis with human serum butyrylcholinesterase protects guinea pigs exposed to multiple lethal doses of soman or VX*. Biochemical Pharmacology, 2011. **81**(1): p. 164–169.

30. Cohen, O., C. Kronman, L. Raveh, O. Mazor, A. Ordentlich, and A. Shafferman, *Comparison of polyethylene glycol-conjugated recombinant human acetylcholinesterase and serum human butyrylcholinesterase as bioscavengers of organophosphate compounds*. Molecular Pharmacology, 2006. **70**(3): p. 1121–1131.

31. Wandhammer, M., E. Carletti, M. Van der Schans, E. Gillon, Y. Nicolet, P. Masson, M. Goeldner, D. Noort, and F. Nachon, *Structural study of the complex stereoselectivity of human butyrylcholinesterase for the neurotoxic V-agents*. Journal of Biological Chemistry, 2011. **286**(19): p. 16783–16789.

32. Henry, B.D., D.R. Neill, K.A. Becker, S. Gore, L. Bricio-Moreno, R. Ziobro, *et al.*, *Engineered liposomes sequester bacterial exotoxins and protect from severe invasive infections in mice*. Nature Biotechnology, 2014. **33**(1): p. 81–88.

33. Leroux, J.C., *Injectable nanocarriers for biodetoxification*. Nature Nanotechnology, 2007. **2**(11): p. 679–684.

34. Fang, R.H., C.M. Hu, B.T. Luk, W. Gao, J.A. Copp, Y. Tai, D.E. O'Connor, and L. Zhang, *Cancer cell membrane-coated nanoparticles for anticancer vaccination and drug delivery*. Nano Letters, 2014. **14**(4): p. 2181–2188.

35. Zhang, L., J.M. Chan, F.X. Gu, J.W. Rhee, A.Z. Wang, A.F. Radovic-Moreno, F. Alexis, R. Langer, and O.C. Farokhzad, *Self-assembled lipid-polymer hybrid nanoparticles: a robust drug delivery platform*. ACS Nano, 2008. **2**(8): p. 1696–1702.

36. Yang, D., D. Pornpattananangkul, T. Nakatsuji, M. Chan, D. Carson, C.M. Huang, and L. Zhang, *The antimicrobial activity of liposomal lauric acids against Propionibacterium acnes*. Biomaterials, 2009. **30**(30): p. 6035–6040.

4.3 Clearance of Autoantibodies

4.3.1 Introduction

Type-II immune hypersensitivities are driven by pathologic antibodies targeting self-antigens, either naturally occurring or due to exposure to an exogenous substance present on the cellular exterior or extracellular matrix. This disease type makes up many of the most prevalent autoimmune diseases including pernicious anemia, Grave's disease, myasthenia gravis as well as autoimmune hemolytic anemia and immune thrombocytopenia [1-4]. In addition, they may occur after the administration of a new drug or following certain infections. Currently, therapies for these immune-mediated diseases remain relatively nonspecific via broad immune suppression [5]. For instance, comprehensive immune suppression through systemic glucocorticoids (i.e. prednisone, methylprednisolone), cytotoxic drugs (i.e. cyclophosphamide, methotrexate, azothioprine), and monoclonal antibodies (i.e. rituximab, belimumab, infliximab), dominate treatment regimens to prevent further tissue destruction [6-8]. Although this approach to therapy is effective for some patients in achieving remission, its efficacy remains variable and there is a well-established risk of adverse side effects, highlighting the need for better tailored therapies [9, 10].

The development of nanoparticle therapeutics has sparked new hope for the treatment of various important human diseases. Herein, we demonstrate the application of a biomimetic nanoparticle for the clearance of pathologic antibodies

using an established murine model of antibody-induced anemia [11]. This disease may be idiopathic, called autoimmune hemolytic anemia (AIHA), or drug induced, called drug-induced anemia (DIA). In both cases, however, auto-antibodies attack surface antigens present on red blood cells (RBCs). Therapy for AIHA is relatively standardized with patients starting on systemic steroids and escalating to cytotoxic drugs and B-cell depleting monoclonal antibodies, and then possibly splenectomy based on patient response to therapy [12, 13]. The shortcoming of suppressing the immune system with drug-based therapies is the considerable iatrogenic risk associated with non-specific therapy and heightened susceptibility to severe infections following spleen removal [9, 10, 14]. DIA, which can be the result of drug-hapten antibodies or drug-independent auto-antibodies, is treated much the same way with the discontinuance of the offending drug and, much more often than in AIHA, performing blood transfusions [15, 16]. A subsequent limitation of repeated transfusions of packed RBCs, is that, although they revive tissue perfusion, they carry the risks of hemolytic transfusion reactions, the formation of alloantibodies, and iron toxicity [17-19].

It has previously been shown that mammalian cellular membrane, from both nucleated and non-nucleated cells, can be fused onto polymeric nanoparticle substrates to form stable core-shell structures [20, 21]. These particles have been shown to retain and present natural cell membrane and surface antigens [22], which bare the target epitopes involved in antibody-mediated cellular clearance found in AIHA and DIA. To demonstrate the interception of pathologic antibodies, we used RBC membrane-cloaked nanoparticles, herein denoted RBC antibody nanosponges (RBC-ANS), to

serve as alternative targets for anti-RBC antibodies and preserve circulating RBCs (Figure 4.15). Unlike conventional immune therapy, these biomimetic nanoparticles have no drug payload to suppress normal lymphocytes or immune effector cells. Additionally, unlike blood transfusions, which serve as a replacement therapy, the RBC-ANS serve to deplete circulating antibody levels, without contributing further toxic metabolites due to the hemolysis of transfused cells. Moreover, it has been demonstrated in animal models of autoimmune diseases that the primary target antigens can vary and shift over the course of the diseases [23]. Exploiting target cell membranes in their entirety overcomes the varying antigen specificities and presents a novel approach in intercepting the auto-reactive antibody mechanism of type-II immune hypersensitivity reactions.

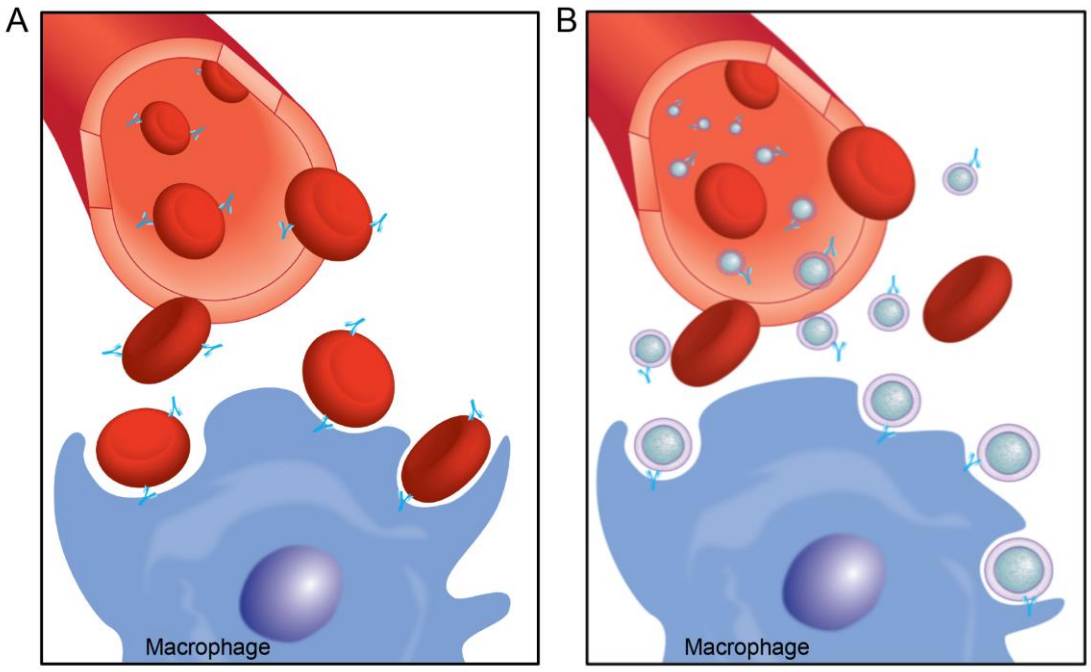

Figure 4.15 Schematic representation of RBC antibody nanosponges (RBC-ANS) neutralizing anti-RBC antibodies (anti-RBC). (A) Anti-RBC opsonize RBCs for extravascular hemolysis, via phagocytosis, as observed in autoimmune hemolytic anemia and drug-induced anemia. (B) RBC-ANS absorb and neutralize anti-RBC, thereby protecting RBCs from phagocytosis.

4.3.2 Experimental Methods

4.3.2.1 Preparation of RBC Antibody Nanosponges

RBC-ANS were prepared following previously described methods [21]. Briefly, ~100 nm PLGA polymeric cores were prepared using 0.67dL/g carboxy-terminated 50:50 poly($_{DL}$-lactide-*co*-glycolide) (LACTEL Absorbable Polymers, Cupertino, CA) in a nanoprecipitation process. The PLGA polymer was first dissolved in acetone at a 10 mg/mL concentration. 1 mL of the solution was then added rapidly to 3 mL of water. For fluorescently labeled formulations, 1,1'-dioctadecyl-3,3,3',3'-tetramethylindodicarbocyanine perchlorate (DiD, excitation/emission = 644/665 nm, Life Technologies) was loaded into the polymeric cores at 0.1 wt%. The mixture was then stirred in open air for 1 hr and placed in vacuum for another 3 hr. The resulting nanoparticle solution was filtered using Amicon Ultra-4 Centrifugal Filters with a molecular weight cutoff of 10 kDa (Millipore, Billerica, MA). RBC membrane coating was then completed by fusing RBC membrane vesicles with PLGA particles via sonication using an FS30D bath sonicator at a frequency of 42 kHz and a power of 100 W for 2 min. The size and the zeta potential of the resulting RBC-ANS were obtained from three dynamic light scattering (DLS) measurements using a Malvern ZEN 3600 Zetasizer, which showed an average hydrodynamic diameter of ~100 and ~115 nm before and after the membrane coating process, respectively. The structure of RBC-ANS was examined with transmission electron microscopy (TEM). A drop of the RBC-ANS solution at 100 μg/mL was deposited onto a glow-discharged carbon-

coated grid for 10 sec and then rinsed with 10 drops of distilled water. A drop of 1 wt% uranyl acetate stain was added to the grid. The sample was then imaged using an FEI 200 kV Sphera microscope. PEGylated PLGA nanoparticle (PEG-NP) was prepared using poly(ethylene glyocol) methyl ether-block-poly(lactide-co-glycolide) (PEG-PLGA) (Sigma Aldrich, St. Louis, MO). The PEG-PLGA polymer was dissolved in acetone at 10 mg/mL and 1 mL solution was added to 3 mL of water. For fluorescently labeled formulations, DiD was loaded into the polymeric cores at 0.1 wt%. The mixture was then stirred in open air for 1 hr and subsequently placed in vacuum for another 3 hr.

4.3.2.2 Binding Capacity and Specificity

Antibodies were first labeled with fluorescein isothiocyanate (FITC). Specifically, 100 µL of polyclonal rabbit anti-mouse RBC IgG (anti-RBC) (Rockland Antibodies and Assays, Gilbertsville, PA) at 10 mg/mL was mixed with 3.0 µL of 10 mg/mL FITC (Thermo Scientific, Rockford, IL) in dimethyl sulfoxide (DMSO). The mixture was incubated at room temperature in the dark for 1 hr and then run through a Sephadex® G-25 column (Sigma-Aldrich, St. Louis, MO) with de-ionized water to purify conjugated FITC-anti-RBC for subsequent experiments. For the antibody retention study, 250 µg of DiD-loaded RBC-ANS were combined with 6 serial dilutions (500 µg, 250 µg, 125 µg, 31.25 µg, 7.81 µg, 1.95 µg) of FITC-labeled antibody in triplicate in a Costar® 96 well plate (Corning Unlimited, Corning, NY). Prior to incubation, the samples' fluorescence intensities were measured using a Tecan

Infinite® M200 reader (TeCan, Switzerland) to determine 100% signal of FITC (515 nm) and DiD (670 nm). Solutions were then incubated for 30 min at 37°C, followed by spinning down in a Legend 21R Microcentrifuge (Thermo Scientific, Rockford, IL) at 21,200 rpm for 5 min to collect pelleted RBC-ANS/anti-RBC complex. Samples were then washed 3 times in 1 mL water and their fluorescence intensity was re-measured to determine signal intensity of FITC in relation to DiD. All DiD signals were greater than 90% original ensuring minimal loss during washing steps. These steps were repeated at optimum concentrations of 250 µg DiD-loaded RBC-ANS or 250 µg DiD-loaded PEG-NP combined with 7.8 µg FITC-anti-RBC and 7.8 µg FITC-conjugated goat anti-mouse Fc IgG (anti-Fc) (Rockland Antibodies and Assays, Gilbertsville, PA) to determine specificity of RBC-ANS against anti-RBC as compared to control samples. To compare binding kinetics, serially diluted concentrations of FITC-anti-RBC (1 mg/mL, 0.5 mg/mL 0.25 mg/mL, 0.125 mg/mL, 0.063 mg/mL and .031 mg/mL) were incubated with a constant substrate concentration (0.25 mg/mL RBC-ANS or equivalent amount of RBC ghosts). Final values were normalized to the maximum binding observed at saturation. Binding capacity was expressed as a ratio of the fluorescent signals at saturation. To test binding capacity in serum, RBC-ANS was incubated with a saturated amount of FITC-anti-RBC in PBS or in the presence of 25 vol% fetal bovine serum (Thermo Scientific, Rockford, IL). Values were expressed as a ratio of the fluorescent signals.

4.3.2.3 Competitive Binding Studies

RBC-ANS were prepared at 1 mg/mL in 1x Dulbecco's phosphate buffered saline (PBS) (Gibco®, Grand Island, NY) and serially diluted to make 5 solutions (1 mg/mL, 500 µg/mL, 250 µg/mL, 100 µg/mL, 50 µg/mL) with 1x PBS as control. For the pre-incubation study, these solutions were combined with 50 µg anti-RBC and incubated for 2 min at 37°C before the addition of 1 mL of washed 5% mouse RBC solution. For the competitive co-incubation study, RBC-ANS and anti-RBC were added simultaneously to 1 mL of 5% RBC solution. Each experiment was done in triplicate. Samples were allowed to incubate for 10 min at 37°C and then washed three times in 1x PBS to thoroughly remove supernatant and collect RBC pellet. Flow cytometry was used to measure the FITC signal of the collected RBC population using a Becton Dickinson FACSCanto II. Flow cytometry data was analyzed using Flowjo software from Treestar.

4.3.2.4 RBC Agglutination Titration

The experiment was carried out per manufacturer (Rockport Antibodies and Assays) instructions. Briefly, 100 µL of anti-RBC (primary antibody) at 156 µg/mL was added to 100 µL of 5% washed RBC in 1x PBS along with 62.5 µL of RBC-ANS (250 µg, 100 µg, 50 µg, 25 µg or 0 µg) and incubated for 45 min at 37°C. The RBC solution was then washed three times by centrifuging the sample at 3,500 rpm for 1 min and exchanging the supernatant with 1x PBS each time. 100 µL of anti-Fc (agglutinating secondary antibody) at 156 µg/mL was added to each sample, which

was vortexed at 625 rpm for 5 min and then spun down at 3,500 rpm for 20 sec. The sample was then re-suspended using a pipette to disrupt the pellet. For the negative control, 100 µL of 6% BSA was used in lieu of secondary antibody. All samples were then viewed via light microscope at 10x magnification and imaged via mounted camera.

4.3.2.5 *In Vivo* Stability and Anti-RBC Binding

Following induction of anemia via intraperitoneal injection of anti-RBC, we randomly assorted 12 ICR mice into two groups of 6. Treatment group received 500 µg anti-RBC incubated with 5 mg RBC-ANS for 5 min at 37°C prior to injection and anti-RBC only mice received anti-RBC incubated in 1x PBS for 5 min. A control group of mice received injections of PBS only. A few drops of blood were collected from each mouse prior to injections on day 0 to establish starting blood counts and repeated on each day of the experiment. Samples were stored in Potassium-EDTA Microvette® tubes (Sarstedt, Newton, NC) and vigorously mixed to prevent clotting. Samples were then run the same day in a Drew Scientific Hemavet 950 (Erba® Diagnostics, Waterbury, CT) and RBC count, hemoglobin and hematocrit were recorded daily.

4.3.2.6 *In Vivo* Neutralization of Circulating Anti-RBC

Using the established intraperitoneal model for antibody delivery, 30 mice were randomized to three groups of 10. Each group of mice received a 100 µL intraperitoneal injection of 2 mg/mL anti-RBC on days 0, 1, 2 and 3. The treatment

group also received a tail vein intravenous injection of 200 µL of RBC-ANS (10 mg/mL) in 1x PBS within 30 min of intraperitoneal antibody delivery. The PEG-NP group received an equivalent intravenous dose of PEG-NP and the anti-RBC only group received 200 µL PBS via intravenous injection. RBC count, hemoglobin and hematocrit of each sample were recorded on days 0, 1, 2, 3, and 4.

4.3.2.7 Anti-RBC Autoimmune Study

Six weeks after the *in vivo* neutralization studies, serum was collected from 12 mice, 6 in each group, and a standard ELISA was performed. Washed ICR mouse RBCs were plated at 1 x 10^6 RBCs per well onto a Costar® 96 well plate. 100 µL of collected serum was added in a sequence of six 1:5 dilutions. Horseradish peroxidase-conjugated goat anti-mouse antibody IgG (Biolegend, San Diego, CA) was used to probe for bound antibodies. The plate was developed using TMB (3,3', 5, 5'-tetramethylbenzidine) substrate and 1 M HCl was used to stop the reaction. Absorbance was measured at 450 nm.

4.3.3 Results and Discussion

We constructed RBC-ANS following a previously reported protocol [21], in which purified mouse RBC membrane was mechanically extruded with 100 nm poly(lactic-*co*-glycolic acid) (PLGA) polymeric cores. The resulting nanoparticles

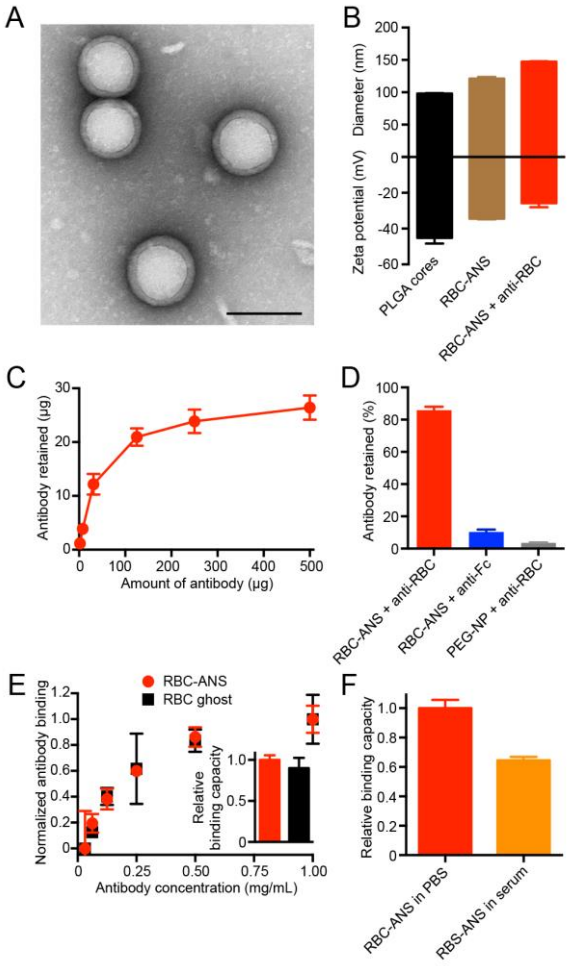

Figure 4.16 *In vitro* characterization of RBC-ANS. (A) TEM image demonstrated the core-shell structure of RBC-ANS (scale bar = 150 nm). (B) Size and surface zeta-potential of pure PLGA cores, RBC-ANS, and RBC-ANS bound with anti-RBC. (C) 250 μg of RBC-ANS incubated with 5 serial dilutions of fluorescent anti-RBC demonstrated particle saturation at ~ 27 μg of antibody, corresponding to ~9:1 particle/antibody mass ratio. (D) Equivalent amounts of RBC-ANS incubated with anti-RBC or anti-Fc demonstrated significantly greater specific binding as compared to nonspecific binding. The corresponding PEGylated PLGA nanoparticle (PEG-NP) incubated with anti-RBC served as a negative control. (E) Comparison of anti-RBC binding kinetics to a fixed amount of RBC-ANS or RBC ghosts. Inset represents relative binding capacity of RBC-ANS versus RBC ghosts at saturation. (F) Relative binding capacity of RBC-ANS in PBS versus in serum at saturation.

revealed a core-shell structure under transmission electron microscopy (TEM) that corresponds to unilamellar membrane coatings over the nanoparticle cores (Figure 4.16A). Physicochemical characterizations showed that upon RBC membrane coating, the nanoparticles had a ~20 nm increase in diameter and a 10 mV increase in surface zeta potential (Figure 4.16B), which were consistent with addition of RBC membrane to the particle surface [24]. A mixture of RBC-ANS with rabbit anti-mouse RBC IgG antibodies (anti-RBC) resulted in a diameter increase of ~26 nm, which can be attributed to the association of the IgG with the RBC-ANS. Such association also resulted in surface charge shielding as was evidenced by the 10 mV increase in the particle zeta potential (Figure 4.16B). To better investigate the binding capacity of RBC-ANS for anti-RBC, 250 μg of RBC-ANS was incubated with fluorescently labeled anti-RBC ranging from 1.75 μg to 500 μg. This titration assay demonstrated a plateau in particle-bound antibody fluorescent signal, or binding maximum, corresponding with an antibody mass of ~27 μg yielding a particle-to-antibody mass ratio of approximately 9:1 (Figure 4.16C). To evaluate the specificity of antibody-antigen binding, RBC-ANS were incubated with fluorescently labeled anti-RBC or goat anti-mouse Fc IgG (anti-Fc, as a negative control) for 10 min at 37°C. Figure 4.16D shows that significantly higher binding signal was observed between RBC-ANS and anti-RBC with very little nonspecific binding with anti-Fc. PEGylated PLGA nanoparticle (PEG-NP) incubated with anti-RBC served as a negative control and showed little retention of the antibody. Further, binding affinity of anti-RBC to RBC-ANS was near identical to that of an equivalent amount of RBC ghosts (Figure

4.16E). In the presence of serum proteins, RBC-ANS still retained greater than 60% of their anti-RBC binding capacity compared with when the incubation was performed in buffer alone (Figure 4.16F). These results are indicative of relatively low nonspecific antibody-nanoparticle binding interactions and demonstrate the necessity for antigen-antibody concordance to achieve neutralization.

To further characterize the binding stability and competitive binding capacity, we varied the amounts of RBC-ANS mixed with a constant amount of fluorescent anti-RBC in 5% RBC solution. To assess *in vitro* binding stability, RBC-ANS were pre-incubated with anti-RBC before mixing with 5% RBC solution (Figure 4.17A,B) and to test competitive binding capacity, RBC-ANS was added simultaneously with anti-RBC to 5% RBC solution (Figure 4.17C,D). After separating the RBCs from any unbound antibodies and RBC-ANS, we measured fluorescent signal associated with the RBCs using flow cytometric analysis. Both pre-incubation and co-incubation studies showed dose-dependent antibody neutralization. High binding ability and stability of RBC-ANS to anti-RBC was shown in the pre-incubation neutralization experiment, which demonstrated a ~60% reduction in RBC-bound antibodies with 100 μg of RBC-ANS and ~95% reduction with 1 mg RBC-ANS as compared to the negative control. Competitive co-incubation showed a reduction of RBC bound antibody signal by ~40% and ~80% at equivalent RBC-ANS doses, respectively. To correlate dose-dependence to clinically relevant diagnostic parameters, we completed an immunoglobulin agglutination test, which is equivalent to the qualitative Direct Antiglobulin Test that is a gold standard laboratory diagnostic often used in the

diagnoses of AIHA [25, 26]. By varying the dose of RBC-ANS from 0 µg to 250 µg we demonstrated a dose-dependent neutralization of anti-RBC (primary antibody) as evidenced by the progressive decrease of RBC agglutination upon addition of an agglutinating secondary antibody (Figure 4.17E to I).

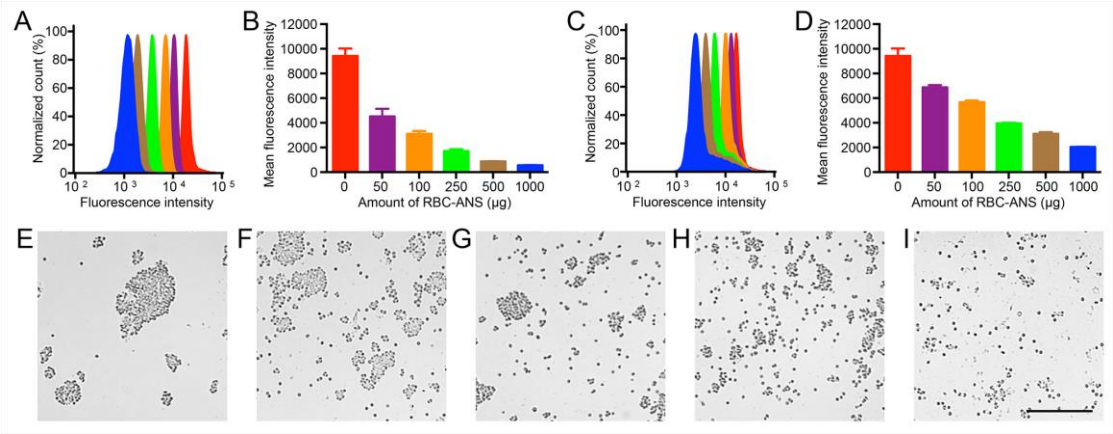

Figure 4.17 *In vitro* dose-dependent neutralization and stability of RBC-ANS/anti-RBC binding. (A) Flow-cytometry histograms of RBC-ANS (from left to right: 1000, 500, 250, 100, 50 and 0 µg) pre-incubated with 50 µg FITC-anti-RBC prior to mixing with 5% RBC solution demonstrated dose-dependent neutralization of anti-RBC. (B) Mean fluorescence intensity of samples in (A). (C) Flow-cytometry histograms of RBC-ANS (from left to right: 1000, 500, 250, 100, 50 and 0 µg) co-incubated with 50 µg FITC-anti-RBC and 5% RBC solution demonstrated dose-dependent, competitive neutralization of anti-RBC. (D) Mean fluorescence intensity of samples in (C). (E-I) Varying amounts of RBC-ANS (from E to I: 0, 25, 50, 100, and 250 µg) were co-incubated with 15.6 µg anti-RBC (primary antibody) and 5% RBC solution, followed by adding equivalent dose of anti-Fc (agglutinating secondary antibody). The samples were then imaged by light microscope at 10x magnification, demonstrating dose related inhibition of RBC agglutination by RBC-ANS.

After confirming *in vitro* that RBC-ANS could selectively bind anti-RBC, we next assessed the ability of the particles to durably retain antibodies *in vivo*. A previously described anemia disease model, induced through intraperitoneal injection of anti-RBC, was used in the study [11]. 500 µg of anti-RBC, a sufficient amount to induce acute anemia, was injected intraperitoneally into mice in the control group. Following the injection, the antibodies could diffuse across the peritoneal membrane, bind to circulating RBCs, and induce their clearance. Mice in the treatment group

received the same dose of anti-RBC incubated beforehand for 5 min at 37°C with 5 mg of RBC-ANS. The relevant clinical parameters used for monitoring anemia responses, including RBC count, hemoglobin level, and hematocrit, of each group were then assessed daily for 4 days. Comparison of the hematological parameters between the control and treatment groups showed that anti-RBC pre-incubated with RBC-ANS was less effective in inducing an anemic response (Figure 4.18). Mice in the treatment group possessed higher RBC count, hemoglobin content, and hematocrit throughout the duration of the study. All parameters were consistent with control mice that had not been challenged with anti-RBC but had their blood drawn daily. This result suggests that the anti-RBC was trapped by the RBC-ANS and was precluded from binding to circulating RBCs. The experiment demonstrates the feasibility of using target-cell mimicking nanoparticles to neutralize pathologic antibodies.

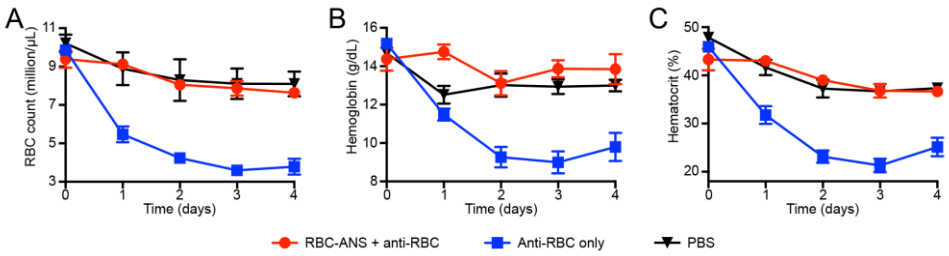

Figure 4.18 *In vivo* binding stability of RBC-ANS and anti-RBC. ICR mice (n = 6) were intraperitoneally injected with 500 µg of anti-RBC pre-incubated with 5 mg RBC-ANS (red), 500 µg anti-RBC alone (blue) or PBS (black). Blood was collected daily to monitor (A) RBC count (million/µL), (B) hemoglobin (g/dL) and (C) hematocrit (%) of the mice.

To further validate the clinical relevance of the RBC-ANS, we administered daily injections of low-dose anti-RBC intraperitoneally to maintain a sustained level of the antibodies for anemia progression. RBC-ANS was injected intravenously with the

aim of neutralizing the circulating antibodies and retarding anemia development. PEG-NPs of analogous size were also administered as a control. Mice were divided into RBC-ANS plus anti-RBC, PEG-NP plus anti-RBC, and PBS plus anti-RBC groups. All mice received 100 μg of anti-RBC daily, through intraperitoneal injection, followed by an intravenous injection of 2 mg of RBC-ANS, PEG-NP, or PBS daily for 4 days. Blood was obtained daily for the duration of the experiment to assess RBC count, hemoglobin and hematocrit. Starting from day 2, significant benefit in anemia related parameters was observed in the RBC-ANS-treated group as compared to PEG-NP control mice and vehicle only mice (Figure 4.19). The inability for PEG-NP to prevent anemia further supports the antigen-specific clearance of anti-RBC mediated by RBC-ANS as opposed to the preservation of RBCs via saturation of the mononuclear phagocyte system [27, 28]. To help assess the safety of the RBC-ANS approach, we also examined the autologous anti-RBC serum titers in mice 6 weeks following RBC-ANS treatment. ELISA assessment of autoantibodies against mouse RBCs showed no observable elevation of autologous anti-RBC responses in mice

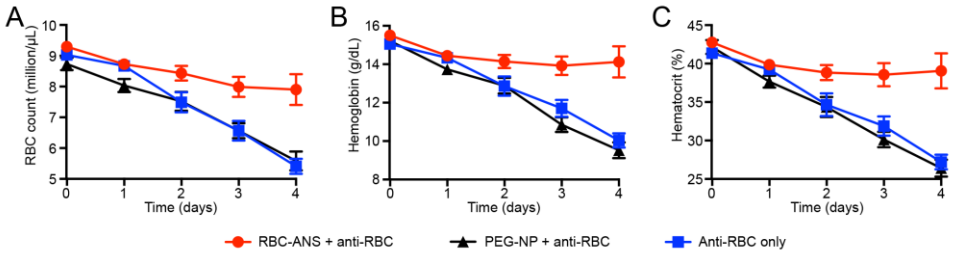

Figure 4.19 *In vivo* neutralization of anti-RBC by RBC-ANS. ICR mice (n = 10) were intraperitoneally injected with 200 μg anti-RBC on day 0, 1, 2 and 3. After each dose of the antibody, the mice received 2 mg RBC-ANS (red), PEG-NP (black) or PBS (blue) via tail vein intravenous injection. Blood was collected daily to monitor (A) RBC count (million/μL), (B) hemoglobin (g/dL) and (C) hematocrit (%) of the mice.

receiving RBC-ANS treatment as compared to the controls. The result confirms that the RBC-ANS/anti-RBC complex does not potentiate a humoral immune response against particle associated membrane antigens (Figure 4.20).

Autoimmune diseases, which include type-II, type-III, and type-IV immune hypersensitivity reactions, are known to attack almost every body tissue, make up over 50 diseases, and contribute to over $65 billion in healthcare costs annually [29]. AIHA was attributed to an autoantibody in 1904 by Donath and Landsteiner and the mechanism of extravascular hemolysis described by Metchinkoff in 1905, making it the first disease known to be caused by this mechanism [30]. Although the etiology is often idiopathic, it can be induced by drugs (cephalosporins, chemotherapies, quinines) as well as malignancies and viral infections [25, 26, 30]. Despite the differences in etiology, the final common disease pathway is the generation of antibodies against RBC membrane components, typically rhesus group and glycophorins, by a B-lymphocyte population that has lost self-tolerance to RBC surface-antigen(s) [31]. Most commonly, the pathologic mechanism is IgG-mediated attack that leads to the opsonization of RBCs for extravascular destruction by phagocytes. Alternatively, AIHA can also be induced by IgM-mediated attack on RBCs, which causes RBC intravascular hemolysis via activation of the complement system [26, 30, 32, 33]. Even though autoantibodies have long been recognized to play a significant role in the disease, to our knowledge, therapies specifically directed at these pathologic antibodies were not previously explored. Existing AIHA therapy continues to target upstream disease mechanisms through reliance on broad immune

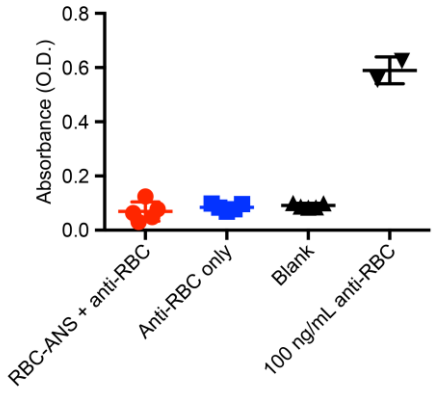

Figure 4.20 Autoimmunity study. RBC-ANS do not elicit autoimmune antibodies against RBCs. Six weeks following administration, ELISA analysis of serum from mice receiving RBC-ANS plus anti-RBC, anti-RBC alone, or PBS showed no observable elevation of anti-RBC titer as compared to controls.

suppression, blood transfusions, or splenectomy for refractory cases [12, 15]. This treatment paradigm holds true for other type-II immune hypersensitivities which are also managed with broad immune suppression such as using systemic glucocorticoids or cytotoxic drugs [3, 34].

Although efficacious for many patients, systemic steroids carry some of the highest risks of iatrogenic illness. Adverse effects of therapy include steroid myopathy, nosocomial infection, aseptic bone necrosis, accelerated osteoporosis, weight gain, metabolic derangements and Cushinoid appearance [35, 36]. In addition to these side effects, if steroid therapy fails, a patient may need to undergo surgery or systemic B-cell depletion with monoclonal antibodies or cytotoxic drugs with side effects of severe infection, antibody transfusion reactions and even the development of malignancies [10, 37]. Given this landscape, it is meaningful to continue development of innovative therapeutic strategies to manage disease burden while minimizing iatrogenic risk. Nanoparticles have already shown promise in reducing the risk of

systemic toxicity of chemotherapy while increasing efficacy both in emerging literature and clinically [38-40]. We demonstrated that nanoparticles can be engineered to intercept binding between pathologic antibodies and their target cells to favorably impact disease status. The particular approach offers a novel therapeutic intervention for type-II immune hypersensitivity reactions by targeting a final pathologic mechanism and presents an attractive alternative to broad-spectrum immune suppression.

Through the stabilization of biological membrane on a polymeric nanoparticle substrate, we unveiled the ability of cell membrane-coated nanoparticles to favorably serve as an antibody-decoy to improve disease parameters. Our results indicate the ability of RBC-ANS to effectively bind to anti-RBC and preclude their interaction with RBCs. The therapeutic potential of the proposed approach was validated *in vivo* with separate administrations of anti-RBC and RBC-ANS via intraperitoneal and intravenous route respectively. While the RBC-ANS reduced the antibody-mediated anemic response, equivalent doses of PEG-NP of analogous physicochemical properties failed to moderate the effect of the anti-RBC. The outcome of the *in vivo* study further indicates that the improved hematological status upon RBC-ANS treatment was mediated by specific antibody-antigen interaction, rather than particle-mediated saturation of phagocytic cells [27, 28]. We also established a lack of humoral response against the RBC membrane antigens following administrations of RBC-ANS and anti-RBC, which validates the safety of the approach as the RBC-ANS, in the presence of anti-RBC, did not potentiate an RBC autoantibody immune response. It

has been previously reported that RBC membrane-coated nanoparticles are primarily metabolized in the liver [21, 41], where particulate metabolism generally promotes a tolerogenic immune response [42, 43]. In addition, several reports have shown that antigen-laden polymeric nanoparticles, in the absence of immune adjuvants, are also immune-tolerizing [44-46]. While rigorous immunological studies in more faithful AIHA animal models are warranted, the present study exhibits the feasibility of applying cell membrane-coated nanoparticles for clearing pathologic antibodies. Adding promise to the approach is the demonstration of both nucleated and non-nucleated mammalian cell membranes that have been successfully stabilized by nanoparticle cores [20, 21]. This capacity to functionalize particles, with a variety of multi-antigen membranes, offers a new platform for the development of a robust line of therapies against additional type-II immune hypersensitivities.

4.3.4 Conclusions

Currently, the paradigm in targeted nanomedicine revolves around high-throughput screening for ligand-receptor recognition and the subsequent nanoparticle functionalization with specific targeting molecules [47, 48]. With regards to type-II immune hypersensitivity reactions, such a functionalization process could prove limited owing to the varying antigen specificities among pathologic antibodies from patient to patient such as in the case of AIHA [11, 23, 45]. Through the appropriate application of biological membranes, which possess the diversity of surface antigens susceptible to pathologic antibodies, biomimetic nanoparticles can be prepared in a

facile manner for selective immunomodulation. Further, drug-loaded cores or those made from different materials, such as metallic or inorganic nanoparticles, can be employed to create multifunctional formulations. We believe the demonstration of pathophysiological-inspired nanoengineering serves as a valuable prototype for additional therapeutic advances, offering the opportunity for selective disease intervention while minimizing iatrogenic risks associated with many traditional drug-based therapies.

4.3.5 References

1. Jacobson, D.L., S.J. Gange, N.R. Rose, and N.M. Graham, *Epidemiology and estimated population burden of selected autoimmune diseases in the United States.* Clinical Immunology and Immunopathology, 1997. **84**(3): p. 223-243.

2. Wakayama, H., Y. Hasegawa, T. Kawabe, T. hara, S. Matsuo, M. Mizuno, T. Takai, H. Kikutani, and K. Shimokata, *Abolition of anti-glomerular basement membrane antibody-mediated glomerulonephritis in FcR gamma-deficient mice.* European Journal of Immunology, 2000. **30**(4): p. 1182-1190.

3. Hudson, B.G., K. Tryggvason, M. Sundaramoorthy, and E.G. Neilson, *Alport's syndrome, Goodpasture's syndrome, and type IV collagen.* New England Journal of Medicine, 2003. **348**(25): p. 2543-2556.

4. Weetman, A.P., *Medical progress: Graves' disease.* New England Journal of Medicine, 2000. **343**(17): p. 1236-1248.

5. Edwards, J.C.W. and G. Cambridge, *B-cell targeting in rheumatoid arthritis and other autoimmune diseases.* Nature Reviews Immunology, 2006. **6**(5): p. 394-403.

6. Wallace, D.J., W. Stohl, R.A. Furie, J.R. Lisse, J.D. McKay, J.T. Merrill, M.A. Petri, E.M. Ginzler, W.W. Chatham, W.J. McCune, V. Fernandez, M.R. Chevrier, Z.J. Zhong, and W.W. Freimuth, *A Phase II, Randomized, Double-Blind, Placebo-Controlled, Dose-Ranging Study of Belimumab in Patients With Active Systemic Lupus Erythematosus.* Arthritis & Rheumatism-Arthritis Care & Research, 2009. **61**(9): p. 1168-1178.

7. Worlledge, S.M., M.C. Brain, A.C. Cooper, J.R. Hobbs, and J.V. Dacie, *Immunosuppressive Drugs in Treatment of Autoimmune Haemolytic Anaemia.* Proceedings of the Royal Society of Medicine-London, 1968. **61**(12): p. 1312-1315.

8. Emilia, G., C. Messora, G. Longo, and M. Bertesi, *Long-term salvage treatment by cyclosporin in refractory autoimmune haematological disorders.* British Journal of Haematology, 1996. **93**(2): p. 341-344.

9. Tabas, I. and C.K. Glass, *Anti-Inflammatory Therapy in Chronic Disease: Challenges and Opportunities.* Science, 2013. **339**(6116): p. 166-172.

10. Hansel, T.T., H. Kropshofer, T. Singer, J.A. Mitchel, and A.J. George, *The safety and side effects of monoclonal antibodies.* Nature Reviews Drug Discovery, 2010. **9**(4): p. 325-338.

11. Meyer, D., C. Schiller, J. Westermann, S. Izui, W.L. Hazenbos, J.S. Verbeek, R.E. Schmidt, and J.E. Gessner, *Fc gamma RIII (CD16)-deficient mice show IgG isotype-dependent protection to experimental autoimmune hemolytic anemia.* Blood, 1998. **92**(11): p. 3997-4002.

12. Lechner, K. and U. Jager, *How I treat autoimmune hemolytic anemias in adults.* Blood, 2010. **116**(11): p. 1831-1838.

13. Arnold, D.M., N.M. Heddle, J. Carruthers, D.J. Cook, M.A. Crowther, R.M. Meyer, Y. Liu, R.J. Cook, A. McLeod, J.A. MacEachern, J. Mangel, D. Anderson, L. Vickars, A. Tinmouth, A.C. Schuh, and J.G. Kelton, *A pilot randomized trial of adjuvant rituximab or placebo for nonsplenectomized patients with immune thrombocytopenia.* Blood, 2012. **119**(6): p. 1356-1362.

14. Kyaw, M.H., E.M. Holmes, F. Toolis, B. Wayne, J. Chalmers, I.G. Jones, and H. Campbell, *Evaluation of severe infection and survival after splenectomy.* American Journal of Medicine, 2006. **119**(3): p. 276e1-276e7.

15. Crowther, M., Y.L. Chan, I.K. Garbett, W. Lim, M.A. Vickers, and M.A. Crowther, *Evidence-based focused review of the treatment of idiopathic warm immune hemolytic anemia in adults.* Blood, 2011. **118**(15): p. 4036-4040.

16. Petz, L.D., *A physician's guide to transfusion in autoimmune haemolytic anaemia.* British Journal of Haematology, 2004. **124**(6): p. 712-716.

17. Salama, A., H. Berghofer, and C. Muellereckhardt, *Red-Blood-Cell Transfusion in Warm-Type Autoimmune Hemolytic-Anemia.* Lancet, 1992. **340**(8834-5): p. 1515-1517.

18. Ahrens, N., A. Pruss, A. Kahne, H. Kiesewetter, and A. Salama, *Coexistence of autoantibodies and alloantibodies to red blood cells due to blood transfusion.* Transfusion, 2007. **47**(5): p. 813-816.

19. Shander, A., M.D. Cappellini, and L.T. Goodnough, *Iron overload and toxicity: the hidden risk of multiple blood transfusions.* Vox Sanguinis, 2009. **97**(3): p. 185-197.

20. Fang, R.H., C.M. Hu, B.T. Luk, W. Gao, J.A. Copp. Y. Tai, D.E. O'Connor, and L. Zhang, *Cancer cell membrane-coated nanoparticles for anticancer vaccination and drug delivery.* Nano Letters, 2014. **14**(4): p. 2181-2188.

21. Hu, C.M.J., L. Zhang, S. Aryal, C. Cheung, R.H. Fang, and L. Zhang, *Erythrocyte membrane-camouflaged polymeric nanoparticles as a biomimetic delivery platform.* Proceedings of the National Academy of Sciences USA, 2011. **108**(27): p. 10980-10985.

22. Hu, C.M.J., R.H. Fang, B.T. Luk, K.N. Chen, C. Carpenter, W. Gao, K. Zhang, and L. Zhang, *'Marker-of-self' functionalization of nanoscale particles through a top-down cellular membrane coating approach.* Nanoscale, 2013. **5**(7): p. 2664-2668.

23. Hall, A.M., F.J. Ward, C.R. Shen, C. Rowe, L. Bowie, A. Devine, S.J. Urbaniak, C.J. Elson, and R.N. Barker, *Deletion of the dominant autoantigen in NZB mice with autoimmune hemolytic anemia: effects on autoantibody and T-helper responses.* Blood, 2007. **110**(13): p. 4511-4517.

24. Hochmuth, R.M., C.A. Evans, H.C. Wiles, and J.T. McCown, *Mechanical Measurement of Red-Cell Membrane Thickness.* Science, 1983. **220**(4592): p. 101-102.

25. Bass, G.F., E.T. Tuscano, and J.M. Tuscano, *Diagnosis and classification of autoimmune hemolytic anemia.* Autoimmunity Reviews, 2014. **13**(4-5): p. 560-564.

26. Packman, C.H., *Hemolytic anemia due to warm autoantibodies.* Blood Reviews, 2008. **22**(1): p. 17-31.

27. Crow, A.R., S. Song, J.W. Semple, J. Freedman, and A.H. Lazarus, *IVIg inhibits reticuloendothelial system function and ameliorates murine passive-immune thrombocytopenia independent of anti-idiotype reactivity.* British Journal of Haematology, 2001. **115**(3): p. 679-686.

28. Samuelsson, A., T.L. Towers, and J.V. Ravetch, *Anti-inflammatory activity of IVIG mediated through the inhibitory Fc receptor.* Science, 2001. **291**(5503): p. 484-486.

29. Persidis, A., *Autoimmune disease drug discovery.* Nature Biotechnology, 1999. **17**: p. 1038-1039.

30. Mack, P. and J. Freedman, *Autoimmune hemolytic anemia: A history.* Transfusion Medicine Reviews, 2000. **14**(3): p. 223-233.

31. Leddy, J.P., S.L. Wilkinson, G.E. Kissel, S.T. Passador, J.L. Falany, and S.I. Rosenfeld, *Erythrocyte-Membrane Proteins Reactive with Igg (Warm-Reacting) Anti-Red Blood-Cell Autoantibodies .2. Antibodies Coprecipitating Band-3 and Glycophorin-A.* Blood, 1994. **84**(2): p. 650-656.

32. Konig, A.L., H. Kather, and D. Roelcke, *Autoimmune Hemolytic-Anemia by Coexisting Anti-I and Anti-Fl Cold Agglutinins.* Blut, 1984. **49**(5): p. 363-368.

33. Semple, J.W. and J. Freedman, *Autoimmune pathogenesis and autoimmune hemolytic anemia.* Seminars in Hematology, 2005. **42**(3): p. 122-130.

34. Daniel, B.S., L. Borradori, R.P. Hall 3rd, and D.F. Murrell, *Evidence-based management of bullous pemphigoid.* Dermatologic Clinics, 2011. **29**(4): p. 613-20.

35. Buttgereit, F., G.R. Burmester, R.H. Straub, M.J. Seibel, and H. Zhou, *Exogenous and Endogenous Glucocorticoids in Rheumatic Diseases.* Arthritis and Rheumatism, 2011. **63**(1): p. 1-9.

36. Saag, K.G., J.R. Caldwell, R. Brasington, and D.E. Furst, *Serious Adverse Events with Low-Dose, Long-Term Corticosteroid-Therapy in Rheumatoid-Arthritis - Reply.* American Journal of Medicine, 1995. **99**(6): p. 693-694.

37. Lenz, H.J., *Management and preparedness for infusion and hypersensitivity reactions.* Oncologist, 2007. **12**(5): p. 601-609.

38. Karve, S., M.E. Werner, R. Sukumar, N.D. Cummings, J.A. Copp, E.C. Wang, C. Li, M. Sethi, R.C. Chen, M.E. Pacold, and A.Z. Wang, *Revival of the abandoned therapeutic wortmannin by nanoparticle drug delivery.* Proceedings of the National Academy of Sciences USA, 2012. **109**(21): p. 8230-8235.

39. Green, M.R., G.M. Manikhas, S. Orlov, B. Afanasyev, A.M. Makhson, P. Bhar, and M.J. Hawkins, *Abraxane((R)), a novel Cremophor((R))-free, albumin-bound particle form of paclitaxel for the treatment of advanced non-small-cell lung cancer.* Annals of Oncology, 2006. **17**(8): p. 1263-1268.

40. O'Byrne, K.J., A.L. Thomas, R.A. Sharma, M. deCatris, F. Shields, S. Beare and S.P. Steward, *A phase I dose-escalating study of DaunoXome, liposomal daunorubicin, in metastatic breast cancer.* British Journal of Cancer, 2002. **87**(1): p. 15-20.

41. Hu, C.M.J., R.H. Fang, J. Copp, B..T. Luk, and L. Zhang, *A biomimetic nanosponge that absorbs pore-forming toxins.* Nature Nanotechnology, 2013. **8**(5): p. 336-340.

42. Crispe, I.N., *Hepatic T cells and liver tolerance.* Nature Reviews Immunology, 2003. **3**(1): p. 51-62.

43. Klugewitz, K., F. Blumenthal-Barby, A. Schrage, P.A. Knolle, A. Hamann, and I.N. Crispe, *Immunomodulatory effects of the liver: Deletion of activated CD4(+) effector cells and suppression of IFN-gamma-producing cells after intravenous protein immunization.* Journal of Immunology, 2002. **169**(5): p. 2407-2413.

44. Basarkar, A. and J. Singh, *Poly (lactide-co-glycolide)-Polymethacrylate Nanoparticles for Intramuscular Delivery of Plasmid Encoding Interleukin-10 to Prevent Autoimmune Diabetes in Mice.* Pharmaceutical Research, 2009. **26**(1): p. 72-81.

45. Getts, D.R., A.J. Martin, D.P. McCarthy, R.L. Terry, Z.N. Hunter, W.T. Yap, M.T. Getts, M. Pleiss, X. Luo, N.J. King, L.D. Shea, and S.D. Miller, *Microparticles bearing encephalitogenic peptides induce T-cell tolerance and ameliorate experimental autoimmune encephalomyelitis.* Nature Biotechnology, 2012. **30**(12): p. 1217-1224.

46. Kim, W.U., W.K. Lee, J.W. Ryoo, S.H. Kim, J. Kim, J. Youn, S.Y. Min, E.Y. Bae, S.Y. Hwang, S.H. Park, C.S. Cho, J.S. Park, and H.Y. Kim, *Suppression of collagen-induced arthritis by single administration of poly(lactic-co-glycolic acid) nanoparticles entrapping type II collagen - A novel treatment strategy for induction of oral tolerance.* Arthritis and Rheumatism, 2002. **46**(4): p. 1109-1120.

47. Fang, R.H., C.M. Hu, K.N. Chen, B.T. Luk, C.W. Carpenter, W. Gao, S. Li, D.E. Zhang, W. Lu, and L. Zhang, *Lipid-insertion enables targeting functionalization of erythrocyte membrane-cloaked nanoparticles.* Nanoscale, 2013. **5**(19): p. 8884-8.

48. Hu, C.M.J., R.H. Fang, B.T. Luk, and L. Zhang, *Polymeric nanotherapeutics: clinical development and advances in stealth functionalization strategies.* Nanoscale, 2014. **6**(1): p. 65-75.

Chapter 4, in full, is a reprint of the material as it appears in *Nature Nanotechnology*, 2013, Che-Ming Hu, Ronnie Fang, Jonathan Copp, Brian Luk, and Liangfang Zhang; *Advanced Materials*, 2015, Fei Wang, Weiwei Gao, Soracha Thamphiwatana, Brian Luk, Pavimol Angsantikul, Qiangzhe Zhang, Che-Ming Hu, Ronnie Fang, Jon Copp, Dissaya Pornpattananangkul, Weiyue Lu, and Liangfang Zhang; *ACS Nano*, 2015, Zhiqing Pang, Che-Ming Hu, Ronnie Fang, Brian Luk, Weiwei Gao, Fei Wang, Erdembileg Chuluun, Pavimol Angstantikul, Soracha Thamphiwatana, Weiyue Lu, Xinguo Jiang, and Liangfang Zhang; and *Proceedings of the National Academy of Sciences USA*, 2014, Jonathan Copp, Ronnie Fang, Brian Luk, Che-Ming Hu, Weiwei Gao, Kang Zhang and Liangfang Zhang. The dissertation author was a major contributor and co-author of these papers.

Chapter 5

Cell Membrane-Coated Nanoparticles for Vaccine Nanotechnology

5.1 Nanoparticle-Detained Toxins for Safe and Effective Vaccination

5.1.1 Introduction

Toxoid vaccines—vaccines based on inactivated bacterial toxins— are routinely used to promote antitoxin immunity for the treatment and prevention of bacterial infections [1-4]. Following chemical or heat denaturation, inactivated toxins can be administered to mount toxin-specific immune responses. However, retaining faithful antigenic presentation while removing toxin virulence remains a major challenge and presents a trade-off between efficacy and safety in toxoid development. Here we show a nanoparticle-based toxin-detainment strategy that safely delivers non-disrupted pore-forming toxins for immune processing. Using erythrocyte membrane-coated nanoparticles and staphylococcal α-hemolysin, we demonstrate effective virulence neutralization via spontaneous particle entrapment. As compared to vaccination with heat-denatured toxin, mice vaccinated with the nanoparticle-detained toxin showed superior protective immunity against toxin adverse effects. We find that the non-disruptive detoxification approach benefited the immunogenicity and efficacy of toxoid vaccines. We anticipate the reported study to open new possibilities in the preparation of antitoxin vaccines against the many virulence factors that threaten public health.

Immunization against bacterial pore-forming toxins (PFTs) has much clinical relevance as these membrane-damaging proteins underlie the virulence mechanisms in

numerous public health threats, including infections by pathogenic *Escherichia coli, Helicobacter pylori, and Staphylococcus aureus* [5-7]. Toward maximizing PFT vaccine efficacy, a major challenge lies in establishing non-toxic toxoids that preserve the antigenic epitopes of the toxin proteins. Conventional toxoid preparation via protein denaturation possesses significant shortfalls that can lead to inadequate vaccine potency and poor quality control [8]. Chemical- and heat-mediated detoxification processes are difficult to fine-tune, and they are known to disrupt a protein's tertiary structure, causing altered antigenic presentation and compromised immunogenicity [9, 10]. Although immunostimulatory adjuvants have been applied to raise the potency of denatured antigens, risk of reactogenicity and other adverse effects may occur and thus render the option less desirable [11].

Efforts to improve vaccine potency and safety have given rise to alternative toxin-inactivation strategies that subvert a toxin's virulence while preserving its native structure. For instance, non-virulent toxin mutants, prepared from recombinant protein engineering, have shown strong therapeutic efficacy in animal models and have entered human clinical trials [12-15]. These encouraging results suggest that toxoid preparation may benefit from minimally disruptive detoxification methods that better preserve a toxin's epitopic expression.

5.1.2 Experimental Methods

5.1.2.1 Preparation of RBC Membrane-Coated NPs

RBCs were collected from 6 week-old male ICR mice (Charles River

Laboratories) by centrifuging the whole blood at 800 x g for 5 min followed by hypotonic treatment to remove interior contents. The RBC ghosts were extruded through 100 nm polycarbonate porous membranes using an extruder (Avanti Polar Lipids) to prepare RBC membrane vesicles with a diameter of approximately 100 nm. Poly(lactic-*co*-glycolic acid) (PLGA) polymeric cores were prepared using 0.67 dL/g carboxy-terminated 50:50 PLGA polymer (LACTEL Absorbable Polymers) through a solvent displacement process. The RBC-membrane-coated nanoparticles were then prepared by fusing the RBC membrane vesicles onto the PLGA nanoparticles through an extrusion process (1 mg PLGA per 1 mL blood). The size and the surface zeta potential of the resulting particle vectors were obtained from three dynamic light scattering (DLS) measurements using a Malvern ZEN 3600 Zetasizer. To examine the core-shell structure of the particle vectors by transmission electron microscopy (TEM), a drop of the particle solution (1 mg/mL) was deposited onto a glow-discharged carbon-coated grid. After 1 min, it was washed with 10 drops of distilled water, stained with 1% uranyl acetate, and then imaged using an FEI Sphera Microscope at 200 kV.

5.1.2.2 Preparation of Nanotoxoid(Hla)

3 μg of Hla (Sigma-Aldrich) was incubated with particle vectors ranging from 0 to 200 μg in 100 μL of aqueous solution for 15 min. The mixtures were then filtered through a Sephacryl® 200-HR size-exclusion column (Sigma-Aldrich) to remove the unbound Hla. For protein analysis, nanotoxoid(Hla) solution was lyophilized, prepared

in lithium dodecyl sulfate (LDS) sample loading buffer (Invitrogen), and separated on a 4-12% Bis-Tris 10-well minigel in MOPS running buffer using a Novex® Xcell SureLock Electrophoresis System (Invitrogen). The resulting gel was transferred to a nitrocellulose membrane, stained with a primary sheep anti-Hla polyclonal antibody (Abcam) and a secondary rabbit anti-sheep IgG HRP conjugate (Millipore). The membrane was then subjected to ECL western blotting substrate (Pierce) and developed with the Mini-Medical/90 Developer (ImageWorks). 3 μg of free Hla was prepared alongside the nanotoxoid(Hla) solution as a standard for comparison. Subsequent characterizations were carried out using a ratio of 3 μg Hla to 200 μg particle vectors.

For the release kinetics study, 1 mL of samples at 1 mg/mL was dialyzed against PBS buffer using a Float-A-Lyzer G2 device with a molecular weight cut-off of 100 kDa (Spectrum Laboratories). At 0, 1, 2, 6, 12, 24, and 48 h time points, 20 μL of retentate was collected and analyzed by western blot analysis using known amounts of Hla as standards. Endotoxin analysis was performed using an LAL Chromogenic Endotoxin Quantitation Kit (Pierce) following manufacturer's instructions. Samples were suspended at 1 mg/mL and run alongside the provided endotoxin standards.

For immunogold staining, nanotoxoid(Hla) solution (1 mg/mL) was deposited onto a glow-discharged grid. After 1 min, the grid was washed with 10 drops of 2% BSA (Sigma-Aldrich), incubated with one drop of polyclonal rabbit anti-Hla antibody (Sigma-Aldrich) for 1 min, washed with 2% BSA, incubated with one drop of gold-labeled anti-rabbit IgG (Sigma-Aldrich) for 1 min, and then washed with distilled

water. Imaging was conducted using an FEI Sphera Microscope at 200 kV.

5.1.2.3 Cellular Uptake

100 μg of Hla was labeled with Alexa 488 dye using the Alexa Fluor® 488 Microscale Protein Labeling Kit (Life Technologies) following the manufacturer's instructions. The fluorescently labeled Hla was then used to prepare nanotoxoid(Hla). The resulting nanotoxoid(Hla) was incubated with mouse dendritic cells derived from the bone marrow of ICR mice at a concentration of 400 μg/mL in culture media. For fluorescent imaging, the cellular membranes were stained with 4 μg of DMPE-rhodamine B (Avanti Polar Lipids). Following 1 h of incubation, the media was aspirated and the cells were washed with PBS, fixed with 10% formalin (Millipore), mounted with DAPI-containing Vectashield® (Invitrogen), and imaged using a 60X oil immersion objective on an Applied Precision DeltaVision Deconvolution Scanning Fluorescence Microscope.

5.1.2.4 Live Whole-Body Imaging

Nanotoxoid(Hla) was prepared with PLGA cores labeled fluorescently with 1,1'-dioctadecyl-3,3,3',3'-tetramethylindodicarbocyanine, 4-chlorobenzenesulfonate salt (Invitrogen). 150 μL of PBS solution containing 200 μg of fluorescent nanotoxoid(Hla) loaded with 3 μg of Hla was injected subcutaneously to the neck region of mice (n=6). At the designated time points, mice were anesthetized with isoflurane (Piramal Healthcare) and imaged using a Xenogen IVIS 200 system. Fluorescent signal intensities were normalized across time points and heat maps were

overlaid on bright field images.

5.1.2.5 Skin Damage by Different Hla Preparations

For heat-treated Hla, 20 μg/mL of Hla in PBS in an eppendorf tube was submerged in a water bath equilibrated at 70°C. Both 30 and 60 min of heating were performed to inactivate the toxin. For nanotoxoid(Hla) preparation, 20 μg/mL of Hla was incubated with 1.33 mg/mL of RBC-membrane-coated nanoparticles in PBS for 15 min. An untreated free Hla solution at 20 μg/mL in PBS was prepared as control. For the skin damage study, ICR mice were shaved to remove the hair on their back. 150 μL each of untreated Hla, 30 min heat-treated Hla, 60 min heat-treated Hla, and nanotoxoid(Hla) formulations were then injected into the superficial dorsal skin of mice. For the apoptosis assay, the skin was removed from the injection site 24 h following the injection for tissue processing. O.C.T.-embedded slides were stained with ApopTag® Peroxidase In Situ Apoptosis Detection Kit (EMD Millipore) for microscopy. Histological analyses were performed with skin removed 24 h following the injections; the skin sections were stained with hematoxylin and eosin (H&E) and visualized under a microscope.

5.1.2.6 Cellular Viability and Apoptosis Studies

The cytotoxicity of Hla, nanotoxoid(Hla), heat-treated Hla (60 min treatment), and the blank particle vectors (denoted as nanotoxoid(-)) were assessed against mouse dendritic cells with a 3-(4,5-dimethylthiazol-2-yl)-2,5-diphenyltetrazolium bromide (MTT) assay (Promega). 24 h prior to the toxicity study, the cells were seeded (2 x

10^4) in 96-well plates. The culture medium was then replaced with 200 μL of fresh medium containing 3 μg of Hla, 200 μg of nanotoxoid(Hla) detaining 3 μg of Hla, 3 μg of heat-treated Hla, or 200 μg of nanotoxoid(-). Following 48 h of incubation, MTT reagent was applied to the cells following a protocol provided by the manufacturer. PBS buffer was used as a negative control.

To detect for induction of cellular apoptosis, dendritic cells were incubated with nanotoxoid(Hla) at a final concentration of 4 mg/mL particle vector and 60 μg/mL Hla in media. Two sets of experiments were conducted, one for 24 h and another for 72 h. At 2 h before each experimental endpoint, a set of untreated cells was incubated with 5% hydrogen peroxide (Sigma-Aldrich) as a positive control. All cells were collected using Accutase solution (eBioscience), washed in media containing divalent cations, and then stained with propidium iodide (PI) (Biolegend) and FITC-labeled Annexin V (Biolegend) following manufacturer's instructions. Cells were then washed again in media and analyzed by flow cytometry using a Becton Dickinson FACSCanto II. Annexin V versus propidium iodide plots were gated based on untreated cells, with the PI^{low}/Annexin V^{low} quadrant representing viable cells, the PI^{low}/Annexin V^{high} quadrant representing early apoptotic cells, and the PI^{high}/Annexin V^{high} quadrant representing late apoptotic or dead cells.

5.1.2.7 Nanotoxoid(Hla) Vaccination in Mice

Vaccination was conducted through subcutaneous injections at the neck of the mice following two different schedules: a prime only on day 0, and a prime plus two

booster vaccinations on day 7 and day 14. For the nanotoxoid(Hla) vaccination, 150 μL of PBS solution containing 200 μg of nanotoxoid(Hla) loaded with 3 μg of Hla was administered. For the heat-treated Hla vaccination, 150 μL of PBS solution containing 3 μg of Hla was administered, in which the Hla was pre-incubated at 70°C for 60 min to denature the toxin proteins. For alum formulations, 75 μL of PBS containing 3 μg of heat-denatured Hla (60 min) was allowed to adsorb to 75 μL alum (Pierce) for 1 h before injection.

5.1.2.8 Hla-Specific Antibody Response Studies

The cocktail plasma collected on day 21 from 8 mice vaccinated with prime-boost nanotoxoid(Hla) were used as the primary immunostaining against the protein content of Hla and nanotoxoid(-) separated by SDS-PAGE. Goat anti-mouse IgG HRP conjugate (Millipore) was used as the secondary staining. The stained nitrocellulose membrane was subjected to ECL western blotting substrate (Pierce) and developed with the Mini-Medical/90 Developer (ImageWorks), followed by western blotting analysis. Quantitative anti-Hla IgG titers were analyzed by ELISA using Hla-coated plates. To obtain anti-Hla IgG titer values, the lowest plasma dilution at which the optical density reading ≥ 0.5 was used. For avidity determination, samples were incubated with 6M urea for 10 min to remove weakly bound IgG prior to addition of the secondary antibody. Statistical analysis was performed with GraphPad Prism using an unpaired two-tailed t-test. To evaluate the functionalities of the anti-Hla IgG titers, 25 μL of the plasma was incubated with 1 μg of Hla for 10 min. The mixture was

subsequently mixed with 200 μL of 5% purified mouse RBCs. After 30 min of incubation, the sample mixtures were spun down at 14,000 rpm in a Beckman Coulter Microfuge® 22R Centrifuge for 10 min. The absorbance of hemoglobin in the supernatant was measured at 540 nm using a Tecan Infinite M200 Multiplate Reader to determine the degree of RBC lysis.

5.1.2.9 Autoimmune Studies

Mice were immunized with nanotoxoid(Hla) on the prime-boost schedule as described above. Serum was collected on day 6 and 21 after initial injection, corresponding to the peak production of IgM, and IgG/IgA antibody isotypes, respectively. Autoimmune titers were analyzed using RBC-coated plates. Goat anti-mouse IgM-HRP, IgA-HRP, or IgG-HRP (Southern Biotech) was used as the secondary antibody for detecting the presence of auto-antibodies against RBCs. For RBC counts, whole blood collected from mice on day 6 or day 21 was analyzed using a Drew Scientific Hemavet.

5.1.2.10 Protective Immunity via Systemic Challenge

Hla at a concentration of 60 μg/mL was prepared in PBS. Mice from the different vaccination groups were injected intravenously through the tail vein with 120 μg/kg of Hla. Following the injections, the mice were monitored for survival for 15 days. The sample size for each group was 10 mice. Statistical analysis was performed with GraphPad Prism using a log-rank significance test.

5.1.2.11 Protective Immunity via Subcutaneous Challenge

Hla at a concentration of 100 μg/mL was prepared in PBS. Mice from the different vaccination groups were injected subcutaneously on their back with 50 μL of the Hla solution. Following the injections, the mice were monitored for skin lesions for 14 days. The sample size for each group was 6 mice.

5.1.3 Results and Discussion

To inactivate PFTs without protein denaturation, we neutralise toxins' membrane-damaging activity using a red blood cell (RBC) membrane-coated nanoparticle system [16, 17]. The particle-stabilized biomembranes serve to anchor PFTs without compromising the toxins' structural integrity (Figure 5.1A,B). Using staphylococcal α-hemolysin (Hla) as a model toxin and mixing it with preformed RBC membrane-coated nanoparticles, we first demonstrated the facile preparation of the Hla-loaded nanotoxoids, denoted as nanotoxoid(Hla). Upon removal of the unbound toxin, Hla retention within the nanotoxoids was examined using western blotting (Figure 5.1C). The results indicate that 200 μg of the particle vectors was sufficient to absorb 3 μg of Hla, translating to an Hla-to-particle ratio ≈ 40:1. At this toxin loading level no observable changes in the particle's size, structure, and zeta potential were detected and endotoxin was determined to be undetectable. A release kinetics study further demonstrated that no subsequent toxin release from the nanotoxoid(Hla) occurred over a period of 48 h (Figure 5.1D), indicating that the Hla was safely locked into the particle vector. By labelling Hla with a fluorescent dye, it was

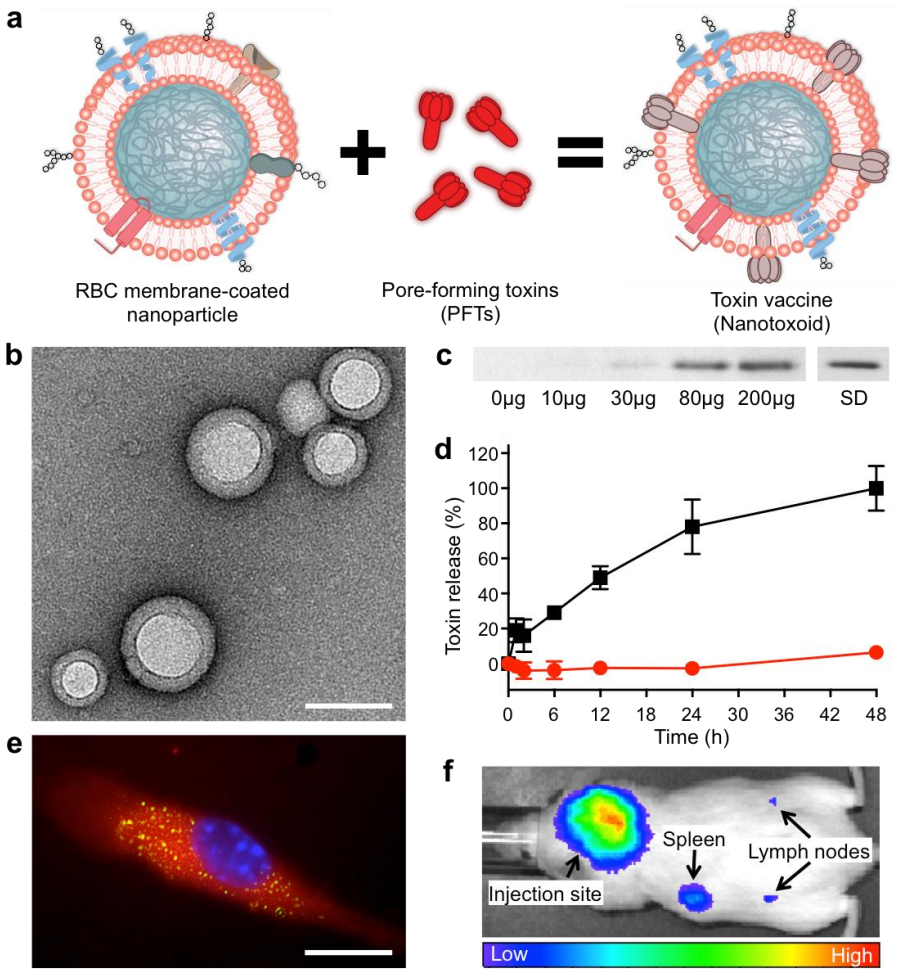

Figure 5.1 Schematic and *in vitro* characterizations. (A) Schematic preparation of nanoparticle-detained toxins, denoted as nanotoxoid, consisting of substrate-supported RBC membranes into which pore-forming toxins (PFTs) can spontaneously incorporate. (B) TEM visualization of the particle vectors with uranyl acetate staining (scale bar = 80 nm). (C) Western blotting results to verify the retention of 3 μg of staphylococcal α-hemolysin (Hla) by varying amounts of the particle vectors using 3 μg of free Hla as a standard (SD). (D) Release of toxin from the Hla-loaded nanotoxoids, denoted as nanotoxoid(Hla), over time in PBS buffer. Red circles indicate nanotoxoid(Hla) and black squares indicate free Hla. Error bars represent standard errors of the mean. (E) Uptake of nanotoxoid(Hla) by a mouse dendritic cell (scale bar = 10 μm). The cell is membrane stained with DMPE-rhodamine B (red) and nuclei stained with DAPI (blue). FITC-labelled Hla (green) was used to monitor the toxin uptake. (F) Live, whole-body fluorescent imaging of nanotoxoid(Hla) at 1 h after subcutaneous administration.

observed that the nanotoxoid(Hla) enabled uptake of toxins by immune cells. Upon incubation with mouse dendritic cells, fluorescence microscopy revealed the nanotoxoid(Hla) as distinct features within the cells (Figure 5.1E), which is consistent with the pattern of endocytic uptake frequently observed with nanoparticle vectors [18,

19]. Through direct engulfment of Hla into the digestive endolysosomal compartments, the nanoparticle-facilitated cellular endocytosis precludes the toxin's perforating attack on cellular membranes and thus allows non-disrupted toxin to be delivered for immune processing. Subcutaneous injection of the nanotoxoid(Hla) to mice showed lymphatic drainage of the particles over time, suggesting the ability of the particle vecto r to deliver Hla efficiently to the immune system *in vivo* (Figure 5.1F).

To assess the toxin inactivation in the nanotoxoid, 200 μg of nanotoxoid(Hla) detaining 3 μg of Hla was injected into the superficial dorsal skin of mice. Untreated free Hla, Hla heated at 70°C for 30 min, and Hla heated at 70°C for 60 min were tested in parallel at an equivalent Hla dose. 24 h following the injections, the skin was sectioned to evaluate the toxicity of the different formulations using both *TUNEL assay* and haematoxylin and eosin (H&E) assay (Figure 5.2A). It was revealed that untreated Hla caused a significant level of cellular apoptosis and observable lesions in the skin. Toxin neutralization by heat was shown to be time-dependent, as Hla heated for 30 min remained damaging to the skin, whereas 60 min of heating removed the toxin virulence. For the skin injected with the nanotoxoid(Hla), the epithelial structure remained intact and no cellular apoptosis was observed outside of hair follicles. Visual examination of mice subcutaneously administered with the nanotoxoid(Hla) also showed no observable lesions 48 h following the injections. This lack of toxin damage was observed consistently in 10 mice per test group. *In vivo* imaging of nanotoxoid(Hla) showed that the particles were eventually cleared over time as there was no trace of the particles after 2 weeks. To further confirm that the nanotoxoid can

safely present the toxin antigens to antigen-presenting cells, an *in vitro* cytotoxicity test was conducted on mouse dendritic cells. Upon 48 h of incubation in 15 μg/mL of Hla content, untreated Hla resulted in 70% decrease in cell viability, whereas both heat-denatured Hla (60 min treatment) and nanotoxoid(Hla) showed no reduction

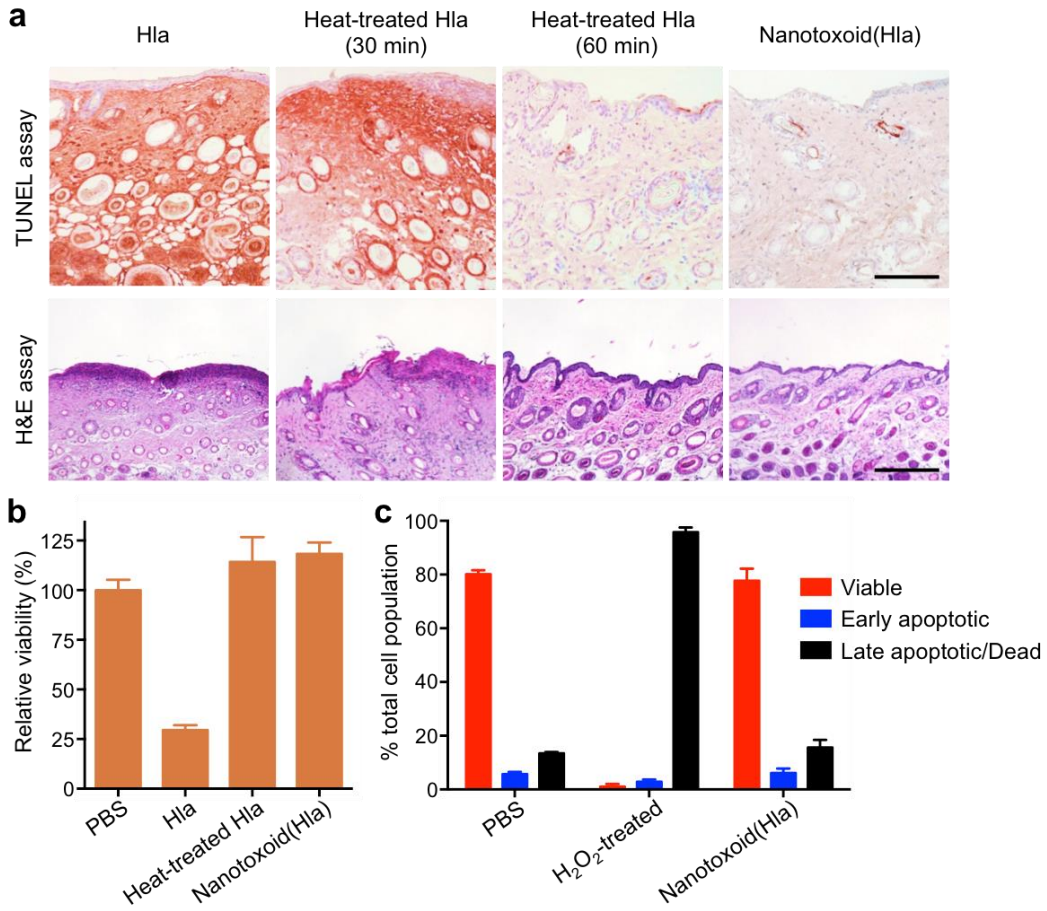

Figure 5.2 Hla virulence neutralization. (A) Free Hla, heat-treated Hla (30 min), heat-treated Hla (60 min), and nanotoxoid(Hla) were injected into the superficial dorsal skin of mice. 24 h following the injections, the skin was removed and examined for apoptosis using a TUNEL assay. Histological analyses were performed with H&E stained skin 48 h following the injections (Scale bar = 400 μm). (B) Toxicity of different Hla formulations against dendritic cells derived from mice. The cells were incubated for 48 h with Hla, heat-treated Hla (60 min) and nanotoxoid(Hla) at 15 μg/mL Hla concentration. Cellular viability was assessed using an MTT assay (n=6). (C) Induction of dendritic cell apoptosis by nanotoxoid(Hla) at 60 μg/mL Hla concentration 72 h after initial incubation. Propidium iodide and Annexin V staining were analysed by flow cytometry (n=6). All errors bars represent standard errors of the mean.

(Figure 5.2B). Flow cytometric analysis showed that the nanotoxoid(Hla) did not induce any additional underlying cellular apoptosis compared to untreated cells over a 72 h period (Figure 5.2C). These results confirm the safety and reliability of the nanotoxoid-based toxin inactivation, which allows non-denatured toxin antigens to interact with tissues and immune cells with the same level of safety as those treated with extended heating.

Next, immunization studies were conducted to examine the vaccine potential of the nanotoxoid(Hla). An emphasis was placed on the elicitation of neutralizing antibodies, which are the hallmark of antitoxin immunity. Two vaccination schedules were performed: a prime only on day 0, and a prime on day 0 followed by two booster vaccinations on day 7 and day 14. To verify that the nanotoxoid(Hla) could indeed elicit Hla-specific antibodies, the plasma from 8 mice immunized with nanotoxoid(Hla) on a prime-boost schedule was pooled together and used as the primary immunostain for western blotting analysis. The results confirmed the presence of anti-Hla immunoglobulin G (IgG) (Figure 5.3A). It is important to note that this cocktail plasma showed no detectable cross-reactivity with the protein content on the blank particle vectors, denoted as nanotoxoid(-). To further confirm the lack of an autoimmune response, we demonstrated that mice immunized with nanotoxoid(Hla) exhibited no serum immunoglobulin M, immunoglobulin A, or immunoglobulin G antibodies against RBC proteins. RBC counts were at a similar level as compared to unvaccinated mice, indicating no induction of autoimmune anaemia (Figure 5.3B). The results indicate that the RBC membranes provide a non-immunogenic substrate

for toxin-detainment, enabling the cargo antigens to be processed selectively without raising potential complications associated with anti-vector immunity [20, 21].

The ability of the nanotoxoid(Hla) to elicit anti-Hla antibodies was then quantified. Determination of antibody responses on day 21 showed that the nanotoxoid(Hla) induced significantly higher Hla-specific antibody titres as compared to the heat-treated Hla (60 min treatment). Enhancements by 7- and 15-fold (geometric mean) under the prime only ($p = 0.0951$, $n=7$) and prime-boost vaccinations ($p=0.0077$, $n=7$), respectively (Figure 5.1.3C). The increased titre level of nanotoxoid(Hla) was sustainable in a time course study over 150 days (Figure 5.3D). Because previous report [22] and our own study have indicated that adjuvants do not significantly boost titre responses for immunizations using denatured Hla, no adjuvant was used in this study in order to best highlight the nanotoxoid(Hla) platform as an effective mode of attenuating toxicity while preserving immunogenicity of toxins. The nanotoxoid(-) vector alone did not induce a detectable antibody response (Figure 5.3C), and the vector mixture with heat-treated Hla showed negligible enhancement in titre levels as compared to heat-treated Hla alone. These results highlight the challenge in raising immunogenicity of denatured toxins and demonstrate the benefit of using detained, but undenatured antigens for vaccination.

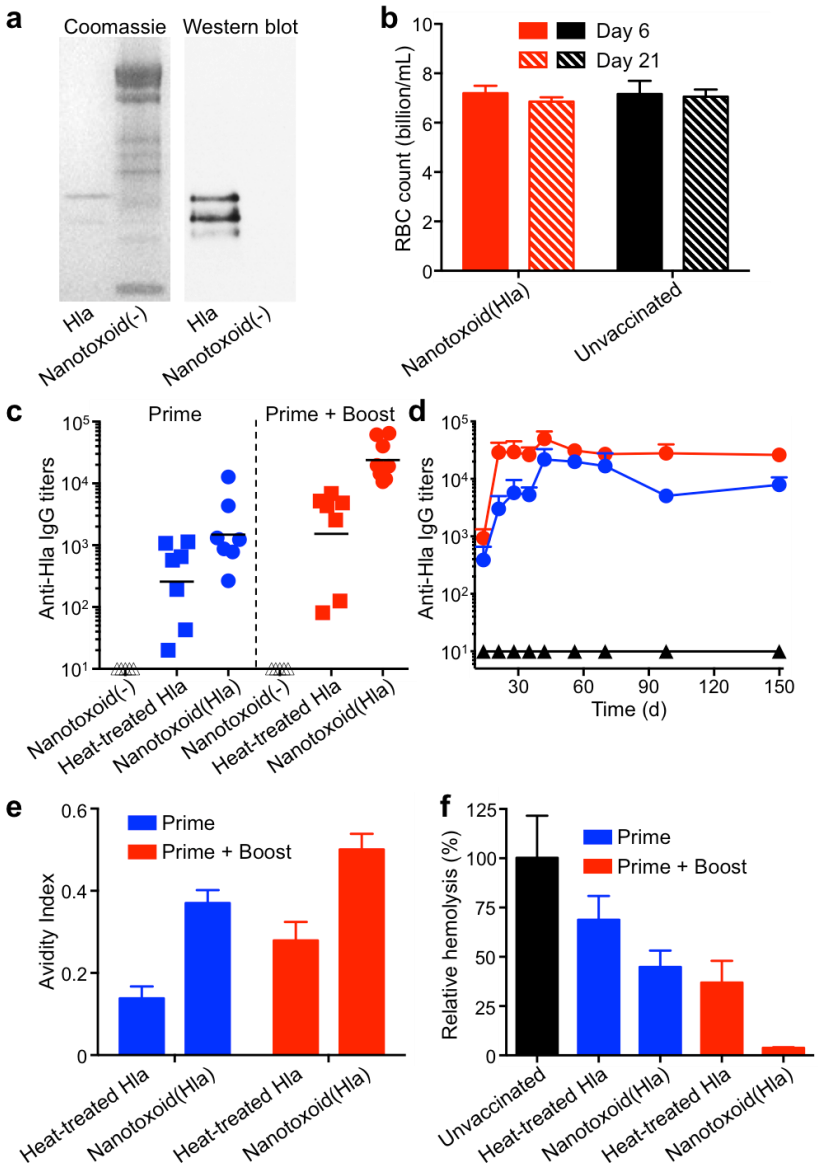

Figure 5.3 Antibody responses. (A) Hla-specific antibody responses were verified in the nanotoxoid(Hla)-vaccinated mice through coomassie staining (left panel) and western blotting (right panel). Blank particle vector, denoted as nanotoxoid(-), was used as a control. (B) RBC counts of mice immunized with nanotoxoid(Hla) (n=6). (C) Anti-Hla IgG titres at day 21 (n=7). Black lines indicate geometric means. Anti-Hla titres from mice vaccinated with non-toxin loaded particle vectors (nanotoxoid(-)) were monitored as controls (triangle). (D) Time course of anti-Hla IgG titres in unvaccinated mice (black triangle) and mice immunized with nanotoxoid(Hla) (prime + boost; red circle) or nanotoxoid(Hla) (prime only; blue circle) (n=7). (E) Avidity index of the anti-sera from immunized mice binding to Hla toxin was quantified (n=7). (f) An RBC haemolysis assay was performed to verify the presence of functional titres (n=7). All error bars represent standard errors of the mean.

The nanotoxoid(Hla) also helped to improve antibody affinity to the targeted toxin, as was evidenced by the increased avidity of the antibody titres (Figure 5.3E). To confirm that the antibody titres were capable of neutralizing Hla, an RBC haemolysis assay was conducted. Hla was mixed with the plasma from vaccinated mice and then incubated with purified mouse RBCs. The plasma from unvaccinated mice was used as a control and the haemolytic activity of Hla was determined by measuring the amount of released haemoglobin. The results showed that plasma from nanotoxoid(Hla)-vaccinated mice was more potent at neutralizing the toxin. For the prime-boost nanotoxoid(Hla) vaccination group, 25 μL of plasma was sufficient to completely inhibit the haemolytic activity of 1 μg of Hla (Figure 5.3F). We speculate that the improved titre responses from nanotoxoid(Hla) were due to epitopic preservation of the undenatured toxin as well as to well documented benefits of particulate antigen vectors, which can enhance antigen uptake and processing by immune cells [23, 24].

Finally, the protective immunity bestowed by the nanotoxoid(Hla) vaccine was evaluated by subjecting the vaccinated mice to both systemic and subcutaneous toxin administration. 21 days following the prime vaccination, the mice received a lethal bolus dose of Hla at 120 μg/kg through intravenous tail vein injection. This toxin dose resulted in 100% mortality within 2 h in the unvaccinated group. For the mice receiving the prime vaccination only, the benefit of the nanotoxoid(Hla) over the heat-treated Hla was evident as the survival rate increased from 10% to 50% (n=10). Moreover, nanotoxoid(Hla) boosters further improved the survival rate to 100% while

a 90% survival rate was achieved by the heat-treated Hla vaccine with boosters (n=10) (Figure 5.4A). Since Hla has also been identified as a key factor in necrotizing skin infections [25], a subcutaneous toxin administration was also conducted to further evaluate the vaccine's effectiveness in mounting immunity in skin tissue. Observation of skin damage following a 50 µL subcutaneous injection of 100 µg/mL Hla on the back region showed reduced lesion areas in all vaccinated mice, reflecting the presence of extravascular IgG that diminished the subcutaneous toxin threat. With the prime only vaccination, the nanotoxoid(Hla) vaccine conferred modestly stronger protection than the heat-treated Hla. Following booster vaccinations, however, the nanotoxoid(Hla) resulted in complete eradication of the toxin damage. In contrast, the mice vaccinated with the heat-treated Hla boosters remained susceptible to the necrotizing toxin (Figure 5.4B).

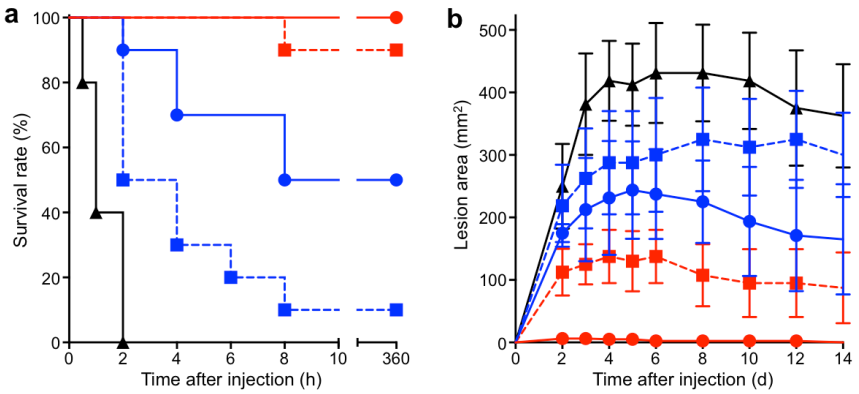

Figure 5.4 Protective immunity. Unvaccinated mice (black) and mice vaccinated with heat-treated Hla (prime; blue square), nanotoxoid(Hla) (prime; blue circle), heat-treated Hla (prime + boost; red square), or nanotoxoid(Hla) (prime + boost; red circle) received intravenous or subcutaneous administration of Hla. (A) Survival rates of mice over a 15-day period following intravenous injections of 120 µg/kg Hla on day 21 via the tail vein (n=10). (B) Skin lesion size comparison following subcutaneous injections of 5 µg of Hla on day 21. The lesion size was measured for 14 days following the administration. Error bars represent standard errors of the mean (n=6).

5.1.4 Conclusions

Compared to the commonly used protein denaturation approach to achieve toxin vaccination, the non-disruptive preparation described here yielded a nanotoxoid with stronger immunogenicity and superior efficacy. Refinement of this approach can benefit from the unique strengths of nanoparticle-based immunoengineering [26, 27], in which vaccine targeting to lymphoid organs and processing by antigen-presenting cells can be enhanced through nanovector designs [24, 28, 29]. Moving forward, this nanotoxoid platform can be generalized for other types of cellular membrane-coated particles [30] and for the neutralization and delivery of other potent toxins to create a broad range of safe and effective antitoxin vaccines. For clinical test and use in humans, it can be applied either on the basis of patients' blood types following a cross-match test or using donor blood from type O- individuals, as in the case of blood transfusion.

5.1.5 References

1. Kitchin, N.R., *Review of diphtheria, tetanus and pertussis vaccines in clinical development.* Expert Review of Vaccines, 2011. **10**(5): p. 605-615.

2. Greenberg, R.N., T.C. Marbury, G. Foglia, and M. Warny, *Phase I dose finding studies of an adjuvanted Clostridium difficile toxoid vaccine.* Vaccine, 2012. **30**(13): p. 2245-2249.

3. Mortimer, E.A., Jr., *Immunization against infectious disease.* Science, 1978. **200**(4344): p. 902-907.

4. Holmgren, J., A.M. Svennerholm, I. Lonnroth, M. Fall-Persson, B. Markman, and H. Lundbeck, *Development of improved cholera vaccine based on subunit toxoid.* Nature, 1977. **269**(5629): p. 602-604.

5. Gentschev, I., G. Dietrich, and W. Goebel, *The E. coli alpha-hemolysin secretion system and its use in vaccine development.* Trends in Microbiology, 2002. **10**(1): p. 39-45.

6. Cover, T.L. and S.R. Blanke, *Helicobacter pylori VacA, a paradigm for toxin multifunctionality.* Nature Reviews Microbiology, 2005. **3**(4): p. 320-332.

7. Bubeck Wardenburg, J. and O. Schneewind, *Vaccine protection against Staphylococcus aureus pneumonia.* The Journal of Experimental Medicine, 2008. **205**(2): p. 287-294.

8. Parish, H.J. and D.A. Cannon, *Staphylococcal infection: antitoxic immunity.* British Medical Journal, 1960. **1**(5175): p. 743-747.

9. Metz, B., G.F. Kersten, P. Hooberhout, H.F. Brugghe, H.A. Timmermans, A. de Jong, H. Meiring, J. ten Hove, W.E. Hennink, D.J. Crommelin, and W. Jiskoot, *Identification of formaldehyde-induced modifications in proteins: reactions with model peptides.* The Journal of Biological Chemistry, 2004. **279**(8): p. 6235-6243.

10. Cryz, S.J., Jr., E. Furer, and R. Germanier, *Effect of chemical and heat inactivation on the antigenicity and immunogenicity of Vibrio cholerae.* Infection and Immunity, 1982. **38**(1): p. 21-26.

11. Vogel, F.R., *Improving vaccine performance with adjuvants.* Clinical Infectious Diseases, 2000. **30 Suppl 3**: p. S266-270.

12. Kennedy, A.D., J. Bubeck Wardenburg, D.J. Gardner, D. Long, A.R. Whitney, K.R. Braughton, O. Schneewing, and F.R. DeLeo, *Targeting of alpha-hemolysin by active or passive immunization decreases severity of USA300 skin infection in a mouse model.* The Journal of Infectious Diseases, 2010. **202**(7): p. 1050-1058.

13. Adhikari, R.P., H. Karauzum, J. Sarwar, L. Abaandou, M. Mahmoudieh, A.R. Boroun, H. Vu, T. Nguyen, V.S. Devi, S. Shulenin, K.L. Warfield, and M.J. Aman, *Novel structurally designed vaccine for S. aureus alpha-hemolysin: protection against bacteremia and pneumonia.* PLoS One, 2012. **7**(6): p. e38567.

14. Jang, S.I., H.S. Lillehoj, S.H. Lee, K.W. Lee, E.P. Lillehoj, Y.H. Hong, D.J. An, W. Jeong, J.E. Chun, F. Bertrand, L. Dupuis, S. Deville, and J.B. Arous, *Vaccination with Clostridium perfringens recombinant proteins in combination with Montanide ISA 71 VG adjuvant increases protection against experimental necrotic enteritis in commercial broiler chickens.* Vaccine, 2012. **30**(36): p. 5401-5406.

15. Kirkham, L.A., A.R. Kerr, G.R. Douce, G.K. Paterson, D.A. Dilts, D.F. Liu, and T.J. Mitchell, *Construction and immunological characterization of a novel nontoxic protective pneumolysin mutant for use in future pneumococcal vaccines.* Infection and Immunity, 2006. **74**(1): p. 586-593.

16. Hu, C.M., L. Zhang, S. Aryal, C. Cheung, R.H. Fang, and L. Zhang, *Erythrocyte membrane-camouflaged polymeric nanoparticles as a biomimetic delivery platform.* Proceedings of the National Academy of Sciences USA, 2011. **108**(27): p. 10980-10985.

17. Hu, C.M., R.H. Fang, J. Copp, B.T. Luk, and L. Zhang, *A biomimetic nanosponge that absorbs pore-forming toxins.* Nature Nanotechnology, 2013. **8**: p. 336-340.

18. Dobrovolskaia, M.A. and S.E. McNeil, *Immunological properties of engineered nanomaterials.* Nature Nanotechnology, 2007. **2**(8): p. 469-478.

19. Moon, J.J., H. Suh, A. Bershteyn, M.T. Stephan, H. Liu, B. Huang, M. Sohail, S. Luo, S.H. Um, H. Khant, J.T. Goodwin, J. Ramos, W. Chiu, and D.J. Irvine, *Interbilayer-crosslinked multilamellar vesicles as synthetic vaccines for potent humoral and cellular immune responses.* Nature Materials, 2011. **10**(3): p. 243-251.

20. Sun, C., L. Feng, Y. Zhang, L. Xiao, W. Pan, C. Li, L. Zhang, and L. Chen, *Circumventing antivector immunity by using adenovirus-infected blood cells for repeated application of adenovirus-vectored vaccines: proof of concept in rhesus macaques.* Journal of Virology, 2012. **86**(20): p. 11031-11042.

21. Roberts, D.M., A. Nanda, M.J. Havenga, P. Abbink, D.M. Lunch, B.A. Ewand, J. Liu, A.R. Thorner, P.E. Swanson, D.A. Gorgone, M.A. Lifton, A.A. Lemckert, L. Holterman, B. Chen, A. Dilraj, A. Carville, K.G. Mansfield, J. Goudsmit, and D.H. Barouch, *Hexon-chimaeric adenovirus serotype 5 vectors circumvent pre-existing anti-vector immunity.* Nature, 2006. **441**(7090): p. 239-243.

22. Skean, J.D. and W.W. Overcast, *Efficacy of staphylococcal vaccines to elicit antistaphylococcal alpha-hemolysin in dairy cows.* Journal of Dairy Science, 1968. **51**(8): p. 1239-1242.

23. Elamanchili, P., M. Diwan, M. Cao, and J. Samuel, *Characterization of poly($_{D,L}$-lactic-co-glycolic acid) based nanoparticulate system for enhanced delivery of antigens to dendritic cells.* Vaccine, 2004. **22**(19): p. 2406-2412.

24. Moon, J.J., H. Suh, A.V. Li, C.F. Ockenhouse, A. Yadava, and D.J. Irvine, *Enhancing humoral responses to a malaria antigen with nanoparticle vaccines*

that expand Tfh cells and promote germinal center induction. Proceedings of the National Academy of Sciences USA, 2012. **109**(4): p. 1080-1085.

25. Inoshima, I., N. Inoshima, G.A. Wilke, M.E. Powers, K.M. Frank, Y. Wang, and J. Bubeck Wardenburg, *A Staphylococcus aureus pore-forming toxin subverts the activity of ADAM10 to cause lethal infection in mice.* Nature Medicine, 2011. **17**(10): p. 1310-1314.

26. Moon, J.J., B. Huang, and D.J. Irvine, *Engineering nano- and microparticles to tune immunity.* Advanced Matererials, 2012. **24**(28): p. 3724-3746.

27. Swartz, M.A., S. Hirosue, and J.A. Hubbell, *Engineering approaches to immunotherapy.* Science Translational Medicine, 2012. **4**(148): p. 148rv9.

28. Reddy, S.T., A.J. van der Vlies, E. Simeoni, V. Angeli, G.J. Randoph, C.P. O'Neil, L.K. Lee, M.A. Swartz, and J.A. Hubbell, *Exploiting lymphatic transport and complement activation in nanoparticle vaccines.* Nature Biotechnology, 2007. **25**(10): p. 1159-1164.

29. Hubbell, J.A., S.N. Thomas, and M.A. Swartz, *Materials engineering for immunomodulation.* Nature, 2009. **462**(7272): p. 449-460.

30. Parodi, A., N. Quattrocchi, A.L. van de Ven, C. Chiappini, M. Evangelopoulos, J.O. Martinez, B.S. Brown, S.Z. Khaled, I.K. Yazdi, M.V. Enzo, L. Isenhart, M. Ferrarri, and E. Tasciotti, *Synthetic nanoparticles functionalized with biomimetic leukocyte membranes possess cell-like functions.* Nature Nanotechnology, 2013. **8**(1): p. 61-68.

5.2 Nanoparticle-Based Anti-Virulence Vaccine for Treatment of MRSA Skin Infection

5.2.1 Introduction

The continued rise of antibiotic-resistant bacteria has become a significant burden on global health and is responsible for an increased rate of life-threatening infections observed in the clinic [1]. The issue continues to rise to the forefront as the development of new antibiotics has slowed to a near halt [2], prompting physicians and scientists to explore alternative strategies to control bacterial infections [3]. Among the different approaches, anti-virulence vaccination is a compelling strategy as it promotes host immunity by training the body to detect and disarm specific mechanisms employed by pathogens during host invasion [4]. This approach has been shown to inhibit the ability of pathogens to colonize within a host and is less susceptible to the development of resistance as it does not exert direct selective pressure on individual bacterium [5]. Anti-virulence vaccination is most commonly accomplished through the use of toxoids, or inactivated forms of live bacterial toxins, which include the commonly used tetanus toxoid [6] and diphtheria toxoid [7]. Conventionally, these toxoids are prepared by denaturation via either chemical or heat treatment in order to eliminate the dangerous effects of the original toxin [8]. However, such inactivation methods are often disruptive and can lead to altered antigen presentation as well as compromised immunogenicity [9]. To overcome the tradeoff

between safety and efficacy, emerging techniques are being developed to produce vaccine candidates that faithfully present antigenic epitopes for immune processing [10].

Methicillin-resistant *Staphylococcus aureus* (MRSA) is an antibiotic-resistant pathogen that represents a significant threat to public health, especially in hospital environments where many patients have weakened immune systems that are incapable of naturally fending off infection [11]. It can cause severe skin lesions and can ultimately be life-threatening upon systemic invasion [12]. The pace of resistance exhibited by MRSA has severely limited treatment options, with many strains of the bacteria being unresponsive to all of the most commonly used antibiotics [13, 14]. This has led researchers to explore other forms of treatment, including the aforementioned anti-virulence therapy. Known to secrete many different types of exotoxins, MRSA represents a good target for such therapies. One of its major virulence factors is α-hemolysin (Hla) [15], a toxin that forms heptameric pores on cell surfaces, which contributes greatly to the pathogenesis of MRSA during the process of infection [16]. In fact, it has been shown that the virulence of the pathogen correlates strongly with the level of Hla production [17, 18]. Further, immunization with a mutant form of Hla has been shown to confer protection against *Staphylococcus aureus* (*S. aureus)* pneumonia in mice [19]. Passive immunization with anti-Hla antibodies also protected against skin lesions caused by subsequent *S. aureus* infection, further attesting to the utility of such a strategy for combating the pathogen.

The application of novel nanomaterials towards vaccine design has the potential to bring about significant improvements via efficient and finely controlled immune manipulation [20-25]. We have previously demonstrated a nanoparticle-mediated toxin detainment strategy for the preparation of a safe and potent toxoid formulation. Biomimetic nanoparticles are fabricated with a cell membrane-derived coating that presents a natural substrate for pore-forming toxins [26, 27], leading to their stable entrapment onto the nanoparticles and enabling safe delivery *in vivo* for immune processing [28]. Owing to the non-disruptive approach of this detainment strategy, the platform was demonstrated to be superior to a traditionally formed toxoid by generating higher anti-Hla titers with increased avidity. Further, vaccination with the detained toxin conferred a significant survival benefit in a murine model of lethal toxin challenge. In the present work, we investigated the protective capabilities of nanoparticle-detained staphylococcal Hla, denoted nanotoxoid(Hla), against live bacterial challenge using a mouse model of MRSA skin infection (Figure 5.5). The immune potentiating effect of the nanoparticle formulation was studied more in-depth by looking at the formation of germinal centers in the draining lymph nodes of vaccinated mice, which was then correlated to anti-Hla titer production. The ability of the nanotoxoid(Hla) vaccine to protect against MRSA infection and lessen bacterial colonization was evaluated in a mouse model of skin lesion formation. Beyond local infection, the effect of the nanoparticle vaccination on bacterial invasiveness was further studied by enumerating the bacterial load in major organs.

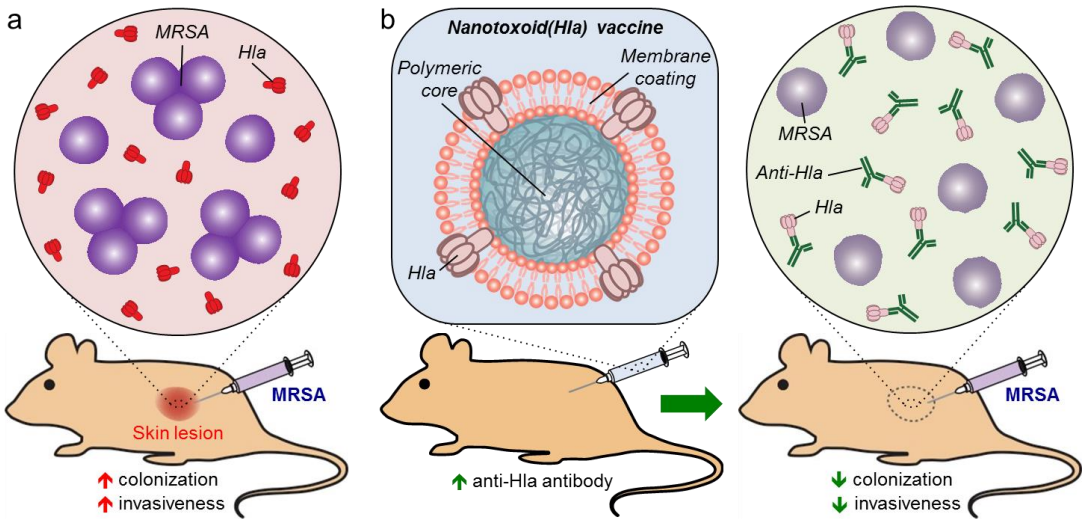

Figure 5.5 Schematic of nanotoxoid(Hla) protection against MRSA infection. (A) Under normal conditions, MRSA bacteria employ Hla to help them colonize the site of challenge, resulting in significant skin lesion formation and systemic invasiveness. (B) After vaccination with the nanotoxoid(Hla) formulation, anti-Hla titers are induced. These antibodies neutralize the toxin produced by the MRSA bacteria at the site of challenge, reducing the ability of the pathogen to colonize and enter into systemic circulation.

5.2.2 Experimental Methods

5.2.2.1 Preparation and Characterization of Nanotoxoid(Hla)

Red blood cell (RBC) membrane-coated nanoparticles were prepared as previously described [26]. Polymeric cores were made using 0.67 dL/g carboxy-terminated 50:50 poly(lactic-*co*-glycolic acid) (PLGA; LACTEL Absorbable Polymers) with a modified nanoprecipitation method. The polymer was dissolved in acetone at a concentration of 10 mg mL^{-1} and added rapidly to 2 mL of deionized water. The mixture was placed under vacuum for 3 h to evaporate the organic solvent. To obtain the membrane material, RBCs collected from 6-week old male CD-1 mice (Harlan Laboratories) were treated with hypotonic medium and washed multiple times

by centrifugation. The final RBC membrane-coated nanoparticles, denoted nanotoxoid(-) were synthesized by sonicating a mixture of the PLGA cores and RBC membrane using a Fisher Scientific FS30D bath sonicator at a frequency of 42 kHz and a power of 100 W for 2 min. The membrane material from 1 mL of mouse blood was used to coat 5 mg of 100 nm PLGA cores. The nanotoxoid(Hla) was generated by incubating 0.2 mg of nanotoxoid(-) with 3 μg of Hla at 37 °C for 15 min. Nanoparticle concentrations for both the nanotoxoid(Hla) and nanotoxoid(-) formulations are expressed as milligrams of PLGA per 1 mL of solution (mg mL^{-1}). The mixture was then filtered through a Sepharose CL-4B (Sigma Aldrich) column to obtain purified nanotoxoid(Hla) free of unbound toxin. The size and the zeta potential of the different nanoformulations were measured by dynamic light scattering (DLS) using a Malvern ZEN 3600 Zetasizer. The structure of the nanotoxoid(Hla) was examined using a Zeiss Libra 120 PLUS EF-TEM Transmission Electron Microscope. Samples were negatively stained with 0.1 wt% uranyl acetate prior to visualization.

5.2.2.2 Nanotoxoid(Hla) Loading Analysis

An immunogold staining assay was carried out to confirm insertion of Hla onto the RBC membrane-coated nanoparticles. One drop of nanotoxoid(Hla) or nanotoxoid(-) solution was added onto a glow-discharged carbon coated 400-mesh copper grid (Electron Microscopy Sciences). The grids were then washed before subjecting to blocking with 1 wt% bovine serum albumin (BSA), primary immunostaining with polyclonal rabbit anti-Hla antibody (Sigma Aldrich), and

secondary staining with gold-labeled anti-rabbit IgG antibody (Sigma Aldrich). Images were obtained using a Zeiss Libra 120 PLUS EF-TEM Transmission Electron Microscope without negative staining. To analyze Hla retention by dot blot analysis, 1 μL of nanotoxoid(Hla) solution at 2 mg mL^{-1} was dropped onto a nitrocellulose membrane and allowed to fully dry under vacuum. Afterwards, the membrane was blocked with 1 wt% BSA solution and then probed with a polyclonal rabbit anti-Hla primary antibody (Sigma Aldrich) followed by a donkey anti-rabbit IgG-horseradish peroxidase (HRP) conjugate secondary antibody (Biolegend). The blot was developed with ECL western blotting substrate (Pierce) using a Mini-Medical/90 Developer (ImageWorks). Nanotoxoid(-) solution at 2 mg mL^{-1} was used as negative control and Hla solution corresponding to 100% loading (30 μg mL^{-1}) was used as positive control. Blot intensity was measured by analyzing the mean gray values of dots via Image J software.

5.2.2.3 Germinal Center Analysis

All animal experiments followed protocols that were reviewed, approved and performed under the regulatory supervision of the University of California, San Diego's institutional biosafety program and the Institutional Animal Care and Use Committee (IACUC). Six-week old male CD-1 mice (Harlan Laboratories) were immunized subcutaneously in the lateral tarsal region just above the ankle with 0.1 mg of nanotoxoid(Hla). Nanotoxoid(-) and PBS were used as negative controls. On day 21 post-immunization, the mice were euthanized and the draining popliteal lymph nodes

were collected for analysis. For immunohistochemical analysis, the lymph nodes were cryosectioned and stained with anti-mouse/human B220-Pacific Blue, anti-mouse IgD-Alexa Fluor 488, and anti-mouse/human GL-7-Alexa Fluor 647 antibodies (Biolegend). For flow cytometry analysis, Lymph nodes were digested in 1 mg mL^{-1} collagenase D (Roche) solution, and stained with the above antibodies. Data was collected using a BD FACSCanto-II flow cytometer and analyzed using Flowjo software.

5.2.2.4 Anti-Hla Titer Analysis

Mice were subcutaneously administered with 0.1 mg of nanotoxoid(Hla), 0.1 mg of nanotoxoid(-) or PBS, followed by a boost 14 days later (n=6). On days 0, 14 and 35, the serum of each mouse was collected to assay for Hla-specific antibody titers by an enzyme-linked immunosorbent assay (ELISA). A 96-well plate was coated overnight with 2 μg ml^{-1} Hla using commercial coating buffer (Biolegend). The wells were then blocked with 5 wt% milk before adding serially diluted serum samples as the primary antibody. Goat anti-mouse IgG-HRP (Biolegend) was then employed as the secondary antibody. The plate was developed with 1-Step Slow TMB-ELISA substrate (Pierce) and measured at 450 nm with a Tecan Infinite M200 Multiplate Reader.

5.2.2.5 MRSA Infection and Vaccine Efficacy

The MRSA strain USA300 TCH1516 (American Type Culture Collection) was used in this study. The bacteria were cultured at 37 °C in tryptic soy broth, harvested

by centrifugation, washed, suspended with PBS and adjusted to the appropriate concentration by optical density measurements before use. Mice immunized with 0.1 mg of nanotoxoid(Hla), 0.1 mg of nanotoxoid(-), or PBS on days 0 and 14 were challenged with 1×10^9 CFU of the bacteria on day 35. The bacteria were inoculated subcutaneously in the back region in an area that was carefully shaved using hair clippers before the challenge. The dermonecrotic area was monitored daily and reported as the width multiplied by the height of the visible lesion. On day 6 post-challenge the mice were euthanized, perfused with PBS via the heart, and the skin, heart, liver, spleen, lungs, and kidneys of each mouse were excised and processed for enumeration. Briefly, organs were homogenized in sterile PBS using a Biospec Mini BeadBeater, diluted 10-fold serially with PBS, plated onto tryptic soy agar, and finally the colonies were counted after 24 h of incubation at 37 °C.

5.2.3 Results and Discussion

Nanoparticles coated with red blood cell (RBC) membrane were prepared using a previously described protocol [29]. Briefly, mouse RBCs were subjected to hypotonic treatment to obtain purified RBC membrane ghosts, which were then fused onto the surface of preformed nanoparticle cores made using poly(lactic-*co*-glycolic acid) (PLGA) through a sonication method. As the RBC membrane coating serves as a natural substrate for the pore-forming Hla, nanotoxoid(Hla) complexes were formed by incubating free Hla with unloaded nanoparticles, herein denoted nanotoxoid(-). Free Hla was subsequently removed from the nanotoxoid(Hla) complexes by size

exclusion chromatography to obtain a purified formulation. Physicochemical characterization showed that the resulting nanotoxoid(Hla) was about 115 nm in diameter and had a surface zeta potential of -32 mV (Figure 5.6A,B), both of which were similar to those of the unloaded nanotoxoid(-), suggesting that toxin insertion did not have a major impact on overall nanoparticle properties. This was further confirmed via transmission electron microscopy (TEM) of negatively stained nanotoxoid(Hla), which revealed that the characteristic core-shell structure of the RBC membrane-coated nanoparticle was preserved even after toxin loading, consistent with what has been previously observed [26, 28](Figure 5.6C).

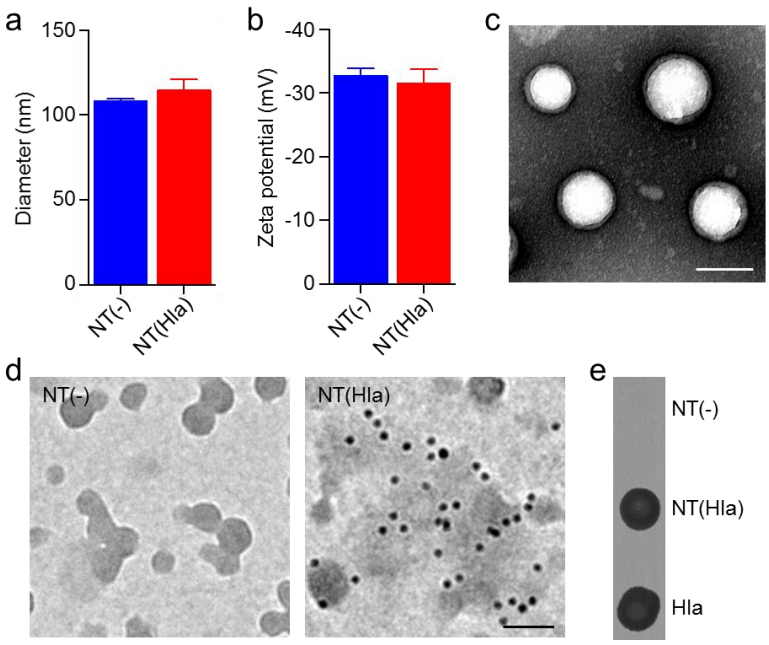

Figure 5.6 Nanotoxoid(Hla) characterization. (A) Size and (B) zeta potential of nanotoxoid(-) [denoted "NT(-)"] and nanotoxoid(Hla) [denoted "NT(Hla)"] (n=3). Error bars represent standard deviation. (C) TEM image of nanotoxoid(Hla) after negative staining with uranyl acetate. Scale bar = 100 nm. (D) TEM images of immunogold-stained NT(-) and NT(Hla) with anti-Hla as the primary immunostain and gold-labeled anti-IgG as the secondary stain. The gold (~10 nm) appears as dark punctates on the images. Scale bar = 100 nm. (E) Dot blotting results using anti-Hla as the primary immunostain. Quantification by image analysis revealed that 95.2% of the Hla input was retained on the final NT(Hla) formulation.

To confirm successful detainment of Hla by the RBC membrane-coated nanoparticles, different immunoassays were performed. On TEM image, Hla-specific antibody labeling of nanotoxoid(Hla) followed by secondary labeling using an immunogold conjugate showed significant colocalization of the electron-dense gold signal with regions of intermediate density occupied by the nanoparticles, indicating a significant presence of Hla-specific epitopes on the nanotoxoid(Hla) (Figure 5.6D). Conversely, nanotoxoid(-) sample subjected to the exact same staining procedure was absent of any gold signal, confirming that the positive signal seen in the nanotoxoid(Hla) was not due to non-specific antibody staining. Dot blot analysis was used to further confirm the presence of Hla on nanotoxoid(Hla) samples (Figure 5.6E). Using anti-Hla as the primary immunostain, nanotoxoid(Hla) gave a positive signal whereas nanotoxoid(-) did not give any discernable signal. As a positive control, free Hla at the initial input concentration used to prepare nanotoxoid(Hla) was tested in parallel, and image analysis of the blot intensities revealed that approximately 95% of the Hla was retained on the nanoparticles after purification, suggesting high affinity of the toxin for the membrane-coated nanoparticles. It has been shown previously that the strong sequestration of toxin by the nanoparticle detainment strategy resulted in little release over time, which effectively neutralized the activity of the toxin and enables safe delivery both *in vitro* and *in vivo* [28].

Next, the ability of the nanotoxoid(Hla) formulation to promote anti-Hla immune responses was studied. Of particular interest was the formation of germinal centers (GCs), which is a critical step in the potentiation of the humoral immune

response against foreign antigens [30, 31]. It is in these regions that B cells mature, and it has been shown that improved retention of antigens via nanoparticle-mediated delivery can better facilitate GC formation [32]. We therefore sought to evaluate lymphatic B cell activation in mice immunized with the nanotoxoid(Hla) formulation. Immunostaining was employed to detect the presence of GCs in the draining lymph nodes (dLNs) of mice immunized subcutaneously with the nanoformulation. PBS and unloaded nanotoxoid(-) were administered as controls. Histological analysis of the dLNs from mice immunized with nanotoxoid(Hla) revealed GL-7^{+} regions characteristic of GC nucleation (Figure 5.7A). In contrast, there was no visual evidence of GC formation in the PBS or nanotoxoid(-) immunization groups, confirming the non-immunogenicity of the naturally derived nanoparticle vector itself [33]. Flow cytometry results (Figure 5.7B) showed that 45.6% of $B220^{+}IgD^{low}$ B cells in the dLNs of the nanotoxoid(Hla) group exhibited a GL-7^{+} germinal center phenotype. In contrast, only 15.7% and 13.6% of cells in mice administered with PBS and nanotoxoid(-), respectively, exhibited the same phenotype.

The ability of nanotoxoid(Hla) to elicit a humoral immune response against Hla was further investigated. Mice were subcutaneously injected with nanotoxoid(Hla), nanotoxoid(-) or PBS on day 0 and were subsequently administered a booster on day 14. The serum of the mice in each group was sampled on days 0, 14 and 35 to assess Hla-specific IgG titers (Figure 5.7C-E). Nanotoxoid(Hla) vaccination elicited significant anti-Hla titers on day 14, and there was a further increase when assayed on day 35. In contrast, the nanotoxoid(-) and PBS vaccinations resulted in no detectable

anti-Hla titers over the course of the study. The nanotoxoid(Hla)-induced antibody responses have previously been shown to be durable, with little to no drop in titers over the course of a five-month period [28]. Taken together, the data demonstrates that the nanotoxoid(Hla) formulation can effectively elicit potent anti-Hla immune responses, despite complete deactivation of the toxin [26]. This is notable finding given that the formulation is absent of immunological adjuvants, which are commonly required for conventional toxoid formulations and help to boost germinal center antibody activity [34].

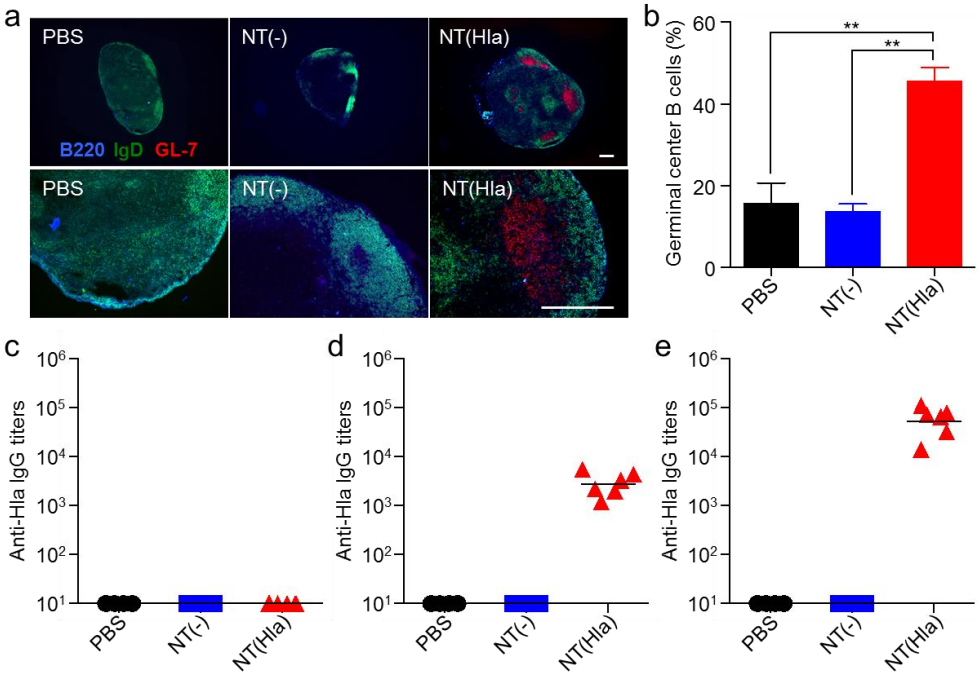

Figure 5.7 Germinal center formation and antibody production induced by nanotoxoid(Hla) vaccination. (A,B) Mice were vaccinated with PBS, nanotoxoid(-) [NT(-)], or nanotoxoid(Hla) [NT(Hla)] (n=3). The draining lymph nodes were collected 21 days later for the analysis of B220 (blue), IgD (green), and GL-7 (red) expression by either immunohistochemistry (A) or flow cytometry (B). Scale bars = 250 μm. For flow cytometric analysis, cells were first gated on $B220^{+}IgD^{low}$ and the numbers reported are the percentage $GL\text{-}7^{+}$ cells within that population. Error bars represent standard error. Statistical significance determined by one-way ANOVA (**P < 0.01). (C-E) Mice were vaccinated with PBS, NT(-), or NT(Hla) on day 0 with a boost on day 14 (n=6). On days 0 (C), 14 (D), and 35 (E), serum was collected and the anti-Hla IgG titers were quantified by ELISA. Lines represent geometric means.

To evaluate the protective capability of the nanotoxoid(Hla) vaccine against MRSA infection, we employed a mouse skin infection model. MRSA represents one of the most common causes of skin infections, both in the community and in hospitals [12]. Because the pathogen is hard to treat with common antibiotics, the infection can quickly progress and lead to serious complications, from physical disfigurement to permanent organ damage, and in many cases even death. For this experiment, mice were immunized with nanotoxoid(Hla) on day 0 and given a booster dose on day 14. Mice injected with nanotoxoid(-) or PBS were used as control groups. On day 35, the mice were subcutaneously challenged with live MRSA bacteria, and the efficacy in the different experimental groups was assessed over time by monitoring the dermonecrotic area resulting from bacterial burden. The progression of skin lesion development in mice immunized with nanotoxoid(Hla) was significantly attenuated compared with mice in the nanotoxoid(-) and PBS groups, which both experienced rapid lesion formation (Figure 5.8A,B). On day 6 post-infection, there was an approximately 5-fold reduction in dermonecrotic area on mice treated with the nanotoxoid(Hla) formulation compared to the control groups.

At the conclusion of the observation period, the bacterial burden was quantified in the infected skin region of each mouse (Figure 5.8C). For the nanotoxoid(-) and PBS groups, the bacterial burden of the infected skin tissue was 1.7×10^7 and 2.2×10^7 CFU, respectively. Mice immunized with nanotoxoid(Hla) showed an average burden of 1.5×10^6 CFU, representing an 11.3- and 14.7-fold reduction compared with the nanotoxoid(-) and PBS groups, respectively. It has previously been

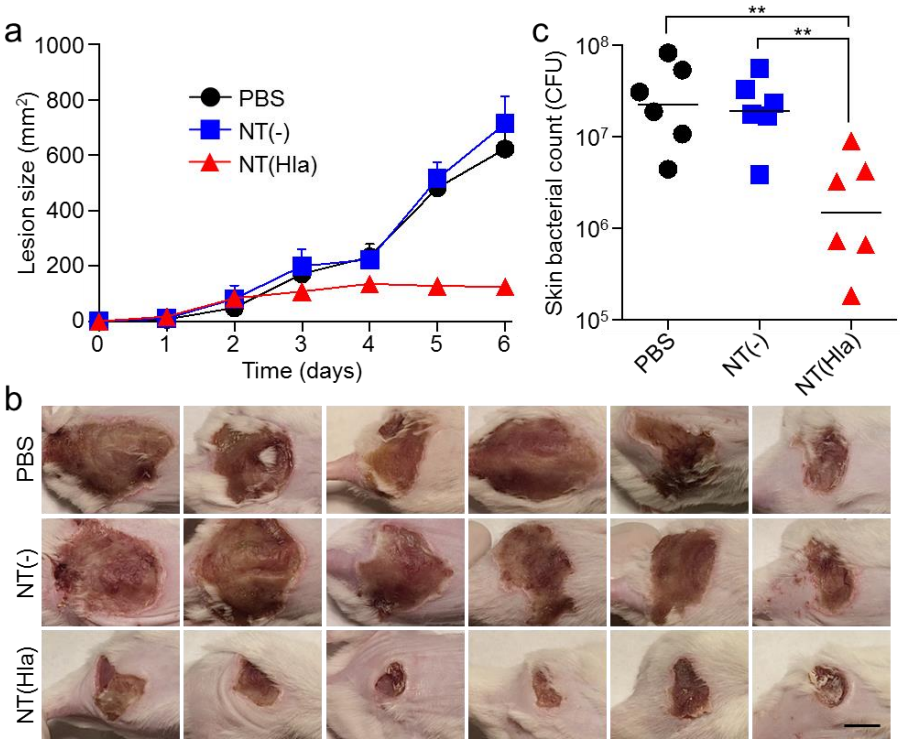

Figure 5.8 Effect of nanotoxoid (Hla) vaccination on MRSA skin colonization. Mice vaccinated with PBS, nanotoxoid(-) [NT(-)], or nanotoxoid(Hla) [NT(Hla)] on days 0 and 14 were challenged subcutaneously with 1 x 10^9 CFU of MRSA bacteria on day 35. (A) The skin lesions were monitored over the course of 6 days (n=6). Lesion size is reported as the product of the largest and smallest dimensions. Error bars represent standard error. (B) Images of skin lesions on day 6 post-infection. Scale bar = 1 cm. (C) On day 6 post-infection, the affected skin and underlying tissue were collected and the bacterial burden enumerated (n=6). Lines represent geometric mean. Statistical significance determined by one-way ANOVA (**$P < 0.01$).

shown that nanotoxoid(Hla) is capable of significantly inhibiting Hla-mediated skin damage in the subcutaneous space, suggesting that the titers generated by the formulation are sufficiently high to enable extravascular neutralizing activity [28]. This prevents the necrotic effect of high Hla concentrations [35], thus preserving integrity of the local tissue. In the present study, the nanoparticle vaccine formulation was likewise able to reduce skin lesion formation, demonstrating its ability to facilitate neutralization of Hla produced by the bacteria *in situ* upon subcutaneous challenge. Given the importance of Hla in MRSA pathogenesis, neutralization of the toxin also

resulted in decreased bacterial burden, likely due to increased clearance by immune cells protected from the cytotoxic activity of Hla [36]. Despite the significant reduction in both lesion formation and bacterial load at the site of infection, the inability of the nanotoxoid(Hla) to completely mitigate disease suggests a sizable role played by other virulence factors, which can serve as targets for future nanotoxoid vaccine formulations.

MRSA infections can quickly progress and enter systemic circulation, leading to a markedly worse prognosis in the clinic [11]. Patients with invasive MRSA can precipitously develop life-threatening infections in different organs such as the blood, heart, bones, and kidneys. As a MRSA skin infection runs the significant risk of further dissemination, the effect of nanotoxoid(Hla) vaccination on MRSA invasiveness after subcutaneous challenge was studied. Mice were vaccinated with nanotoxoid(Hla), nanotoxoid(-), or PBS on day 0 with a booster dose on day 14 and subcutaneously inoculated with MRSA on day 35. On day 6 post-infection, the bacterial counts in the heart, kidneys, spleen, lungs, and liver were analyzed (Figure 5.9). In most of the organs that were analyzed, the nanotoxoid(Hla) group showed a significant drop in bacterial burden compared to the nanotoxoid(-) and PBS control groups. Of note, the kidneys and spleen, two organs that traditionally experience heavy bacterial burden per unit weight [37], both had reductions of approximately two orders of magnitude. The sharp decrease in organ penetration can likely be attributed primarily to better immune management at the site of infection, which results in improved integrity of the skin protective barrier and fewer bacteria entering the

circulation system. Additionally, the presence of high amounts of neutralizing titers within the body can further hamper the capacity of invading MRSA bacteria to colonize individual organs, as shown by previous studies on the effect of anti-Hla vaccination in animal models of sepsis [38]. Overall, the results demonstrate that nanotoxoid(Hla) not only prevents superficial damage, but also decreases MRSA invasiveness, which can ultimately help to prevent many of the harsh complications associated with MRSA infections.

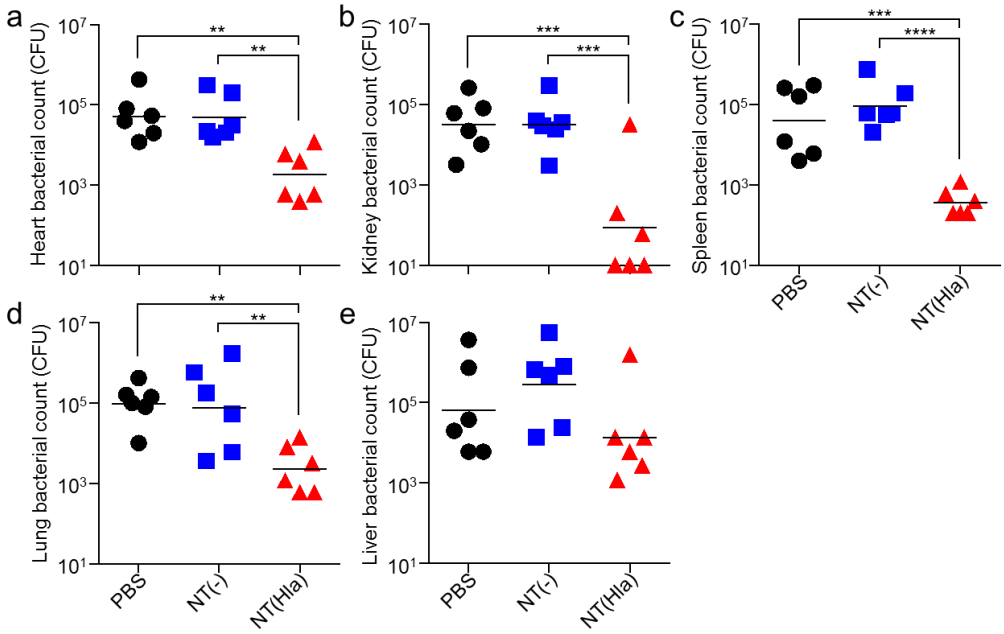

Figure 5.9 Effect of nanotoxoid(Hla) vaccination on MRSA invasiveness. Mice vaccinated with PBS, nanotoxoid(-) [NT(-)], or nanotoxoid(Hla) [NT(Hla)] on days 0 and 14 were challenged subcutaneously with 1 x 10^9 CFU of MRSA bacteria on day 35. On day 6 post-infection, the major organs, including the heart (A), kidneys (B), spleen (C), lungs (D), and liver (E) were collected and the bacterial burden of each was enumerated (n=6). Lines represent geometric means. Statistical significance determined by one-way ANOVA (**P < 0.01, ***P < 0.001 and ****P < 0.0001).

5.2.4 Conclusions

This study investigated the use of nanoparticle-detained toxins for anti-virulence vaccination as a prophylactic strategy against live MRSA skin infection. Such strategies address an important need in the clinical management of bacterial infections as the rise of antibiotic resistance has been difficult to overcome. An increasing emphasis has been placed on novel strategies that transcend traditional treatment paradigms. The nanotoxoid(Hla) has been shown capable of safely delivering the Hla toxin in its native form without the need for subunit engineering or denaturation. Additionally, the anti-Hla titers elicited by the nanoformulation are of high avidity and long-lived. In the present study, we demonstrated that nanotoxoid(Hla) was capable of promoting strong humoral immunity in an adjuvant-free setting via efficient germinal center formation. Using a mouse skin infection model, it was demonstrated that immunity could substantially attenuate the ability of live bacteria to colonize and systemically invade their hosts, which could ultimately abrogate the negative consequences of severe MRSA infections.

Successful validation of nanotoxoid(Hla) vaccination for protection against live MRSA challenge opens the door for further development of similar platforms against many other common yet deadly bacterial pathogens. Pore-forming toxins are one of the most common protein toxins found in nature, and represent a large class of virulence factors that have natural affinity for cell membrane substrates [39], and the reported detainment strategy has been shown effective in neutralizing such toxins secreted by several different organisms, including *Escherichia coli*, *Helicobacter*

pylori, and Staphylococcus aureus [26]. By targeting the common mechanism by which many virulence factors function, nanotoxoids can be applied to an entire class of toxins without specific knowledge of each factor's precise molecular structure. This strategy opens the door for this platform to be used as a diverse vaccine carrier for multi-toxin vaccination, as many pathogens secrete multiple membrane-attacking virulence factors [40]. By presenting multiple virulent antigens, nanotoxoids can further increase vaccine efficacy and limit bacterial colonization. In addition, changing the membrane coating material [41-43] could further broaden applicability to toxins that do not specifically target RBCs. Overall, the nanoparticle-based anti-virulence vaccine platform is primed to help usher in a new generation of treatments that can address some of the most critical needs in the current management of bacterial infection.

5.2.5 References

1. Howard, D.H., R.D. Scott, R. Packard, and D. Jones, *The global impact of drug resistance*. Clinical Infectious Diseases, 2003. **36**(Suppl 1): p. S4-S10.

2. Bush, K., P. Courvalin, G. Dantas, J. Davies, B. Eisenstein, P. Huovinen, G.A. Jacoby, R. Kishony, B.N. Kreiswirth, E. Kutter, S.A. Lenrer, S. Levy, K. Lewis, O. Lomovskaya, J.H. Miller, S. Mobashery, L.J. Piddock, S. Projan, C.M. Thomas, A. Tomasz, P.M. Tulkens, T.R. Walsh, J.D. Watson, J. Witkowski, W. Witte, G. Wright, P. Yeh, and H.I. Zgurskaya, *Tackling antibiotic resistance*. Nature Reviews Microbiology, 2011. **9**(12): p. 894-896.

3. Clatworthy, A.E., E. Pierson, and D.T. Hung, *Targeting virulence: a new paradigm for antimicrobial therapy.* Nature Chemical Biology, 2007. **3**(9): p. 541-548.

4. Ramachandran, G., *Gram-positive and gram-negative bacterial toxins in sepsis: a brief review*. Virulence, 2014. **5**(1): p. 213-218.

5. Rasko, D.A. and V. Sperandio, *Anti-virulence strategies to combat bacteria-mediated disease.* Nature Reviews Drug Discovery, 2010. **9**(2): p. 117-128.

6. Blencowe, H., J. Lawn, J. Vandelaer, M. Roper, and S. Cousens, *Tetanus toxoid immunization to reduce mortality from neonatal tetanus*. International Journal of Epidemiology, 2010. **39**(Suppl 1): p. i102-i109.

7. Kurosky, S., K.L. Davis, and S.J. Karve, *Tetanus toxoid, diphtheria toxoid, and acellular puertussis (Tdap) vaccine compliance among adolescents in the United States*. Value in Health, 2014. **17**(3): p. A278.

8. Cryz, S.J., E. Furer, and R. Germanier, *Effect of chemical and heat inactivation on the antigenicity and immunogenicity of Vibrio cholerae.* Infection and Immunity, 1982. **38**(1): p. 21-26.

9. Kernodle, D.S., *Expectations regarding vaccines nad immune therapies directed against Staphylococcus aureus alpha-hemolysin*. Journal of Infectious Diseases, 2011. **203**(11): p. 1692-1693.

10. Karauzum, H., R.P. Adhikari, J. Sarwar, V.S. Devi, L. Abaandou, C. Haudenschild, M. Mahmoudieh, A.R. Boroun, H. Vu, T. Nguyen, K.L. Warfield, S. Shulenin, and M.J. Aman, *Structurally designed attenuated subunit vaccines for S. aureus LukS-PV and LukF-PV confer protection in a mouse bacteremia model*. PLoS One, 2013. **8**(6): p. e65384.

11. Klevens, R.M., M.A. Morrison, J. Nadle, S. Petit, K. Gershman, S. Ray, L.H. Harrison, R. Lynfield, G. Dumyati, J.M. Townes, A.S. Craig, E.R. Zell, G.E. Fosheim, L.K. McDougal, R.B. Carey, and S.K. Fridkin, *Invasive methicillin-resistant Staphylococcus aureus infections in the United States*. JAMA, 2007. **298**(15): p. 1763-1771.

12. Lowy, F.D., *Staphylococcus aureus infections*. New England Journal of Medicine, 1998. **339**(8): p. 520-532.

13. Rivera, A.M. and H.W. Boucher, *Current concepts in antimicrobial therapy against select gram-positive organisms: methicillin-resistant Staphylococcus aureus, penicillin-resistant pneumococci, and vancomycin-resistant enterococci*. Mayo Clinic Proceedings, 2011. **86**(12): p. 1230-1243.

14. Boucher,H., L.G. Miller, and R.R. Razonable, *Serious infections caused by methicillin-resistant Staphylococcus aureus*. Clinical Infectious Diseases, 2010. **51**(Suppl 2): p. S183-S197.

15. Otto, M., *Basis of virulence in community-associated methicillin-resistant Staphylococcus aureus*. Annual Review of Microbiology, 2010. **64**: p. 143-162.

16. Li, M., B.A. Diep, A.E. Villaruz, K.R. Braughton, X.F. Jiang, F.R. Deleo, H.F. Chambers, Y. Lu, and M. Otto, *Evolution of virulence in epidemic community-associated methicillin-resistant Staphylococcus aureus*. Proceedings of the National Academy of Sciences USA, 2009. **106**(14): p. 5883-5888.

17. Wardenburg, J.B. and O. Schneewind, *Vaccine protection against Staphylococcus aureus pneumonia*. Journal of Experimental Medicine, 2008. **205**(2): p. 287-294.

18. O'Reilly, M., J.C. de Azavedo, S. Kennedy, and T.J. Foster, *Inactivation of the alpha-haemolysin gene of Staphylococcus aureus 8325-4 by site-directed mutagenesis and studies on the expression of its haemolysins*. Microbial Pathogenesis, 1986. **1**(2): p. 125-138.

19. Kennedy, A.D., J.B. Wardenburg, D. J. Gardner, D. Long, A.R. Whitney, K.R. Braughton, O. Schneewind, and F.R. DeLeo, *Targeting of alpha-hemolysin by active or passive immunization dectreases severity of USA300 skin infection in a mouse model*. Journal of Infectious Diseases, 2010. **202**(7): p. 1050-1058.

20. Moon, J.J., B. Huang, and D.J. Irvine, *Engineering nano- and microparticles to tune immunity*. Advanced Materials, 2012. **24**(28): p. 3724-3746.

21. Fang, R.H., A.V. Kroll, and L. Zhang, *Nanoparticle-based manipulation of antigen-presenting cells for cancer immunotherapy*. Small, 2015. **11**(41): p. 5483-5496.

22. Tao, Y., E.G. Ju, Z.H. Li, J.S. Ren, and X.G. Qu, *Engineered CpG-antigen conjugates protected gold nanoclusters as smart self-vaccines for enhanced immune response and cell imaging*. Advanced Functional Materials, 2014. **24**(7): p. 1004-1010.

23. Balmert, S.C. and S.R. Little, *Biomimetic delivery with micro- and nanoparticles*. Advanced Materials, 2012. **24**(28): p. 3757-3778.

24. Li, Z., K. Dong, Y. Zhang, E. Ju, Z. Chen, J. Ren, and X. Qu, *Biomimetic nanoassembly for targeted antigen delivery and enhanced Th1-type immune response*. Chemical Communications, 2015. **51**(88): p. 15975-15978.

25. Li, Z. Z. Liu, M. Yin, X. Yang, J. Renm, and X. Qu, *Combination delivery of antigens and CpG by lanthanides-based core-shell nanoparticles for enhanced*

immune response and dual-mode imaging. Advanced Healthcare Materials, 2013. **2**(10): p. 1309-1313.

26. Hu, C.M., R.H. Fang, J. Copp, B.T. Luk, and L. Zhang, *A biomimetic nanosponge that absorbs pore-forming toxins*. Nature Nanotechnology, 2013. **8**(5): p. 336-340.

27. Wang, F., W. Gao, S. Thamphiwatana, B.T. Luk, P. Angsantikul, Q. Zhang, C.M. Hu, R.H. Fang, J. Copp, D. Pornpattananangkul, W. Lu, and L. Zhang, *Hydrogel retaining toxin-absorbing nanosponges for local treatment of methicillin-resistant Staphylococcus aureus infection*. Advanced Materials, 2015. **27**(22): p. 3437-3443.

28. Hu, C.M., R.H. Fang, B.T. Luk, and L. Zhang, *Nanoparticle-detained toxins for safe and effective vaccination*. Nature Nanotechnology, 2013. **8**(12): p. 933–938..

29. Copp, J.A., R.H. Fang, B.T. Luk, C.M. Hu, W. Gao, K. Zhang, and L. Zhang, *Clearance of pathological antibodies using biomimetic nanoparticles*. Proceedings of the National Academy of Sciences USA, 2014. **111**(37): p. 13481–13486.

30. Moon, J.J., H. Suh, M.E. Polhemus, C.F. Ockenhouse, A. Yadava, and D.J. Irvine, *Antigen-displaying lipid-enveloped PLGA nanoparticles as deliveyr agenst for a Plasmodium vivax malaria vaccine*. PLoS One, 2012, **7**(2): p. e31472.

31. McHeyzer-Williams, L.J. and M.G. McHeyzer-Williams, *Antigen-specific memory B cell developemt*. Annual Review of Immunology, 2005. **23**: p. 487-513.

32. Moon, J.J., H. Suh, A.V. Li, C. F. Ockenhouse, A. Yadava, and D.J. Irvine, *Enhancing humoral responses to a malaria antigen with nanoparticle vaccines that expand Tfh cells and promote germinal center induction*. Proceedings of the National Academy of Sciences USA, 2012. **109**(4): p. 1080-1085.

33. Rao, L., L.L. Bu, J.H. Xu, B. Cai, G.T. Yu, X. Yu, Z. He, Q. Huang, A. Li, S.S. Guo, W.F. Zhang, W. Liu, Z.J. Sun, H. Wang, T.H. Wang, and X.Z Zhao, *Red blood cell membrane as a biomimetic nanocoating for prolonged circulation time and reduced accelerated blood clearance*. Small, 2015. **11**(46): p. 6225-6236.

34. DeFranco, A.L., D.C. Rookhuizen, and B. Hou, *Contribution of Toll-like receptor signaling to germinal center antibody responses*. Immunological Reviews, 2012. **247**(1): p. 64-72.

35. Berube, B.J. and J. Bubeck Wardenburg, *Staphylococcus aureus α-toxin: nearly a century of intrigue*. Toxins, 2013. **5**(6): p. 1140-1166.

36. Miller, L.S. and J.S. Cho, *Immunity against Staphylococcus aureus cutaneous infections*. Nature Reviews Immunology, 2011. **11**(8): p. 505-518.

37. Kokai-Kun, J.F., T. Chanturiya, and J.J. Mond, *Lysostaphin as a treatment for systemic Staphylococcus aureus infection in a mouse model*. Journal of Antimicrobial Chemotherapy, 2007. **60**(5): p. 1051-1059.

38. Adhikari, R.P., H. Karauzum, J. Sarwar, L. Abaandou, M. Mahmoudieh, A.R. Boroun, H. Vu, T. Nguyen, V.S. Devi, S. Shulenin, K.L. Warfield, and M.J. Aman, *Novel structurally designed vaccine for S. aureus α-hemolysin: protection against bacteremia and pneumonia*. PLoS One, 2012. **7**(6): p. e38567.

39. Fang, R.H., B.T. Luk, C.M. Hu, and L. Zhang, *Engineered nanoparticles mimicking cell membranes for toxin neutralization*. Advanced Drug Delivery Reviews, 2015. **90**: 69-80.

40. Aman, M.J. and R. P. Adhikari, *Staphylococcal bicomponent pore-forming toxins: targets for prophylaxis and immunotherapy*. Toxins, 2014. **6**(2): p. 950-972.

41. Fang, R.H., C.M. Hu, B.T. Luk, W. Gao, J.A. Copp, Y. Tai, D.E. O'Connor, and L. Zhang, *Cancer cell membrane-coated nanoparticles for anticancer vaccination and drug delivery*. Nano Letters, 2014. **14**(4): p. 2181–2188.

42. Hu, C.M., R.H. Fang, K.C. Wang, B.T. Luk, S. Thamphiwatana, D. Dehaini, P. Nguyenm, P. Angstanikul, C.H. Wen, A.V. Kroll, C. Carpenter, M. Ramesh, V. Qu, S.H. Patel, J. Zhu, W. Shi, F.M. Hofman, T.C. Chen, W. Gao, K. Zhang, S. Chien, and L. Zhang, *Nanoparticle biointerfacing by platelet membrane cloaking*. Nature, 2015. **526**(7571): p. 118121.

43. Gao, W., R.H. Fang, S. Thamphiwatana, B.T. Luk, J. Li, P. Angsantikul, Q. Zhang, C.M. Hu, and L. Zhang, *Modulating antibacterial immunity via bacterial membrane-coated nanoparticles*. Nano Letters, 2015. **15**(2): p. 1403-1409.

Chapter 5, in full, is a reprint of the material as it appears in *Nature Nanotechnology*, 2013, Che-Ming Hu, Ronnie Fang, Brian Luk, and Liangfang Zhang, and *Advanced Functional Materials*, 2014, Fei Wang, Ronnie Fang, Brian Luk, Che-Ming Hu, Soracha Thamphiwatana, Diana Dehaini, Pavimol Angsantikul, Ashley Kroll, Zhiqing Pang, Weiwei Gao, Weiyue Lu, and Liangfang Zhang. The dissertation author was a major contributor and co-author of these papers.

Chapter 6

Conclusions

6.1 Understanding the Fundamentals of Membrane Coating

The unique structural features and stealth properties of the recently developed red blood cell membrane-cloaked nanoparticle (RBC-NP) platform raise curiosity over the interfacial interactions between natural cellular membranes and polymeric nanoparticles substrates. RBC membranes completely cover negatively charged polymeric nanoparticles in a right-side-out orientation and enhance the polymer cores' colloidal stability. The hydrophilic glycans and the negatively charged sialic acid residues present on RBC membranes contribute to the structural organization of RBC-NPs, which possess a unilamellar, right-side-out membrane cloak. This membrane cloaking process is applicable to negatively charged particle substrates with a diameter ranging from at least 65 to 340 nm. Upon cloaking, the resulting membrane-coated nanoparticles faithfully possess the complicated surface chemistry of natural cellular membranes. Nanoparticles coated with red blood cell membranes were endowed with the "marker-of-self" CD47 imunomodulatory protein at an equivalent density to natural RBCs. By translocating the membrane in its entirety and all the associated membrane proteins onto a nanoparticle substrate, the resulting nanoparticle then possesses the same functionalities as the original cell. These in-depth examinations of RBC-NPs provide a closer look at the fusion process between RBC membranes and synthetic nanoparticles. This coating process presents a robust and versatile approach for interfacing biological components with synthetic nanomaterials, and paves the way for the development of novel bio-inspired and biomimetic nanodevices.

6.2 Cell Membrane-Coated Nanoparticles for Targeted Biomimetic Nanodelivery

Red blood cell membrane-coated nanoparticles (RBC-NPs) represent a promising drug delivery platform due to the ability of the particles to circulate for extended periods of time in the blood stream. RBC-NPs were able to efficiently deliver a model chemotherapeutic drug, doxorubicin, to solid tumor sites for significantly improved tumor growth inhibition compared with conventional free drug treatment. The RBC-NPs also demonstrated excellent immunocompatibility as well as an advantageous safety profile compared with free drug, making them attractive for potential translation. The surface of RBC-NPs can be modified with active targeting ligands that serve to improve the accumulation of nanoparticles at sites of interest. A lipid-insertion method is used to circumvent the need for the particles to come into contact with harsh solvents and reagents that are normally required for conjugation techniques. The technique can easily be generalized to a variety of targeting ligands, ranging from small molecules to much larger biomacromolecules. In addition, the inherent characteristics of cell membranes can be exploited for active targeting. By coating nanoparticles with platelet membrane, nanoparticles can be formulated that take advantage of natural biological interactions to target drugs to sites of damaged vasculature as well as invasive pathogens. The cell membrane coating strategy provides a new class of nanomedicine for targeted therapeutics.

6.3 Cell Membrane-Coated Nanoparticles as "Nanosponges" for Biodetoxification

Coating polymeric nanoparticles with natural cell membranes enables new applications that would otherwise be extremely difficult to achieve using traditional synthetic approaches. One example is to serve as a "nanosponge" to soak up harmful molecules within the body such as pore-forming toxins that attack membrane structures, toxic organophosphates that inhibit neurological functions, and autoantibodies that target normal healthy cells in the body. By targeting the working mechanism behind each of these pathological entities, RBC-NPs can bind and neutralize a wide range of toxins. It was shown that RBC-NPs are capable of neutralizing α-hemolysin, the main hemolytic toxin secreted by methicillin-resistant *Staphylococcus aureus*. This provides a treatment strategy for an otherwise difficult to treat infection. In both preventative and therapeutic settings, the RBC nanosponges were able to divert the toxins away from their natural targets and improve the survival of mice injected with a lethal dose of the toxin. Further, RBC nanosponges could effectively neutralize organophosphates, which are poisons commonly found in insecticides and nerve agents and can cause neuromuscular disorders. RBC-NPs could also be used to treat some autoimmune diseases by diverting autoantibodies away from cells, thereby reducing the presence of associated symptoms. With many more applications to be explored, cell membrane-coated nanoparticles present a facile means of targeting a wide range of toxic molecules for detoxification.

6.4 Cell Membrane-Coated Nanoparticles for Vaccine Technology

Lastly, cell membrane-cloaked nanoaprticles have been shown to be an effective strategy for vaccine technology. Nanosponge-toxin complexes can be used to generate immunity against pore-forming virulence factors. For example, a nanotoxoid formulation of α-hemolysin bound to RBC-NPs was shown to be completely safe while also generating a high and long-lasting specific antibody titer response against the toxin. The anti-α-hemolysin antibodies produced naturally *in vivo* were able to mitigate almost all adverse effects associated with the administration of the toxin in both an intravenous and subcutaneous setting. In addition, this nanotoxoid strategy can be used for the treatment of bacterial infections. Vaccination with the α-hemolysin/nanosponge complex in mice effectively triggered the formation of germinal centers that induced high anti-α-hemolysin titers, which resulted in the inhibition of skin lesion formation by live methicillin-resistance *Staphylococcus aureus* (MRSA). The vaccination not only reduces the development of skin lesions at the site of bacterial challenge, but also serves to reduce the invasiveness of MRSA, preventing dissemination into other organs. Overall, this biomimetic nanoparticle-based toxin detainment strategy represents a promising new paradigm for the development of potent targeted nanoparticle-based vaccines.